

Title	Design and characterization of InP based Mach-Zehnder modulators at 2µm wavelength
Authors	Sadiq, Muhammad Usman
Publication date	2016
Original Citation	Sadiq, M. U. 2016. Design and characterization of InP based Mach-Zehnder modulators at 2µm wavelength. PhD Thesis, University College Cork.
Type of publication	Doctoral thesis
Rights	© 2016, Muhammad Usman Sadiq. - http://creativecommons.org/licenses/by-nc-nd/3.0/
Download date	2023-05-04 16:11:42
Item downloaded from	http://hdl.handle.net/10468/3485

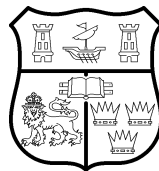
Design and Characterization of InP based Mach-Zehnder Modulators at $2\mu\text{m}$ wavelength

Muhammad Usman Sadiq

M.Sc

112220001

**Thesis submitted for the degree of
Doctor of Philosophy**



NATIONAL UNIVERSITY OF IRELAND, CORK

SCHOOL OF SCIENCE
DEPARTMENT OF PHYSICS
TYNDALL NATIONAL INSTITUTE INSTITUTE

April 2016

Head of Department: Prof. John McInerney

Supervisors: Mr. Brian Corbett
Dr. Brendan Roycroft

Contents

List of Figures	iv
List of Tables	x
List of Acronyms	xi
Acknowledgements	xvi
Abstract	xvii
List of publications	xix
1 Introduction	1
1.1 Evolution of optical communication systems	1
1.2 Optical Modulators	3
1.2.1 Photonic Integration	5
1.2.2 InP based modulators suitable for Photonic Integration	7
1.2.3 Development of InP MZMs 2000-onwards	8
1.3 Motivation of this work	12
1.4 Main contribution and outline of this thesis	13
2 Electro-optic effects in III-V semiconductors	26
2.1 Mach-Zehnder Interferometer	26
2.2 III-V compound semiconductor materials	33
2.3 Light propagation through a medium	36
2.4 Electro-optic effects in III-V semiconductors	37
2.4.1 Linear electro-optic effect	38
2.4.2 Quadratic electro-optic effect	43
2.4.3 Electroabsorption Effect: The Franz-Keldysh effect	44
2.4.4 Electroabsorption Effect: The Quantum Confined Stark Effect	46
2.5 QCSE in shaped quantum well	49
2.5.1 Ramped Quantum wells	50
2.5.2 Refractive index change	53
2.6 Summary	55
3 Traveling wave electrode design	61
3.1 Planar transmission structures	62
3.1.1 Microstrip line	62
3.1.2 Coplanar transmission lines	64
3.2 Electrode selection	66
3.2.1 Lumped electrode	67
3.2.2 Traveling wave electrode	68
3.3 Hybrid co-planar TWE	70
3.4 Electrode design considerations	72
3.4.1 Velocity matching	72
3.4.2 Microwave and optical losses	73
3.4.3 Characteristic impedance	74
3.5 TWE frequency response	74
3.5.1 Case I: Perfect impedance match	77

3.5.2	Case II: Velocity mismatch only	80
3.5.3	Case III: Microwave loss only	81
3.6	Equivalent circuit model	82
3.7	Microwave properties using circuit model	89
3.7.1	Major source of microwave loss	90
3.7.2	Traveling wave electrode optimization	92
3.8	Summary	99
4	InP based TWE Mach-Zehnder modulators at 1.55 μm	104
4.1	Material design and characterization	105
4.1.1	Modulator material design and structure	105
4.1.2	Photoluminescence characterization	107
4.1.3	Modulation efficiency	107
4.2	MMI coupler design and optimization	116
4.3	Modulator characterization	119
4.3.1	DC characterization	121
4.3.2	Electrical small-signal characterization	123
4.3.3	Electro-optic response	129
4.4	Summary	134
5	InP based Mach-Zehnder modulators at 2 μm	139
5.1	The need of InP based MZMs for 2000 nm	140
5.2	Mach-Zehnder modulator - First generation	141
5.2.1	Modulator material design and structure	142
5.2.2	Photoabsorption response	144
5.2.3	Modulator design and layout	146
5.2.4	DC characterization	148
5.2.5	Electrical small-signal characterization	152
5.2.6	Electro-optic response	152
5.3	Mach-Zehnder modulator - Second generation	157
5.3.1	Modulator material design and structure	158
5.3.2	Photoabsorption response	160
5.3.3	DC characterization	160
5.3.4	Modulator electro-optic response	163
5.4	Modulator packaging	165
5.4.1	RF interposer design	165
5.4.2	EM simulation setup and results	169
5.4.3	Experimental verification of packaged modulator	174
5.5	40 Gb/s WDM transmitter	178
5.5.1	Experimental setup for WDM transmission	178
5.5.2	Transmission performance of InP MZM	181
5.6	Summary	183
6	Summary and future work	188
6.1	Summary	188
6.2	Future work	191
6.2.1	DC characterization of n-i-p-n	193

A	Material Properties	200
B	ABCD transmission matrix	201

List of Figures

1.1	Transmission capacity per optical fiber in research and commercial systems [11].	2
1.2	Dimensions and power requirements of C form-factor pluggables formats (CFP) for optical transceivers [19].	5
1.3	Examples of InP based photonic integrated circuits (PICs): (a) 4- and an 8-channel WDM transmitter. A single PIC integrates 74 components on a chip area of $3\text{ mm} \times 5\text{ mm}$ [24]. (b) Four InP MZMs integrated to form dual polarization IQ modulator with multiple monitor and control functions on a $6.4\text{ mm} \times 2.6\text{ mm}$ chip [18].	6
1.4	Layout of InP based IQ modulators using: (a) CPW-TWE [42]. (b) CPS-CL [46].	9
2.1	(a) Schematic of a general Mach-Zehnder modulator structure. (b) Transfer function of modulator for ideally symmetric balanced design ($b = 0$). (c) Transfer function of modulator for non-symmetric design ($b = 0.8$).	28
2.2	(a) Schematic of a general Mach-Zehnder modulator structure with 1×2 MMI and 2×2 MMI at input and output respectively. (b) Schematic of the output 2×2 MMI. The phase difference between two output arms is $\pi/2$	30
2.3	Transfer function of MZM with 2×2 MMI at the output. Blue trace shows the optical power in upper arm and red trace in lower arm.	32
2.4	Measured transfer function of InP based MZM operating at $2\mu\text{m}$. The length of phase shifting electrode is 2.5 mm with reverse bias applied to a single arm only.	32
2.5	RF switching curve of a Mach-Zehnder modulator. Modulator is biased at quadrature point of transfer function.	33
2.6	Lattice constant and bandgap energies of III-V semiconductor materials. The legend on right side shows different optical bands of operation with C and L band of highest interest to telecommunications [9].	34
2.7	(100) InP wafer with $[0\bar{1}1]$ and $[011]$ directions parallel to major flat and minor flat respectively (EU/Japanese standard). The solid circle represents the isotropic ellipsoid of InP crystal in absence of field with refractive index of n in all directions. The dotted ellipse represents the index variation due to LEO.	42
2.8	Example of absorption spectrum in bulk semiconductor with and without external field (F) [9].	45

2.9	(a) Bandgap absorption in thermal equilibrium (No external field). No absorption is allowed for photon with energy $E < E_g$ (b) Electron-hole transition for photon with energy $E < E_g$ due to tilting of bandgap in the Franz-Keldysh effect in the presence of external field.	45
2.10	(a) Electron-hole wave confinement in a typical potential well in the absence of an external field. (b) Deformed wave function with reduced energy level in the presence of an external field. .	48
2.11	Schematic representation of quantum wells in the growth direction in: (a) Wafer A (Ramp up). (b) Wafer B (Ramp down). . .	50
2.12	Normalized photo-absorption spectra for the oppositely ramped MQW structures at different biases (a) Wafer A (Ramp up). (b) The photoabsorption spectrum of Wafer A (Ramp up) at forward bias of 0.4 V. Inset shows the resolved peaks due to e1-lh and e1-hh. (c) Wafer B (Ramp down).	52
2.13	Current-voltage characteristics of 1 mm long metallized ridge with and without TE polarized light at 1550 nm. Inset shows the SEM image of the fabricated sample with $2.5 \mu\text{m}$ wide ridge.	53
2.14	(a) Measured Δn for Wafer A and B for TE polarization. (b) Measured $\Delta\phi$ for Wafer A and B for TE polarization.	54
3.1	Commonly used transmission lines	63
3.2	(a) Schematic of a CPW transmission. (b) Plot of signal pad width vs. gap width for different impedance values at 25 GHz on $100 \mu\text{m}$ InP substrate [27].	65
3.3	Schematic of the capacitively traveling-wave electrode design. This can be seen as EAM or one arm of the MZM [12].	67
3.4	Single arm driven lumped electrode MZM design	68
3.5	Equivalent circuit model of MZM with lumped electrode	68
3.6	Single arm driven traveling wave electrode MZM design. . . .	69
3.7	Co-propagation of electrical and optical waves in lossless velocity matched scenario.	69
3.8	Electric and magnetic field distribution in hybrid coplanar TWE.	71
3.9	Equivalent circuit of traveling wave modulator as single electrical transmission line with load and source impedance	75
3.10	(a) Frequency response of the modulator with with $Z_{mod} = 30 \Omega$ and TWE length of 1 mm for different terminations Z_T . (b) Average voltage of the modulator for different termination values	79
3.11	Frequency response of the modulator with with $Z_{mod} = Z_T = Z_s = 50 \Omega$ and TWE length of 1 mm for different value of microwave index.	80
3.12	Plot of function in Eq 3.15 and its intersection with optical and electrical 3-dB bandwidth.	81

3.13	(a) Cross section of phase shifting electrode. All the structural parameters are defined in Table 3.1. (b) Equivalent circuit model of electrode structure. (c) General transmission line equivalent model.	83
3.14	(a) Equivalent circuit of TWE with source and termination connections.(b) Transmission matrix representation of the equivalent circuit with source and termination connections.	89
3.15	Microwave loss due to different elements of the equivalent circuit shown in Fig 3.13b. Simulated parameters are in listed in Table 3.2.	90
3.16	Influence of specific contact resistance ($\rho_{spec,p}$) on microwave loss.	92
3.17	Transmission line properties as a function of intrinsic region thickness (d_i).	95
3.18	Transmission line properties as a function of ridge width (w_c). .	96
3.19	Transmission line properties as a function of bottom n-conducting layer thickness(d_{nb}).	97
3.20	Transmission line properties as a function of signal metal width (w_m) and electrode gap (w_{gap}). Dotted line shows the ridge width (w_c)	98
4.1	(a) PL wavelength map of the Sample A1593C. The wafer is orientated with major flat on the top.(b) FWHM map for different emission wavelengths across A1593C wafer.	108
4.2	Image of fabricated test ridges with ridge widths varying from 2 μm to 4 μm . Both the P and n metal contacts are on the top. . .	109
4.3	Current-voltage (IV) measurement for metalized 2.0 μm wide ridge waveguide. Inset shows the measured leakage current at the reverse bias of 8 V is 2 μA	109
4.4	Experimental setup showing an optical waveguide device under test.	110
4.5	Schematic of the experimental setup. DC probes were used to apply voltage to the device. Lensed fibres were aligned precisely to the input and output waveguides of the device using XYZ controllers.	110
4.6	Measured TE and TM Fabry-Perot spectrum for ridge of 2.5 μm wide and 1.5 mm long ridge waveguide.	111
4.7	Measured TE polarized Fabry-Perot spectrum for ridge of 2.5 μm wide and 1.5 mm long ridge waveguide over a short wavelength span.	111
4.8	Measured fringe shift as a function of reverse bias for a 1.5 mm long waveguide and 2.5 μm wide ridge: (a) TE Polarization (b) TM Polarization (c) The TE Fabry-Perot fringes for reverse biases of 0 V and 7 V.	113
4.9	(a) Measured refractive index change with applied bias for TE and TM polarizations. (b) Measured phase change with applied bias based on refractive index change.	115

4.10	Schematic representation of (a) 1×2 MMI. (b) 2×2 MMI. . . .	116
4.11	Microscopic image fabricated 2×2 MMI devices with variations in length of an MMI sections.	118
4.12	Trend of coupling loss with deviation from the measured optimum MMI length.	119
4.13	(a) SEM image of fabricated array of InP based MZM devices. (b) Scaled up image of fabricated MZM device.	120
4.14	IV characteristics of fabricated MZM devices. Inset shows the measured leakage current at the reverse bias of 10 V is less than $1 \mu\text{A}$	121
4.15	Normalized optical transmission characteristics for TE polarized input light for: (a) MZM with 1.5 mm electrode length at 1550 nm. (b) MZM with 2.5 mm electrode length at 1550 nm.	122
4.16	Normalized optical transfer function for MZM with 1.5 mm electrode for different input wavelengths for TE polarization.	123
4.17	Schematic of high frequency measurement setup.	124
4.18	Small-signal measurement results for MZM with different TWE lengths. Solids line represent HFSS simulation results: (a) Electrical S_{11} (1.5 mm). (b) Electrical S_{21} (1.5 mm). (c) Electrical S_{11} (2.5 mm). (d) Electrical S_{21} (2.5 mm).	125
4.19	(a) Top view of the simulated CPW TWE structure in HFSS. (b) Cross section of the simulated CPW TWE structure (along A-A'). (c) HFSS model of G-S-G bondpads connected back to back.	128
4.20	Extracted transmission line parameters: (a) Characteristic impedance. (b) Microwave loss. (c) Microwave index. Black dotted line represents the optical group index ($n_{opt}=3.8$).	129
4.21	Measured EO response of InP MZM with 1.5 mm TWE.	130
4.22	EO response measurement setup.	131
4.23	Large signal response measurement setup.	132
4.24	Large signal modulation response at 1550 nm: (a) 10 Gb/s. (b) 28 Gb/s.	133
4.25	Measured ER and SNR for 10 Gb/s NRZ eye.	133
5.1	Variation of bandgap by increasing In composition from 0.53 to 0.85 in bulk $\text{In}_x\text{Ga}_{1-x}\text{As}$. Red dots show the measured bandgap variation in 10 nm thick quantum well. Dotted line represents the lattice constant of InP [8].	143
5.2	(a) Photoabsorption measurement setup. (b) Sample under test with DC probes to apply the reverse bias. Visible green light is used to show the surface normal illumination.	145
5.3	(a) Bias dependent spectral response of 15 quantum well strain-balanced structure under surface normal illumination. (b) Exciton absorption peak wavelength with the applied reverse voltage.	146
5.4	(a) Mask layout of a single MZM showing RF GSG pads, DC phase control electrodes, input and output MMIs. (b) Dimensions of the input/output RF GSG pad.	147

5.5	(a) SEM image of the fabricated devices with different lengths of phase shifting arm. (b) Measurement showing the leakage current with varying length of the phase shifting arm.	149
5.6	DC testing of a single modulator device. Reverse bias is applied to single arm of the modulator through DC probes.	150
5.7	(a) Optical transmission characteristics of modulator as a function of DC voltage supplied to one arm of the interferometer. (b) Dual-electrode (push-pull) operation of modulator.	151
5.8	Measured Electrical S-parameters for devices with different electrode length: (a) S11. (b) S21.	153
5.9	EO response measurement setup at 2000 nm.	155
5.10	Large signal response measurement setup.	156
5.11	Measured EO response of the 2 mm TWE MZM at a bias voltage of 6.74 V.	157
5.12	Measured optical eye diagram at 10 Gb/s for 2^7-1 PRBS signal.	157
5.13	Simulated mode profile in 2 μm deep etched ridge structure using Fimmwave by PhotonD: (a) 15 MQW (47 % confinement). (b) 25 MQW (72 % confinement).	159
5.14	Measured capacitance-voltage properties of the circular diodes.	159
5.15	(a) Bias dependent spectral response of 25 quantum well strain-balanced structure under surface normal illumination. (b) Excitonic peak shift with the applied reverse bias measured for the PIN diode structures with 15 and 25 multiple quantum wells.	162
5.16	MZM transmission response with reverse bias applied to a single arm of modulator with 25 quantum wells. The length of phase shifting arm is 2.0 mm.	163
5.17	(a) Normalized EO response for modulators based on 15 and 25 MQWs. (b) Measured NRZ eye diagram of the 25 MQW modulator at 10 Gb/s.	164
5.18	Layout of the mini-SMP connector from Pasternack (PE 44490). The dimensions in square brackets are in mm.	166
5.19	(a) Cross section CBCPW with finite width side ground planes. Solid lines show the CBCPW mode and dashed line show the parallel plate (PPL) mode. (b) Plan view of CBCPW. L_g is the length and W_g is width of ground plane.	167
5.20	Layout of the RF interposer.	169
5.21	3-D simulation model in HFSS.	170
5.22	HFSS simulation results of the interposer structure with different number of vias (a) S21. (b) S11.	171
5.23	Plan view of the different structures simulated in HFSS: (a) RF interposer wire bonded to MZM with discontinuous ground. (b) RF interposer wire bonded to MZM with continuous ground and additional BWs. (c) Scaled up image of wire bond transition of RF interposer to MZM with dimensions.	173

5.24	Simulation results of RF interposer wire bonded to a MZM device. Blue trace represents the MZM with discontinuous ground + RF interposer, red trace shows the the MZM with continuous ground + RF interposer and green trace represents the MZM device only. (a) S21. (b) S11.	174
5.25	Array of fabricated RF interposer boards before soldering of the connectors.	175
5.26	CAD model of the mounting assembly designed for testing of the packaged modulator.	175
5.27	(a) Image of the fabricated off-chip termination resistor. (b) Image of test bench with packaged modulator device. (c) Optical image of the packaged InP MZM chip. Inset shows the measured diagram at 10Gb/s after packaging.	176
5.28	Delamination of bondpad during wire bonding process.	177
5.29	WDM transmission experimental setup.	180
5.30	Transmission spectra of the HC-PBGF sample used in the experiment; black trace: attenuation of the as-drawn fiber; red trace: insertion loss of the pigtailed sample. The inset shows an optical microscope image of the HC-PBGF [7].	181
5.31	WDM spectrum before (after 1st TDFA) and HC-PBGF transmission.	181
5.32	BER vs. OSNR performance of individual externally modulated WDM channels on 100 GHz grid after transmission over 1.15 km HC-PBGF.	182
5.33	Eye diagram of NRZ-OOK externally modulated channel after transmission at: (a) 1994.00 nm. (b) 1995.29 nm.	182
6.1	Schematic representation of biasing arrangement for: (a) Conventional p-i-n . (b) n-i-p-n.	192
6.2	(a) Simulated optical coupling between upper and lower waveguide. (b) SEM image of laser to lower waveguide coupler using MGVI approach [5].	193
6.3	Current-voltage characteristics of circular test structure fabricated on n-i-p-n. Measured leakage current is 26 μ A.	194
6.4	(a) Photoabsorption spectra for the n-i-p-n epitaxial layer structure under applied bias showing the phototransistor behavior. (b) Normalized photoabsorption spectra for the n-i-p-n	195
6.5	Measured Δn for TE polarized light at 1550 nm in 1 mm long ridge waveguides. The ridges were fabricated both along [011] direction (perpendicular to major flat) and $[0\bar{1}1]$ (parallel to major flat) for ridge widths of 2.0 and 2.5 μ m.	196
B.1	A two port network.	201

List of Tables

1.1	Major results from research on InP MZMs 2000 - onwards. . . .	11
2.1	P-i-n waveguide orientation dependence on refractive index change.	55
3.1	Definition of structure and material parameters of TWE. . . .	82
3.2	TWE structure parameters used in the simulation.	89
3.3	Contact layer properties for different values of $\rho_{spec,p}$	92
4.1	Epitaxial layer structure grown (Sample: A-1593).	106
4.2	Optimized MMI dimensions (Sample: A-1593 see Table 4.1). . .	118
5.1	Epitaxial layer structure grown (Sample: A-1545).	143
5.2	Epitaxial layer structure grown (Sample: A-1914).	158
5.3	Comparison of 3-dB electrical small-signal bandwidth of MZM devices fabricated on two epitaxial layer structures.	163
5.4	Table listing dimensions of the RF interposer.	169
A.1	Electrical peroperties of InP.	200

List of Acronyms

ASE	Amplified sponatneous emission
BER	Bit error rate
BCB	Benzocyclobutene
CFP	C form-factor pluggables
CPS	Coplanar stripline
CPW	Coplanar waveguide
DC	Direct current
DCA	Digital communication analayzer
DWDM	Dense wavelength division multiplexing
EAM	Electro-absorption modulator
EDFA	Erbium doped fiber amplifier
EO	Electro-optic
ER	Extinction ratio
FKE	Franz-Keldysh effect
FWHM	Full-width half maximum
GaAs	Gallium Arsenide
GSG	Ground signal ground
InAlAs	Indium Aluminum Arsenide
InGaAlAs	Indium Gallium Aluminum Arsenide
InGaAs	Indium Gallium Arsenide
InGaAsP	Indium Gallium Arsenide Phosphide
InP	Indium Phosphide
IQ	Inphase quadrature

LEO	Linear electro-optic effect
LiNbO₃	Lithium Niobate
MMI	Multimode interference
MOVPE	Metal organic vapour phase epitaxy
MSA	Multiple-suppliers agreement
MQW	Multiple quantum well
MZM	Mach-Zehnder modulator
NRZ	Non-return to zero
OOK	On-off keying
OSNR	Optical signal to noise ratio
PM	Polarization multiplexing
PL	Photoluminescence
PRBS	Pseudo-random binary sequence
QAM	Quadrature amplitude modulation
QCSE	Quantum confined Stark effect
QEO	Quadratic electro-optic effect
QPSK	Quadrature phase shift keying
RF	Radio frequency
SSMF	Standard single mode fiber
SNR	Signal to noise ratio
TDFA	Thulium Doped Fiber Amplifier
TE	Transverse electric
TM	Transverse magnetic
TWE	Traveling wave electrode
WDM	Wavelength division multiplexing

I, Muhammad Usman Sadiq, certify that this thesis is my own work and has not been submitted for another degree at University College Cork or elsewhere.

Muhammad Usman Sadiq

*In the Name of Allah, the Most Beneficent, the Most
Merciful.*

Dedicated to the loving memory of my mother.

Acknowledgements

I feel immense pleasure to write this part of thesis that will conclude my unforgettable and life-changing journey of three years and nine months, working as postgraduate student in III-V Photonics Devices group at Tyndall National Institute. It is ending with a lot of good memories which I will cherish the rest of my life. I had an opportunity to work with and learn from a team of many talented people during my PhD. Without their continuous moral support and technical guidance this research work couldn't be accomplished.

First of all, I would like to thank my supervisor Mr. Brian Corbett for accepting me as his PhD student. Despite his engagements and busy schedule, he was always available to solve any problem I ever came across. His encouragement and appreciation always made me work even harder and stay focused to get to the right results. I am also very grateful to my co-supervisor Dr. Brendan Roycroft, who didn't only polish my experimental skills but also taught me how to make the way forward in research. Our long discussions on either simulations or experiments were always very insightful for me.

All the results couldn't be achieved without countless hours spent in clean room by Dr. James O' Callaghan to fabricate these modulators. His presence and witty comments in the meetings were always very delightful. It was a great pleasure working with him. Here, I would like to mention Dr. Kevin Thomas for all the growth runs for the modulator materials. I am also very thankful to Dr. Frank Peters and all the members of PIC group specially Padraic Morissey, Phillip Macaroni and Moises Jezzini for the useful discussions in weekly meetings. Many thanks to Dr. Fatima Gunning and Dr. Hongyou Zhang for their cooperation and support in setting up the transmission experiment in Photonic Systems Lab. I would also like to thank other members of the III-V devices group: John Justice, Nan Ye, Prasanah, Rogero and Joveria.

I would also like to extend my gratitude to all the people with whom I shared my office during these years: Pleun, Mehboob, Farzan, Carmel (I wish you good luck for your new career as a lawyer), Pietro, Donagh and Karim. I will definitely miss our Friday evening squash sessions.

To have your compatriots around you especially when you are thousands of miles away from your home is a blessing. Thank you Asfandyar, Rashid, Omar, Ansar, Ghalib, Rehan, Saim, Junaid, Haroon, Danish and Razaq for your company and friendship. I wish you all best of luck for your future.

I acknowledge with thanks to the Science Foundation Ireland, UCC Department of Physics and Tyndall National Institute for providing me financial support and state of the art resources to undertake this research.

Most of all, I would like to thank my family for their unconditional love and support. Special thanks to my father (Dr. Muhammad Sadiq), brother (Dr. Nouman Sadiq) and sister (Maria Hasan). I couldn't achieve anything without your prayers, believe and backing.

Abstract

In the recent years, the optical fiber transmission systems have seen an explosive surge in traffic, mainly comprising of Internet data generated by the vastly used handheld and portable devices. The rapid growth requires optical modulation data rates of 100 Gb/s and higher, per wavelength channel. In order to scale up the capacity of the current optical fiber systems, the deployment of optical transceivers implementing higher order optical modulation formats is inevitable. Thus research on the next generation photonic systems is not only challenged by the need of the higher data rates, it also needs photonic components which are cost-effective, compact in size with lower power consumption with higher device density on a single chip which is possible through photonic integration on a common platform such as Indium Phosphide (InP).

The Mach-Zehnder modulators (MZMs) based on InP are the key building blocks of such photonic integrated circuits (PICs) due to low drive voltage and higher electro-optic (EO) bandwidth. They are the most suitable candidates to replace the widely deployed large foot print Lithium Niobate (LiNbO_3) based MZMs. This thesis is focused on the design and development of travelling wave InP MZMs operating in the conventional optical C-band and also at 2000 nm which is one of the newly proposed possible alternatives for optical transmission to avoid highly anticipated ‘Capacity Crunch’ in the currently deployed standard single mode fiber (SSMF) in the next decade.

The traveling wave InP MZMs utilize the coplanar waveguide travelling wave electrode (CPW-TWE) structure which is optimized using an equivalent circuit model and 3D electro-magnetic (EM) simulations to maximize the bandwidth of the modulator. Based on different design variables, the main factors limiting the bandwidth performance of the optical modulators are identified. InP MZMs working around the 1550 nm wavelength range were developed and characterized under DC and high frequency in order to validate the optimal TWE design. The modulators achieve a π phase shift in the interferometer arms through the quantum confined Stark effect (QCSE) based electro-refraction in 20 periods of strained InAlGaAs/InAlGaAs multiple quantum wells (MQWs). The modulators demonstrate a DC switching voltage (V_π) of 4.5 V with an 3-dB EO bandwidth of 7.5 GHz with a linear roll-off enabling the large signal performance of the devices upto 28 Gb/s for NRZ modulation.

An important aspect of the presented work is the development of the first InP MZMs for operation around 2000 nm wavelengths for used in future optical transmission systems. To make the operation feasible around 2000 nm wave-

length, compressively strained InGaAs QWs are used in the optical waveguide. Based on the optimized TWE structure, the developed modulators exhibit a 3-dB EO bandwidth of 9 GHz with switching voltage as low as 3.2 V for a 3 mm long electrode. It is also shown that maximizing the electro-optical overlap by increasing the number of quantum wells can significantly reduce the V_π , hence the modulator driving conditions for higher order modulation formats, without sacrificing the EO modulation bandwidth and device dimensions. Further, the devices are packaged using specially designed RF interposer to be used in an efficient, high-capacity WDM transmitter for communication over 1.15 km hollow-core photonic bandgap fiber (HC-PBGF) in the 2 μm spectral region. A WDM capacity of 40 Gb/s is accomplished by using four 10 Gb/s NRZ-OOK externally modulated channels employing the InP MZM for the first time and transmission performance is evaluated using a direct detection receiver.

To further improve the EO bandwidth and V_π of the TWE-CPW based InP MZM, a n-p-i-n structure is also proposed and the DC performance of the test devices is reported.

List of publications

Journal Articles

1. **M. U. Sadiq** et al., "40 Gb/s WDM Transmission Over 1.15-km HC-PBGF Using an InP-Based Mach-Zehnder Modulator at 2 μm ," *Journal of Light-wave Technology*, vol. 34, no. 8, pp. 1706-1711 (2016).
2. **M. U. Sadiq** et al., "A 10 Gb/s InP-based Mach-Zehnder modulator for operation at around 2 μm wavelengths" *Opt. Express* 23(9), pp. 10905-10913 (2015).
3. **M. U. Sadiq** et al., "Study of electro-optic effect in asymmetrically ramped AlInGaAs multiple quantum well structures", *Phys. Status Solidi A*, pp. 930-935 (2015).
4. N. Ye, M. R. Gleeson, **M. U. Sadiq** et al., "InP Based Active and Passive Components for Communication Systems at 2 μm " *Journal of Lightwave Technology* 33(5), pp. 971-975 (2014).

Conference Proceedings

1. N. Kavanagh, **M. U. Sadiq** et al., "Exploring a new transmission window for telecommunications in the 2 μm waveband," *International Conference on Transparent Optical Networks (ICTON)*, Trento, Italy (2016).
2. **M. U. Sadiq** et al., "40 Gbps WDM transmission over 1.15 km HC-PBGF using the first InP-based Mach Zehnder modulator at 2 μm ," *European Conference on Optical Communication (ECOC)*, Valencia, Spain (2015).
3. **M. U. Sadiq** et al., "Experimental Study of Electro-Optic Effect in Asymmetrically Ramped AlInGaAs Multiple Quantum Well Structure" *International Conference on Indium Phosphide and Related Materials*, Santa Barbara, California, USA (2015).
4. **M. U. Sadiq** et al., "Efficient modelling approach for an InP based Mach-Zehnder modulator" *25th Irish Signal and Systems conference*, Limerick, Ireland (2014).

5. P. J. Marraccini, P. E. Morrissey, M. Jezzini, **M. U. Sadiq** et al., “Phase Matched Transmission Line Design for High-Speed Optical Modulators” 25th Irish Signal and Systems conference, Limerick, Ireland (2014).

Chapter 1

Introduction

In the past two decades, there has been a phenomenal increase in the internet data traffic over fiber optic transmission systems which is estimated to be around 40% on average year-on-year depending on the geographical region [1]. This massive growth in data traffic is driven by widespread use of social networking, cloud computing and high bandwidth video streaming services. Almost any network based service we use through our laptops or hand-held devices at some point is converted to photons that travel down a vast network of optical fibers, which is estimated to be two billion kilometers, corresponding to a string of glass which can be wrapped 50,000 times around the globe [2]. According to a recent (2014) visual network index (VNI) report by Cisco [3], the global IP traffic has seen fivefold increase over the past 5 years and a further threefold increase is expected over next 5 years. In addition, by year 2018 the busy-hour internet traffic will reach 1 Pbit/s with average internet traffic of 300 Tb/s and the total number of devices connected to the networks will be three times the total global population. This relentless growth of data volume over decades has been dealt with the huge intrinsic bandwidth of conventional standard single mode fibers (SSMF) through technological evolution.

1.1 Evolution of optical communication systems

The increase of transmission capacity per fiber on yearly basis is shown in Fig 1.1. Since the deployment of optical fiber communication systems in 1970s, the first major breakthrough in terms of fiber capacity was achieved in 1990s, by the availability of wavelength division multiplexing (WDM) and optical amplifiers, which allowed the capacity of system to be enhanced from a few Gb/s to over 1 Tb/s resulting in an increase of capacity by more than 10 000 times [4].

The steep growth in WDM enabled optical transmission capacity was around 2.5 dB/year. This rapid growth also reflects the advancements of electronic, optical and optoelectronic device technologies employed in the fiber optic communication systems in that time frame, leading to the single channel rates up to 10 Gb/s [5]. Dense WDM (DWDM) technology with 50 GHz channel spacing in combination with optical amplification readily populated the available spectrum of ~ 5 THz, which is basically the amplification range of an Erbium doped optical amplifier (EDFA) in optical C-band (1530 – 1565 nm). This rapid growth in capacity slowed down in early 2000 when the optical and electrical bandwidths became equal as the channel rates were increased beyond 10 Gb/s [5]. Simple intensity modulation format (ON/OFF keying) were used for both the channel rates of 2.5 Gb/s up to 10 Gb/s. However, the move to further increase the single channel modulation rate to 40 Gb/s was hindered by the fact that simple intensity modulated signal is highly prone to the fiber impairments such as chromatic dispersion (CD) and polarization mode dispersion (PMD) for data rates > 10 Gb/s, thereby limiting the optical reach for the long-haul optical communication system deployment [6].

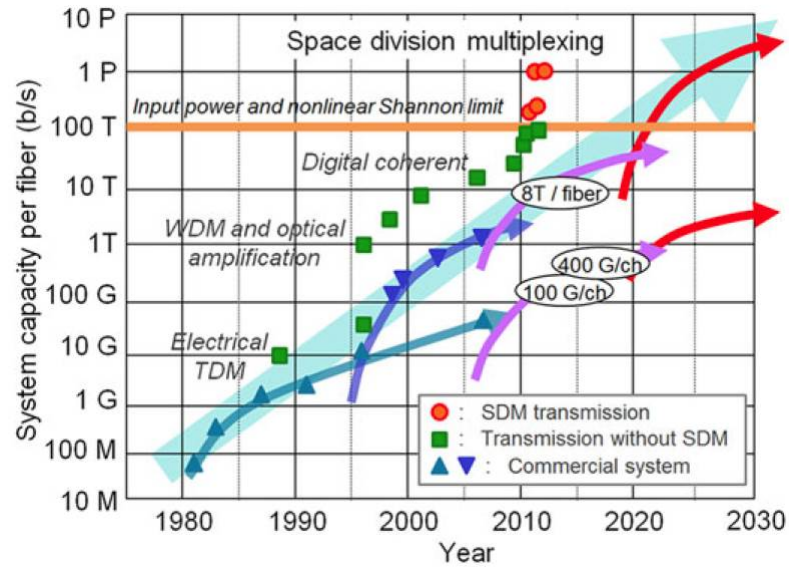


Figure 1.1: Transmission capacity per optical fiber in research and commercial systems [11].

The consequence was the change in research focus to increase the spectral efficiency (SE), which means to pack more information in the 5 THz bandwidth of the Erbium doped fiber amplifier (EDFA) efficiently [5]. From 2002 onwards, much research was performed on advanced optical modulation formats such binary and quaternary phase shift keying (BPSK, QPSK) using direct detection

with differential demodulation (DPSK) [7]. Using 40 Gb/s DPSK modulation format with 50 GHz WDM channel spacing increased the SE to 0.8 b/s/Hz and it allowed long-haul transmission with better optical signal to noise ratio (OSNR) performance using advanced filtering, due to higher resilience to fiber impairments compared to simple intensity modulated 40 Gb/s signal [8,9]. To further increase the SE, hence the system capacity, the transmission systems had rely on the concept of optical parallelism [2]. The SE of ~ 2 b/s/Hz was achieved by using QPSK modulation format, which in combination with polarization division multiplexing (PDM) further increased the SE by another factor of 2 with the reduction in baud rates by a factor of 4 [10]. Thus the use of PM-QPSK enabled the reduction of baud rates or symbol rates for 40 Gb/s and 100 Gb/s data rate to 25 and 10 Gbaud respectively. The reduced symbol rates were within the operational capabilities of fast analogue to digital converters (ADCs) and opened the door for the coherent receivers which were sidelined with the rise of WDM and EDFA technology in early 90s [11]. In addition, it also reduced the high bandwidth requirement on the electro-optics used. The use of digital coherent receivers with advanced signal processing techniques has enabled the commercial deployment of system at 40 Gb/s and 100 Gb/s using PM-QPSK in late 2000 [12–15]. In addition to PM-QPSK, higher order quadrature amplitude modulation (QAM) formats such as 16-QAM, 64 QAM and higher is another option to increase the capacity of the system [16]. However, the major compromise in using these higher order optical modulation formats is the requirement of higher OSNR, which directly translates to the maximum attainable transmission distance before optical regeneration. As the bandwidth demand on optical transmission systems is a continuous process, so future systems will need per channel modulation data rates of 400 Gb/s or even 1 Tb/s with much efficient use of available spectrum which implies that the use of higher order modulation formats will be inevitable [17].

1.2 Optical Modulators

In above section, a brief summary of the evolution of single channel modulation data rates and total capacity per fiber has been discussed. The last decade, specially the past five years has seen the rise in implementation of digital coherent technology complemented by availability of high speed ADCs and advanced DSP based techniques for fiber impairment mitigation [18, 19]. The research on future 100 Gb/s, 200 Gb/s and 400 Gb/s coherent optical transceivers based

on PM-QPSK and PM-M-QAM modulation formats is driven by the three main factors [18]:

- Reduction in foot-print of optical transceiver assemblies
- Low power consumption
- Cost reduction of hardware implementation

A typical coherent optical transceiver is comprised of the following main photonic components, narrow linewidth tunable lasers, high-speed optical modulators, high-speed optical detectors, polarization splitters/combiners and 90° optical hybrids [19]. As the main focus of this work is on the design and implementation of high-speed optical modulators, so I will limit my discussion to modulators only.

To achieve high modulation rates the optical modulators are they key building blocks of optical transmitters assemblies. Lithium Niobate (LiNbO_3) based Mach-Zehnder modulators (MZMs) have been widely deployed in today's advanced optical communication systems. Although, presently MZM technology based on LiNbO_3 is very mature and widely tested. Also, modulators with low switching voltage (V_π), high electro-optic (EO) bandwidth and low insertion loss are available from different vendors. These modulators are widely deployed in different applications ranging from 10 Gb/s to 100 Gb/s transmitters based on either simple ON-OFF keying or advanced modulation formats [19–22]. First generation 100 Gb/s PM-QPSK transceiver systems also used double nested IQ LiNbO_3 modulators. Such transceivers are generally assembled in a industry standard package MSA-168 by combining together discrete photonic components from different vendors through multiple-supplier agreements (MSA) [19, 23]. The major drawbacks of using the LiNbO_3 modulators in such optical transceiver assemblies are:

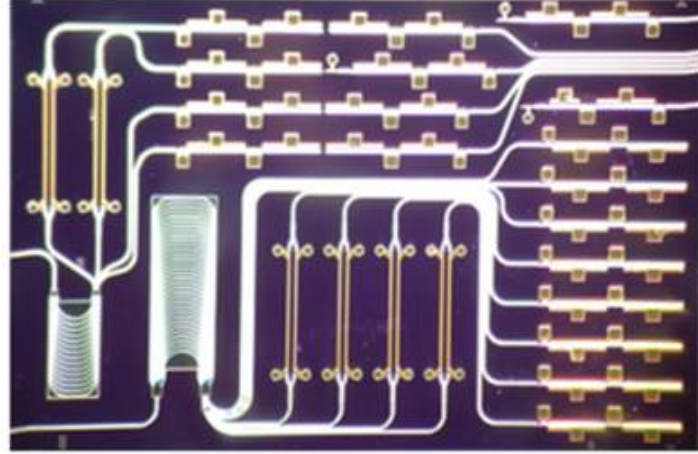
- Large module size of packaged modulator chip.
- Inability to integrate monotonically with other active and passive photonic components.



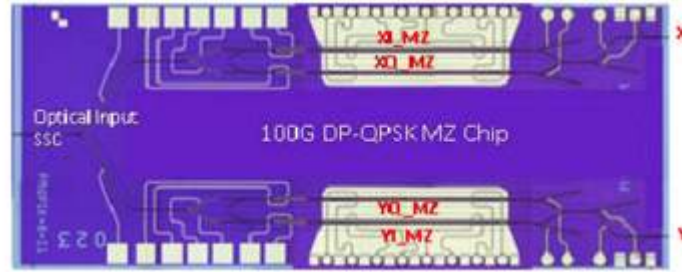
Figure 1.2: Dimensions and power requirements of C form-factor pluggables formats (CFP) for optical transceivers [19].

1.2.1 Photonic Integration

The technology limitations mentioned above will eventually restrict the use of LiNbO_3 MZMs as the second and third generation of optical transceivers will be dominated by the requirement of different set of photonic components as the next level transceiver assemblies are much more compact with lower power dissipation [19, 20]. Next generation pluggable transceiver packages such as CFP, CFP2 are not only much more compact in size but also have expected to operate with lower power dissipation [23]. The size and power requirements of discrete components and different pluggable packages are shown in Fig 1.2. Current and future photonic devices are dictated by the requirements of these pluggables modules and will require a new level of integration in order to reduce the device foot print, increase the device density on a single chip and reduce power dissipation.



(a)



(b)

Figure 1.3: Examples of InP based photonic integrated circuits (PICs): (a) 4- and an 8-channel WDM transmitter. A single PIC integrates 74 components on a chip area of $3 \text{ mm} \times 5 \text{ mm}$ [24]. (b) Four InP MZMs integrated to form dual polarization IQ modulator with multiple monitor and control functions on a $6.4 \text{ mm} \times 2.6 \text{ mm}$ chip [18].

InP based photonic integrated circuits (PICs) address all the requirements of compact device foot print and low power needs of these evolving transceiver modules. PICs based on InP enable the possibility to integrate laser, modulators, semiconductor optical amplifiers (SOAs), photodetectors (PDs) within a single chip. With the advancement in InP based semiconductor growth and processing technology, along with reduction in killer defect densities in InP wafers to a comparable level with Silicon CMOS [24], large scale PICs have become a reality. In addition, the commercial availability InP based generic integration foundaries will be a game changer specially to implement optical transmitter chips operating at 100 Gb/s or beyond [24–26] as highly dense and compact level of photonic integration will be possible at a reduced cost. Generic foundary based integration will also help to realize InP PICs for applications beyond telecommunications such as optical metrology, medical diag-

nostics and gas sensing [24, 25]. Fig 1.3 shows a few examples of InP based PICs. In the recent years several PICs have been demonstrated. First large scale PIC circuit chip with aggregate data rate of 100 Gb/s came in operation on commercial level in 2005 [27]. This chip achieved an aggregate data rate of 100 Gb/s using 10 Distributed feed back (DFB) tunable lasers integrated with 10 eletro-absorption modulators (EAMs) with all modulated channel multiplexed to a single output using arrayed waveguide grating (AWG). Following this several PICs demonstrating aggregate data rate of ranging from 100 Gb/s to multiple Tb/s have been demonstrated using InP based MZMs instead of EAMs to implement advanced PM-QPSK modulation format [25, 28, 29]. Recently, a 2.25 Tb/s InP monolithic integrated coherent transmitter PIC has been demonstrated. This single chip contains 40 \times 57 Gb/s PM-QPSK transmitters (40 DFB tunable lasers, 80 nested MZMs) all integrated together with total of over 1700 integrated functions [30]. Such large scale PIC chips show the potential of InP based technology to realize compact small-form factor compatible optical transceivers.

1.2.2 InP based modulators suitable for Photonic Integration

InP based optical modulators are the main functional blocks of the small-form factor optical transmitter PICs utilizing advanced modulation formats to achieve high data rates per wavelength channel. As mentioned above, the large module size of LiNbO₃ based MZMs makes them incompatible for the coherent pluggable modules. The large size of such modulators is due to the fact that they mainly rely on phase change due to the linear electro-optic effect (LEO) in the LiNbO₃ material, which results in long phase shifting electrodes to achieve lower V_π . Although, the LEO coefficient in InP (~ 1.4 pm/V) based material is 15 to 20 times less than LiNbO₃ (~ 30 pm/V). However, the low value of LEO coefficient can be overcome by the high refractive index of the InP based materials which is usually around 3.5 as compared to 2.2 in LiNbO₃. As the refractive index change due to LEO with applied field is proportional to the cube of refractive index (See section 2.2), which provides a four-fold improvement in over all index change. For the same electric field, the index change in LiNbO₃ based modulator is just ~ 5 times high as compared to InP based MZM. Moreover, refractive index change in InP based MZM devices is further enhanced greatly by quantum confined Stark effect (QCSE) in multiple quantum well structures, this enhancement allows InP based phase MZMs to be compact in size [31]. In addition, photonic integration capability and low power consumption, makes

MZMs on InP platform even more attractive for future generation transmission systems.

InP MZMs based on QCSE for 10 Gb/s optical communications were first reported in early 1990s followed by commercial deployment of 2.5 Gb/s modulators co-packaged with single wavelength lasers in 1995. Due to lack of uniformity in processing technology, InP MZMs were not able to compete with 10 Gb/s LiNbO₃ modulators [32, 33]. Still, due to the potential of integration with lasers and other components, the research on InP MZMs continued and many ground breaking results were achieved in terms of higher EO-bandwidth and lower V_π . Mostly, research on InP based modulators was performed using p-i-n epitaxial layers structure by driving RF electrodes on each inteferometric arms independently [31]. To drive the arms of MZMs either the lumped or coplanar waveguide (CPW) traveling wave electrodes (TWEs) can be used. Another approach is using two interferometric arms in series push-pull by capacitively loading (CL) a coplanar strip (CPS) electrode structure. CL approach was introduced by R.G Walker in [34] in 1991 for Gallium Arsenide (GaAs) based modulators. Fig 1.4 shows the typical implementation of an IQ modulator using two nested InP based MZMs. The major difference between two schemes is that for CPW-TWE IQ modulators four electrical drivers are needed to drive the device in push-pull configuration. While for CPS-CL-TWE, only two electrical drivers are needed.

1.2.3 Development of InP MZMs 2000-onwards

InP MZMs based on either CPW or CPS-CL electrodes have evolved in terms of performance in the last 15 years. A summary of the major contributions in continuous development of InP based MZM developed from 2000 onwards is shown in Table 1.1.

First major result in terms high EO-optic bandwidth was reported by S. Akiyama *et al* [35] in 2002 and it demonstrated a 40 Gb/s eye diagram using MZM based on semi-insulating (SI) InP for the first time. As the capacitance per unit length of a conventional p-i-n structure is usually very high and it is difficult to achieve a 50 Ω impedance until unless the i-region is made thicker which reduces EO efficiency of the modulator increasing V_π . This problem was overcome in [35] by introducing a novel structure by creating small sections of low and high capacitance on phase shifting section, which resulted in better impedance matching and EO bandwidth improvement. Followed by this in 2003, another way to reduce the capacitance and enhance EO bandwidth was introduced by K.

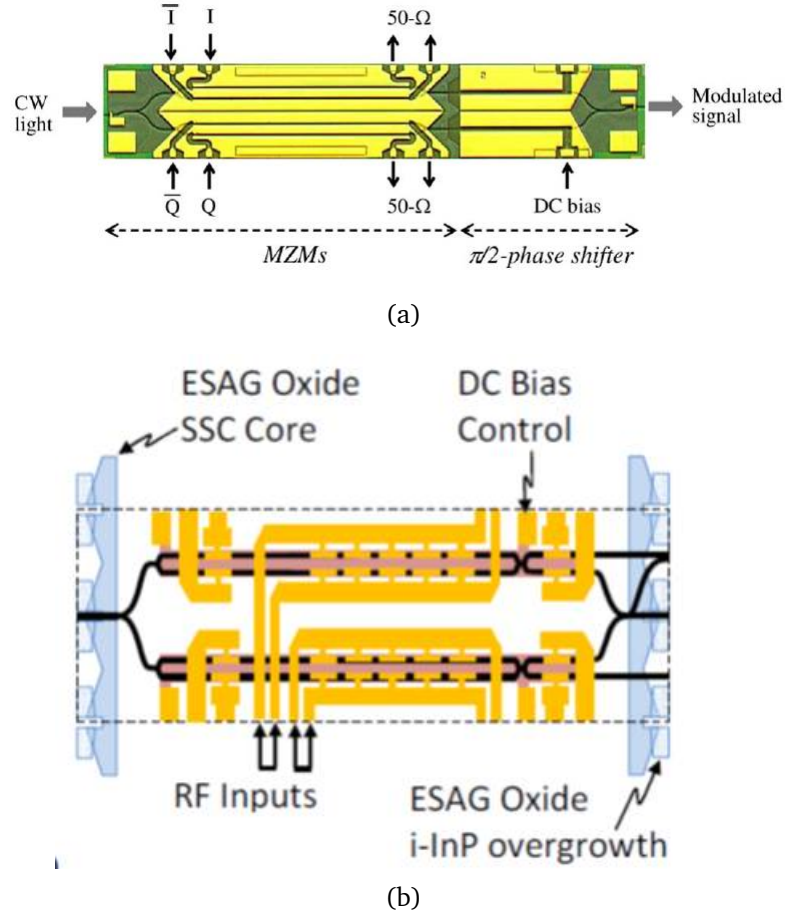


Figure 1.4: Layout of InP based IQ modulators using: (a) CPW-TWE [42]. (b) CPS-CL [46].

Suzuki *et al* in [36] by replacing p-i-n structure with n-i-n structure. This structure allowed a thicker i-region with a Fe-doped InP as current blocking layer to reduce the capacitance at the expense of reduced electro-optic efficiency. However, reduced efficiency was compensated by longer length of phase shifting electrode (3 mm) due to lower electrical and optical losses associated with n-doped InP. In 2004, a 45 GHz EO bandwidth MZM was published by D. Hoffmann *et al* in [37] using capacitive loading (CL) series push-pull arrangement to achieve better impedance match and low chirp. In addition to the higher reported bandwidth, a special feature of the reported device was the integration of a spot size converter (SSC) to reduce the coupling loss (~ 4 dB improvement) between fiber and MZM chip. In the similar year, based on the CL-TWE SI-InP MZM structure, S. Akiyama *et al* [38] reported a 40 GHz EO bandwidth with 3 V V_π which was 2.3 V lower than their previous implementation using CPW in [35]. In year 2005, a negative chirp 10 Gb/s MZM on N^+ InP substrate

with integrated SSCs was demonstrated by Oclaro (Bookham previously) [39]. The device exhibited the lowest insertion loss of 4.5 dB and also showed that chirp conditions can be adjusted by applying different biases to the RF electrodes. Based on the same platform, zero chirp modulation characteristics were demonstrated in 2007 by the same group by including DC phase imbalance electrodes [40]. In the same year, the group at Fraunhofer HHI presented their SI-InP modulator based on CL-TWE with improved bandwidth of 45 GHz and 63 GHz with further optimizations in electrode design suitable for 80 Gb/s NRZ modulation [41].

Another design of InP MZM was demonstrated by N. Kikuchi *et al* in 2007 but this time using n-p-i-n structure. In this design a p-doped layer acted as the current blocking layer. Using two such modulators integrated as an IQ nested structure in push-pull mode ($V_{\pi}=1.5$ V) 80 Gb/s data rate using DQPSK modulation format was reported [42]. In the following year, similar group presented the SOA integrated MZM to overcome the insertion loss of the modulator but only operating at 10 Gb/s [43].

From 2008 till now, all the modulators described above served as a basic platform for further improvements in EO bandwidth and switching voltage through RF engineering and MQW material optimization. With the development of these compact and low drive voltage modulators, the main emphasis of the research was to establish the applicability of these MZM devices to implement higher order modulation formats to enhance the data rate per wavelength.

The results of implementation of advanced modulation formats using the InP MZMs in IQ nested arrangement have been published by a number of groups in recent years. A 40 Gb/s DQPSK per wavelength channel was demonstrated by many groups from 2008-2009 [44, 45]. In 2010, 45.6 Gb/s per channel was achieved using external polarization multiplexed (PM-DQPSK) by Infinera [28]. Following this work, there has been a continuous improvement in per wavelength channel data rate. A transmitter capable of 160 Gb/s PM-QPSK using CL SI-InP MZM monolithically integrated in IQ arrangement was demonstrated in 2011 by Fraunhofer HHI [46]. In the same year, 112 Gb/s per wavelength using PM-QPSK was demonstrated by Infinera [29]. In 2013, another InP MZM transmitter module based on CPW electrode demonstrated the suitability for 128 Gb/s DP-QPSK was presented by Sumitomo Electric Industries [47]. In this work, the IQ modulators for both the polarization states were fabricated on a single chip. In 2014, Oclaro demonstrated fully integrated dual IQ InP MZM modulator on N^+ InP substrate with the improvement in EO band-

Table 1.1: Major results from research on InP MZMs 2000 - onwards.

Organization /Year	Structure	MQW	V_π (V)	EO-Bandwidth (GHz)	Electrode type
Fujitsu/2002 [35]	p-i-n	25 InGaAsP/InGaAsP	5.3	26	CPW
NTT/2003 [36]	n-i-n	13 InAlGaAs/InAlAs	2.2	40	CPW
Fraunhofer HHI/2004 [37]	p-i-n	20 InGaAsP/InGaAsP	2.2	45	CL
Fujitsu/2004 [38]	p-i-n	33 InGaAsP/InGaAsP	3.0	40	CL
Oclaro/2005 [39, 40]	p-i-n	20 InGaAsP/InGaAsP	4.0	~15	lumped
Fraunhofer HHI/2007 [41]	p-i-n	20 InGaAsP/InGaAsP	2.8	63	CL
NTT/2007 [42]	n-p-i-n	InAlGaAs/InAlAs	1.5	30	CPW
Infinera/2008 [44]	p-i-n	ND	2-2.5	suitable for 20 Gb/s	ND
Oclaro/2009 [45]	p-i-n	InGaAsP/InGaAsP	<3.5	15	lumped
Infinera/2010 [28]	p-i-n	ND	2-2.5		ND
Fraunhofer HHI/2011 [46]	p-i-n	20 InGaAsP/InGaAsP	2.5	> 40	CL
Sumitomo Electric/2013 [47]	p-i-n	InAlGaAs/InAlGaAs	1.8	> 40	CPW
Oclaro/2014 [18]	p-i-n	36 InAlGaAs/InGaAs	$V_{2\pi} < 5$	>20	CPW
NTT/2014 [48]	n-i-p-n	InAlGaAs/InAlAs	2.9	-	-
Teraxion/2015 [49]	p-i-n	32 InGaAsP/InGaAsP	1.5	>40	CL
This work/2016	p-i-n	20 InAlGaAs/InAlGaAs	4.5*	~ 7.5 suitable for 28 Gb/s	CPW
This work/2016** [50, 51]	p-i-n	25 InGaAs/InAlGaAs	2.7*	9	CPW

ND: Not disclosed

*: Single arm driven

**: MZM developed for operation around 2000 nm

width of individual MZM to 20 GHz [18]. In the same year, n-i-p-n epitaxial structure for realizing InP MZM was proposed by NTT, where p-doped (Zn as p-dopant) InAlAs layer was used as a current blocker [48]. The authors suggested that this structure allows InP MZM phase shifters to be orientated along [011] direction i.e. perpendicular to major flat of InP wafer (EU/Japanese standard) (See chapter 2). From the fabrication point of view, this orientation is favorable to integrate a buried heterostructure (BH) laser diode with MZM [33, 48]. The results of this work were only limited to DC performance of the device. Initial results based on n-i-p-n are also included in Chapter 6 of this thesis. In 2015, TeraXion presented CL-InP MZM with a reduced V_π of 1.5 V as compared to their previously reported value of 2.5 V by increasing number of MQWs from 22 to 32. The reported insertion loss of device is < 7.5 dB [49]. The InP MZM devices summarized in Table 1.1 show a constant improvement in EO bandwidth with a reduction in V_π which is one of the main requirements to implement higher order phase modulation formats for coherent optical transmitters.

1.3 Motivation of this work

The major limitation on the bandwidth is imposed by the non-linearities of the silica-based standard single mode fiber (SSMF) and the optical amplifiers which mostly operate within the 4-5 THz bandwidth of the C-band (1530 – 1565 nm). Nevertheless, as shown in Fig 1.1, the use of the spectrally efficient advanced optical modulation formats with pulse shaping and decreasing WDM channel spacing has allowed a significant increase in the capacity of the long-haul optical transmission systems even within this limited bandwidth [1, 2, 5, 12]. Commercially available WDM products have a capacity of around 10 Tb/s. Recently, a record-breaking transmission capacity of 38.4 Tb/s using 64 QAM with a spectral efficiency (SE) of 8 b/s/Hz over 762 km was demonstrated through a field trial [52]. These transmission results are already within a factor 2 of the theoretically predicted nonlinear Shannon limit for the current optical fiber systems [1, 2, 4, 11, 53]. Several other experiments have even shown higher transmission capacity greater than 50 Tb/s over standard SMF using the state-of-the-art transmitters, receivers and DSP techniques to mitigate fiber impairments [54, 55]. It clearly suggests that the current fiber infrastructure is rapidly approaching its anticipated ultimate transmission capacity limit (100 Tb/s per fiber) in next 5 years and by the year 2020 there may be the predicted ‘capacity crunch’ [53] unless further radical innovation and breakthroughs in current

physical layer technology are achieved.

To circumvent such capacity limitations, the research community has proposed many ground breaking solutions such as exploiting the spatial dimension of an optical fiber by using space division multiplexing (SDM) based on multiple-input-multiple-output (MIMO) signal processing which has shown notable data transmission performance with the total capacity of around 1 Pb/s in recent years [11, 56].

Another potential solution proposed in recent years is to shift the optical transmission to the 2 μm wavelength region. To date the mid-infrared (MIR) wavelength range (2 - 20 μm) has been particularly interesting for spectroscopic sensing and detection applications [57]. However, in this thesis, we focus on the use of the 2 μm wavelength for data communication over an entirely new physical layer based on hollow-core photonics bandgap fibers (HC-PBGF). HC-PBGFs guide light in a hollow core which is surrounded by a complex glass microstructure and offers many interesting optical properties for optical communications such as ultra-low optical nonlinearity, low latency and excellent power handling as compared to SMF. In addition, it has potential to achieve a loss as low as 0.2 dB/km at 2 μm [58, 59]. In combination with the recently developed ultra-broadband (1.85-2.05 μm), low noise and high gain Thulium Doped Fiber Amplifier (TDFA) [60–62], HC-PBGF has emerged as a potential option for future transmission systems [63].

1.4 Main contribution and outline of this thesis

In order to make optical transmission at 2 μm viable, a new range of different photonic components such as lasers [64, 65], modulators [50, 51], optical hybrids [66], arrayed waveguide gratings (AWGr) [67] and photo-detectors (PD) [68] had to be developed. Initially, the availability of these active and passive photonic components at 2 μm was limited. The first optical transmission experiments were successfully using photonic components based on different platforms using HC-PBGF fiber as a transmission medium demonstrating a steady increase in the transmission capacity with time. Most of these experiments used directly modulated lasers, optical injection locked lasers together with commercially available LiNbO_3 MZM based transmitters to implement various modulation formats [69–72]. Conventional LiNbO_3 based modulators at 2 μm usually have very high switching voltage ($V_\pi \sim 11\text{-}13$ V), large module size and may also suffer from bias point instability. Moreover, they cannot be

integrated with III-V active components which make them unsuitable for the realization of cost-effective, low power and small form factor compatible photonic subsystems with high functionality.

This thesis is focused on the design and development of the InP based Mach-Zehnder modulators operating at conventional $1.5\ \mu\text{m}$ wavelengths and also at the newly proposed optical transmission wavelength of $2\ \mu\text{m}$. MZMs operating at $2\ \mu\text{m}$ with EO bandwidth of $\sim 9\ \text{GHz}$ suitable for 10 Gb/s NRZ modulation are the first reported devices on InP platform and demonstrate V_π of 2.7 V only, which is ~ 4 times lower than commercially available LiNbO₃ MZM exhibiting 10 GHz EO bandwidth.

This dissertation is organized as follows:

Chapter 1 had discussed the evolution of optical communication systems and role of InP based PICs to realize compact and low power transceivers for future transmission systems. Results from the state-of-the-art InP MZMs developed in last 15 years are also summarized to highlight the continuous effort of research community to realize compact pluggable package compliant InP MZM devices. The concept of capacity crunch in the current fiber infrastructure expected in the next few years is explained. This phenomenon formed the basis of this research work as one of the solutions proposed to avoid this capacity crisis is to shift the optical transmission wavelength to 2000 nm and it will be not be possible without realizing photonic devices specially lower power and compact MZMs suitable for this wavelength operation.

Chapter 2 introduces the basic layout and operation of a Mach-Zehnder interferometer (MZI) based on multi-mode interference (MMI) couplers. It provides a theoretical background of different electro-optic effects in III-V semiconductors utilized to achieve electric field induced phase change in the interferometric arms of a MZM. Importance of device orientation with respect to InP wafer and its impact on the over all change in refractive index is highlighted. In addition, electro-absorption effect i.e. QCSE is explained qualitatively and then demonstrated experimentally by evaluating refractive index change through QCSE in asymmetrically ramped MQW structures around 1550 nm.

Chapter 3 explains merits and demerits of different types of RF transmission lines used to realize RF electrode structures for driving InP based MZMs. Also, different trade-offs in high frequency design of electrodes to achieve high bandwidth optical modulators are explained in detail through a comprehensive equivalent circuit model of a traveling wave electrode.

Chapter 4 discusses the III-V modulator specific material design and experimental procedures to validate the material properties through fabrication of test structures. It also explains different experimental techniques to characterize the DC and high frequency performance of fabricated InP MZM devices. The RF electrode design rules established in previous chapter are validated by the experimental results from fabricated high speed QCSE based InP MZM devices operating at 1550 nm. Further, a comparison of measured results with simulation results is also shown and the EO bandwidth limiting factors are also highlighted.

Chapter 5 focuses on the design and characterization of high speed InP MZMs at a new optical transmission wavelength of 2000 nm. The knowledge developed in previous chapters regarding design, fabrication and testing of high speed InP based MZMs at 1550 nm served as the basis to realize different test structures and MZM devices for operation at 2000 nm. It is experimentally demonstrated that switching voltage of MZM can be greatly reduced by enhancing the electro-optical overlap efficiency by increasing the number of MQWs without sacrificing high-speed performance of the modulators. In addition, high frequency design of a low cost PCB based RF interposer for the modulator packaging is discussed. The performance of RF package is tested by wire bonding the fabricated modulator devices and 50 Ω termination resistors on to the interposer and measuring the large signal response of mounted modulator device. Finally, packaged modulator performance is evaluated in terms of OSNR vs. BER by transmitting 40 Gb/s WDM signal over 1.15 km HC-PBGF.

In the end, a conclusive summary of the contributions of this research work is given in **Chapter 6**. Ideas for future research directions that can be drawn from this research and have potential leading to proposals for further developments of InP based MZMs are also discussed.

Note: The main contribution of author in this work is the design and characterization of epitaxial material; high frequency design and simulations of modulator and RF package; DC and high frequency characterization of the fabricated modulator devices. Fabrication was performed by the other group members.

References

- [1] D. J. Richardson, “Filling the Light Pipe,” *Science*, vol. 330, no. 6002, pp. 327–328, 2010.
- [2] P. J. Winzer, “Scaling Optical Fiber Networks: Challenges and Solutions,” *Opt. Photon. News*, vol. 26, no. 3, pp. 28–35, Mar 2015.
- [3] Cisco, “Cisco Visual Networking Index: Forecast and Methodology, 2014-2019,” Cisco, Tech. Rep., 2015.
- [4] R. J. Essiambre and R. W. Tkach, “Capacity Trends and Limits of Optical Communication Networks,” *Proceedings of the IEEE*, vol. 100, no. 5, pp. 1035–1055, May 2012.
- [5] P. J. Winzer, “High-Spectral-Efficiency Optical Modulation Formats,” *J. Lightwave Technology*, vol. 30, no. 24, pp. 3824–3835, Dec 2012.
- [6] P. J. Winzer and R. J. Essiambre, “Advanced Optical Modulation Formats,” *Proceedings of the IEEE*, vol. 94, no. 5, pp. 952–985, May 2006.
- [7] A. H. Gnauck and P. J. Winzer, “Optical phase-shift-keyed transmission,” *Journal of Lightwave Technology*, vol. 23, no. 1, pp. 115–130, Jan 2005.
- [8] G. Charlet, J. C. Antona, S. Lanne, P. Tran, W. Idler, M. Gorlier, S. Borne, A. Klekamp, C. Simonneau, L. Pierre, Y. Frignac, M. Molina, F. Beaumont, J. P. Hamaide, and S. Bigo, “6.4Tb/s (159×42.7 Gb/s) Capacity Over 21×215 ; 100 km Using Bandwidth-Limited Phase-Shaped Binary Transmission,” in *Optical Communication, 2002. ECOC 2002. 28th European Conference on*, vol. 5, Sept 2002, pp. 1–2.
- [9] B. Mikkelsen, C. Rasmussen, P. Mamyshev, and F. Liu, “Partial DPSK with excellent filter tolerance and OSNR sensitivity,” *Electronics Letters*, vol. 42, no. 23, pp. 1363–1364, November 2006.

- [10] A. H. Gnauck, G. Charlet, P. Tran, P. J. Winzer, C. R. Doerr, J. C. Centanni, E. C. Burrows, T. Kawanishi, T. Sakamoto, and K. Higuma, "25.6-Tb/s WDM Transmission of Polarization-Multiplexed RZ-DQPSK Signals," *Journal of Lightwave Technology*, vol. 26, no. 1, pp. 79–84, Jan 2008.
- [11] T. Mizuno, H. Takara, A. Sano, and Y. Miyamoto, "Dense Space-Division Multiplexed Transmission Systems Using Multi-Core and Multi-Mode Fiber," *Journal of Lightwave Technology*, vol. 34, no. 2, pp. 582–592, Jan 2016.
- [12] K. Roberts, M. O'Sullivan, K. T. Wu, H. Sun, A. Awadalla, D. J. Krause, and C. Laperle, "Performance of Dual-Polarization Qpsk for Optical Transport Systems," *Journal of Lightwave Technology*, vol. 27, no. 16, pp. 3546–3559, Aug 2009.
- [13] H. Sun, K.-T. Wu, and K. Roberts, "Real-time measurements of a 40 Gb/s coherent system," *Opt. Express*, vol. 16, no. 2, pp. 873–879, Jan 2008.
- [14] P. J. Winzer, G. Raybon, H. Song, A. Adamiecki, S. Corteselli, A. H. Gnauck, D. A. Fishman, C. R. Doerr, S. Chandrasekhar, L. L. Buhl, T. J. Xia, G. Wellbrock, W. Lee, B. Basch, T. Kawanishi, K. Higuma, and Y. Painchaud, "100-Gb/s DQPSK transmission: From laboratory experiments to field trials," *Journal of Lightwave Technology*, vol. 26, no. 20, pp. 3388–3402, Oct 2008.
- [15] M. Birk, P. Gerard, R. Curto, L. Nelson, X. Zhou, P. Magill, T. Schmidt, C. Malouin, B. Zhang, E. Ibragimov, S. Khatana, M. Glavanovic, R. Lofland, R. Marcoccia, R. Saunders, G. Nicholl, M. Nowell, and F. Forghieri, "Real-Time Single-Carrier Coherent 100 Gb/s PM-QPSK Field Trial," *Journal of Lightwave Technology*, vol. 29, no. 4, pp. 417–425, Feb 2011.
- [16] C. Schubert, J. K. Fischer, C. Schmidt-Langhorst, R. Elschner, L. Molle, M. Nölle, and T. Richter, "New trends and challenges in optical digital transmission systems," in *Photonics in Switching (PS), 2012 International Conference on*, Sept 2012, pp. 1–3.
- [17] Fujitsu, "Path to 400 G," Tech. Rep., 2013.
- [18] S. C. Heck, S. K. Jones, R. A. Griffin, N. Whitbread, P. A. Bromley, G. Harris, D. Smith, L. N. Langley, and T. Goodall, "Miniaturized InP dual I & Q

- mach zehnder modulator with full monitoring functionality for CFP2,” in *Optical Communication (ECOC), 2014 European Conference on*, Sept 2014, pp. 1–3.
- [19] W. Forysiak and D. S. Govan, “Progress Toward 100-G Digital Coherent Pluggables Using InP-Based Photonics,” *Journal of Lightwave Technology*, vol. 32, no. 16, pp. 2925–2934, Aug 2014.
- [20] S. Chandrasekhar, X. Liu, P. J. Winzer, J. E. Simsarian, and R. A. Griffin, “Compact All-InP Laser-Vector-Modulator for Generation and Transmission of 100-Gb/s PDM-QPSK and 200-Gb/s PDM-16-QAM,” *Journal of Lightwave Technology*, vol. 32, no. 4, pp. 736–742, Feb 2014.
- [21] A. H. Gnauck, P. J. Winzer, S. Chandrasekhar, X. Liu, B. Zhu, and D. W. Peckham, “Spectrally Efficient Long-Haul WDM Transmission Using 224-Gb/s Polarization-Multiplexed 16-QAM,” *Journal of Lightwave Technology*, vol. 29, no. 4, pp. 373–377, Feb 2011.
- [22] E. L. Wooten, K. M. Kissa, A. Yi-Yan, E. J. Murphy, D. A. Lafaw, P. F. Hallemeier, D. Maack, D. V. Attanasio, D. J. Fritz, G. J. McBrien, and D. E. Bossi, “A review of lithium niobate modulators for fiber-optic communications systems,” *IEEE Journal of Selected Topics in Quantum Electronics*, vol. 6, no. 1, pp. 69–82, Jan 2000.
- [23] R. A. Griffin, “InP-based high-speed transponder,” in *Optical Fiber Communication Conference*. Optical Society of America, 2014, p. W3B.7.
- [24] K. A. Williams, E. A. J. M. Bente, D. Heiss, Y. Jiao, K. Ławniczuk, X. J. M. Leijtens, J. J. G. M. van der Tol, and M. K. Smit, “InP photonic circuits using generic integration,” *Photon. Res.*, vol. 3, no. 5, pp. B60–B68, Oct 2015.
- [25] M. Smit, X. Leijtens, H. Ambrosius, E. Bente, J. van der Tol, B. Smalbrugge, T. de Vries, E.-J. Geluk, J. Bolk, R. van Veldhoven, L. Augustin, P. Thijs, D. D’Agostino, H. Rabbani, K. Lawniczuk, S. Stopinski, S. Tahvili, A. Corradi, E. Kleijn, D. Dzibrou, M. Felicetti, E. Bitincka, V. Moskalenko, J. Zhao, R. Santos, G. Gilardi, W. Yao, K. Williams, P. Stabile, P. Kuindersma, J. Pello, S. Bhat, Y. Jiao, D. Heiss, G. Roelkens, M. Wale, P. Firth, F. Soares, N. Grote, M. Schell, H. Debregeas, M. Achouche, J.-L. Gentner, A. Bakker, T. Korthorst, D. Gallagher, A. Dabbs, A. Melloni, F. Morichetti, D. Melati, A. Wonfor, R. Penty,

- R. Broeke, B. Musk, and D. Robbins, "An introduction to InP-based generic integration technology," *Semiconductor Science and Technology*, vol. 29, no. 8, p. 083001, 2014.
- [26] P. R. A. Binetti, M. Lu, E. J. Norberg, R. S. Guzzon, J. S. Parker, A. Sivananthan, A. Bhardwaj, L. A. Johansson, M. J. Rodwell, and L. A. Coldren, "Indium Phosphide Photonic Integrated Circuits for Coherent Optical Links," *IEEE Journal of Quantum Electronics*, vol. 48, no. 2, pp. 279–291, Feb 2012.
- [27] R. Nagarajan, C. H. Joyner, R. P. Schneider, J. S. Bostak, T. Butrie, A. G. Dentai, V. G. Dominic, P. W. Evans, M. Kato, M. Kauffman, D. J. H. Lambert, S. K. Mathis, A. Mathur, R. H. Miles, M. L. Mitchell, M. J. Missey, S. Murthy, A. C. Nilsson, F. H. Peters, S. C. Pennypacker, J. L. Pleumeekers, R. A. Salvatore, R. K. Schlenker, R. B. Taylor, H.-S. Tsai, M. F. V. Leeuwen, J. Webjorn, M. Ziari, D. Perkins, J. Singh, S. G. Grubb, M. S. Reffle, D. G. Mehuys, F. A. Kish, and D. F. Welch, "Large-scale photonic integrated circuits," *IEEE Journal of Selected Topics in Quantum Electronics*, vol. 11, no. 1, pp. 50–65, Jan 2005.
- [28] S. W. Corzine, P. Evans, M. Fisher, J. Gheorma, M. Kato, V. Dominic, P. Samra, A. Nilsson, J. Rahn, I. Lyubomirsky, A. Dentai, P. Studenkov, M. Missey, D. Lambert, A. Spannagel, R. Muthiah, R. Salvatore, S. Murthy, E. Strzelecka, J. L. Pleumeekers, A. Chen, R. Schneider, R. Nagarajan, M. Ziari, J. Stewart, C. H. Joyner, F. Kish, and D. F. Welch, "Large-scale InP Transmitter PICs for PM-DQPSK Fiber Transmission Systems," *IEEE Photonics Technology Letters*, vol. 22, no. 14, pp. 1015–1017, July 2010.
- [29] M. Kato, R. Malendevich, D. Lambert, M. Kuntz, A. Damle, V. Lal, A. Dentai, O. Khayam, R. Nagarajan, J. Tang, J. Zhang, H. S. Tsai, T. Butrie, M. Missey, J. Rahn, D. Krause, J. McNicol, K. T. Wu, H. Sun, M. Reffle, F. Kish, and D. Welch, "10 channel, 28 Gbaud PM-QPSK, monolithic InP Terabit Superchannel receiver PIC," in *Photonics Conference (PHO), 2011 IEEE*, Oct 2011, pp. 340–341.
- [30] J. Summers, T. Vallaitis, P. Evans, M. Ziari, P. Studenkov, M. Fisher, J. Sena, A. James, S. Corzine, D. Pavinski, J. Ou-Yang, M. Missey, D. Gold, W. Williams, M. Lai, D. Welch, and F. Kish, "Monolithic inP-based coherent transmitter photonic integrated circuit with 2.25 Tbit/s capacity," *Electronics Letters*, vol. 50, no. 16, pp. 1150–1152, July 2014.

- [31] N. Dagli, *High Speed Photonic Devices*. Taylor and Francis Group, LLC, 2007.
- [32] C. Lawetz, J. C. Cartledge, C. Rolland, and J. Yu, "Modulation characteristics of semiconductor mach-zehnder optical modulators," *Journal of Lightwave Technology*, vol. 15, no. 4, pp. 697–703, Apr 1997.
- [33] E. Chen and A. Murphy, *Broadband Optical Modulators Science, Technology, and Applications*. CRC Press, 2011.
- [34] R. G. Walker, "High-speed III-V semiconductor intensity modulators," *IEEE Journal of Quantum Electronics*, vol. 27, no. 3, pp. 654–667, Mar 1991.
- [35] S. Akiyama, S. Hirose, T. Watanabe, M. Ueda, S. Sekiguchi, N. Morii, T. Yamamoto, A. Kuramata, and H. Soda, "Novel InP-based Mach-Zehnder modulator for 40 gb/s integrated lightwave source," in *Semiconductor Laser Conference, 2002. IEEE 18th International*, 2002, pp. 57–58.
- [36] K. Tsuzuki, T. Ishibashi, T. Ito, S. Oku, Y. Shibata, R. Iga, Y. Kondo, and Y. Tohmori, "40 Gbit/s InP Mach-Zehnder modulator with a π voltage," *Electronics Letters*, vol. 39, pp. 1464–1466(2), October 2003.
- [37] D. Hoffman, S. Staroske, and K. O. Velthaus, "45 Ghz bandwidth travelling wave electrode Mach-Zehnder modulator with integrated spot size converter," in *Indium Phosphide and Related Materials, 2004. 16th IPRM. 2004 International Conference on*, May 2004, pp. 585–588.
- [38] S. Akiyama, S. Hirose, H. Itoh, T. Takeuchi, T. Watanabe, S. Sekiguchi, A. Kuramata, and T. Yamamoto, "40 Gb/s InP-based Mach-Zehnder modulator with a driving voltage of 3 Vpp," in *Indium Phosphide and Related Materials, 2004. 16th IPRM. 2004 International Conference on*, May 2004, pp. 581–584.
- [39] I. Betty, M. G. Boudreau, R. A. Griffin, and A. Feckes, "An empirical model for high yield manufacturing of 10Gb/s negative chirp InP Mach-Zehnder modulators," in *Optical Fiber Communication Conference, 2005. Technical Digest. OFC/NFOEC*, vol. 3, March 2005, pp. 3 pp. Vol. 3–.
- [40] I. Betty, M. G. Boudreau, R. Longone, R. A. Griffin, L. Langley, A. Maestri, A. Pujol, and B. Pugh, "Zero Chirp 10 Gb/s MQW InP Mach-Zehnder Transmitter with Full-Band Tunability," in *Optical Fiber Communication*

- and the National Fiber Optic Engineers Conference, 2007. OFC/NFOEC 2007. Conference on, March 2007, pp. 1–3.
- [41] H. N. Klein, H. Chen, D. Hoffmann, S. Staroske, A. G. Steffan, and K. O. Velthaus, “1.55 μm Mach-Zehnder Modulators on InP for Optical 40/80 Gbit/s Transmission Networks,” in *Indium Phosphide and Related Materials Conference Proceedings, 2006 International Conference on*, 2006, pp. 171–173.
 - [42] N. Kikuchi, H. Sanjoh, Y. Shibata, K. Tsuzuki, T. Sato, E. Yamada, T. Ishibashi, and H. Yasaka, “80-Gbit/s InP DQPSK modulator with an n-p-i-n structure,” in *Optical Communication (ECOC), 2007 33rd European Conference and Exhibition of*, Sept 2007, pp. 1–2.
 - [43] T. Yasui, Y. Shibata, K. Tsuzuki, N. Kikuchi, Y. Kawaguchi, M. Arai, and H. Yasaka, “Lossless 10-Gbit/s InP n-p-i-n Mach-Zehnder Modulator Monolithically Integrated with Semiconductor Optical Amplifier,” in *Optical Fiber communication/National Fiber Optic Engineers Conference, 2008. OFC/NFOEC 2008. Conference on*, Feb 2008, pp. 1–3.
 - [44] J. Mo, R. Griffin, T. Goodall, and Z. He, “Advanced InP technology for high performance 40 Gb/s (rz-) DQPSK transponder,” in *Communications and Photonics Conference and Exhibition (ACP), 2009 Asia*, vol. 2009-Supplement, Nov 2009, pp. 1–6.
 - [45] S. Corzine, P. Evans, M. Kato, G. He, M. Fisher, M. Raburn, A. Dentai, I. Lyubomirsky, R. Nagarajan, M. Missey, V. Lal, A. Chen, J. Thomson, W. Williams, P. Chavarkar, S. Nguyen, D. Lambert, T. Butrie, M. Reffle, R. Schneider, M. Ziari, C. Joyner, S. Grubb, F. Kish, and D. Welch, “10-channel \times 40Gb/s per Channel DQPSK Monolithically Integrated Inp-Based Transmitter PIC,” in *Optical Fiber Communication Conference/National Fiber Optic Engineers Conference*. Optical Society of America, 2008, p. PDP18.
 - [46] K. Prosyk, T. Brast, M. Gruner, M. Hamacher, D. Hoffmann, R. Millett, and K. O. Velthaus, “Tunable InP-based optical IQ modulator for 160 Gb/s,” in *Optical Communication (ECOC), 2011 37th European Conference and Exhibition on*, Sept 2011, pp. 1–3.
 - [47] H. Yagi, T. Kitamura, N. Kono, H. Kobayashi, N. Inoue, K. Horino, D. Kimura, K. Fujii, Y. Yoneda, C. Fukuda, and H. Shoji, “Low driving

- voltage InP-based Mach-Zehnder modulators for compact 128 Gb/s DP-QPSK module,” in *Lasers and Electro-Optics Pacific Rim (CLEO-PR), 2013 Conference on*, June 2013, pp. 1–2.
- [48] Y. Ogiso, Y. Ohiso, Y. Shibata, and M. Kohtoku, “[011] waveguide stripe direction n-i-p-n heterostructure InP optical modulator,” *Electronics Letters*, vol. 50, no. 9, pp. 688–690, April 2014.
- [49] G. Letal, K. Prosyk, R. Millett, D. Macquistan, S. Paquet, O. Thibault-Maheu, J. F. Gagné, P. L. Fortin, R. Dowlathshahi, B. Rioux, T. SpringThorpe, M. Hisko, R. Ma, and I. Woods, “Low loss InP c-band IQ modulator with 40GHz bandwidth and 1.5V v_{π} ,” in *Optical Fiber Communications Conference and Exhibition (OFC), 2015*, March 2015, pp. 1–3.
- [50] M. U. Sadiq, M. R. Gleeson, N. Ye, J. O’Callaghan, P. Morrissey, H. Y. Zhang, K. Thomas, A. Gocalinska, E. Pelucchi, F. C. G. Gunning, B. Roycroft, F. H. Peters, and B. Corbett, “10 Gb/s InP-based Mach-Zehnder modulator for operation at 2 μ m wavelengths,” *Opt. Express*, vol. 23, no. 9, pp. 10 905–10 913, May 2015.
- [51] M. U. Sadiq, H. Zhang, J. O’Callaghan, B. Roycroft, N. Kavanagh, K. Thomas, A. Gocalinska, Y. Chen, T. Bradley, J. R. Hayes, Z. Li, S. U. Alam, F. Poletti, M. N. Petrovich, D. J. Richardson, E. Pelucchi, P. O’Brien, F. H. Peters, F. Gunning, and B. Corbett, “40 gb/s wdm transmission over 1.15-km hc-pbgf using an inp-based mach-zehnder modulator at 2 μ m,” *Journal of Lightwave Technology*, vol. 34, no. 8, pp. 1706–1711, April 2016.
- [52] T. Rahman, D. Rafique, B. Spinnler, E. Pincemin, C. L. Bouette, J. Jauffrit, S. Calabro, E. de Man, S. Bordaïs, U. Feiste, J. Slovak, A. Napoli, G. Khanna, N. Hanik, C. Andre, C. Okonkwo, M. Kushnerov, A. M. J. Koonen, C. Dourthe, B. Raguenees, B. Sommerkorn-Krombholz, M. Bohn, and H. de Waardt, “Record field demonstration of C-band multi-terabit 16QAM, 32QAM and 64QAM over 762km of SSMF,” in *Opto-Electronics and Communications Conference (OECC), 2015*, June 2015, pp. 1–3.
- [53] A. D. Ellis, J. Zhao, and D. Cotter, “Approaching the Non-Linear Shannon Limit,” *Journal of Lightwave Technology*, vol. 28, no. 4, pp. 423–433, Feb 2010.

- [54] M.-F. Huang, A. Tanaka, E. Ip, Y.-K. Huang, D. Qian, Y. Zhang, S. Zhang, P. Ji, I. B. Djordjevic, T. Wang, Y. Aono, S. Murakami, T. Tajima, T. J. Xia, and G. A. Wellbrock, "Terabit/s Nyquist Superchannels in High Capacity Fiber Field Trials Using DP-16QAM and DP-8QAM Modulation Formats," *Journal of Lightwave Technology*, vol. 32, no. 4, pp. 776–782, Feb 2014.
- [55] S. Beppu, K. Kasai, M. Yoshida, and M. Nakazawa, "2048 QAM (66 Gbit/s) single-carrier coherent optical transmission over 150 km with a potential SE of 15.3 bit/s/Hz," *Opt. Express*, vol. 23, no. 4, pp. 4960–4969, Feb 2015.
- [56] S. O. Arik, J. M. Kahn, and K.-P. Ho, "MIMO Signal Processing for Mode-Division Multiplexing: An overview of channel models and signal processing architectures," *IEEE Signal Processing Magazine*, vol. 31, no. 2, pp. 25–34, March 2014.
- [57] A. Spott, M. Davenport, J. Peters, J. Bovington, M. J. R. Heck, E. J. Stanton, I. Vurgaftman, J. Meyer, and J. Bowers, "Heterogeneously integrated 2.0 μm cw hybrid silicon lasers at room temperature," *Opt. Lett.*, vol. 40, no. 7, pp. 1480–1483, Apr 2015.
- [58] F. Poletti, N. V. Wheeler, M. N. Petrovich, N. Baddela, E. Numkam Fokoua, J. R. Hayes, D. R. Gray, Z. Li, R. Slavik, and D. J. Richardson, "Towards high-capacity fibre-optic communications at the speed of light in vacuum," *Nature Photonics*, vol. 7, no. 4, pp. 279–284, Mar. 2013.
- [59] P. J. Roberts, F. Couny, H. Sabert, B. J. Mangan, D. P. Williams, L. Farr, M. W. Mason, A. Tomlinson, T. A. Birks, J. C. Knight, and P. S. Russell, "Ultimate low loss of hollow-core photonic crystal fibres," *Opt. Express*, vol. 13, no. 1, pp. 236–244, Jan 2005.
- [60] Z. Li, A. M. Heidt, J. M. O. Daniel, Y. Jung, S. U. Alam, and D. J. Richardson, "Thulium-doped fiber amplifier for optical communications at 2 μm ," *Opt. Express*, vol. 21, no. 8, pp. 9289–9297, Apr 2013.
- [61] Z. Li, A. M. Heidt, N. Simakov, Y. Jung, J. M. O. Daniel, S. U. Alam, and D. J. Richardson, "Diode-pumped wideband thulium-doped fiber amplifiers for optical communications in the 1800 – 2050 nm window," *Opt. Express*, vol. 21, no. 22, pp. 26 450–26 455, Nov 2013.
- [62] A. M. Heidt, Z. Li, and D. J. Richardson, "High power diode-seeded fiber amplifiers at 2 μm - from architectures to applications," *IEEE Journal of*

- Selected Topics in Quantum Electronics*, vol. 20, no. 5, pp. 525–536, Sept 2014.
- [63] M. N. Petrovich, F. Poletti, J. P. Wooley, A. Heidt, N. Baddela, Z. Li, D. Gray, R. Slavík, F. Parmigiani, N. Wheeler, J. Hayes, E. Numkam, L. Gr  ner-Nielsen, B. P  lsd  ttir, R. Phelan, B. Kelly, J. O’Carroll, M. Becker, N. Mac-Suibhne, J. Zhao, F. G. Gunning, A. Ellis, P. Petropoulos, S. Alam, and D. Richardson, “Demonstration of amplified data transmission at 2 μm in a low-loss wide bandwidth hollow core photonic bandgap fiber,” *Opt. Express*, vol. 21, no. 23, pp. 28 559–28 569, Nov 2013.
 - [64] J. O’Carroll, D. Byrne, B. Kelly, R. Phelan, F. C. G. Gunning, P. M. Anandarajah, and L. P. Barry, “Dynamic characteristics of InGaAs/InP multiple quantum well discrete mode laser diodes emitting at 2 μm ,” *Electronics Letters*, vol. 50, no. 13, pp. 948–950, June 2014.
 - [65] R. Phelan, J. O’Carroll, D. Byrne, C. Herbert, J. Somers, and B. Kelly, “In_{0.75}Ga_{0.25}As/ InP Multiple Quantum-Well Discrete-Mode Laser Diode Emitting at 2 μm ,” *IEEE Photonics Technology Letters*, vol. 24, no. 8, pp. 652–654, April 2012.
 - [66] N. Ye, M. Gleeson, H. Yang, H. Zhang, B. Roycroft, K. Thomas, A. Gocalinska, E. Pelucchi, Z. Li, D. Richardson, H. Chen, A. M. J. Koonen, W. Jia, J. Zhao, F. G. Gunning, F. Peters, and B. Corbett, “Demonstration of 90 $^\circ$ optical hybrid at 2 μm wavelength range based on 4 x 4 MMI using diluted waveguide,” in *Optical Communication (ECOC), 2014 European Conference on*, Sept 2014, pp. 1–3.
 - [67] H. Zhang, M. Gleeson, N. Ye, N. Pavarelli, X. Ouyang, J. Zhao, N. Kavanagh, C. Robert, H. Yang, P. E. Morrissey, K. Thomas, A. Gocalinska, Y. Chen, T. Bradley, J. P. Wooley, J. R. Hayes, E. N. Fokoua, Z. Li, S. U. Alam, F. Poletti, M. N. Petrovich, D. J. Richardson, B. Kelly, J. O’Carroll, R. Phelan, E. Pelucchi, P. O’Brien, F. Peters, B. Corbett, and F. Gunning, “Dense wdm transmission at 2 μm enabled by an arrayed waveguide grating,” *Opt. Lett.*, vol. 40, no. 14, pp. 3308–3311, Jul 2015.
 - [68] N. Ye, H. Yang, M. Gleeson, N. Pavarelli, H. Zhang, J. O’Callaghan, W. Han, N. Nudds, S. Collins, A. Gocalinska, E. Pelucchi, P. O’Brien, F. C. G. Gunning, F. H. Peters, and B. Corbett, “InGaAs Surface Normal Photodiode for 2 μm Optical Communication Systems,” *IEEE Photonics Technology Letters*, vol. 27, no. 14, pp. 1469–1472, July 2015.

- [69] N. M. Suibhne, Z. Li, B. Baeuerle, J. Zhao, J. Wooler, S. ul Alam, F. Poletti, M. Petrovich, A. Heidt, N. Wheeler, N. Baddela, E. R. N. Fokoua, I. Giles, D. Giles, R. Phelan, J. O'Carroll, B. Kelly, B. Corbett, D. Murphy, A. D. Ellis, D. J. Richardson, and F. G. Gunning, "WDM Transmission at 2 μm over Low-Loss Hollow Core Photonic Bandgap Fiber," in *Optical Fiber Communication Conference/National Fiber Optic Engineers Conference 2013*. Optical Society of America, 2013, p. OW11.6.
- [70] H. Zhang, Z. Li, N. Kavanagh, J. Zhao, N. Ye, Y. Chen, N. V. Wheeler, J. P. Wooler, J. R. Hayes, S. R. Sandoghchi, F. Poletti, M. N. Petrovich, S. U. Alam, R. Phelan, J. O'Carroll, B. Kelly, D. J. Richardson, B. Corbett, and F. C. G. Gunning, "81 gb/s WDM transmission at 2 μm over 1.15 km of low-loss hollow core photonic bandgap fiber," in *Optical Communication (ECOC), 2014 European Conference on*, Sept 2014, pp. 1–3.
- [71] Z. Liu, Y. Chen, Z. Li, B. Kelly, R. Phelan, J. O'Carroll, T. Bradley, J. P. Wooler, N. V. Wheeler, A. M. Heidt, T. Richter, C. Schubert, M. Becker, F. Poletti, M. N. Petrovich, S. u. Alam, D. J. Richardson, and R. Slavík, "High-Capacity Directly Modulated Optical Transmitter for 2- μm Spectral Region," *Journal of Lightwave Technology*, vol. 33, no. 7, pp. 1373–1379, April 2015.
- [72] H. Zhang, N. Kavanagh, Z. Li, J. Zhao, N. Ye, Y. Chen, N. V. Wheeler, J. P. Wooler, J. R. Hayes, S. R. Sandoghchi, F. Poletti, M. N. Petrovich, S. U. Alam, R. Phelan, J. O'Carroll, B. Kelly, L. Grüner-Nielsen, D. J. Richardson, B. Corbett, and F. C. G. Gunning, "100 Gbit/s WDM transmission at 2 μm : transmission studies in both low-loss hollow core photonic bandgap fiber and solid core fiber," *Opt. Express*, vol. 23, no. 4, pp. 4946–4951, Feb 2015.

Chapter 2

Electro-optic effects in III-V semiconductors

This chapter explains the fundamental physical effects required to realize a high speed InP based Mach-Zehnder modulator. In Section 2.1, basic operation of Mach-Zehnder interferometer is discussed. Section 2.2 explains the advantage of utilizing InP-based ternary and quaternary compound semiconductors for multiple quantum well structures to realize optical waveguides and phase shifting sections of the modulator. Section 2.4 introduces the electro-optic effects which are most important to achieve the phase shift in reverse biased shifting region of a MZM. Through basic calculations, the importance of selecting the proper waveguide orientation with respect to the crystal axis of InP wafer is highlighted. In addition, the principle of quantum confined Stark effect (QCSE) is explained with the help of experimental study of two sequentially grown epitaxial layer structures with intrinsic region consisting of oppositely ramped asymmetric quantum wells in Section 2.5. Also, the effects of loss of excitonic confinement in quantum well structures is explained by comparing the phase and refractive index change with applied field in both the structures.

2.1 Mach-Zehnder Interferometer

The Mach-Zehnder interferometer (MZI) based electro-optic (EO) modulator design is perhaps the most successful modulator design that converts phase into intensity modulation. It is based on the interferometric principle which is used to determine the relative phase shift between two light beams which have been split from a single light source and then recombining them. The idea was first proposed by Ludwig Mach and Ludwig Zehnder in 1891 and then refined

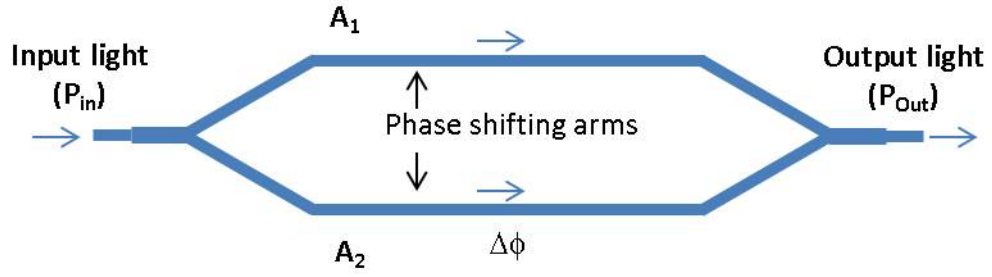
in 1892 [1, 2]. The EO modulators based on this principle are called Mach-Zehnder modulators (MZMs). In MZ modulators used in the telecommunications industry, the interferometer paths are fabricated using electro-optically active materials such as LiNbO_3 , polymers or III-V semiconductors. For semiconductor materials, the optical waveguides are defined using a p-i-n structure, where the intrinsic region consists of multiple quantum well (MQW) structures and confines the optical mode. The simplest form of MZI based EO modulator has three sections consisting of a divider and a combiner at the input and output respectively connected by two phase shifting arms (modulation sections) as shown in Fig 2.1.

The operation of this simple configuration is straightforward. The input light is split into two phase shifting arms of the interferometer equally using a 50:50 splitter (MMI, Y-branch coupler). The length of phase shifting arms is equal and it is adjusted keeping in view the both the electrical and optical signal losses. By applying an electric field across the phase shifter which is a p-i-n diode structure, the refractive index in the phase shifter is changed. Each of the phase shifters can also be manipulated individually. This refractive index variation property of the material under applied bias is known as EO effect. Different EO effects and their influence on the performance of a MZM will be explained later. At the output, the light from two phase shifting arms is combined again using another combiner. By applying reverse DC bias on one of the phase shifting arms, the phase difference between two arms can be varied from 0° to 180° . For this particular configuration, 0° phase difference between two arms results in constructive interference and 180° phase difference results in destructive interference. The constructive and destructive interference is represented by ON and OFF state of the MZM amplitude transfer function shown in Fig 2.1b. The light is transmitted for the ON state and radiated away for the OFF state. The drive voltage required to achieve π phase difference between two arms is termed as the ‘switching voltage’ (V_π) and it depends on the length of phase shifter and strength of the EO effect.

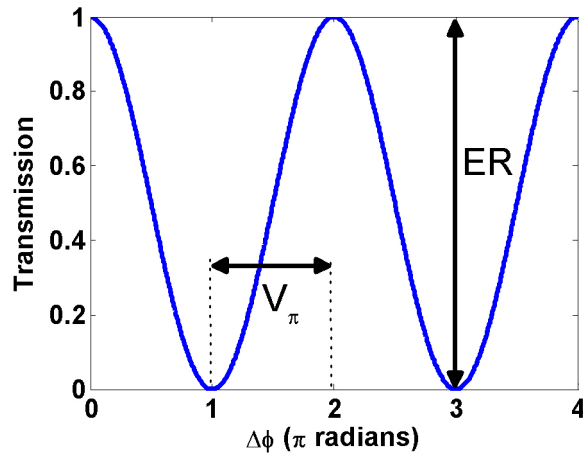
If the phase shift is linear with the applied voltage then the optical power transfer function (T) of a MZM is simply a cosine function by dividing P_{out} by P_{in} as given below in Eq 2.1,

$$T = \frac{P_{out}}{P_{in}} = \frac{1}{2}[1 + b\cos(\Delta\phi + \phi_0)] \quad (2.1)$$

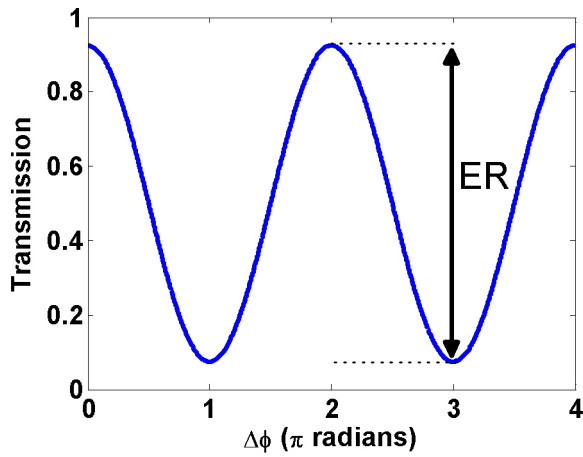
where b, represents the optical imbalance between two arms of MZI defined as:



(a)



(b)



(c)

Figure 2.1: (a) Schematic of a general Mach-Zehnder modulator structure. (b) Transfer function of modulator for ideally symmetric balanced design ($b = 0$). (c) Transfer function of modulator for non-symmetric design ($b = 0.8$).

$$b = \frac{2A_1A_2}{A_1^2 + A_2^2} \quad (2.2)$$

A_1 and A_2 represent the optical field amplitudes in two phase shifting arms, ϕ_0 is the initial phase shift between arms, $\Delta\phi$ is the refractive index change induced phase difference between two light paths due to voltage applied. Considering an ideal lossless case $A_1 = A_2$ i.e. $b = 1$ and $\phi_0 = 0$, then Eq 2.1 can be simplified to Eq 2.3.

$$T = \frac{1}{2}[1 + \cos(\Delta\phi)] = \cos^2\left(\frac{\Delta\phi}{2}\right) \quad (2.3)$$

The resulting transfer function for the ideal case of single input-single output MZM is shown in Fig 2.1b. However, if there is an unequal splitting of optical power at the input y-branch coupler, then imbalance factor b will be < 1 . Transfer function for $b = 0.8$ is shown in Fig 2.1c. It can be clearly seen the unbalancing limits the extinction ratio (ER) of the transmission curve of MZM and also increases the insertion loss of the modulator.

The above case is the most general model of the MZM comprising of Y-branch couplers at the input and output [3]. However, a major disadvantage associated with this arrangement of single input and single output is that during the OFF state the radiated light can back scatter into the modulator chip resulting in unwanted reflections and overheating of modulator device. Another approach is to use the multimode interference (MMI) couplers both at the input and output. Properly designed MMI couplers have greater fabrication tolerance as compared to Y-branch couplers [4]. In addition, the MMI couplers are much more compact when deeply etched and present low excess loss, low polarization sensitivity and wide band operation and have been successfully used as power splitters and combiners [5, 6]. The schematic of MZM implementation with MMI couplers is shown in Fig 2.2a. In this case a 1×2 MMI coupler is used at the input for splitting the light and a 2×2 MMI coupler is used at the output. The use of the 2×2 MMI at the output is very useful as it allows the light to be switched from one output port to the other output port rather being absorbed as in the case of single output combiner. The operation of the MZM with 2×2 MMI at the output is rather complicated as compared to a single output. To explain it in a better way, the transfer matrix method is used to describe the behavior of this arrangement. All the three main elements of the MZM structure i.e. 1×2 MMI, phase shifter and 2×2 MMI can be represented by a transfer matrix. Cascading the matrices will give the total response of the

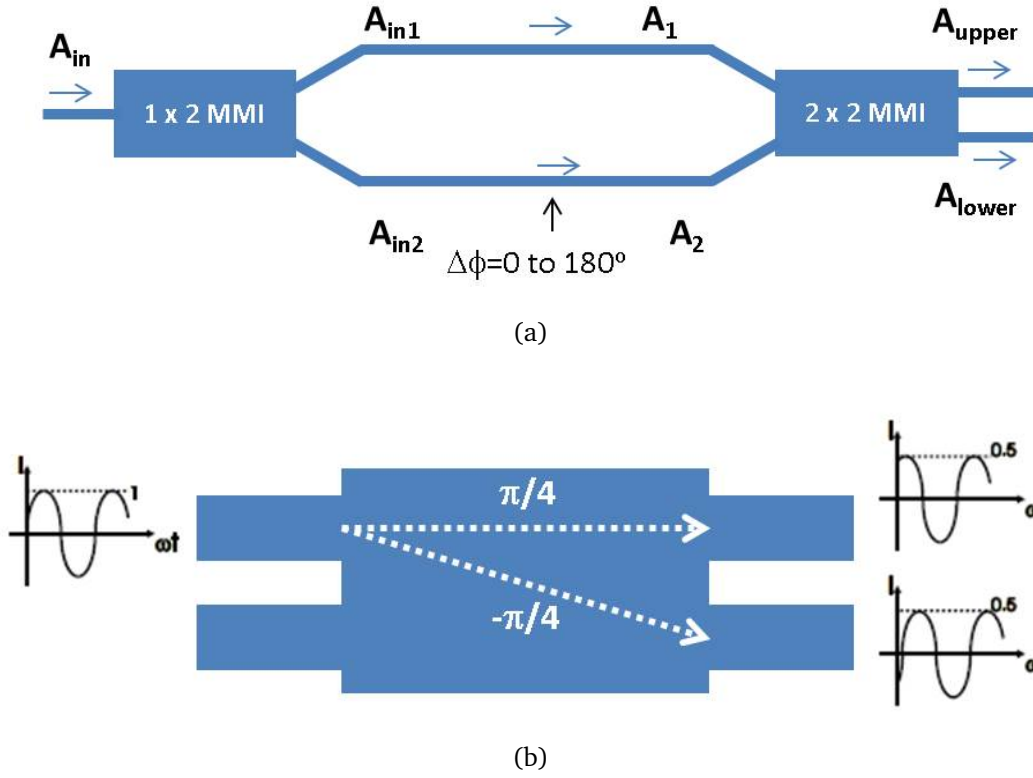


Figure 2.2: (a) Schematic of a general Mach-Zehnder modulator structure with 1×2 MMI and 2×2 MMI at input and output respectively. (b) Schematic of the output 2×2 MMI. The phase difference between two output arms is $\pi/2$.

MZM.

If the input light is equally split at the output of 1×2 MMI to both the phase shifting arms then in the form of matrix it can be written as Eq 2.4.

$$\begin{bmatrix} A_{in1} \\ A_{in2} \end{bmatrix} = \begin{bmatrix} \frac{1}{\sqrt{2}} \\ \frac{1}{\sqrt{2}} \end{bmatrix} \cdot A_{in} \quad (2.4)$$

By applying bias to a single arm or both arms of the modulator, the phase can be varied. In this case the phase change is applied only to the lower arm. In matrix form this phase change in the shifters can be represented simply as a 2×2 matrix as in Eq 2.5.

$$\begin{bmatrix} A_1 \\ A_2 \end{bmatrix} = \begin{bmatrix} 1 & 0 \\ 0 & e^{i\Delta\phi} \end{bmatrix} \cdot \begin{bmatrix} A_{in1} \\ A_{in2} \end{bmatrix} \quad (2.5)$$

where $\Delta\phi$ is the reverse bias induced phase change. At the output of 2×2 MMI, the field at both the upper arm and lower arm is

$$\begin{bmatrix} A_{upper} \\ A_{lower} \end{bmatrix} = \begin{bmatrix} \frac{1}{\sqrt{2}} & \frac{-i}{\sqrt{2}} \\ \frac{-i}{\sqrt{2}} & \frac{1}{\sqrt{2}} \end{bmatrix} \cdot \begin{bmatrix} A_1 \\ A_2 \end{bmatrix} \quad (2.6)$$

The overall transmission response of MZM in for both the outputs can be calculated by simply cascading the matrices from output to input.

$$T_{MZM} = \begin{bmatrix} \frac{1}{\sqrt{2}} & \frac{-i}{\sqrt{2}} \\ \frac{-i}{\sqrt{2}} & \frac{1}{\sqrt{2}} \end{bmatrix} \cdot \begin{bmatrix} 1 & 0 \\ 0 & e^{i\Delta\phi} \end{bmatrix} \cdot \begin{bmatrix} \frac{1}{\sqrt{2}} \\ \frac{1}{\sqrt{2}} \end{bmatrix} \quad (2.7)$$

By employing matrix multiplication and applying Euler's identity T_{MZM} is reduced to Eq 2.8

$$T_{MZM} = \frac{1}{2} \cdot \begin{bmatrix} (1 + \sin\Delta\phi) - i\cos\Delta\phi \\ \cos\Delta\phi + i(\sin\Delta\phi - 1) \end{bmatrix} \quad (2.8)$$

The output power in both the arms of the output MMI can be calculated using Eq2.9 and 2.10.

$$P_{upper} = \left| \frac{1}{2} \cdot ((1 + \sin\Delta\phi) - i\cos\Delta\phi) \right|^2 = \frac{1}{2} \cdot (1 + \sin\Delta\phi) \quad (2.9)$$

$$P_{lower} = \left| \frac{1}{2} \cdot (\cos\Delta\phi + i(\sin\Delta\phi - 1)) \right|^2 = \frac{1}{2} \cdot (1 - \sin\Delta\phi) \quad (2.10)$$

The MZM transfer functions are shown graphically in Fig 2.3. It can be seen that when phase difference between the two arms is $+90^\circ$ the power transfers to the upper arm and for -90° phase difference, the power is coupled to the lower arm. For 0° or 180° phase shift between the arms means that optical power is equally coupled to both the output waveguides. The devices are considered lossless and only linear phase change with applied voltage is considered for to make the description simple and clear. The derived transfer functions are good approximation in the case of LiNbO_3 and polymers based modulators where only the linear electro-optic effect (LEO) is present. However, in the case of modulators based on III-V semiconductors, which also have a quadratic electro-optic (QEO) effect then the transfer function is cannot be represented by a simple cosine function and is more complicated and can be distorted. An example of transfer function measured for the InP based modulator operating at $2 \mu\text{m}$ wavelength is shown in Fig 2.4. It can be observed that the optical power transfer function is not periodic which indicates the presence of higher order EO effects. The details of device layout and performance is explained in Chapter 5.

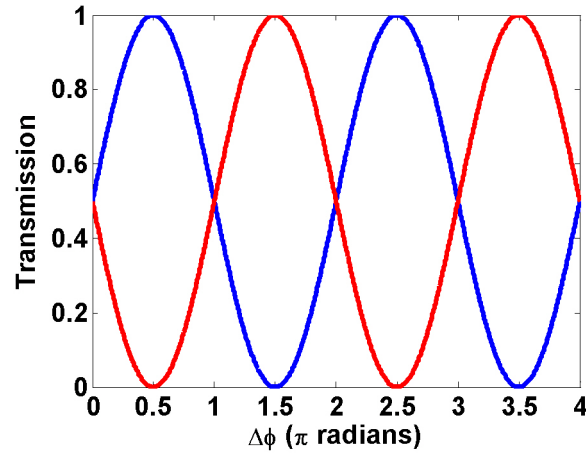


Figure 2.3: Transfer function of MZM with 2×2 MMI at the output. Blue trace shows the optical power in upper arm and red trace in lower arm.

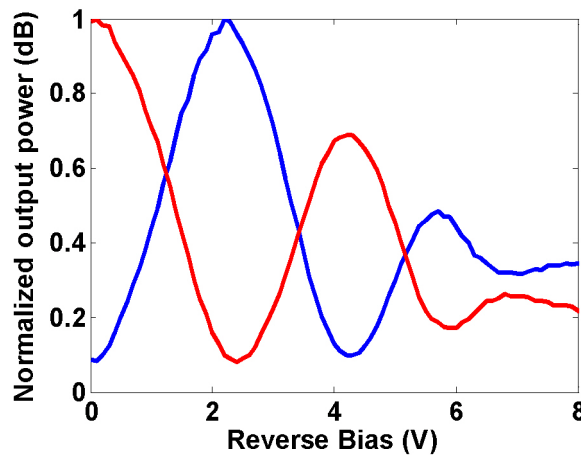


Figure 2.4: Measured transfer function of InP based MZM operating at $2\mu\text{m}$. The length of phase shifting electrode is 2.5 mm with reverse bias applied to a single arm only.

The main purpose of the MZM is to convert the electrical modulating signal to an optical signal modulation to be used in either short or long-haul optical communication systems. Once the DC transfer function of an MZM is determined as discussed above. The MZM can be biased at a fixed DC bias point and an external electrical modulating signal of certain frequency can be applied to achieve different optical modulation formats depending on the position of DC operating point. Details of the advanced optical modulation formats can be found in [7]. The simplest of modulation formats is non-return to zero (NRZ) or ON-OFF keying. By biasing the MZM at 50% of transmission point (also called quadrature point indicated by red circle in Fig 2.5) and applying the driving sig-

nal of peak to peak voltage equal to V_π , the intensity modulated optical signal can be generated as shown in RF switching curve in Fig 2.5.

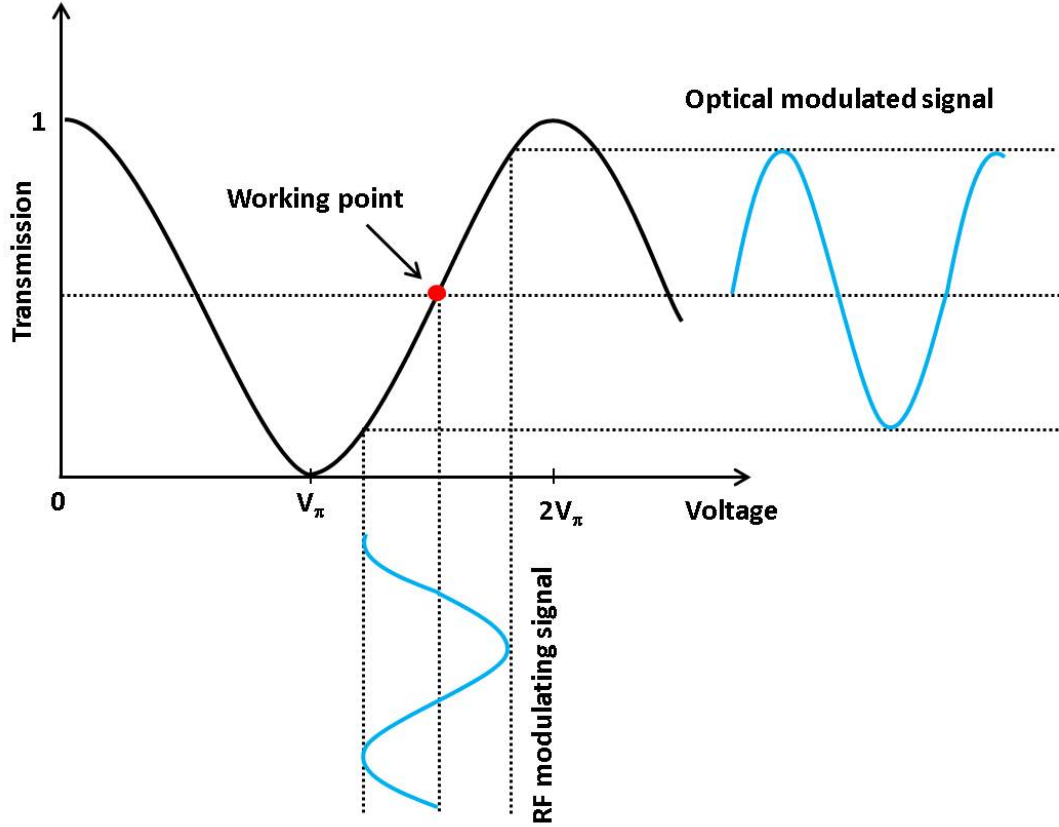


Figure 2.5: RF switching curve of a Mach-Zehnder modulator. Modulator is biased at quadrature point of transfer function.

2.2 III-V compound semiconductor materials

In addition to LiNbO_3 and polymers, III-V semiconductor materials are the most important electro-optically active materials in existence. These materials play an important role in realization of various active and passive photonic components such as lasers, modulators, photodetectors. They are compounds of group III and ground V of the periodic table. Binaries such as Indium phosphide (InP) and Gallium Arsenide (GaAs) are available as wafers on industrial scale. Ternaries and quaternaries are grown as epitaxial layers to form the p-i-n hetero-structures grown by metal organic vapour phase epitaxy (MOVPE) or molecular beam epitaxy (MBE) [8]. By controlling composition and thicknesses of these epitaxial layers i.e. MQWs in the i-region, the devices can be either made to emit or absorb light [9]. Fig 2.6 shows the variation of bandgap

or wavelength versus lattice constant of different III-V compounds based on InP and GaAs. For the operation of Mach-Zehnder modulators particularly, it is important for bandgap to be $\sim 120\text{-}150\text{ nm}$ ($70\text{-}86\text{ meV}$) below the wavelength of operation. The main purpose of this band edge detuning is to make the material transparent for the input wavelength and reduce the optical propagation loss (details are explained in Section 2.5). The composition and thickness of wells and barriers in the MQW structure determine the bandgap of the grown material structure and it is important to choose them carefully.

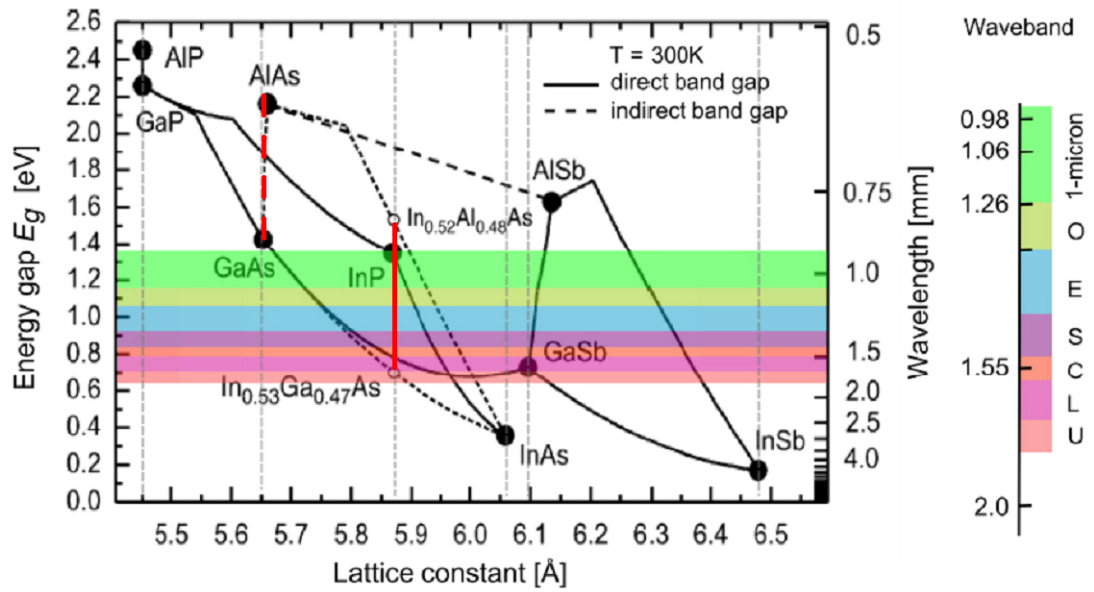


Figure 2.6: Lattice constant and bandgap energies of III-V semiconductor materials. The legend on right side shows different optical bands of operation with C and L band of highest interest to telecommunications [9].

The quality of the grown III-V material can be limited by the quality of the interfaces. The quality of the material is determined by the lattice defects introduced by the lattice mismatch between the substrate and all grown epitaxial layers. The lattice constants of all the layers including barriers and wells need to be matched to the substrate on which they are grown. High mismatch between the lattice constant results in generation of dislocation which can lead to degradation of both electrical and EO properties of the grown material [9]. Despite this problem, introducing strain in the III-V based epitaxial layers can be advantageous. It allows much wider choice of bandgap available, which may not be achievable using the equivalent unstrained wells. A practical example is the realization of $2\text{ }\mu\text{m}$ InP based MZMs in this thesis for which bandgap around $1800\text{-}1900\text{ nm}$ is required. This bandgap can only be achieved using

compressive strained Indium Gallium Arsenide (InGaAs) wells [10]. However, the presence of strain in the wells poses structural limits. First limit is the critical thickness of the strained layer itself which restricts the thermodynamic stability of each layer. Increasing the strain decreases the critical thickness of the layer. The critical thickness is the minimum thickness up to which a layer can be grown without being relaxed and producing dislocations. The second limit is the overall stress on the whole stack while growing strained wells. This stress can lead to relaxation of the top and bottom of the epitaxial material stack [9, 11]. Nevertheless, this can be avoided by oppositely strained barrier layers. This is called strain balancing/compensation, which allows the compositional deviation from the precise lattice matching.

It is important to highlight why InP based materials were chosen over GaAs to develop modulators in this work. Historically, there has been a competition between GaAs and InP based compound semiconductors. GaAs has been a preferred base material over InP due to high intrinsic resistivity, high electron mobility, low fabrication cost, high process yield and ability to operate in harsh radiation environment. Mature foundry processes originally developed for monolithic microwave integrated circuits (MMICs) were available to be used for GaAs based optoelectronic devices. Based on these factors, initial research in optical modulators was focused on GaAs based materials [8, 12–14]. In Fig 2.6, it can be seen that bandgap of GaAs and InP is around 1.424 eV and 1.35 eV respectively. The dashed red line shows the lattice matched compositions for GaAs. Optical modulators can be realized using AlGaAs /GaAs hetero-structures. AlGaAs is lattice matched to GaAs for all the fractions of Al but the bandgap is too high to realize lasers and photodetectors based on GaAs platform and for these devices there should be a different material active region to operate in telecom wavelengths [9, 14]. On the other hand, InP based quaternaries such as Indium Gallium Aluminum Arsenide (InGaAlAs) and Indium Gallium Arsenide Phosphide (InGaAsP) can cover the bandgap between $0.75\ \mu\text{m}$ (1.46 eV) to $1.65\ \mu\text{m}$ (0.75 eV) and all the compositions in this range are lattice matched to the InP substrate represented by a solid red line in Fig 2.6. This allows realization of active and passive components such as tunable laser, MZMs and amplifiers based on InP based platform. Photonic integration techniques further allow all these components to be integrated on a single InP chip to realize dense, compact and multi-wavelength coherent transmitters and receivers [15]. The ability to realize densely integrated and multi-functional photonic integrated circuits (PICs) on InP is the main reason that future high-

speed optical communication systems are relying more on InP technology as compared to GaAs.

2.3 Light propagation through a medium

When the light travels through a medium, its propagation properties are determined the susceptibility (χ) of the medium, which is a complex tensor given by Eq 2.11.

$$\chi = \chi' - j\chi'' \quad (2.11)$$

Both the real and imaginary part of χ determine how the light wave propagating in a medium is absorbed or amplified. With out any EO effect in a lossless medium, permittivity (ϵ) can be written as Eq 2.12,

$$\epsilon = \chi_o \epsilon_o = n^2 \epsilon_o \quad \chi'_o = n^2, \chi''_o = 0 \quad (2.12)$$

Optical modulators based on III-V semiconductor materials take advantage of the EO properties of these materials. Whenever, there is an EO effect, the χ of propagation medium changes from χ to χ_{eo} by $\Delta\chi$. The $\Delta\chi$ has both real and imaginary components [16].

$$\Delta\chi = \Delta\chi' - j\Delta\chi'' \quad (2.13)$$

$$\epsilon = \chi_{eo} \epsilon_o = (\chi_o + \Delta\chi) \epsilon_o = n^2 \epsilon_o + (\Delta\chi) \epsilon_o \quad (2.14)$$

χ_{eo} can be written in the complex form in general such that $\chi_{eo} = \chi'_{eo} - j\chi''_{eo}$ and the real and imaginary parts of χ_{eo} can be defined as

$$\chi'_{eo} = n^2 + \Delta\chi' \quad \text{and} \quad \chi''_{eo} = \Delta\chi'' \quad (2.15)$$

The propagation of a plane wave in the z direction in any electro-optically active material with χ_{eo} is given by Eq 2.16

$$E(z, t) = E e^{j(\omega t - k_{eo} z)} \quad (2.16)$$

where k_{eo} is the propagation constant in the material and can be defined as

$$k_{eo} = \omega \sqrt{\mu_o \epsilon_{eo}} = \omega \sqrt{\mu_o n^2 \epsilon_o} \left[\left(1 + \frac{\Delta\chi'}{2n^2}\right) - j \left(\frac{\Delta\chi''}{2n^2}\right) \right] \quad (2.17)$$

Substituting Eq 2.17 in 2.16 results in Eq 2.18

$$E(z, t) = \left[E e^{j\omega t} e^{-j\omega \sqrt{\mu_o n^2 \epsilon_o} z} \right] e^{-j\omega \sqrt{\mu_o n^2 \epsilon_o} \frac{\Delta \chi'}{2n^2} z} e^{-\omega \sqrt{\mu_o n^2 \epsilon_o} \frac{\Delta \chi''}{2n^2} z} \quad (2.18)$$

The intensity of the plane wave can be written as

$$I(z) = \frac{2}{\sqrt{\mu_o / \epsilon_{eo}}} |E(z, t)|^2 = \left[\frac{2E^2}{\sqrt{\mu_o / n^2 \epsilon_{eo}}} \right] e^{-\omega \sqrt{\mu_o n^2 \epsilon_o} \frac{\Delta \chi''}{n^2} z} \quad (2.19)$$

From the above expressions, it can be seen that a plane wave acquires an additional electro-optic phase shift of $\omega \sqrt{\mu_o \epsilon_o} \frac{\Delta \chi'}{2n}$ after propagation of distance z through the material. Also, the intensity of a plane wave can be attenuated or amplified depending on the sign of $\Delta \chi''$.

The real (χ') and imaginary part (χ'') of the χ for any material are further related to each other through Kramers-kronig relation.

$$\chi'(\omega) = \frac{1}{\pi} P.V \int_0^\infty \frac{\chi''(\omega')}{\omega' - \omega} d\omega' \quad (2.20)$$

$$\chi''(\omega) = -\frac{1}{\pi} P.V \int_0^\infty \frac{\chi'(\omega')}{\omega' - \omega} d\omega' \quad (2.21)$$

Where P.V stands for the Cauchy principle value that excludes the singular point $\omega' = \omega$. The significance of relation of χ' and imaginary part χ'' through Kramers-Kronig can be described as follows: Any change in the absorption spectra of the material will result in refractive index spectra change and if the any of them is known over a wide spectral range, the complementary function can be calculated through the use of above relations [16].

2.4 Electro-optic effects in III-V semiconductors

The electro-optic effects in general can be further classified as field effects and carrier effects. There are three main field induced effects namely linear electro-optic (LEO) or Pockels effect, quadratic electro-optic (QEO) or Kerr effect and electro-absorption effect. The Pockels effect is linearly proportional to the applied field and is only found in the crystals which lack inversion symmetry [8]. Because of this reason, LEO is absent in pure silicon (Si) and Si-based modulators rely on carrier induced refractive index changes or strain induced refractive index change [17]. The quadratic effects are universal and are found in all, transparent semiconductors [8]. As compared to LEO, QEO is usually

very small and in presence of both effects LEO dominates. Lastly, field induced electro-absorption effects are related to the bandgap of the semiconductor, where the applied electric field changes the energy difference between the conduction and valance band in a semiconductor. In bulk semiconductors it is called as Franz-Keldysh effect (FKE). However, it is strongest in the multiple quantum well (MQW) structures, where its called qunatum confined Stark effect (QCSE). In both of these effects, applied bias voltage changes the optical absorption, which leads to the phase change through the Karmers-Kronig relations explained above. For the carrier based effects, there are two modes of operation. Carriers can be injected or depleted in the intrinsic region of the p-i-n optical waveguide to achieve a refractive index change [17]. Even though high refractive index changes can be achieved, the carrier injection limits the modulation bandwidth which depends on carrier lifetime which is typically 1-20 ns in III-V materials [18]. The carrier lifetime can be reduced at the expense of increased V_π by introducing intentional material defects or by changing the injection mode to depletion mode, where carriers are removed [8]. The details of carrier induced refractive index change can be found in [19]. The InP based MZM developed in this work mainly use LEO and QCSE in based refractive index change in which reverse electric field is applied across the MQW based intrinsic region of the phase shifting waveguides.

2.4.1 Linear electro-optic effect

When materials such as III-V compound semiconductors e.g. InP or GaAs, are subjected to an external field, the atoms or molecules constituting the material are polarized due to oppositely charged forces on positively and negatively charged parts of these molecules or atoms resulting in redistribution of these bound charges. The net result of this redistribution is a change in the permittivity tensor. When the change in inverse of permittivity tensor is linearly proportional to the applied field, the response is called linear electro-optic effect which is also known as pockels effect [20]. The induced polarization field P can be represented as $P = \chi E$. In the presence of an external field the electrical flux density D (C/m^2) can be written as $D = \epsilon_o E + \epsilon_o P = \epsilon_o(1 + \chi)E = \epsilon_o \epsilon_r E$, where ϵ_o is the permittivity of free space and ϵ_r is the relative permittivity of the material subjected to external field. The refractive index of material is defined as $n = \sqrt{\epsilon_r}$. Based on which D can be written as, $D = \epsilon_o n^2 E$. It means that the refractive index of the material depends on the the relative permittivity and any change to the permittivity of a medium results in a change in the refractive

index.

Generally in tensor form D can be written as in Eq 2.22,

$$\begin{bmatrix} D_x \\ D_y \\ D_z \end{bmatrix} = \begin{bmatrix} \epsilon_{xx} & \epsilon_{xy} & \epsilon_{xz} \\ \epsilon_{yx} & \epsilon_{yy} & \epsilon_{yz} \\ \epsilon_{zx} & \epsilon_{zy} & \epsilon_{zz} \end{bmatrix} \cdot \begin{bmatrix} E_x \\ E_y \\ E_z \end{bmatrix} = \epsilon_o \begin{bmatrix} n_{xx}^2 & n_{xy}^2 & n_{xz}^2 \\ n_{yx}^2 & n_{yy}^2 & n_{yz}^2 \\ n_{zx}^2 & n_{zy}^2 & n_{zz}^2 \end{bmatrix} \cdot \begin{bmatrix} E_x \\ E_y \\ E_z \end{bmatrix} \quad (2.22)$$

where $\epsilon_{xx}, \epsilon_{xy} \dots$ are the dielectric constants of the medium. The elements of the dielectric tensor should be symmetric i.e. $\epsilon_{kl} = \epsilon_{lk}$. Eq 2.22 can be rearranged to Eq 2.23.

$$\begin{bmatrix} E_x \\ E_y \\ E_z \end{bmatrix} = \frac{1}{\epsilon_o} \begin{bmatrix} \left(\frac{1}{n^2}\right)_{xx} & \left(\frac{1}{n^2}\right)_{xy} & \left(\frac{1}{n^2}\right)_{xz} \\ \left(\frac{1}{n^2}\right)_{yx} & \left(\frac{1}{n^2}\right)_{yy} & \left(\frac{1}{n^2}\right)_{yz} \\ \left(\frac{1}{n^2}\right)_{zx} & \left(\frac{1}{n^2}\right)_{zy} & \left(\frac{1}{n^2}\right)_{zz} \end{bmatrix} \cdot \begin{bmatrix} D_x \\ D_y \\ D_z \end{bmatrix} \quad (2.23)$$

The energy density in a medium is given as $W = \frac{1}{2}E.D$. Using the Eq 2.23 with the help of some basic matrix operations, the final expression can be written in the form of Eq 2.24. The complete derivation can be found in [20].

$$x^2 \left(\frac{1}{n^2}\right)_1 + y^2 \left(\frac{1}{n^2}\right)_2 + z^2 \left(\frac{1}{n^2}\right)_3 + 2yz \left(\frac{1}{n^2}\right)_4 + 2xz \left(\frac{1}{n^2}\right)_5 + 2xy \left(\frac{1}{n^2}\right)_6 = 1 \quad (2.24)$$

Where x,y and z are the dielectric axis of a crystal. Eq 2.24 represents an ellipse and is called as ellipsoid or optical indicatrix in the presence of an electric field [20]. The index ellipsoid is the most convenient way to describe the behavior of an anisotropic material. The linear change in permittivity tensor elements

$$\left(\frac{1}{n^2}\right)_i \quad (i = 1, \dots, 6)$$

in the presence of an external electric field is given by Eq 2.25.

$$\Delta(1/n^2)_i = r_{ijk} E_k + \dots \quad (2.25)$$

where E_k is the kth component of applied electrical field, r_{ijk} is linear electro-optic coefficient or pockels coefficient. In the matrix form the above Eq can be written as Eq 2.26.

$$\begin{bmatrix} \Delta(1/n^2)_1 \\ \Delta(1/n^2)_2 \\ \Delta(1/n^2)_3 \\ \Delta(1/n^2)_4 \\ \Delta(1/n^2)_5 \\ \Delta(1/n^2)_6 \end{bmatrix} = \begin{bmatrix} r_{11} & r_{12} & r_{13} \\ r_{21} & r_{22} & r_{23} \\ r_{31} & r_{32} & r_{33} \\ r_{41} & r_{42} & r_{43} \\ r_{51} & r_{52} & r_{53} \\ r_{61} & r_{62} & r_{63} \end{bmatrix} \cdot \begin{bmatrix} E_x \\ E_y \\ E_z \end{bmatrix} \quad (2.26)$$

The electro-optic coefficient tensor $[r_{ij}]$ is a third-rank 6×3 matrix. The value of electro-optic coefficients in $[r_{ij}]$ tensor depends on the crystal symmetry. For the crystals having a center of symmetry, such as Si, the electro-optic tensor elements are zero and there will be no LEO effect [20]. III-V compound semiconductors and other materials grown epitaxially on them have no center of symmetry and they have Zinc Blende ($\bar{4}3$) crystal structure with the only non zero electro-optic coefficients of $r_{41}=r_{52}=r_{63}$. This reduces the electro-optic coefficient tensor as represented in Eq 2.27. It must be noted that III-V materials are not intrinsically birefringent and it is only introduced when the external electric field is applied.

$$\begin{bmatrix} \Delta(1/n^2)_1 \\ \Delta(1/n^2)_2 \\ \Delta(1/n^2)_3 \\ \Delta(1/n^2)_4 \\ \Delta(1/n^2)_5 \\ \Delta(1/n^2)_6 \end{bmatrix} = \begin{bmatrix} 0 & 0 & 0 \\ 0 & 0 & 0 \\ 0 & 0 & 0 \\ r_{41} & 0 & 0 \\ 0 & r_{41} & 0 \\ 0 & 0 & r_{41} \end{bmatrix} \cdot \begin{bmatrix} E_x \\ E_y \\ E_z \end{bmatrix} \quad (2.27)$$

The total refractive index change in the presence of applied field will be the sum of the original index terms shown in Eq 2.24 plus the $\Delta(1/n^2)$ terms calculated using the Eq 2.27. The new index ellipsoid equation for any Zinc Blende crystal calculated in the presence of electric field is expressed in Eq 2.28.

$$\frac{x^2 + y^2 + z^2}{n^2} + 2r_{41}(yzE_x + zxE_y + xyE_z) = 1 \quad (2.28)$$

where n is the refractive index of material such that $n=n_x=n_y=n_z$ due to cubic crystalline symmetry of Zinc Blende. If the electric field is applied in Z-direction Eq 2.28 reduces to Eq 2.29 such that $E_x = E_y = 0$ and the only electric field component is E_z .

$$\frac{x^2 + y^2 + z^2}{n^2} + 2r_{41}xyE_z = 1 \quad (2.29)$$

From Eq 2.29 it can be seen that once the electric field is applied, the index ellipsoid is no longer a diagonal and two off-diagonal elements ($r_{41}xyE_z$) are present, resulting in the 45° rotation of the index ellipsoid in x-y plane. The index ellipsoid can be easily diagonalized again using simple coordinate transformation with respect to x-y plane. In the new coordinate system x',y' and z, the equation of diagonalized index ellipsoid becomes ,

$$x'^2 \left(\frac{1}{n^2} + r_{41}E_z \right) + y'^2 \left(\frac{1}{n^2} - r_{41}E_z \right) + \frac{z^2}{n^2} = 1 \quad (2.30)$$

It is clear from Eq 2.30, that there will be no refractive index change for the light polarization in z-direction i.e. transverse magnetic (TM) polarized optical mode, which has electric field component only normal to the crystal plane. The total refractive index for the optical mode polarized in x' direction and traveling in y' direction is given by Eq 2.31

$$n_{x'} = n + \Delta n_{x'} = n + \frac{1}{2}n^3r_{41}E_z \quad (2.31)$$

Similarly, for the optical mode polarized in y' direction and traveling in x' direction , the total refractive index is represented by Eq 2.31

$$n_{y'} = n + \Delta n_{y'} = n - \frac{1}{2}n^3r_{41}E_z \quad (2.32)$$

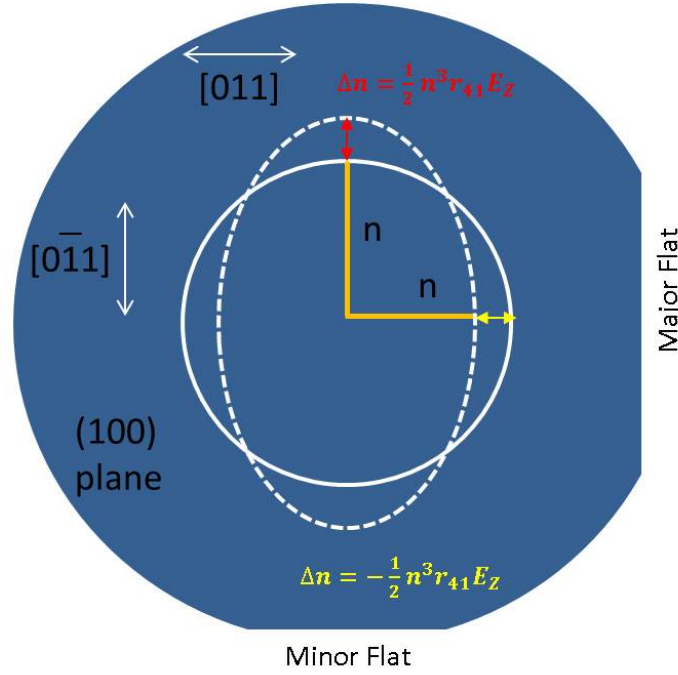


Figure 2.7: (100) InP wafer with $[0\bar{1}1]$ and $[011]$ directions parallel to major flat and minor flat respectively (EU/Japanese standard). The solid circle represents the isotropic ellipsoid of InP crystal in absence of field with refractive index of n in all directions. The dotted ellipse represents the index variation due to LEO.

Fig 2.7 shows the graphical representation of this effect of increase and decrease in refractive index as a function of waveguide orientation in Eq 2.31 and 2.32 respectively. It depicts the major flat and minor flat of (100) InP wafer used in the fabrication of devices in this work. The direction $[0\bar{1}1]$ is parallel to the major flat and $[011]$ is perpendicular to the major flat. For TE polarized input light, the optical waveguide oriented parallel to $[0\bar{1}1]$ i.e. major flat, the intrinsic refractive index increases by factor $\frac{1}{2}n^3r_{41}E_z$ due to LEO effect. On the other hand, for the waveguides that run parallel to minor flat i.e. $[011]$ direction, the refractive index is decreased by factor $\frac{1}{2}n^3r_{41}E_z$ for TE polarization. The typical reported value of LEO coefficient r_{41} in InP is around 1.4 pm/V [11,20]. For TM polarization, there will be no refractive index modulation due to LEO. It implies that to maximize the refractive index change in the phase shifter of an InP based MZM comprising of p-i-n structure, the optical waveguides should be fabricated in the direction parallel to the major flat of (100) plane InP wafer. Higher refractive index change will result in higher phase change efficiency, which in turn reduces the V_π . In this thesis, the same InP wafer crystal orientations explained here is used in the next chapters.

2.4.2 Quadratic electro-optic effect

In the Eq 2.25, only the term depending on the linear electric field was considered. However, in reality, the refractive index of all materials also show a quadratic dependence on the externally applied field. This effect is present in all materials irrespective of crystal symmetry and is known as Kerr effect or quadratic electro-optic effect (QEO) [20]. Eq 2.25 can be expanded to Eq 2.10 include the quadratic dependence of the refractive index change on electric field due to the second order distortion. Terms higher than second order can be neglected.

$$\Delta(1/n^2)_i = r_{ijk}E_k + R_{ijkl}E_kE_l + \dots \quad (i = 1, \dots, 6) \quad (2.33)$$

where R_{ijkl} is the quadratic electro-optic fourth rank tensor. The R_{ijk} coefficients are usually very weak as compared to r_{ij} coefficients for LEO effects. In matrix form, the above equation can be expressed as shown below. The R_{ijk} tensor used is for Zinc Blende crystal structure.

$$\begin{bmatrix} \Delta(1/n^2)_1 \\ \Delta(1/n^2)_2 \\ \Delta(1/n^2)_3 \\ \Delta(1/n^2)_4 \\ \Delta(1/n^2)_5 \\ \Delta(1/n^2)_6 \end{bmatrix} = \begin{bmatrix} R_{11} & R_{12} & R_{12} & 0 & 0 & 0 \\ R_{12} & R_{11} & R_{12} & 0 & 0 & 0 \\ R_{12} & R_{12} & R_{11} & 0 & 0 & 0 \\ 0 & 0 & 0 & R_{44} & 0 & 0 \\ 0 & 0 & 0 & 0 & R_{44} & 0 \\ 0 & 0 & 0 & 0 & 0 & R_{44} \end{bmatrix} \cdot \begin{bmatrix} E_x^2 \\ E_y^2 \\ E_z^2 \\ E_z^2 \\ E_yE_z \\ E_xE_z \\ E_xE_y \end{bmatrix} \quad (2.34)$$

For the z-directed electric field such that ($E_x=E_y=0$), the index ellipsoid in the matrix form can be written as in Eq 2.35.

$$\begin{bmatrix} x & y & z \end{bmatrix} \cdot \begin{bmatrix} \frac{1}{n^2} + R_{12}E_z^2 & 0 & 0 \\ 0 & \frac{1}{n^2} + R_{12}E_z^2 & 0 \\ 0 & 0 & \frac{1}{n^2} + R_{11}E_z^2 \end{bmatrix} \cdot \begin{bmatrix} x \\ y \\ z \end{bmatrix} \quad (2.35)$$

Due to absence of any non-diagonal elements in the ellipsoid equation, the transformation to $x'-y'$ coordinate systems has no effect on the ellipsoid equation. The final expressions for the index change due to QEO can be written as Eq 2.36 and 2.37.

$$\Delta n_{x'} = \frac{1}{2} n^3 R_{12} E_z^2 \quad (2.36)$$

$$\Delta n_{y'} = \frac{1}{2} n^3 R_{11} E_z^2 \quad (2.37)$$

Generally, a single value is quoted for quadratic electro-optic coefficient in literature such that $R_{11} \approx R_{12}$ [20]. From Eq 2.35, it is clear that refractive index change due to QEO is isotropic and is also independent of polarization. Typical values of QEO coefficient in InP is in the range of 10^{-19} - $10^{-21} \text{ m}^2/\text{V}^2$ [20] and is highly wavelength dependent and it can be strongly enhanced at wavelengths near the bandgap of material by the electro-absorption effects explained the next section.

2.4.3 Electroabsorption Effect: The Franz-Keldysh effect

Electroabsorption induced electro-optic effects involve the bandgap of the semiconductor. According to basic semiconductor theory, when the incident photon energy is less than bandgap of semiconductor i.e. $h\nu < E_c - E_v$, it cannot be absorbed to excite an electron from valence band to conduction band. However, experiments show that in the presence of an external electric field, the absorption behavior of the semiconductor is complex and in longer wavelength region an exponential tail is introduced in the fundamental absorption edge of the material as shown in Fig 2.8. This tail in absorption spectrum is explained by photon-assisted tunneling of electrons from valence band to conduction band, thus allowing the absorption of photon with energy slightly less than the bandgap of the semiconductor to be absorbed. This effect is called the Franz-Keldysh effect (FKE) which was predicted independently by German physicist W. Franz [21] and Russian physicist L.V. Keldysh [22]. Fig 2.9, depicts this effect graphically. When the external electric field is applied to a semiconductor, the semiconductor bandgap is tilted in the direction of the applied electric field such that electron and hole wave functions penetrate in the bandgap. The result is the non-zero overlap between electron and hole wave functions, facilitating low energy photons to be absorbed.

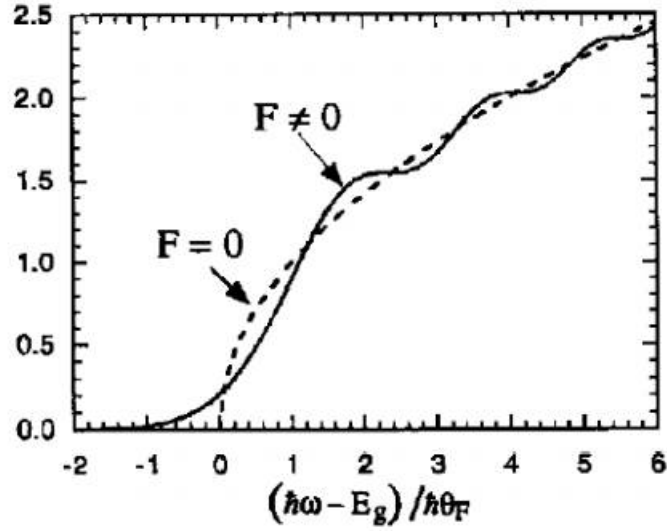


Figure 2.8: Example of absorption spectrum in bulk semiconductor with and without external field (F) [9].

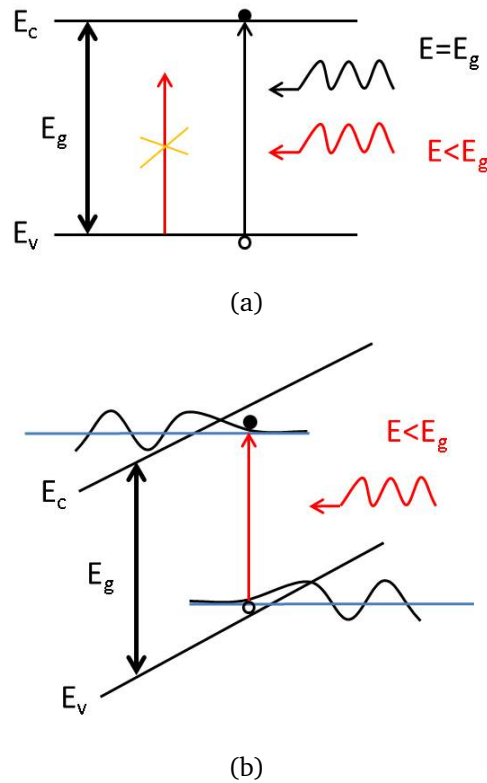


Figure 2.9: (a) Bandgap absorption in thermal equilibrium (No external field). No absorption is allowed for photon with energy $E < E_g$ (b) Electron-hole transition for photon with energy $E < E_g$ due to tilting of bandgap in the Franz-Keldysh effect in the presence of external field.

In the above discussion for FKE, for simplicity, the effect of Coulomb interac-

tion between electron and holes generated during the absorption process for the photons with energy larger than bandgap was neglected. In practice, when the energy of the absorbed photon is larger than the semiconductor bandgap, an electron transition takes place from valence to conduction band leaving behind a positively charged localized hole. As the electron-hole move to their lowest energy states, there will be Coulomb attraction between electron-hole pair resulting in formation of an exciton [23, 24]. The exciton will experience three dimensional Coulomb forces similar as the hydrogen atom. The energy of the exciton pair is less than the energy of free electron-hole pairs. The result is the creation of exciton energy levels just below the bandgap of the semiconductor. The creation of these states will allow the absorption of photons with energy just below the bandgap. However, in bulk semiconductor the excitonic effects cannot be observed at the room temperature as the binding energy of the excitons is less than the thermal energy of particles at the room temperature which readily ionizes the electron-hole pair (typically in 300 fs). The S^{th} state bound exciton energy (E_{X3D}) in bulk semiconductor is given by Eq 2.38 [25].

$$E_{X3D} = -\frac{R_y}{S^2} \quad (2.38)$$

where R_y is the Rydberg energy

$$R_y = \frac{m_r e^4}{2\hbar^2 (4\pi\epsilon_r\epsilon_o)^2}$$

2.4.4 Electroabsorption Effect: The Quantum Confined Stark Effect

As compared to bulk semiconductors, in quantum well/barrier structures, the situation is different. A quantum well is formed when a lower bandgap (E_{QW}) well is sandwiched between high bandgap barriers (E_B). The width of barrier is usually kept 5 to 10 nm to avoid the coupling of electron and hole wave function in two neighboring wells. Due to conduction and valence band potential barriers, the electrons and holes are localized in the well structures. The potential barriers result in the formation of discrete energy levels for both conduction and valence band. An example of a single quantum well with lowest energy level E_{e1} for conduction band and the highest energy level for the holes E_{hh1} with the respective wave functions confined in the well is shown in Fig 2.10a. Some holes in the valence band are heavier and some are lighter. Each energy level for the holes is further classified as light-hole (E_{lh}) and heavy-hole

(E_{hh}). Usually, E_{hh} is the highest energy level and in this example only heavy hole energy level is shown for explanation of basic phenomenon. Without any external field applied the electron and hole wave functions for the each subband level is symmetric around the center of well. Due to localization of electron and hole wave functions with the well, the binding energy and oscillator strength of exciton formed will be high as compared to the bulk material. High confinement allows sharp excitonic peaks to be visible even at room temperature. The exciton binding energy for 2D case is give by Eq 2.39 and is usually less than 15 meV [25].

$$E_{X3D} = -\frac{R_y}{(S - \frac{1}{2})^2} \quad (2.39)$$

From Eq 2.39, it can be deduced that for 1st bound state, $S=1$, the exciton binding energy is four times higher in two dimensional exciton as compared to three dimensional case. Also, the photon energy absorbed in the quantum well is given by Eq 2.40, where the exciton binding energy must be taken into account.

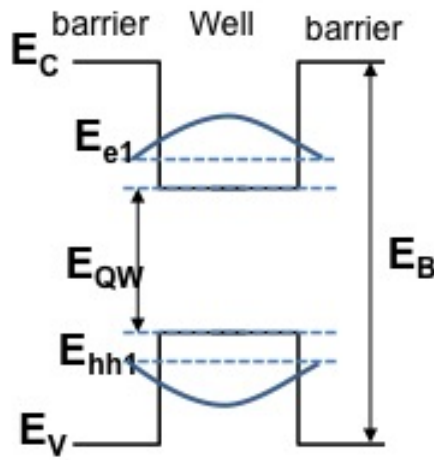
$$h\nu = E_{QW} + E_{e1} + E_{hh1} - E_{ex} \quad (2.40)$$

When the electric field is applied in direction perpendicular to the single quantum well layers as shown in Fig 2.10b, the effect which causes the red shift of the absorption spectrum is called the quantum confined Stark effect (QCSE). It can be seen that the field pulls the electron and hole towards the opposite side of the wells resulting in the reduction of energy of electron-hole pair with a corresponding shift of the exciton absorption peak. The distinct feature of the QCSE is that the excitonic resonances are not smeared away as in case of FKE by the applied electric field and can be observed even at the high applied fields. The electron and holes are basically impeded by the walls of the well from tunneling out of the well. Also, since the quantum well structures are usually of the order of 10 nm as compared to three dimensional exciton size (30 nm) in bulk material, despite the reduction of electron-hole wave function overlap due to spatial separation with the applied field, the excitonic peaks still exist with slight broadening. The persistence of the excitons in the case of GaAs-AlGaAs quantum well structures was explained by Miller et al. in [26]. The dependence of excitonic peak shift with applied electric field is quadratic and it is proportional to the fourth power of the quantum well thickness. Details of the complete analysis based on the variational method can be found in [27].

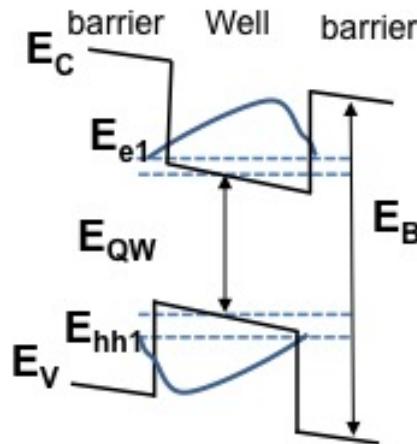
Mathematically, field induced excitonic peak shift (ΔE) is given as Eq 2.41.

$$\Delta E = \text{const.} E^2 L_{QW}^4 \quad (2.41)$$

It is clear that increasing the well thickness (L_{QW}), increases the field induced shift. But at the same time it broadens the excitonic peak due to reduced exciton binding energy in the wider wells. The reduced binding energies will eventually result in deterioration of the absorption change. The effect of loss of excitonic confinement and its effect on the refractive index change and absorption will be discussed in detail in the next section.



(a)



(b)

Figure 2.10: (a) Electron-hole wave confinement in a typical potential well in the absence of an external field. (b) Deformed wave function with reduced energy level in the presence of an external field.

As mentioned previously, the electro-refractive index spectra is inherently related to the the absorption spectra change generated by electro-absorption effects i.e. both the FKE and QCSE. If change in absorption ($\Delta\alpha$) is known then the change in real part of refractive index change Δn can be calculated through Kramers-Kronig equation:

$$\Delta n = \frac{\lambda_i^2}{2\pi^2} P.V \int_0^\infty \frac{\Delta\alpha}{\lambda_i^2 - \lambda^2} d\lambda \quad (2.42)$$

In III-V MQW based modulators, there is a choice to either use $\Delta\alpha$ or Δn to achieve optical modulation. In electro-absorption modulators (EAMs), quantum wells are designed to achieve maximum $\Delta\alpha/\Delta V$ at the wavelength of operation, which is near the band edge (ΔV is the change in applied reverse bias). However, near band edge, there will be always a Δn induced phase shift associated with absorption change causing frequency chirp in the data modulated signal [8]. The MZMs are electro-refractive modulators, which operate at a wavelength detuned from the bandgap. In MZM case, the selection of detuning wavelength and MQW design is to maximize $\Delta n/\Delta V$ and reduce the absorption induced optical loss. It should be noted that the Δn achieved using electro-refraction is much higher than achieved through LEO.

2.5 QCSE in shaped quantum well

There are a number of possibilities in the rich MQW design space which can be exploited to achieve better modulation characteristics for MZMs. The possibilities include the MQW material system selection, the well / barrier widths which can induce coupling as well as the quantum well number and shape. MZMs exploring the possibilities of an enhanced electro-optic effect in rectangular [28], asymmetric coupled [29, 30], two step [31] and three step QW structures [32] have been reported. In the above section, the QCSE effect has been discussed only qualitatively. In this section, the performance of asymmetrically ramped MQW structures based on the InAlGaAs material system for use in an electro-refractive modulator is discussed and experimentally demonstrated. The electro-optic effects on TE polarized light at 1550 nm are experimentally compared for two $10 \times$ QW structures which are mirrored in their growth direction. First the performance of two expitaxial structure is compared in terms of QCSE induced red shift in the absorption spectrum. Then the index, Δn , and phase change, $\Delta\phi$, with applied bias in both the structures is used to for further

performance comparison.

2.5.1 Ramped Quantum wells

As explained in Section 2.2, the tri-metal InAlGaAs alloy is lattice-matched to InP for an In composition of 53% and the bandgap of the alloy can be varied from 1650 nm to 850 nm by varying the ratio of Al to Ga from 0 to 1. Thus shaped quantum wells can be envisaged. In order to study the effect of ramp shape on electro-optic properties two different epitaxial structures with increasing (Wafer A) and decreasing (Wafer B) ramps of the bandgap in the quantum wells have been grown using low-pressure (80 mbar) MOVPE on n-doped (100) InP substrates at 630 °C. The structures were grown sequentially to avoid variations in the growth environment. Shaping of quantum wells was achieved by linearly ramping the flux of Al and Ga through mass flow controllers into the reactor during epitaxial growth, resulting in a linear grade in Al to Ga concentration ratio whilst maintaining a ‘total’ group-III flux throughout ramp. Each wafer contains 10 MQWs with a thin undoped InP cladding on the P-doped side leading to the total intrinsic region thickness of 308 nm. A P-doped InP cladding layer is followed by a highly P-doped InGaAs layer for contacting purposes. For each wafer the thickness of the well (barrier) is 12 nm (8 nm). Each 12 nm well comprises 5 nm base and 7 nm ramp sections with the bandgap ramp in opposite direction for the respective wafers. The grown samples emit photoluminescence (PL) peaks at 1337 nm and 1310 nm for Wafers A and B respectively with full width half maximum (FWHM) of 59 nm.

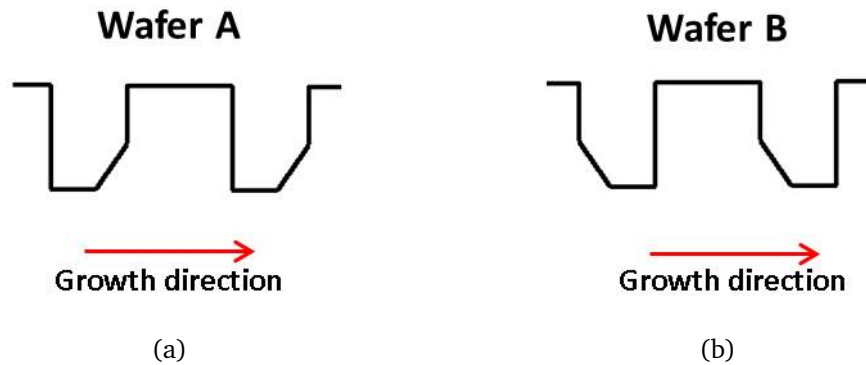


Figure 2.11: Schematic representation of quantum wells in the growth direction in: (a) Wafer A (Ramp up). (b) Wafer B (Ramp down).

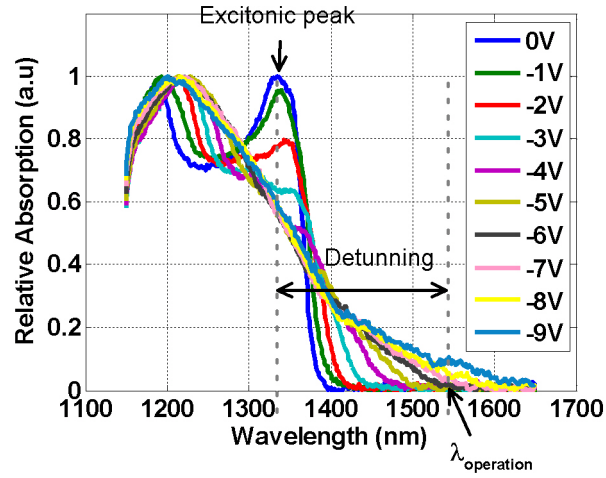
The quantum well structures in both the wafers are shown schematically in Fig 2.11. The EO characteristics of the respective designs have been inves-

tigated by fabricating 1 mm diameter photodiodes with surface normal access with top InGaAs contact layer removed. This configuration allows the measurement of the direct absorption associated with TE polarized light under biased conditions. The photoabsorption measurement setup will be explained later in Chapter 5 of thesis (see Fig 5.2). Here we show the measurement results only.

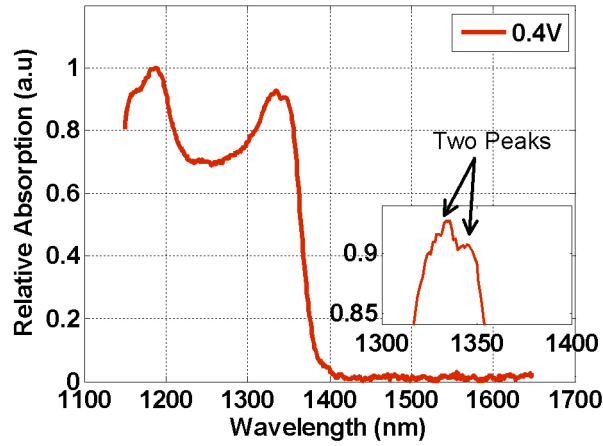
Fig 2.12a shows the photoabsorption spectra of Wafer A (ramp up) as a function of reverse bias. A strong excitonic resonance peak is observed at 1333 nm at 0 V bias corresponding to an inbuilt electric field of 35 kV/cm from the PN junction. However, when the photoabsorption spectrum is measured at the forward bias of 0.4 V as shown in Fig. 1(b), we can observe two clear resonance peaks at 1333 nm and 1347 nm respectively. These peaks can be attributed to ground-state light-hole (e1-lh) and ground-state heavy-hole (e1-hh) transitions respectively as discussed before. The merger of two resonance peaks can be due to background doping effect which causes 1e-lh and 1e-hh peaks to merge [33,34] or it can also happen due to additional alloy broadening during growth process [35].

The red shift of the absorption peak with the applied reverse bias can be seen and is due to the Stark effect shown in Fig 2.10. While the electrons and holes are still confined within the wells, the increase in reverse bias reduces the electron-hole overlap as explained before. The increase of the field results in the broadening of the excitonic resonance and a decrease in exciton binding energy. At a reverse bias of -5 V, the 1e-1hh loses its quantum confinement which results in de-localization of the exciton. Due to the quenching of the exciton at high reverse bias, the absorption tail extends into the 1550 nm region which is the intended wavelength of operation. The extension of absorption tail will result in higher absorption at 1550 nm for TE polarized light which will result in higher Δn .

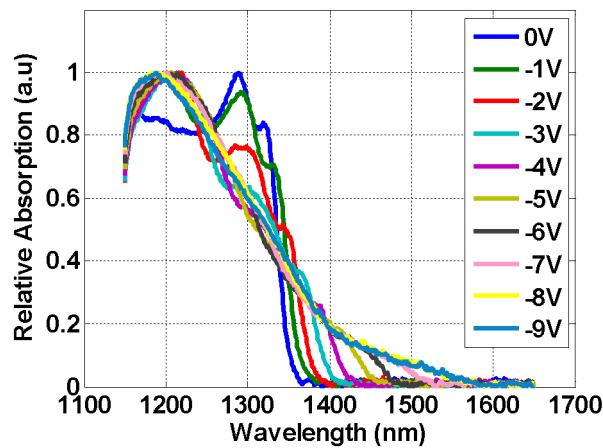
The photoabsorption spectrum of Wafer B (ramp down) as a function of reverse bias is shown in Fig 2.12c. As opposed to Wafer A, two well resolved excitonic features due to light and heavy hole transitions can be seen in the measured spectrum. The multiple resonance peaks occur at 1290 nm (1e-lh) and 1319 nm (1e-hh) respectively. With the increase in reverse bias, Wafer B behaves similarly to Wafer A and there is a clear Stark shift. However, the excitonic feature retains its shape even for a reverse bias voltage of -7 V unlike Wafer A. It also indicates that the exciton lifetime in Wafer B is longer than in Wafer A. This results in a lower absorption tail around 1550 nm as evident from Fig 2.12c.



(a)



(b)



(c)

Figure 2.12: Normalized photo-absorption spectra for the oppositely ramped MQW structures at different biases (a) Wafer A (Ramp up). (b) The photoabsorption spectrum of Wafer A (Ramp up) at forward bias of 0.4 V. Inset shows the resolved peaks due to e1-lh and e1-hh. (c) Wafer B (Ramp down).

2.5.2 Refractive index change

To further evaluate the EO effect in the asymmetric MQW structures, both wafers are processed into ridge waveguides of different widths varying from 2 to 4 μm using standard lithography and $\text{Cl}_2/\text{CH}_4/\text{H}_2$ based inductively coupled plasma (ICP) etching. The ridges are aligned along the $[0\bar{1}1]$ axis to achieve refractive index change due to both LEO + QCSE as explained in Section 2.4. The ridges are passivated, metallized and cleaved into 1 mm long bars. The measured leakage current in the fabricated ridges is less than 1 μA for all applied biases as shown in Fig 2.13. Both the wafers have breakdown voltages of around 16 V in the dark. An increased photo-detected current can be observed in Fig 2.13 when TE polarized light at 1550 nm is coupled into the waveguide due to absorption associated with the QCSE. For the same input power the photodetected current at -10 V in Wafer A is around 0.48 mA as compared to 0.22 mA in Wafer B. The current is plotted on logarithmic scale to allow a clear visualization of dark and photodetected current. The higher absorption in Wafer A is mainly due to the extension of the absorption tail at 1550 nm due to exciton ionization. Although, Δn due to high absorption tail will be high, resulting in lower V_π but in interferometric arrangement of MZM it will result in imbalance between the arms affecting the transfer function ER and also increases the insertion loss of the device.

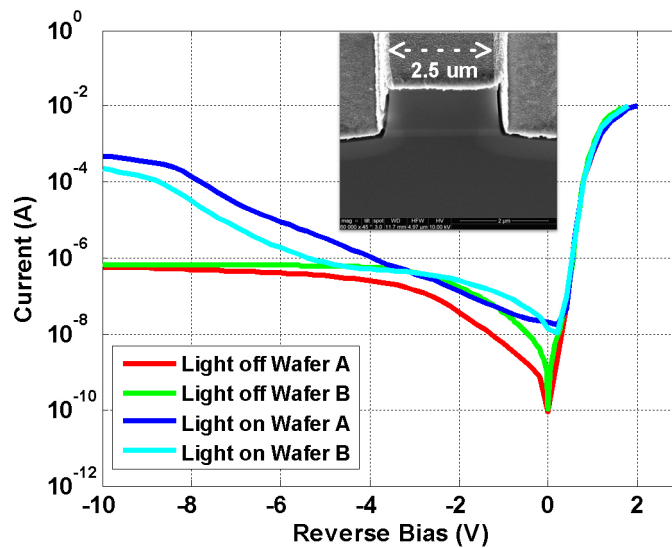
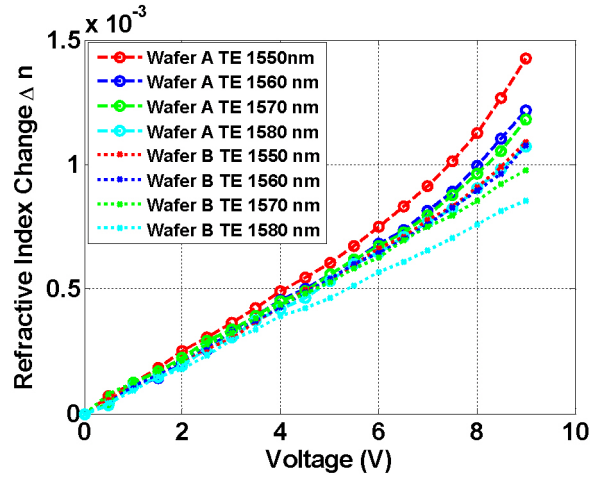
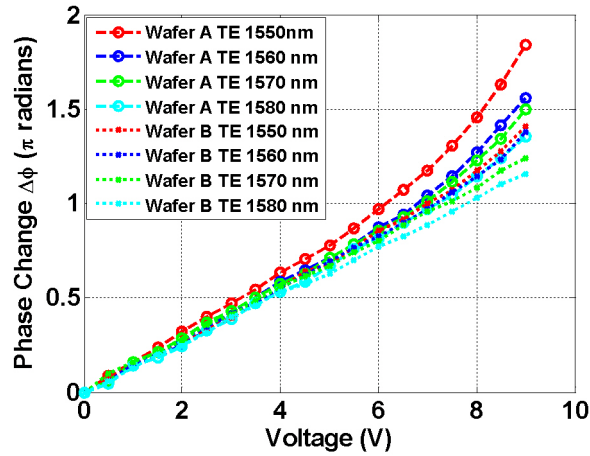


Figure 2.13: Current-voltage characteristics of 1 mm long metallized ridge with and without TE polarized light at 1550 nm. Inset shows the SEM image of the fabricated sample with 2.5 μm wide ridge.



(a)



(b)

Figure 2.14: (a) Measured Δn for Wafer A and B for TE polarization. (b) Measured $\Delta\phi$ for Wafer A and B for TE polarization.

The change in refractive index (Δn) and phase change ($\Delta\phi$) is measured in 1 mm long uncoated waveguides by measuring the Fabry-Perot fringe shift with applied reverse voltage for TE polarized input light at different wavelengths ranging from 1550 nm to 1580 nm. Measurement setup and procedure to extract both Δn and $\Delta\phi$ is described in Chapter 4 (See section 4.1). The extracted Δn and $\Delta\phi$ at different wavelengths are plotted in Fig 2.14a and 2.14b respectively. It can be seen that Wafer A has a voltage length product ($V_\pi \cdot L$) of 6 V·mm as compared to 7 V·mm for Wafer B at 1550 nm. The reduction of the switching voltage (V_π) in Wafer A is due to the higher absorption as shown in Fig 2.12a and 2.13 respectively. Due to the lower exciton lifetime in Wafer A as compared to Wafer B, the exciton peak broadening is higher which results in higher residual absorption. It is also evident from Fig 2.14a and 2.14b that for

Wafer A at 1550 nm, the Δn and $\Delta\phi$ curves are linear with voltage up to -4 V and become non-linear as the quantum confinement is lost. On the other hand, the Δn and $\Delta\phi$ response for Wafer B are relatively more linear up to -7 V. Also, it is important to note that there is a difference of more than 20 nm between the PL peaks of Wafer A (1337 nm) and Wafer B (1310 nm). For a better comparison, both Δn and $\Delta\phi$ are also measured at a longer wavelength of 1580 nm, where the residual absorption in Wafer A will be minimal. A $V_\pi L$ of 7.2 V·mm was measured which is less than for Wafer B. Further material optimization of Wafer B i.e. by increasing the number of quantum wells and increasing the electro-optical mode overlap would make it a good candidate material to achieve low V_π ($3 V_\pi \cdot \text{mm}$) for an optical modulator with low optical insertion loss.

2.6 Summary

This Chapter highlights the most important electro-optic effects in III-V semiconductors utilized to achieve the maximum refractive index change (Δn) with minimum absorption at the wavelength of operation in InP based MZMs. For p-i-n arrangement, the effect of direction of phase shifter waveguide in MZM with respect to crystal axis of the (100) plane InP wafer is concluded in Table 2.1. In order to maximize the over-all Δn due to TE polarized input light, the phase shifters should be fabricated parallel to the major flat of InP wafer. In this orientation the sign of the Δn due to LEO is positive and adds up to the refractive index change due to QCSE. For TM polarization, there will be no refractive index change due to LEO and only QCSE will play its role in the modulation of refractive index.

Table 2.1: P-i-n waveguide orientation dependence on refractive index change.

MZM Orientation (TE polarization only)	LEO	QCSE
[011]	$-\Delta n$	$+\Delta n$
$[0\bar{1}1]$	$+\Delta n$	$+\Delta n$

It is important to highlight that, that the sign of Δn due to LEO will be reversed if the waveguide arrangement is n-i-p, where n is top contact layer,

which means the waveguide orientation should be selected accordingly. This sign reversal is due to the change in the direction of reverse bias induced external electric field. This fact will be demonstrated experimentally in chapter 6 of this thesis.

Also, in order to develop a better understanding of quantum-confined Stark effect (QCSE), the experimental analysis of QCSE induced Δn and $\Delta\phi$ has been performed on InAlGaAs MQW structures on an InP substrate with mirrored asymmetrically ramped bandgaps. Room temperature photoabsorption spectroscopy shows that there are significant excitonic absorption changes when the electric field is applied perpendicular to the multiple quantum well layers due to the QCSE. For both the structures, the quantum confinement is lost in the presence of high electric field. In the wafer with the ramp down profile in the wells along the growth direction, the excitonic resonance is still retained at -7 V reverse bias as compared to the wafer with a ramp up where the excitonic peak is quenched at -5 V. This leads to a lower switching voltage associated with the higher absorption change which induces non-linear phase change at high reverse bias. The phase change in the ramp down structure is relatively linear with voltage and shows low absorption. The switching voltage can further be reduced by increasing the number of wells and optimizing both the phase electrode length and total thickness of the intrinsic region keeping the capacitance requirement for high-speed (demonstrated in Chapter 5 with rectangular wells). The strong electro-optic properties of asymmetric quantum wells show their suitability for high speed and low switching voltage InP based electrorefractive modulators. The best comparison of their enhanced performance as compared to typical rectangular shaped QW structures should be done by sequentially growing alternate epitaxial layer structures with equal number of both well types i.e. rectangular and asymmetrically ramped wells [32]. However, in this work only the EO performance of asymmetrically ramped wells is compared with respect to each other only. Also, for final MZM devices only rectangular MQWs have been used to achieve the modulation at 1550 nm and 2000 nm wavelengths.

References

- [1] L. Zehnder, “Ein neuer interferenzrefraktor,” *Zeitschrift fur Instrumentenkunde*, 1891.
- [2] L. Mach, “Über einen interferenzrefraktor,” *Zeitschrift fur Instrumentenkunde*, 1892.
- [3] H. Taakeuchi, K. Kasaya, and K. Oe, “Low-switching-voltage InGaAsP/InP waveguide interferometric modulator for integrated optics,” *Photonics Technology Letters, IEEE*, vol. 1, no. 8, pp. 227–229, Aug 1989.
- [4] Q. Wang, J. Lu, and S. He, “Optimal design method of a low-loss broadband Y branch with a multimode waveguide section,” *Appl. Opt.*, vol. 41, no. 36, pp. 7644–7649, Dec 2002.
- [5] Y. Ma, S. Park, L. Wang, and S. T. Ho, “Ultracompact multimode interference 3-dB coupler with strong lateral confinement by deep dry etching,” *Photonics Technology Letters, IEEE*, vol. 12, no. 5, pp. 492–494, May 2000.
- [6] L. Spiekman, Y. Oei, E. Metaal, F. Green, I. Moerman, and M. Smit, “Extremely small multimode interference couplers and ultrashort bends on InP by deep etching,” *Photonics Technology Letters, IEEE*, vol. 6, no. 8, pp. 1008–1010, Aug 1994.
- [7] P. Winzer and R. Essiambre, “Advanced optical modulation formats,” *Proceedings of the IEEE*, vol. 94, no. 5, pp. 952–985, May 2006.
- [8] A. Chen and E. Murphy, *Broadband Optical Modulators Science, Technology, and Applications*. CRC Press, 2011.
- [9] S. William, *RF Photonic Technology in Optical Fiber Links*. Cambridge University Press, 2002.

- [10] M. U. Sadiq, M. R. Gleeson, N. Ye, J. O'Callaghan, P. Morrissey, H. Y. Zhang, K. Thomas, A. Gocalinska, E. Pelucchi, F. C. G. Gunning, B. Roycroft, F. H. Peters, and B. Corbett, "10 Gb/s InP-based Mach-Zehnder modulator for operation at 2 μ m wavelengths," *Opt. Express*, vol. 23, no. 9, pp. 10 905–10 913, May 2015.
- [11] P. Bhattacharya, *Properties of III-V Quantum Wells and Superlattices*. The Institution of Engineering and Technology, 2011.
- [12] D. L. Lile, "The history and future of InP based electronics and optoelectronics," in *Indium Phosphide and Related Materials, 1998 International Conference on*, May 1998, pp. 6–9.
- [13] R. Walker, N. Cameron, Y. Zhou, and S. Clements, "Optimized Gallium Arsenide Modulators for Advanced Modulation Formats," *Selected Topics in Quantum Electronics, IEEE Journal of*, vol. 19, no. 6, pp. 138–149, Nov 2013.
- [14] P. Schindler, D. Korn, C. Stamatiadis, M. O'Keefe, L. Stampoulidis, R. Schmogrow, P. Zakyntinos, R. Palmer, N. Cameron, Y. Zhou, R. Walker, E. Kehayas, S. Ben-Ezra, I. Tomkos, L. Zimmermann, K. Petermann, W. Freude, C. Koos, and J. Leuthold, "Monolithic GaAs Electro-Optic IQ Modulator Demonstrated at 150 Gbit/s with 64QAM," *Journal of Light-wave Technology*, vol. 32, no. 4, pp. 760–765, Feb 2014.
- [15] N. Andriolli, F. Fresi, F. Bontempi, A. Malacarne, G. Meloni, J. Klamkin, L. Poti, and G. Contestabile, "Inp monolithically integrated coherent transmitter," *Opt. Express*, vol. 23, no. 8, pp. 10 741–10 746, Apr 2015.
- [16] S. Chang, *Fundamentals of Guided-Wave Optoelectronic Devices*. Cambridge University press, 2010.
- [17] G. T. Reed, G. Mashanovich, F. Y. Gardes, and D. J. Thomson, "Silicon optical modulators," *Nature Photonics*, vol. 4, no. 8, pp. 518–526, Jul 2010.
- [18] K. Ishida, H. Nakamura, H. Matsumura, T. Kadoi, and H. Inoue, "InGaAsP/InP optical switches using carrier induced refractive index change," *Applied Physics Letters*, vol. 50, no. 3, pp. 141–142, 1987.
- [19] B. Bennett, R. A. Soref, and J. del Alamo, "Carrier-induced change in refractive index of InP, GaAs and InGaAsP," *Quantum Electronics, IEEE Journal of*, vol. 26, no. 1, pp. 113–122, Jan 1990.

- [20] N. Dagli, *High Speed Photonic Devices*. Taylor and Francis Group, LLC, 2007.
- [21] W. Franz, "Einfluß eines elektrischen Feldes auf eine optische Absorptionsskante," *Zeitschrift für Naturforschung*, vol. 13, no. 6, pp. 484–489, 1958.
- [22] L. Keldysh, "The effect of a strong electric field on the optical properties of insulating crystals," *J. Exptl. Theoret. Phys. (U.S.S.R.)*, vol. 34, no. 5, pp. 1138–1141, 1958.
- [23] I. Merkulov and V. Perel, "Effects of electron-hole interaction on electroabsorption in semiconductors," *Physics Letters A*, vol. 45, no. 2, pp. 83 – 84, 1973.
- [24] J. D. Dow and D. Redfield, "Electroabsorption in Semiconductors: The Excitonic Absorption edge," *Phys. Rev. B*, vol. 1, pp. 3358–3371, Apr 1970.
- [25] S. Chuang, *Physics of Optoelectronic Devices*. Wiley-Interscience publication, 1995.
- [26] D. A. B. Miller, D. S. Chemla, T. C. Damen, A. C. Gossard, W. Wiegmann, T. H. Wood, and C. A. Burrus, "Band-Edge Electroabsorption in Quantum Well structures: The Quantum-Confined Stark Effect," *Phys. Rev. Lett.*, vol. 53, pp. 2173–2176, Nov 1984.
- [27] G. Bastard, E. E. Mendez, L. L. Chang, and L. Esaki, "Variational calculations on a quantum well in an electric field," *Phys. Rev. B*, vol. 28, pp. 3241–3245, Sep 1983.
- [28] R. A. Griffin, S. K. Jones, N. Whitbread, S. C. Heck, and L. N. Langley, "InP Mach-Zehnder Modulator Platform for 10/40/100/200-Gb/s operation," *IEEE Journal of Selected Topics in Quantum Electronics*, vol. 19, no. 6, pp. 158–166, Nov 2013.
- [29] T. Arakawa, T. Hariki, Y. Amma, M. Fukuoka, M. Ushigome, and K. Tada, "Low-voltage Mach-Zehnder Modulator with InGaAs/InAlAs Five-Layer Asymmetric Coupled Quantum Well," *Japanese Journal of Applied Physics*, vol. 51, no. 4R, p. 042203, 2012.
- [30] E. T. Kunkee, C. C. Shih, Q. Chen, C. J. Wang, and L. J. Lembo, "Electrorefractive Coupled Quantum Well Modulators: Model and Experimental Results," *IEEE Journal of Quantum Electronics*, vol. 43, no. 8, pp. 641–650, Aug 2007.

- [31] D.-S. Shin, P. K. L. Yu, and S. A. Pappert, “High-power electroabsorption modulator using intra-step-barrier quantum wells,” *Journal of Applied Physics*, vol. 89, no. 2, pp. 1515–1517, 2001.
- [32] H. Mohseni, H. An, Z. A. Shellenbarger, M. H. Kwakernaak, and J. H. Abeles, “Enhanced electro-optic effect in GaInAsP-InP three-step quantum wells,” *Applied Physics Letters*, vol. 84, no. 11, pp. 1823–1825, 2004.
- [33] K.-K. Law, R. H. Yan, A. C. Gossard, and J. L. Merz, “Electric-field-induced absorption changes in triangular quantum wells grown by pulsed-beam molecular-beam-epitaxy technique,” *Journal of Applied Physics*, vol. 67, no. 10, pp. 6461–6465, 1990.
- [34] I. Bar-Joseph, C. Klingshirn, D. A. B. Miller, D. S. Chemla, U. Koren, and B. I. Miller, “Quantum-confined stark effect in InGaAs/InP quantum wells grown by organometallic vapor phase epitaxy,” *Applied Physics Letters*, vol. 50, no. 15, pp. 1010–1012, 1987.
- [35] E. F. Schubert, E. O. Göbel, Y. Horikoshi, K. Ploog, and H. J. Queisser, “Alloy broadening in photoluminescence spectra of $\text{Al}_x\text{Ga}_{1-x}\text{As}$,” *Phys. Rev. B*, vol. 30, pp. 813–820, Jul 1984.

Chapter 3

Traveling wave electrode design

The three basic elements which should be considered for the design of a electro-optic modulators are: the type of electro-optic (EO) effect used, the material design based on EO effect and then the device layout i.e. optical waveguide design and high-frequency electrode design. This chapter focuses on the basic concepts related to the high frequency design of the electro-optic modulators. Theoretical model and design considerations for the high-speed modulators including the effects of different material parameters and device geometry are discussed in detail. The different types of transmission line structures generally used in the design of high-speed devices are presented in Section 3.1. Based on the appropriate choice of the transmission line, different electrode configurations and their limitations are introduced in Sections 3.2 and 3.3. High-frequency electrode design rules and derivation of modulator frequency response is shown in Sections 3.4 and 3.5, where the effect of each design parameter on the modulator electro-optic bandwidth is described with the help of special test cases. Finally, an equivalent circuit model of the electrode structure is devised in Section 3.6, by comparing it to a general transmission line model. The equivalent circuit model is then used to optimize the modulator bandwidth performance by adjusting the variables related to optical waveguide geometry, semiconductor material properties and electrode configuration. The main goal of optimization is to reduce microwave propagation losses, enhance electrode characteristic impedance and match electrical and optical propagation velocities.

3.1 Planar transmission structures

The first step in the high-speed electrode design is to choose the most suitable transmission line structure to deliver the high frequency microwave signal to the optical device. Due to the small size of the high-speed optical modulators, appropriate choice and design of the microwave transmission feed lines and contact pads are necessary to achieve the desired performance. One of the main requirements of the traveling wave electrode structure is that the transmission structure should be planar in configuration to allow easy device access through RF probes and should be compatible with the standard packaging technology i.e. wire bonding and flip-chip bonding technology. Fig 3.1 shows the most commonly used different types of planar transmission lines in microwave circuits.

3.1.1 Microstrip line

The most popular type of planar transmission line is the microstrip line which is widely used in both active and passive monolithic integrated microwave circuits (MMICs). It originated from the stripline which like a coaxial transmission line supports a true transverse electromagnetic (TEM) mode i.e. electric and magnetic fields have no component in the direction of propagation. The stripline consists of a central conductor covered in a dielectric slab with top and bottom ground planes. Due to the inaccessibility of the circuit plane for mounting transistors, lumped capacitors and resistors, the stripline was replaced by the microstrip line. The microstrip line comprises of a central conductor line printed on a grounded dielectric medium of a certain permittivity (ϵ_r) Fig 3.1b. In contrast to the stripline (Fig 3.1a), where the field is contained in a homogeneous dielectric medium, the microstrip line has its field lines distributed in two media i.e. in air above the substrate and in dielectric medium between upper conductor and ground plane. The presence of field in inhomogeneous dielectric medium restricts microstrip line to support a pure TEM mode as the phase matching condition at the air-dielectric interface for the electric and magnetic field can not be satisfied [1,2]. Thus only at very low frequencies up to ~ 30 kHz microstrip line shows pure TEM characteristic but as the frequency increases the currents on the conductor develops transverse components. These transverse components are due to the presence longitudinal components of the field which leads to the concept of the quasi-TEM mode. In the case of InP based modulator, the microstrip structure must be fabricated on highly doped n^+ -InP substrate

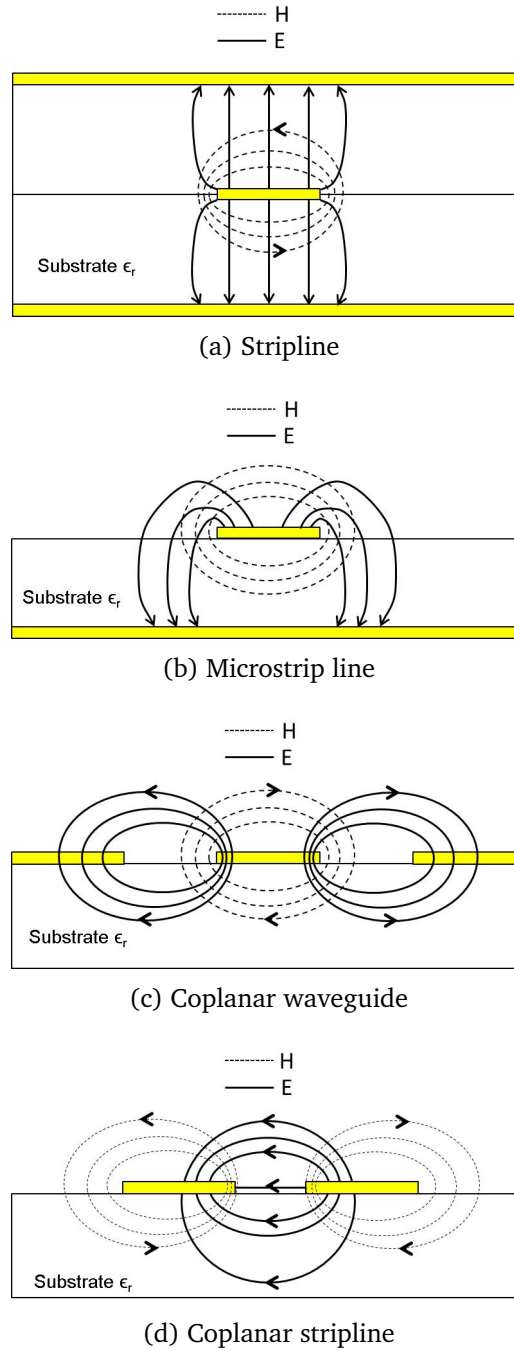


Figure 3.1: Commonly used transmission lines

which can cause many practical problems to realize high bandwidth optical modulator. Foremost is the microwave loss arising from the current flow in the conductive substrate loss due to skin effect. Also, above the microwave frequency range, the thickness of dielectric substrate must be reduced in order to ensure the propagation of only quasi-TEM mode without coupling to any higher order modes. Substrate thinning process not only adds an additional fabrication

step, it also requires very precise control as the characteristic impedance of the microstrip structure is directly dependent on the substrate thickness. Another potential disadvantage of designing high speed modulator on the n^+ -InP substrate is realizing low loss and low capacitance passive interconnects and probe contact pads to access the phase shifting region of the device. Although, this issue can be solved using the metal-insulator-semiconductor (MIS) arrangement as discussed in [3], [4] and the microwave loss can be reduced to ~ 0.5 dB/mm but it requires an extra development step which complicates overall design and fabrication process.

3.1.2 Coplanar transmission lines

From the above discussion, it is clear that the microstrip is not the most suitable structure for the design of a high-speed optical modulator. Most of the practical issues related to the modulator design based on microstrip transmission lines can be addressed using coplanar transmission line (CTL) structures [2] such as coplanar waveguide (CPW) and coplanar strip (CPS) as shown in Fig 3.1. The term ‘coplanar’ means that both the ground and signal conductors lie on the same plane. Easy access of the signal and ground planes in CTLs and high integration capability has resulted in widespread use of both CPW and CPS transmission lines in many high-speed photonic devices specially modulators [3–7]. The CPW was first introduced by C.P.Wen in 1969 in [8], where he also devised the first analytic formulas for calculating the quasi-static wave parameters using the conformal mapping technique. The CPW consist of two ground planes surrounding and running parallel to the central signal conductor and allows low wave-propagation dispersion as compared to the microstrip lines for very high frequency operations. One of the distinct advantage of using CPW lines is that both the signal and ground planes are deposited on the top of the dielectric substrate which can be semi-insulating (SI) instead of highly conductive substrate as in microstrip based structures. The use of SI substrate reduces the extra microwave loss due to substrate conductivity and allows the fabrication of large low capacitance contact pads, making the devices suitable for on-chip testing through standard microwave probes and opto-electronic packaging. Utilizing the CPW as TWE structures in MZM design also simplifies the fabrication process by eliminating the need of substrate thinning, backside metallization and extra through-substrate plated via holes to contact the ground plane. The inclusion of via holes can severely affect the modulator bandwidth performance due to extra inductance and loss induced by via connections. The characteristic

impedance of the CPW structure is almost independent of the substrate thickness and is mainly controlled by the signal pad width and the spacing of the ground planes to the central conductor. Any required characteristic impedance can be reached using different combinations of the signal conductor width and ground electrode gap spacing as shown in 3.2. Also, as the ground planes provide shielding between the adjacent devices, the use of CPW transmission lines will allow multiple modulator devices to be placed closely together. Such arrangement will help to realize densely packed large-scale InP-based photonic integrated circuits (PICs) by integrating large number of discrete components on a single transmitter chip [4], [9], [10].

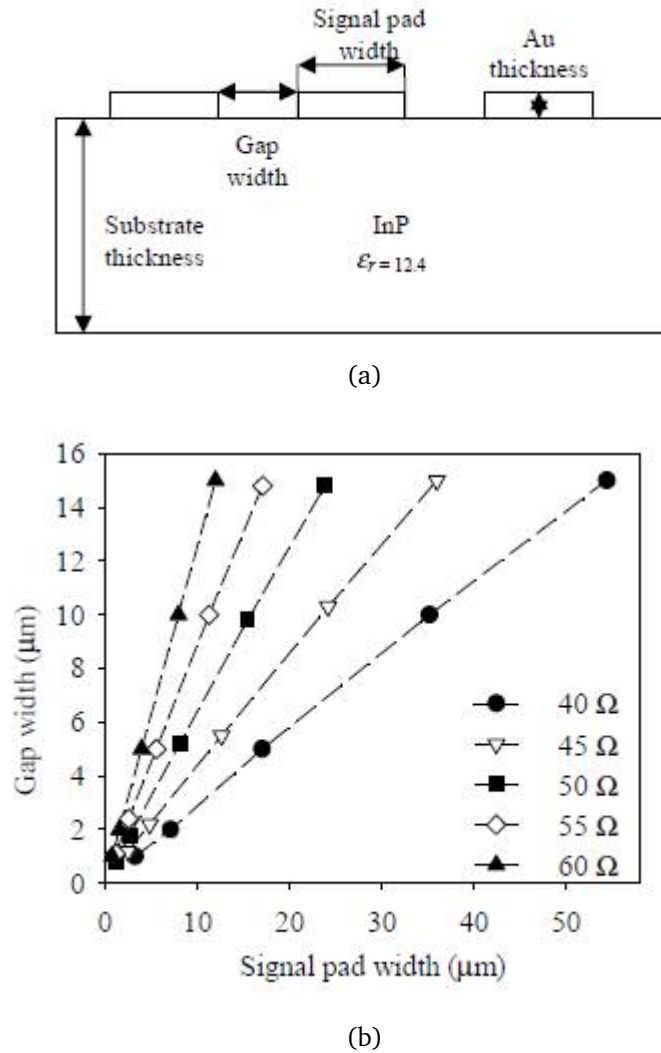


Figure 3.2: (a) Schematic of a CPW transmission. (b) Plot of signal pad width vs. gap width for different impedance values at 25 GHz on 100 μm InP substrate [27].

In addition to the CPW, another promising approach to design traveling wave MZM is using CPS transmission lines. The basic structure is shown in Fig 3.1(d). The CPS and the conventional CPW with infinite ground planes have the complimentary metal structures, which means that where CPW has metal, CPS has a slot and vice versa. The complementary structure further classifies them as balanced and unbalanced structures as CPS is balanced electrically with respect to ground whereas CPW is unbalanced. This feature gives CPW structure better compatibility with the external high-speed coaxial connectors such as K (2.92 mm) or V (1.85 mm) connectors, which are also unbalanced transmission lines. Such high speed connectors can either be directly attached on to the device or to another external RF interposer which can be then wire bonded to the modulator chip. In any case, no special transition structure design is needed as transition will be between two symmetric structures. On the other hand, transition from symmetric coaxial connector to asymmetric CPS TWE based MZM will incur extra microwave loss specially at frequencies greater than 25 GHz. This extra loss can be avoided by designing special wide-band transition structure from CPW i.e. ground-signal-ground (G-S-G) to CPS ground-signal (GS) transition to make the modulator devices more suitable for the standard electro-optic packaging [11]. Despite of the requirement of transition structure at the RF input/output interface, the CPS transmission line has been widely used in high bandwidth optical modulators as the capacitively loaded TWE [5], [7], [12]. Capacitively loaded traveling-wave electrodes (CL-TWE) have a segmented structure which employs a separate CPS transmission line which is placed parallel to the optical waveguide as shown in Fig 3.3. The characteristic impedance of the line is higher than 50Ω . The capacitance in the optical waveguide which is a p-i-n structure is segmented and periodically connected to the microwave transmission line. Through proper design, the length of these small periodic structures and spacing between them, allows better control of the microwave velocity and characteristic impedance as compared to CPW TWE structure.

3.2 Electrode selection

The static operation of the modulator has been discussed in Chapter 2. InP MZMs based on LEO effect and QCSE always operate in reverse bias mode and as a result very low or negligible current flows through the p-i-n junction. The EO bandwidth of such reverse biased devices is mainly limited by the intrinsic capacitance of the optical waveguide depending on the electrode design. Elec-

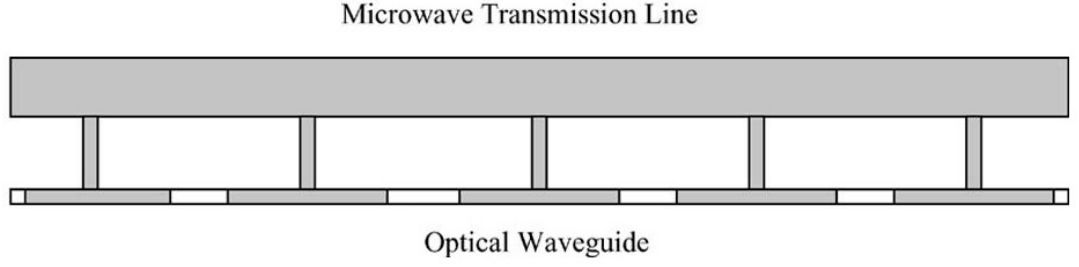


Figure 3.3: Schematic of the capacitively traveling-wave electrode design. This can be seen as EAM or one arm of the MZM [12].

tric field is applied across the intrinsic region, which results in refractive index change leading to the optical phase change causing intensity modulation at the output of MZI. The electric field is formed by the modulating electrical signal applied at a specific bias point through the metal electrode which is deposited on the top of the optical waveguide. The modulator bandwidth directly depends on the electrical properties of the metal electrode. There are two types of electrode design generally used: lumped and traveling wave electrodes. Both the approaches are discussed briefly in the next section.

3.2.1 Lumped electrode

For InP MZMs based on lumped electrode design, the electrodes are driven as capacitors. A number of InP based MZMs have been reported with lumped electrodes [9], [13]. A p-type ohmic metal contact is deposited on the top of one arm of the MZI. To deliver the signal to the electrode a square metal block is deposited next to the optical waveguide, which is electrically connected to the middle point of the lumped electrode as shown in Fig 3.4. These bond pads are included in design because the metal on the optical waveguide cannot be contacted directly as it is usually $2\ \mu\text{m}$ to $3\ \mu\text{m}$ in width, which is too narrow to be accessed through wire bonds and probes. The bandwidth of the modulator will be limited by electrical transit time determined by the the capacitance of the bond pad and intrinsic capacitance of the electrode section.

The equivalent circuit of the MZM with lumped electrode configuration is represented in Fig 3.5 , where C_p is pad capacitance, C_i is the junction capacitance of the optical waveguide, R_s is the series resistance due to doped layers and Z_s is the source impedance. If $C_p \ll C_s$, then the 3-dB bandwidth can be

expressed as Eq 3.1,

$$f_{3dB} = \frac{1}{2\pi RC_i} \quad (3.1)$$

where R is the sum of R_s and Z_s . It also explains the trade off between the bandwidth and V_π i.e. if the the electrode length is increased to decrease V_π , 3-dB bandwidth will be reduced due to increase in capacitance and vice versa.

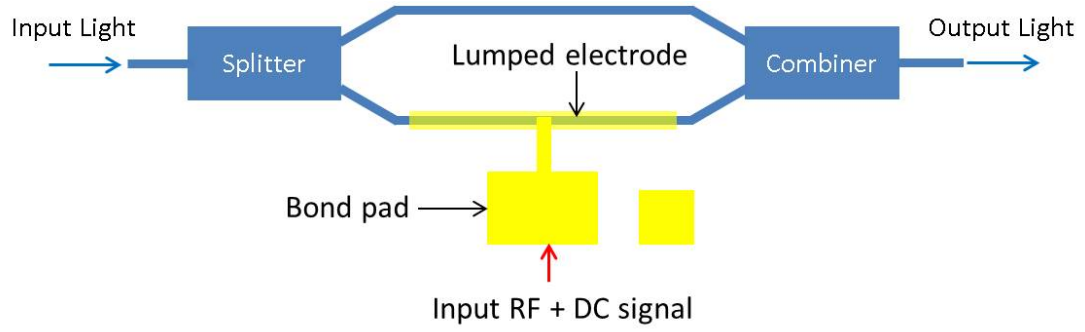


Figure 3.4: Single arm driven lumped electrode MZM design

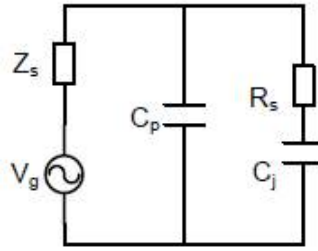


Figure 3.5: Equivalent circuit model of MZM with lumped electrode

3.2.2 Traveling wave electrode

A traveling wave structure is formed when optical and electric fields interact over the propagation distance while they travel down their respective waveguides. The fundamental idea of TWE is that the bandwidth of modulator is not restricted by the RC time constant as the capacitance is distributed along the length of phase shifting electrode. The capacitance of the transmission line, dominated by the active junction capacitance is compensated by the inductance of electrode. Since the bandwidth is not capacitance limited, the electrode length can be kept long, typically thousands of wavelengths. The longer electrode length will relax the large driving voltage requirement significantly. However, the electrode length must be adjusted very carefully in design process

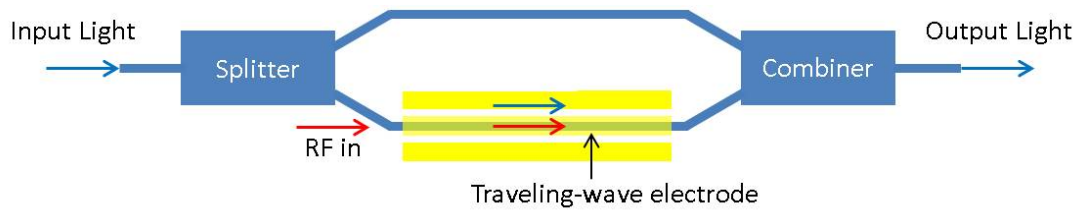


Figure 3.6: Single arm driven traveling wave electrode MZM design.

keeping in view the microwave and optical losses, which are the main bandwidth limiting factors in traveling wave case. EO modulators based on traveling wave design have been successfully demonstrated in different material systems such as LiNbO_3 [14], Si [15], GaAs [16], InP [5–7] and polymers [17]. In addition to TWE application in EO modulators, this approach is very desirable in many other high speed photonic devices.

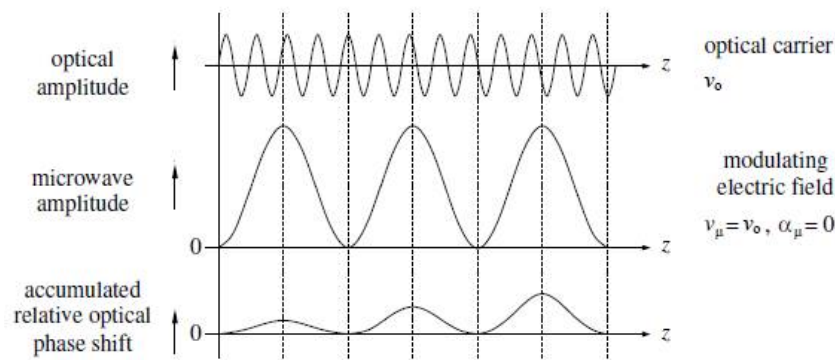


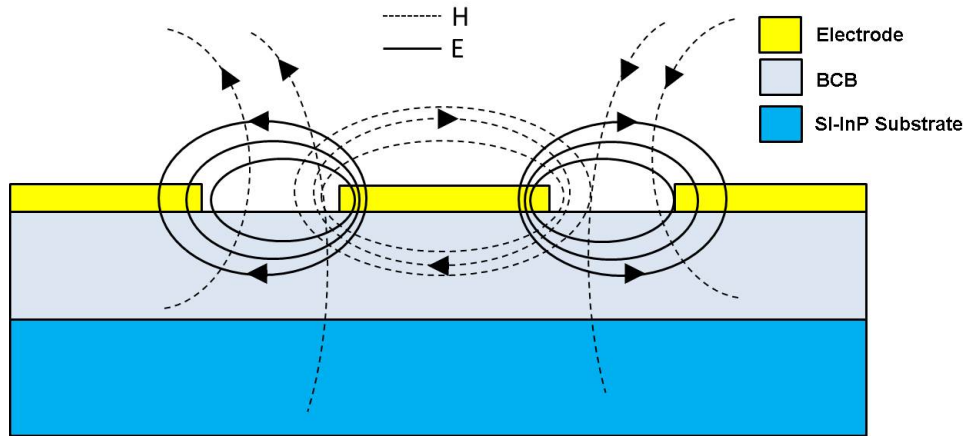
Figure 3.7: Co-propagation of electrical and optical waves in lossless velocity matched scenario.

Figure 3.6 shows the schematic of a MZM device based on traveling wave approach. As compared to lumped electrode scenario, high frequency electrical signal is applied at one end of the optical waveguide rather than in the middle. Ideally, both the electrical and optical waves should travel at the same velocity with very low microwave and optical losses for coherent phase accumulation. Fig 3.7 illustrates the lossless case of co-propagation of electrical and optical waves without any velocity difference. The accumulated optical phase shift experienced by the optical field retains the sinusoidal shape of the modulating microwave field along the direction of propagation. However, in practice, with increasing frequency, the optical signal sees the drop of electrical signal along the length of electrode due to velocity mismatch and absorption losses of the microwave signal along the waveguide length. Total accumulated phase is calculated by the integral of interacting modulating fields.

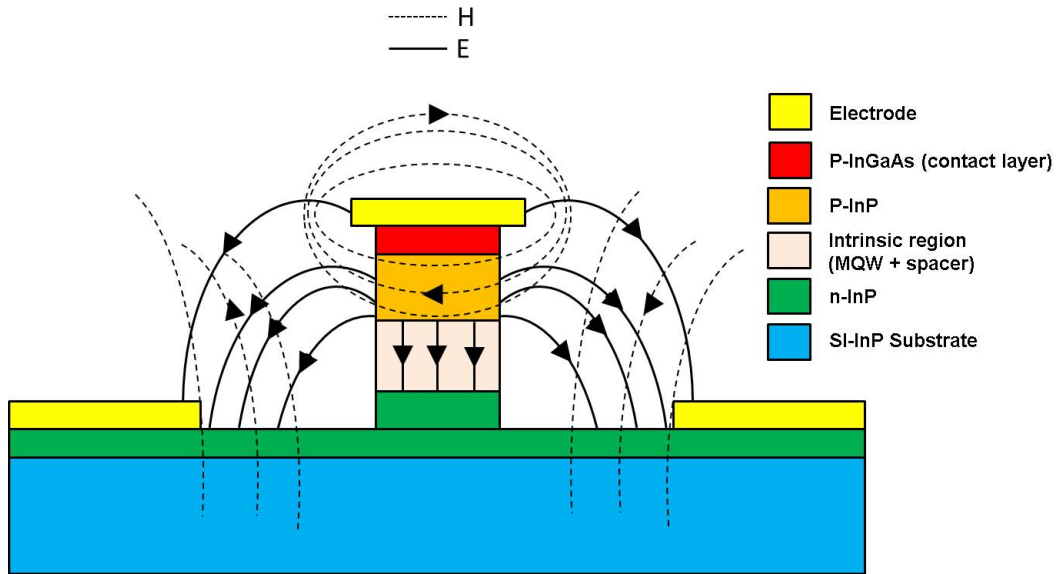
3.3 Hybrid co-planar TWE

The schematic of hybrid co-planar TWE MZM is depicted in Fig 3.8. The term ‘hybrid-coplanar’ arises from the fact that the propagating mode of such arrangement has properties of both microstrip and CPW modes. The RF signal is fed to the phase shifting section of the modulator by a Ground-Signal-Ground (GSG) pad which is optimized for $50\ \Omega$ impedance with CPW mode as its major mode of propagation. The GSG pad is then tapered down to meet the dimensions of the optical ridge and then turned along the optical wave guide to allow co-propagation of the RF and optical signals. The output RF signal is collected using another set of GSG pads. For electro-optic (EO) bandwidth measurement of modulator, the output GSG pad must be terminated to avoid electrical reflections at the output. On the contrary, if the electrical signal is not terminated with proper impedance value then a standing wave pattern will be formed on the electrode, reducing the optical modulation efficiency. The effect of the termination impedance mismatch will be discussed in detail in later sections.

Figure 3.8a shows the cross section of the GSG pads with the corresponding field distribution. To ensure minimum microwave absorption loss in the feed in paths, both the output and input GSG pads are placed on planarized Benzocyclobutene (BCB) deposited on the top of semi-insulating (SI) InP substrate. The pitch of the GSG pads should be selected to match the pitch of testing microwave probes and the pad dimensions should also be compatible with the packaging technology. The structure in Fig 3.8b shows the cross section of the phase shifting arm and it contains the signal electrode on top of the optical ridge waveguide and a ground electrode on both sides. The coplanar waveguide (CPW) mode fed in to the GSG pad is transferred into a microstrip mode as soon as the phase shifting region starts. Thus, the currents are primarily carried in the metal and nearly all the voltage drop is across the undoped region of the optical waveguide. Mode transformation from CPW to microstrip is due to the presence of a highly doped n-type InP plane under the optical waveguide which acts as a ground plane. It is reasonable to consider hybrid-coplanar geometry as quasi-TEM waveguide as both the CPW and microstrip are quasi-TEM waveguides. Fig 3.8b also shows the field distribution in the phase shifting region of MZM. The electric field distribution is like microstrip mode, where the profile of p-i-n structure forces the electric field to travel in ridge rather than in air with higher propagation speed. The n-doped layer acts as the ground plane preventing the further penetration of field into substrate. The magnetic field distribution on the other hand is nearly same as CPW on any



(a) Cross section of GSG bondpad section.



(b) Cross section of phase shifting electrode.

Figure 3.8: Electric and magnetic field distribution in hybrid coplanar TWE.

SI substrate and the field lines are free to penetrate in the n-InP and substrate. The quasi-static penetration of magnetic field is far less than the skin depth of SI-InP substrate, which is in mm-range. Also as n-InP is a nonmagnetic material so the skin depth becomes unimportant and magnetic field doesn't see n-layer at all. The physical separation of electric and magnetic fields will result in a slow-wave mode propagation, which is usually supported by Metal-Insulator-Semiconductor (MIS) structures [18]. The slow-wave mode means that the propagation speed of electromagnetic mode will be less than in a CPW line de-

posited on the pure SI-InP substrate. The decrease in propagation speed is due to raise in the imaginary part of refractive index of the doped semiconductor layers.

3.4 Electrode design considerations

Design requirements of the hybrid-coplanar TWE EO modulators are well established in literature and can be found in [5, 16, 19]. The main requirements are summarized as follows:

3.4.1 Velocity matching

As discussed in previous Section 3.2, the aim of traveling wave design of the electrode is to achieve the modulating electrical wave which travels at the same speed as the optical wave. Any velocity mismatch between two wave will result in phase walkoff causing reduction of induced phase modulation by antiphase modulation. The phase walkoff further increases with either interaction length and frequency. For a lossless RF electrode, the relationship between electrical bandwidth (f_{3dB}) and velocity mismatch factor is expressed as

$$f_{3dB} = \frac{1.4c}{\pi|n_o - n_\mu|l} \quad (3.2)$$

where c is the speed of light in vacuum, n_o and n_μ are the optical and microwave refractive indices respectively, l is the phase shifting electrode length. From Eq 3.2, it is clear that decreasing the velocity mismatch increases the 3-dB electrical bandwidth. Hence, both the optical and electrical waves propagation speed should be as close as possible to improve the 3-dB EO bandwidth. Once the microwave and optical refractive indices are known, the respective velocities can be easily calculated. But one of the unclear issue here is that which velocities should be matched as the velocities which are needed to be matched present a choice and it can either phase velocity or group velocity. This issue has been explained in detail by R. Spickermann *et al* in [20]. It is well known in theory that the the rate at which phase of the wave propagates i.e. the velocity at which the phase of any one frequency component of the wave travels is the phase velocity. The group velocity is defined as the rate at which the shape of the waveform i.e. the envelope or modulation of the waveform propagates. In an optical wave guide, as soon as optical signal starts interacting with the microwave modulating signal, it is no longer a single frequency and it is phase

modulated. The center of gravity of this phase modulated waveform travels with the group velocity. It means that the optical group velocity should be same as the electrical waveform group velocity so that interaction between them is coherent leading to monotonic phase accumulation along the phase electrode.

3.4.2 Microwave and optical losses

The second most important design parameter is controlling the microwave and optical losses in the phase shifter. The origin of microwave losses can be attributed to three processes: metallic conductor loss, doped semiconductor loss and radiation losses. The radiation losses are usually very low as compared to the other two and can be ignored. The conductor losses are mainly due to the skin effect and can be minimized by depositing thick and broad low resistance electrodes on the top of the optical waveguide as shown in Fig 3.8b. With the increasing frequency, the skin depth of the conductor (δ_c) decreases and introduces the metal loss by pushing the electromagnetic wave towards the surface of the conductor. Mathematically (δ_c) can be written as Eq 3.3

$$\delta_c = \frac{1}{\sqrt{\pi f \mu_r \mu_o \sigma}} \quad (3.3)$$

Where μ_r is the permeability of the material and σ is the conductivity of metal. The skin depth of gold (Au) is 385 nm at 40 GHz, so to avoid the microwave attenuation due to δ_c the electrode thickness should be atleast three times the skin depth i.e. $1.5 \mu m$ in this particular case [14].

The microwave and optical losses from semiconductor are interdependent and can not be treated individually. In an optical ridge, light is vertically confined in the intrinsic region which consists of MQWs and undoped InP spacer layers. Lateral confinement is provided by the deep etched optical waveguide ridge. The highest EO interaction will be achieved if electric field is highest in the intrinsic region. Spacer layers have been added above and below the MQWs to keep the optical mode away from the p and n doped region. Any overlap of the optical mode with doped layers can increase optical absorption. Optical absorption from a p-doped semiconductor layer is almost 10 times as high as a comparably doped n-doped semiconductor layer. To minimize the absorption losses due to doping, the doping profile of the p-doped layer above the InP spacer is increased gradually from 10^{17} cm^{-3} to 10^{19} cm^{-3} . However, low p-doping can increase the RF microwave loss so a compromise has to be made. To achieve low contact resistance between the signal electrode and p-doped

InP layer, a 20-100 nm highly doped (10^{19} cm^{-3}) Indium Gallium Arsenide (InGaAs) layer should be added. The individual effect of the resistance of each cladding layer and contact resistance on the electrical bandwidth must be accounted for in the design of optimum TWE structure.

3.4.3 Characteristic impedance

The characteristic impedance (Z_o) of traveling wave MZM is another critical design parameter which requires very careful optimization. It is determined by the capacitance of the intrinsic region, which also defines the phase efficiency of MZM. In practice, the feed in RF lines and phase shifting electrodes should have Z_o of 50Ω to avoid large electrical signal reflections both at the input and output. If the driver is not well matched to the input feed line of the modulator, the incoming signal will be reflected without any contribution to the modulation. The mismatch at the input will not only increase the overall power consumption but may also distort the input driver signal itself. In addition to the GSG pad section, the phase shifting electrode section must be optimized to match the source and load impedance. However, usually in InP based MZMs have impedance in the range of 20Ω - 30Ω due to large capacitance per unit length arising from their high phase efficiency of p-i-n waveguide structure [5, 6, 21].

Two widely applied RF electrode design approaches for InP-Based MZMs are demonstrated in [3, 5]. The first approach, uses the conventional coplanar hybrid TWEs on each interferometric arm of MZI. The second approach is to use the p-i-n epitaxy in series push pull mode by capacitively loading the coplanar stripline electrode as shown in Fig 3.3. However in this work, we picked the conventional electrode approach to design InP based MZM devices. Also, from above discussion, it is clear that the main requirements of for the successful design of MZMs are coupled i.e. large bandwidth, low V_π and low optical insertion loss, so usually compromises are necessary in design process and both the microwave and optical design issues should be considered in design phase.

3.5 TWE frequency response

The frequency response of any high-speed EO modulator is one of the most important quality metric of its performance and it is quantified by its electro-optic bandwidth. In [19], the electro-optic bandwidth of a traveling wave MZM is

defined as the electrical -3 dB frequency for which optical intensity modulation has fallen to 70.7 % of the reference level, resulting in a 3 dB reduction in received signal, simulating a 3 dB reduction in RF drive power. This is most commonly used definition of electro-optical bandwidth in literature. In order to determine the electro-optic bandwidth of an EO modulator analytically, the first factor to be determined is the accumulated phase shift experienced by a photon entering and exiting the optical waveguide. This phase shift is proportional to the modulating voltage applied across the intrinsic region of the optical waveguide structure with constant of proportionality containing parameters such as optical ridge dimensions, wavelength of operation, index of refraction of microwave and optical, the electro-optical overlap and the electro-optical coefficient. Due to the traveling wave nature of the applied input voltage, the total amount of phase shift attained by a photon is cumulative of all the phase shifts induced by the instantaneous voltage as seen by the photon at the particular position along the optical waveguide [22].

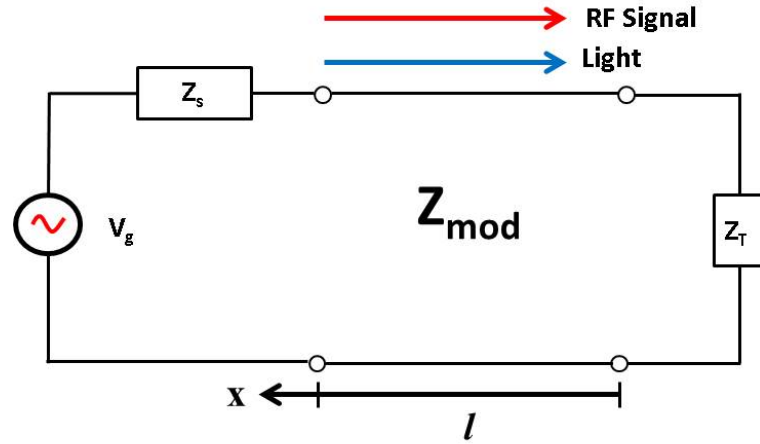


Figure 3.9: Equivalent circuit of traveling wave modulator as single electrical transmission line with load and source impedance

The equivalent circuit of the traveling wave modulator is shown in Fig 3.9, where the whole TWE is considered electrically as the transmission line model. The modulating voltage at any point x along the transmission line of length l is given as [22, 23]

$$V(x, \omega_m) = \frac{V_g}{2} \cdot (1 + \rho_1) \cdot e^{j\beta_{opt}l} \cdot \frac{e^{(\gamma - j\beta_{opt}) \cdot x} + \rho_2 e^{-(\gamma - j\beta_{opt}) \cdot x}}{e^{\gamma l} + \rho_1 \rho_2 e^{-\gamma l}} \quad (3.4)$$

$$\rho_1 = \frac{Z_{mod} - Z_s}{Z_{mod} + Z_s}$$

$$\rho_2 = \frac{Z_T - Z_{mod}}{Z_T + Z_{mod}}$$

$$\beta_{opt} = \frac{\omega_m}{c} \cdot n_{opt}$$

$$\beta_{opt} = \frac{\omega_m}{c} \cdot n_{opt}$$

$$\beta_\mu = \frac{\omega_m}{c} \cdot n_\mu$$

$$\gamma = \alpha + j\beta_\mu$$

where,

V_g amplitude of driving voltage,

ω_m modulation frequency,

l total length of traveling wave electrode,

c speed of light in vacuum,

ρ_1 electrode input reflection coefficient,

ρ_2 electrode output reflection coefficient,

Z_{mod} modulator characteristic impedance,

Z_s input source impedance,

Z_T termination impedance,

γ complex microwave transmission constant,

α microwave attenuation constant,

β_μ microwave propagation constant of electrical signal in electrode,

β_{opt} optical propagation constant in optical waveguide,

n_μ microwave refractive index,

n_{opt} optical refractive index,

The average voltage (V_{avg}) experienced by a photon as it traverses a modulator of interaction length l is expressed as integral of the instantaneous voltage seen by photon while traveling along the length of electrode. By integrating Eq 3.4,

$$V_{avg} = \frac{1}{l} \int_0^l V(x, \omega_m) dx = \frac{V_g \cdot (1 + \rho_1) \cdot e^{j\beta_{opt} \cdot l}}{2 \cdot (e^{\gamma \cdot l} + \rho_1 \rho_2 e^{-\gamma \cdot l})} \cdot (V_+ + \rho_2 V_-) \quad (3.5)$$

$$V_{\pm} = e^{\pm j\phi_{\pm}} \frac{\sin(\phi_{\pm})}{\phi_{\pm}}$$

$$\phi_{\pm} = \frac{(-j\gamma \mp \beta_{opt}) \cdot l}{2}$$

In Eq 3.5, V_+ is the single pass voltage experienced by a photon due to forward traveling microwave signal, V_- is the single pass voltage experienced by a photon due to reverse traveling microwave signal, ϕ_+ is the complex phase differential between the microwave and optical signals for a forward traveling microwave signal and ϕ_- is the complex phase differential between the microwave and optical signals for a reverse traveling microwave signal.

Under small signal modulation, the modulation reduction factor can be defined as :

$$r(\omega_m) = \left| \frac{V_{avg}(\omega_m)}{V_{avg}(0)} \right| \quad (3.6)$$

By normalizing the Eq 3.6, the frequency response of a TWE modulator can be written as Eq 3.7.

$$r(\omega_m) = \left| \frac{1 - \rho_1 \rho_2}{1 + \rho_2} \cdot \frac{V_+ + \rho_2 V_-}{e^{\gamma l} - \rho_1 \rho_2 e^{-\gamma l}} \right| \quad (3.7)$$

Equation 3.7 includes all the important design parameters mentioned in Section 3.4 to achieve a broad-band TWE EO modulator. The complex phase difference term ϕ_{\pm} takes into account the velocity match between optical and electrical waves including the microwave propagation loss (α). The terms ρ_1 and ρ_2 determine the effect of impedance mismatch of TWE modulator to source and load impedance on the modulator bandwidth performance. To develop a better understanding of the dependence of design variables on the modulation performance, different cases are discussed below.

3.5.1 Case I: Perfect impedance match

If the impedance of the modulator i.e. Z_{mod} is fully matched to the source and load impedance such that $Z_{mod} = Z_T = Z_s = 50 \Omega$ which makes $\rho_1 = \rho_2 = 0$, Eq 3.6 reduces to [22].

$$V_{avg} = \frac{V_g}{2} e^{-i\phi_+} \frac{\sin\phi_+}{\phi_+} \quad (3.8)$$

and $r(\omega_m)$ becomes,

$$r(\omega_m) = e^{\frac{-\alpha l}{2}} \left| \frac{\sin(\phi_+)}{\phi_+} \right| \quad (3.9)$$

where,

$$\phi_+ = \frac{(-j\gamma - \beta_{opt}) \cdot l}{2} = \frac{l}{2} \cdot \left[\frac{\omega_m}{c} (n_\mu - n_{opt}) - j\alpha \right] = \frac{\pi f_m l (n_\mu - n_{opt})}{c} - \frac{j\alpha l}{2}$$

In this particular case, the only factors affecting the 3-dB electro-optical bandwidth will be microwave loss and velocity mismatch.

Practically, in conventional TWE approach, it is difficult to achieve the modulator impedance as 50Ω . To study the effect of impedance mismatch, we assume here a perfect lossless velocity matched case for simplicity i.e. $\alpha = 0$ and $n_\mu = n_{opt}$, which makes $V_+ = 1$. The microwave source impedance is always $Z_s = 50 \Omega$ which means that the modulator frequency response in this case depends mainly on two variables, modulator impedance Z_{mod} and termination impedance Z_T . By choosing Z_{mod} to be 30Ω , the dependence of modulator frequency response on Z_T can easily be isolated. Fig 3.10 shows the intensity modulation response of the modulator device corresponding to 1 mm long TWE for different values of the terminations.

When the device is terminated by the matched impedance of 30Ω , the frequency response is maximum. Similarly from Fig 3.10b, it is also clear that the available modulating voltage will be constant through out the frequency range as there is no microwave loss. The termination impedance value different than 30Ω pre-emphasizes the RF signal, causing the formation of standing wave on the TWE which influences the modulation bandwidth. In comparison to the matched termination case, the frequency response for the terminations less than 30Ω show a strong peaking characteristic at high frequencies. The peaking effect can help to increase the bandwidth of TWE modulator and will be beneficial in compensating the metal and semiconductor losses. However, the trade-off is that less modulating voltage is available at low to drive the modulator at low frequencies, thus reducing the signal-to-noise ratio (SNR). The reduction in SNR will lead to nonlinear phase response of the device which will result in pattern effects for large signal modulation response. On the other

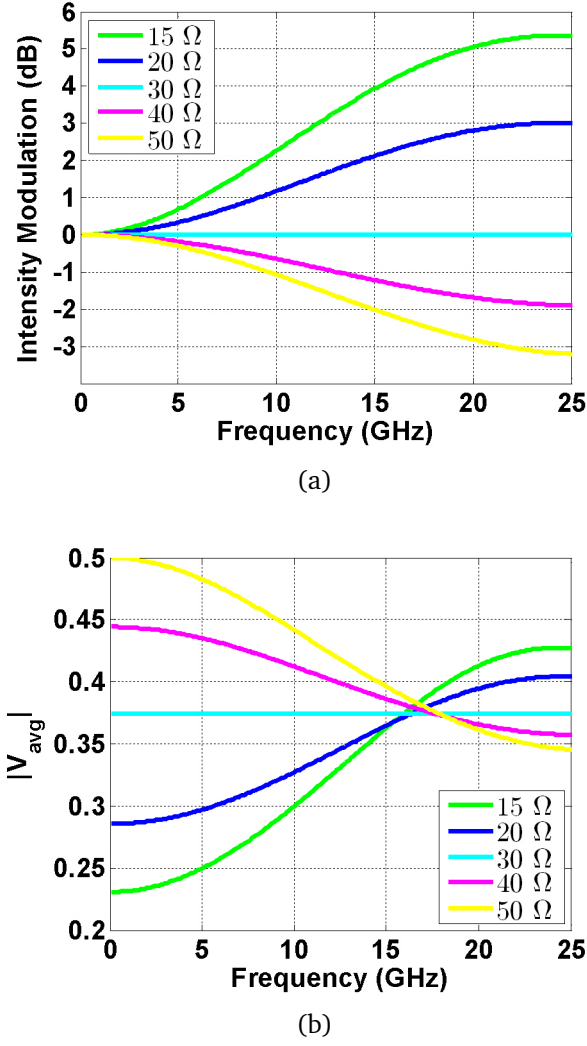


Figure 3.10: (a) Frequency response of the modulator with $Z_{mod} = 30 \Omega$ and TWE length of 1 mm for different terminations Z_T . (b) Average voltage of the modulator for different termination values

hand, when TWE modulator is terminated with Z_T greater than 30Ω , the modulation response decreases rapidly with the frequency due to the same effect, greatly reducing the modulation bandwidth [22, 23].

The case study points out the importance of impedance match. There are two main conclusions to this case study: first is to increase the modulator impedance it self by minimizing the capacitance to match it as close as possible to the standard 50Ω load impedance by comprising the phase efficiency. Second option is to select the $Z_T < Z_{mod}$, which will introduce bandwidth peaking in the frequency response. The drawback of second approach is that the bandwidth gained due to peaking effect is limited by the tolerated large signal distortion, which may get very high if the mismatch is too large.

3.5.2 Case II: Velocity mismatch only

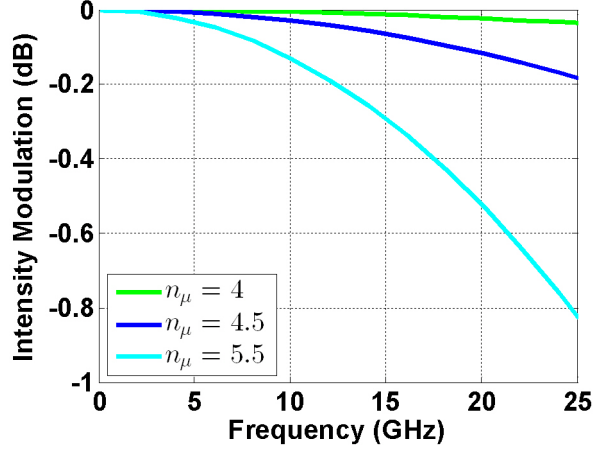


Figure 3.11: Frequency response of the modulator with $Z_{mod}=Z_T=Z_s=50 \Omega$ and TWE length of 1 mm for different value of microwawe index.

If the microwave loss is also ignored i.e. $\alpha = 0$, Eq 3.9 becomes,

$$r(\omega_m) = \left| \frac{\sin \delta}{\delta} \right| \quad (3.10)$$

where, δ is velocity walk-off factor defined as

$$\delta = \frac{\pi f_m l (n_\mu - n_{opt})}{c}$$

As defined earlier, the electro-optic bandwidth of the modulator is the frequency at which the optical intensity modulation reduction factor $r(\omega_m)$ drops to 70.7 % of the reference level which allows Eq 3.6 to be written as Eq 3.11

$$r(\omega_m) = \frac{1}{\sqrt{2}} \quad (3.11)$$

Inserting Eq 3.10 into Eq 3.11, the 3-dB modulator bandwidth is given by Eq 3.12, and it is only limited by the velocity walk-off factor.

$$f_{3dB} = \frac{1.4c}{\pi l |n_{opt} - n_\mu|} \quad (3.12)$$

Fig 3.11 shows the effect of velocity mismatch on the frequency response of the modulator with TWE length of 1 mm. The value of optical group index (n_{opt}) considered here is 3.6, and microwave index is varied from 4 to 5.5. As expected the frequency response drop increases with the increasing velocity walk-off factor. The drop in bandwidth due to velocity mismatch of 1.9

is around 0.8 dB less than 1 dB at the frequency of 25 GHz. It means for a short device the velocity walk-off may not be the most critical design parameter. However, velocity-mismatch will degrade the performance further with increasing length and frequency.

3.5.3 Case III: Microwave loss only

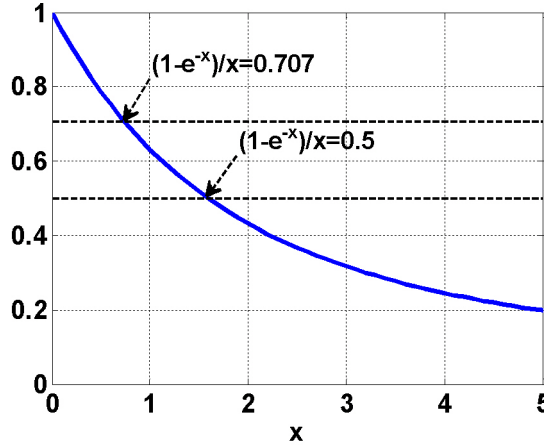


Figure 3.12: Plot of function in Eq 3.15 and its intersection with optical and electrical 3-dB bandwidth.

The third test case is formed when the propagating electrical and optical waves are perfectly velocity matched with the source and load impedances matched to device impedance. In this case, the 3-dB bandwidth of the modulator will be dominated by the microwave loss only. Mathematically, Eq 3.9 reduces to Eq 3.13 by using the Euler's identity,

$$r(\omega_m) = e^{-\frac{\alpha l}{2}} \left| \frac{\sin\left(\frac{-j \cdot \alpha l}{2}\right)}{\frac{-\alpha l}{2}} \right| \quad (3.13)$$

$$r(\omega_m) = \frac{1 - e^{-\alpha l}}{e^{-\alpha l}} \quad (3.14)$$

Inserting Eq 3.14 into Eq 3.11

$$\frac{1 - e^{-\alpha l}}{e^{-\alpha l}} = \frac{1}{\sqrt{2}} \quad (3.15)$$

$$\alpha l = 0.738 Np$$

where 1 Np = 8.686 dB,

$$\alpha l = 6.41 \text{ dB}$$

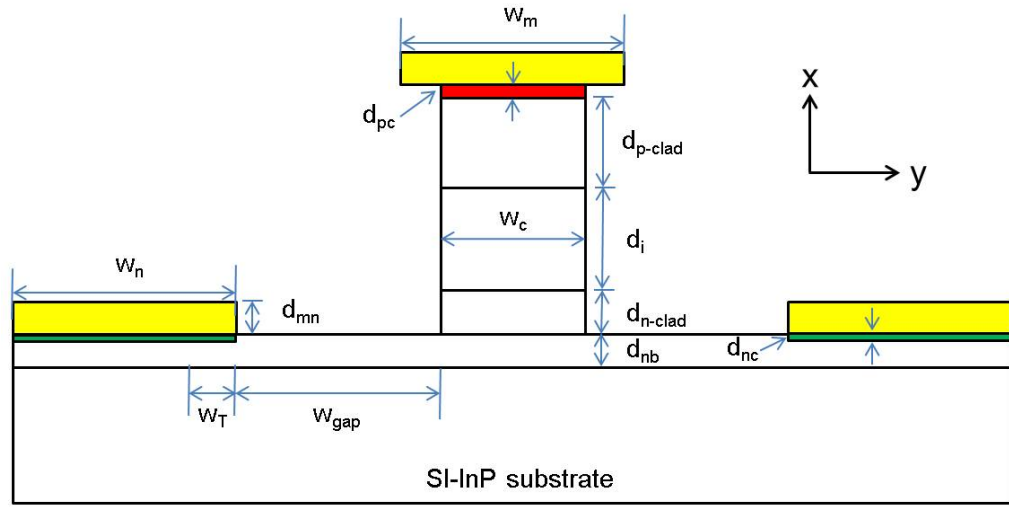
Figure 3.12 shows plot of relation $\frac{1-e^{-x}}{x}$, where $x = \alpha l$ and its intersection with $\frac{1}{\sqrt{2}}$ and $\frac{1}{2}$ is shown. The 3 dB modulation bandwidth corresponds to 1.5 dB reduction in modulated optical power. The value of x is 0.7384 and 1.5936 for 3 dB electrical and optical response respectively. Therefore, in velocity and impedance matched case, the frequency at which the electrical loss falls to -6.4 dB, is the 3 dB electro-optical bandwidth.

3.6 Equivalent circuit model

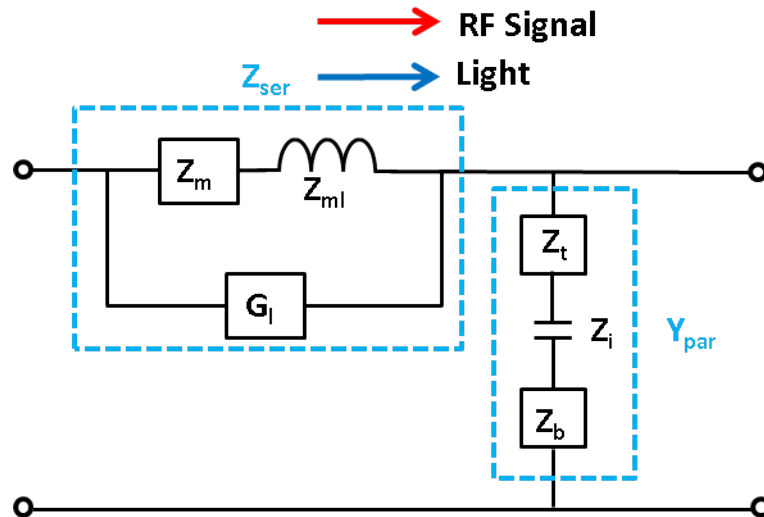
Table 3.1: Definition of structure and material parameters of TWE.

Layer	Width	Thickness	Permittivity	conductivity
p-metal	w_m	d_{mp}	ϵ_{mp}	σ_{mp}
n-metal	w_n	d_{mn}	ϵ_{mn}	σ_{mn}
p-contact	w_{cp}	d_{cp}	ϵ_{cp}	σ_{cp}
p-cladding	w_{pclad}	d_{pclad}	ϵ_{pclad}	σ_{pclad}
intrinsic region	w_i	d_i	ϵ_i	∞
n-cladding	w_{nclad}	d_{nclad}	ϵ_{clad}	σ_{nclad}
n-bottom		d_{nb}	ϵ_{nb}	σ_{nb}
n-contact		d_{cn}	ϵ_{cn}	σ_{cn}
substrate		d_{sub}	ϵ_{sub}	σ_{sub}

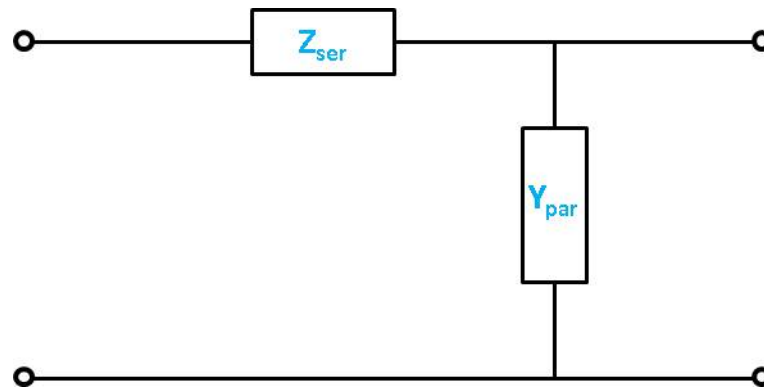
w_c is the optical ridge width



(a)



(b)



(c)

Figure 3.13: (a) Cross section of phase shifting electrode. All the structural parameters are defined in Table 3.1. (b) Equivalent circuit model of electrode structure. (c) General transmission line equivalent model.

The bandwidth of the modulator based on TWE is determined by 3 main factors: velocity matching between optical and microwave carrier, impedance matching and the microwave losses. In the previous section, the individual effect of these three factors on the modulator bandwidth performance have been discussed in detail by considering the whole TWE as a single electrical transmission line with characteristic impedance (Z_{mod}) and microwave transmission constant (γ). However, when the operating frequency is up to 40 GHz, the electrode length is basically comparable to multiples of electrical wavelength. In this case, the electrode cannot be treated as simple circuit based on lumped elements. Instead, a specific transmission line model is essential to accurately calculate transmission line parameters Z_{mod} , γ to analyze the modulation frequency response. Total electrode length is divided in to multiple sections and each section is treated as a single transmission line, which can be later cascaded to get the overall response of electrode. The properties of a transmission line deposited directly on dielectric substrates can be readily calculated from the analytical formulas developed over years [24] but such formulas fail to describe the behavior of InP based TWE structures as they are deposited on multiple semiconductor layers stacked on the top of SI-InP substrate to form a p-i-n structure. In design phase, the microwave loss factors generated by these doped semiconductor layers have to be considered precisely in order to predict the device response.

In general three dimensional (3D) full-wave analysis is the most accurate method to study the microwave mode propagation properties in microstrip and CPW transmission lines fabricated on multiple layer stack of semiconductor materials. However, full-wave analysis is numerically intensive, requiring considerable computational time. The active TWE structure can also be described by a quasi-TEM equivalent circuit model. This analysis can accurately describe the propagation characteristics of quasi-TEM waveguides and it is not only computationally efficient, it also gives a deeper physical insight into TWE design [25]. All the metal and semiconductor layers can be represented by an equivalent circuit element which can be directly calculated from the device geometry using closed form analytical formulas. Once the equivalent circuit parameters are determined, propagation constant and electrode impedance can be easily calculated, which are then used to determine the small-signal frequency response of the TWE modulator using Eq 3.8.

Different equivalent circuit models such as [25,26] have been developed for TWE structures on multilayer semiconductors and have shown good agreement with the full-wave solutions and experimental results. Here we use the equivalent

lent circuit model described in [26–28]. The model is based on a parallel plate approximation in combination with a CPW approximation. Fig 3.13a shows the cross section of a typical TWE with the structural dimensions and material properties which are then used to calculate different elements of the equivalent circuit shown in 3.13b. Table 3.1 defines all the variables of Fig 3.13a. Each element of equivalent circuit of hybrid-co-planar TWE structure is discussed below.

Z_m in Eq 3.16 is the transverse wave impedance of metal air layer assuming the wave impedance of air is much larger than of the metal.

$$Z_m = \frac{\eta_m}{w_c} \cdot \coth \left[(1 + j) \frac{d_m}{\delta_m} \right] \quad (3.16)$$

where η_m is the wave impedance in air and δ_m is metal skin depth defined below:

$$\eta_m = \sqrt{\frac{j\omega\mu_o}{\sigma_m}}$$

$$\delta_m = \sqrt{\frac{2}{\omega\mu_o\sigma_m}}$$

Z_{ml} is the impedance of CPW inductance $L_m(H/m)$ and is given by

$$Z_{ml} = i\omega L_m \quad (3.17)$$

G_l is the conductance of semiconductor layers and represent the longitudinal resistance due to doped multilayers in the direction of propagation and is represented by Eq 3.18.

$$G_l = \frac{w_c d_{pc}}{3\rho_{pc}} + \frac{w_c d_{pclad}}{3\rho_{pclad}} + \frac{w_c d_{nclad}}{3\rho_{nclad}} \quad (3.18)$$

Z_t is the transverse impedance of each layer in x-direction i.e. p-contact layer, p-cladding layer and n-cladding layer. The impedance of each layer is basically a parallel combination of a capacitor and a resistor. Total impedance is given by the sum of impedance of individual layer and is given in Eq 3.19.

$$Z_t = \frac{1}{w_c} \left(\frac{\rho_{cp} d_{cp}}{1 + j\omega\rho_{cp}\epsilon_{cp}} + \frac{\rho_{pclad} d_{pclad}}{1 + j\omega\rho_{pclad}\epsilon_{pclad}} + \frac{\rho_{nclad} d_{nclad}}{1 + j\omega\rho_{nclad}\epsilon_{nclad}} \right) \quad (3.19)$$

The impedance of the bottom n-conducting layer is given by Z_b in Eq 3.20,

where b is designated to represent the impedance from the bottom layer of the mesa. Basically, it accounts for the the spreading resistance term under the top mesa, the bulk resistance of the gap w_{gap} between the mesa and the bottom contact and the resistance of the bottom contact. Due to structural symmetry, the spreading resistance has a factor of 1/2 and another factor of 1/3 due to the current distribution.

$$Z_b = \frac{\rho_{nb}}{1 + j\omega\rho_{nb}\epsilon_{nb}} \cdot \frac{w_c/6 + w_{gap} + w_T}{2d_{nb}} \cdot w_T \quad (3.20)$$

where w_T is the contact transfer length given as,

$$w_T = \sqrt{\frac{\rho_{cn}}{\rho_{nb}} \cdot \frac{1 + j\omega\rho_{nb}\epsilon_{nb}}{1 + j\omega\rho_{cn}\epsilon_{cn}} \cdot d_{cn}d_{nb}}$$

Z_i is another important element of the equivalent circuit, which represents the impedance of the intrinsic capacitance (C_i). Once the active region is depleted under applied reverse bias C_i can be approximated as $\frac{\epsilon_o\epsilon_i w_c}{d_i}$ and can be written as Eq 3.21 in impedance form,

$$Z_i = \frac{1}{i\omega C_i} \quad (3.21)$$

Using the above analytical formulas the equivalent circuit elements can be readily calculated and the influence of device geometry including material parameters can be analyzed. The transmission line properties can be evaluated by comparing the equivalent circuit model of TWE structure shown in Fig 3.13b to the general transmission line model shown in Fig 3.13c. The transmission line model is comprised of series impedance and shunt impedance, represented by Z and Y per unit length receptively. Using the basic circuit theory, the coupled differential equations for the voltage and current waves can be written in terms of Z_{ser} and Y_{par} as in Eq 3.22. These differential equations relate voltage (V) and current (I) on a infinitesimal section of the transmission line.

$$\frac{dV}{dz} = -IZ_{ser} \quad (3.22a)$$

$$\frac{dI}{dz} = -VY_{par} \quad (3.22b)$$

Further manipulation of these equations lead to second order wave equation for both V and I given as,

$$\frac{d^2 V}{dz^2} = \gamma^2 V \quad (3.23a)$$

$$\frac{d^2 I}{dz^2} = \gamma^2 I \quad (3.23b)$$

The general solution for the wave equation is given by Eq 3.24,

$$V(z) = V_o^+ e^{-\gamma z} + V_o^- e^{\gamma z} \quad (3.24a)$$

$$I(z) = I_o^+ e^{-\gamma z} + I_o^- e^{\gamma z} \quad (3.24b)$$

where γ is the propagation constant is given by Eq 3.25, using which the microwave loss (α_μ) and propagation phase constant (β) can be determined.

$$\gamma = \sqrt{Y_{ser} Z_{par}} = \alpha_\mu + j\beta \quad (3.25)$$

The characteristic impedance of transmission line can be defined as

$$Z_o = Z_{mod} = \sqrt{\frac{Z_{ser}}{Y_{par}}} \quad (3.26)$$

From the equivalent circuit of the TWE structure, it can be observed that total series impedance Z_{ser} is basically sum of the transverse metal impedance, impedance due to CPW inductance, both of them are parallel to the longitudinal conductance from the doped semiconductor layers. On the other hand, the total admittance (Y_{par}) is basically the sum of transverse impedance of top layer, impedance due to intrinsic capacitance and impedance due to resistance arising from the conducting bottom n-layer. Mathematically, Z_{ser} and Y_{par} can be written as Eq 3.27 and Eq 3.28

$$Z_{ser} = (Z_m + Z_{ml}) \parallel \frac{1}{G_l} \quad (3.27)$$

$$Y_{par} = (Z_t + Z_b + Z_i)^{-1} \quad (3.28)$$

Using the Eq 3.25 - 3.28, the transmission properties of the small electrode section can be readily calculated. These properties can be related to the linear two port network parameters (S-parameters) as given below

$$S_{11} = S_{22} = \frac{(Z^2 - 1)\sinh(\gamma l)}{2Z\cosh(\gamma l) + (Z^2 + 1)\sinh(\gamma l)} \quad (3.29)$$

$$S_{21} = S_{12} = \frac{2Z}{2Z\cosh(\gamma l) + (Z^2 + 1)\sinh(\gamma l)} \quad (3.30)$$

l is the length of electrode section, γ is the propagation constant as defined previously in Eq 3.25, Z is the normalized modulator impedance defined as Z_{mod}/Z_{ref} , Z_{ref} is the impedance of the measurement system and it is usually 50Ω . To determine the electrical response of the the electrode structure, the electrode sections can be cascaded as shown in Fig 3.14. S-parameters of each small electrode section can be converted to transmission matrix or T-matrix. The T-matrix directly relates the waves on input and output of each small electrode section in cascade. The T-matrix of the cascaded two port network can be given by the product of T-matrix of each section from left to right. Finally, the T-matrix of the cascaded network can be converted back to S-parameters. The transformation from S to T parameters and T to S-parameter is given in Eq 3.31 and Eq 3.32 respectively.

$$T = \frac{1}{S_{21}} \begin{bmatrix} S_{12}S_{21} - S_{11}S_{22} & S_{11} \\ -S_{22} & 1 \end{bmatrix} \quad (3.31)$$

$$S = \frac{1}{T_{22}} \begin{bmatrix} T_{12} & T_{11}.T_{22} - T_{12}.T_{21} \\ 1 & -T_{21} \end{bmatrix} \quad (3.32)$$

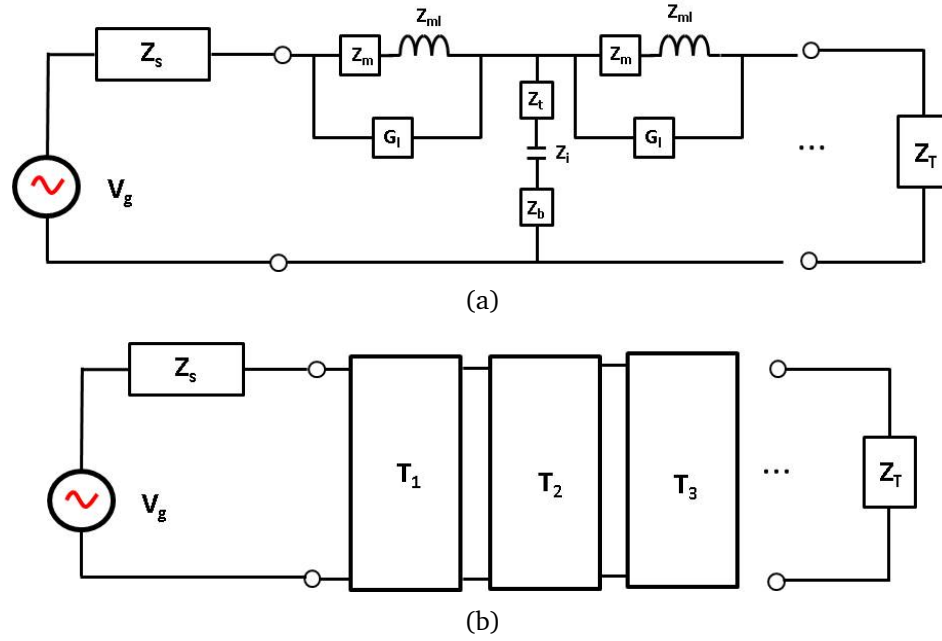


Figure 3.14: (a) Equivalent circuit of TWE with source and termination connections.(b) Transmission matrix representation of the equivalent circuit with source and termination connections.

3.7 Microwave properties using circuit model

Table 3.2: TWE structure parameters used in the simulation.

Layer	Width (μm)	Thickness (μm)	Permittivity	Resistivity (Ωm)
p-metal	$w_m = 4$	$d_{mp} = 2$		$\rho_{mp} = 2.5e^{-8}$
n-metal	$w_n = 40$	$d_{mn} = 2$		$\rho_{mn} = 2.5e^{-8}$
p-contact	$w_c = 2$	$d_{cp} = 0.1$	13.8	$\rho_{cp} = 0.02685$
p-cladding	$w_{pclad} = 2$	$d_{pclad} = 0.835$	12.56	$\rho_{pclad} = 1.714e^{-3}$
intrinsic region	$w_i = 2$	$d_i = 0.6$	13.8	
n-cladding	$w_{nclad} = 2$	$d_{nclad} = 0.2$	12.56	$\rho_{nclad} = 2.43e^{-5}$
n-bottom		$d_{nb} = 0.8$	12.56	$\rho_{nb} = 2.43e^{-5}$
n-contact		$d_{cn} = 0.01$	12.56	$\rho_{cn} = 0.01$
substrate		$d_{sub} = 30$		SI

w_c is the ridge width

In this section, the transmission line properties are analyzed based on the equivalent circuit model presented in the previous section.

3.7.1 Major source of microwave loss

Before optimizing the TWE structure, it will be interesting to determine the major source of microwave loss arising from different resistive elements of the equivalent circuit. These elements are real parts of air-metal impedance, resistance from the semiconductor layers in optical mesa which are, p-contact, p-cladding and n-cladding and resistance from the bottom n-conducting layer. By artificially setting the real part of Z_m , Z_t and Z_b to zero without changing the imaginary parts, the contribution from each element can be easily identified as shown in Fig 3.15. It can be seen that the major source of the microwave source is the metal resistance which can be reduced by using thicker metal electrodes. By setting it to zero, the microwave loss drops from 3.4 dB/mm to 1.7 dB/mm at 25 GHz. The remaining losses mainly come from top and bottom doped semiconductor layers. The resistance from bottom conducting layer only has minute effect on the loss, when the thickness is optimum (effect of thickness of n-conducting layer is shown in Fig 3.19). When the resistance from the top semiconductor layers of mesa is also taken off, the loss value drops to zero. It shows that the resistance of the top mesa layers have the second highest contribution to microwave loss after the metal. It also verifies that due to very low value of longitudinal conductance, G_l has no contribution at all to the microwave loss.

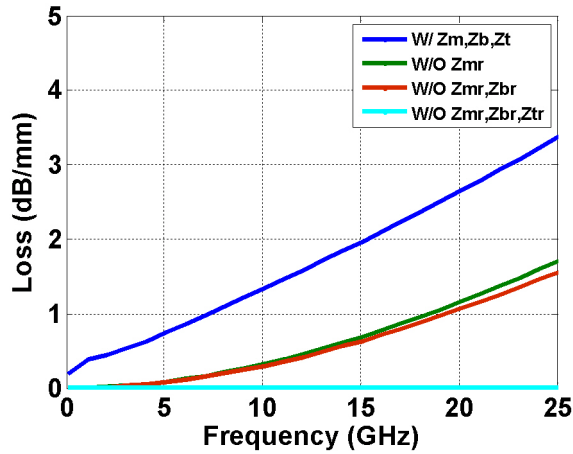


Figure 3.15: Microwave loss due to different elements of the equivalent circuit shown in Fig 3.13b. Simulated parameters are in listed in Table 3.2.

Another important issue worth considering here is the contribution of the p-contact resistance (R_c) to the microwave loss from the top mesa layers. The signal metal electrode on the top of the ridge makes an ohmic contact with the p-doped semiconductor. A thin $0.1 \mu\text{m}$ layer of high doped InGaAs is included

to help achieve low ohmic contact resistance. To get a clear picture of TWE performance, the p-contact resistance should be included in the equivalent circuit model. However, due to the very thin nature of the p-contact layer, it cannot be modelled separately [29]. The alternative way to include p-contact resistivity is to calculate the p-contact resistance separately using Eq 3.33 and add it to resistance of the contact layer as shown below,

$$R_c = \frac{\rho_{spec,p}}{w_c l} \quad (3.33)$$

$$R_{pc} = R_c + \sum_{n=1}^2 \frac{d_{pc}}{\sigma_{pc} w_c l} \quad (3.34)$$

where $\rho_{spec,p}$ is the specific contact resistance on p-metal, ρ_{pc} of the contact layers can be calculated in the. The effective conductivity of the p-contact pad can be directly calculated using Eq 3.34

$$R_{pc} = \frac{\rho_{spec,p}}{w_c l} + \sum_{n=1}^2 \frac{d_{pc}}{\sigma_{pc} w_c l} \quad (3.35)$$

Finally conductivity of contact layer (σ_c) based on R_c can be calculated as follows,

$$\sigma_{pc} = \frac{d_{pc}}{R_{pc} w_c l} \quad (3.36)$$

Table 3.3 shows different values of R_c and corresponding conductivity of contact layer. It can be seen that $\rho_{spec,p}$ has major effect on the R_c . Fig 3.16 shows the effect of contact resistance on the microwave loss. As expected, higher the contact resistance, higher will be the microwave loss and vice versa. To ensure, low value of contact resistance, the electrode deposition process i.e. metal layer stack and annealing conditions should be optimized very carefully during the fabrication process.

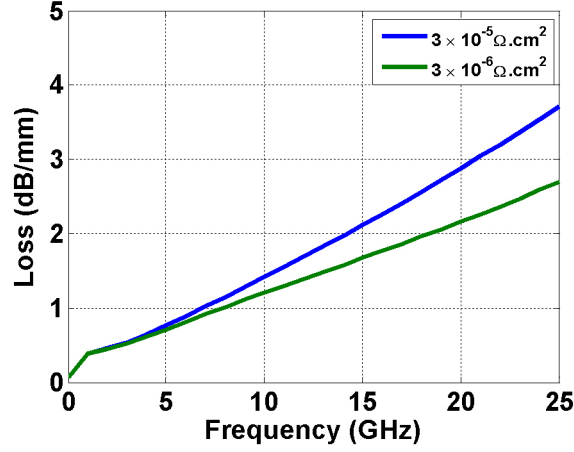


Figure 3.16: Influence of specific contact resistance ($\rho_{spec,p}$) on microwave loss.

Table 3.3: Contact layer properties for different values of $\rho_{spec,p}$.

p-contact resistivity ($\Omega.cm^2$)	R_c (Ω)	Conductivity (S/m)	Resistivity ($\Omega.m$)
3×10^{-5}	15	37.2	.02685
1×10^{-5}	5.03	99	.010
3×10^{-6}	1.53	326	3.06×10^{-3}
1×10^{-6}	0.53	943	1.06×10^{-3}

3.7.2 Traveling wave electrode optimization

Keeping the geometrical and material parameters of TWE structure as variables, most important transmission line properties such as microwave loss, characteristic impedance (Z_m) and electrical S_{21} have been studied. Initial values of different variables of TWE structure (shown in Fig 3.13a) are depicted in Table 3.2. These values were selected after the comprehensive literature review most important of which are [22, 25–29]. The main selection criteria was to achieve the design goals of the TWE i.e. velocity matching, high impedance close to 50Ω and low microwave losses by choosing the most appropriate device dimensions and material properties. In all the simulations, $\sigma_c = 0.02685$ has been used, which corresponds to the $R_c = 15 \Omega$ and $\rho_{spec,p} = 3 \times 10^{-5} \Omega.cm^2$ respectively.

High impedance means to reach as close as possible to 50Ω . The easiest way to do is to increase the thickness of the intrinsic region of the optical optical, which is basically a parallel plate capacitor. Fig 3.17 shows the effect of variation of d_i from 0.2 to $1 \mu m$ on Z_m , α and electrical S_{21} . It can be

seen that increasing d_i , increases the structure impedance from 22 to 42 Ω at 20 GHz, which is due to the reduction in capacitance of the intrinsic region. Thicker intrinsic region reduces the microwave loss by at least 5 dB/mm at 20 GHz. However, thicker intrinsic region, reduces the available modulating electric field across the MQWs. It means that higher V_π will be required for the same length of device with the thicker intrinsic region to achieve the same EO effect. Here, we choose d_i as 0.6 μm which gives Z_m and α of 35 Ω and 2.7 dB/mm respectively at 20 GHz.

Another, important parameter which can control the capacitance and microwave loss is the ridge width (w_c). Keeping the other simulation parameters same as shown in Table 3.2, w_c is varied in Fig 3.17. The narrowing of the horizontal dimension of the optical ridge has effects on all the resistive, capacitive and inductive elements of the TWE structure. Reducing the ridge width decreases the capacitance due to decrease in area of the intrinsic region but at the same time it will increase the inductance and resistance of the transmission line. The overall prevailing effect is reduction in capacitance here which results in low α and microwave index (n_μ) and high Z_m . Despite the fact that simulations suggest a better RF performance for the narrow widths, it cannot be too narrow, otherwise there will be high optical input coupling losses and also fabrication challenges posed by high aspect ratio. Likewise, ridge cannot be too wide, otherwise it may support multimode optical propagation. Based on these considerations, an optical ridge with of 2 μm has been used in the simulations.

The results in Fig 3.19 depict the RF performance for different thickness of the bottom n-conducting layer (d_{nb}). From the TWE structure and equivalent circuit model, it is obvious that increasing the thickness of $d_{p\text{clad}}$ and $d_{n\text{clad}}$ increases the series resistance of the admittance part resulting in the increase of microwave loss. In addition to the thicknesses, resistance of the p-cladding and n-cladding layer depends on the the doping concentration on these layers and should be high enough to avoid the large microwave loss. On the other hand, increasing d_{nb} results in decrease of the microwave loss. From the thickness variation, it is clear that d_{nb} should be greater than 0.5 μm for low microwave loss. It can also be observed that Z_{mod} is independent of the thickness of bottom n-conducting layer.

Once the simulation variables related to optical waveguide geometry are optimized. The next step is to choose the signal electrode width (w_m) and ground electrode gap (w_{gap}). The best electrode configuration choice is less clear. For this purpose, simulation is performed by changing both the variables i.e. w_m

and w_{gap} simultaneously at 20 GHz, keeping other TWE structural and material parameters fixed as optimized. Fig 3.20 shows the simulation results for Z_{mod} , α and n_μ . Fig 3.20 shows that at wider electrode widths compared to the ridge width decreases the microwave loss and impedance but the microwave index increases. Similarly, reducing the w_{gap} with w_m fixed increases the microwave loss slightly and decreases impedance. The reason for lower microwave loss is that the electric field due to a wider signal electrode is more concentrated in air than in the doped p-i-n structure. Also, there can be a small increase in loss with increase in w_{gap} . This increase arises from the resistive n-plane, to which the electric field is exposed if the ground electrodes are moved too far away from the signal electrode. As discussed above, there is an optimum thickness (d_{nb}) of n doped plane below the ridge as well to minimize this loss. In this case, the thickness of n-plane (d_{nb}) below ridge is $0.8 \mu\text{m}$.

It can be further observed that a wider signal electrode reduces both Z_m and n_μ at a constant electrode gap. If the electrode gap is also increased at a fixed w_m , both Z_m and n_μ get higher once again. At the frequency range of our interest, Z_m is proportional to $\sqrt{\frac{L_m}{C_i}}$, where L_m is the inductance of the signal line and C_i is the capacitance of the intrinsic region. Increasing the signal electrode width decreases the inductance which in turn reduces Z_m . In order to maintain the value of inductance, the gap between electrodes has to be increased as well, at the cost of a slight increase in microwave loss. The optimized solution is to keep the signal metal width same as the ridge width. However, for the ease of fabrication process it is better to keep the signal electrode slightly wider than ridge, hence a value of $2.5 \mu\text{m}$ for w_m , is chosen. The electrode structure wider than optical ridge width is supported by Benzocyclobutene (BCB), which is used for the of the electrode structure planarization for the ease of performing measurements.

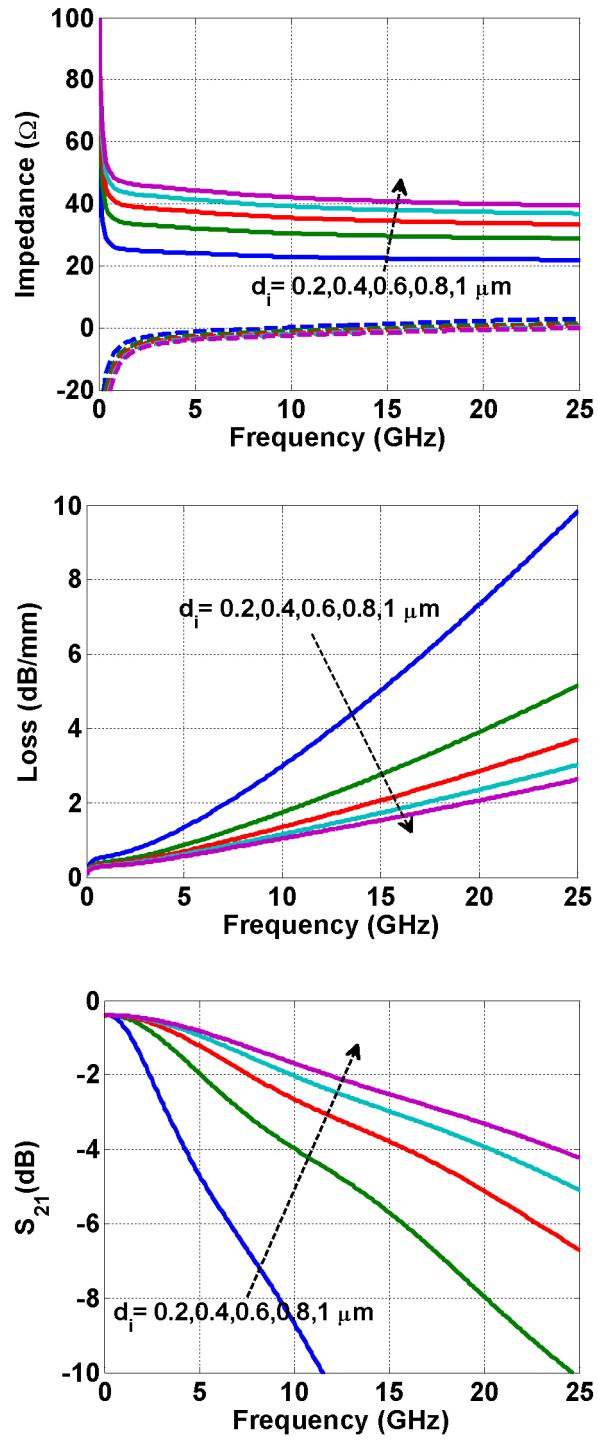


Figure 3.17: Transmission line properties as a function of intrinsic region thickness (d_i).

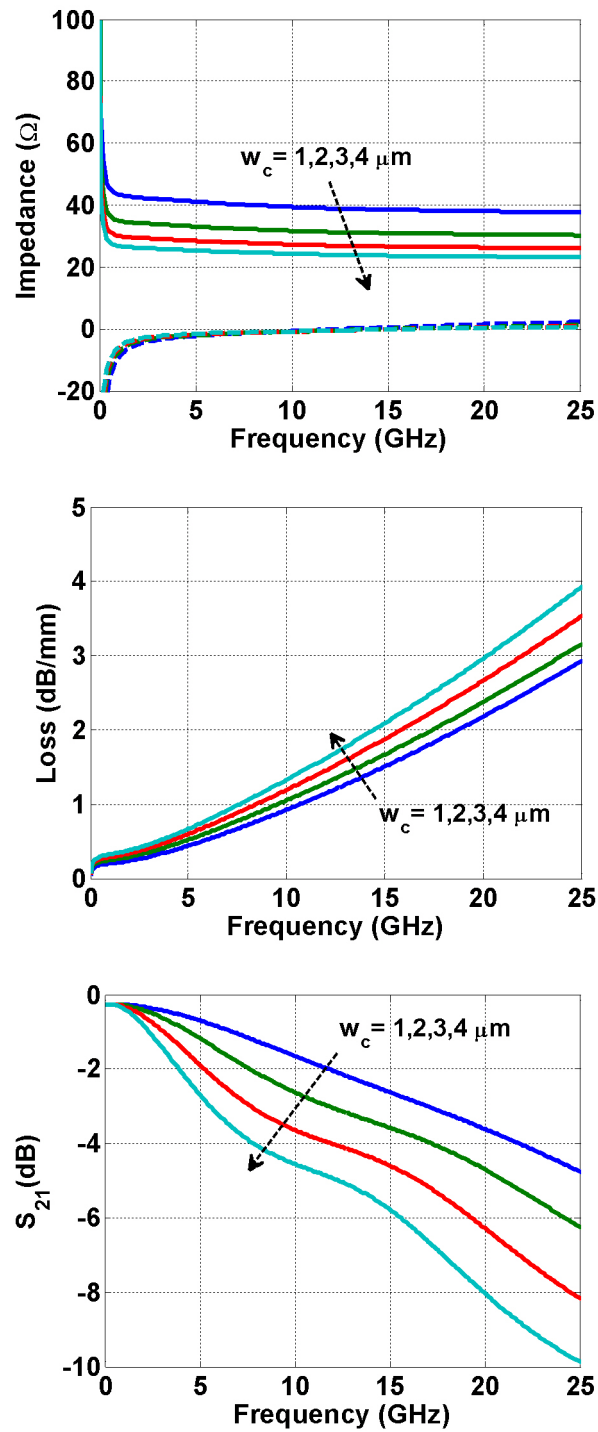


Figure 3.18: Transmission line properties as a function of ridge width (w_c).

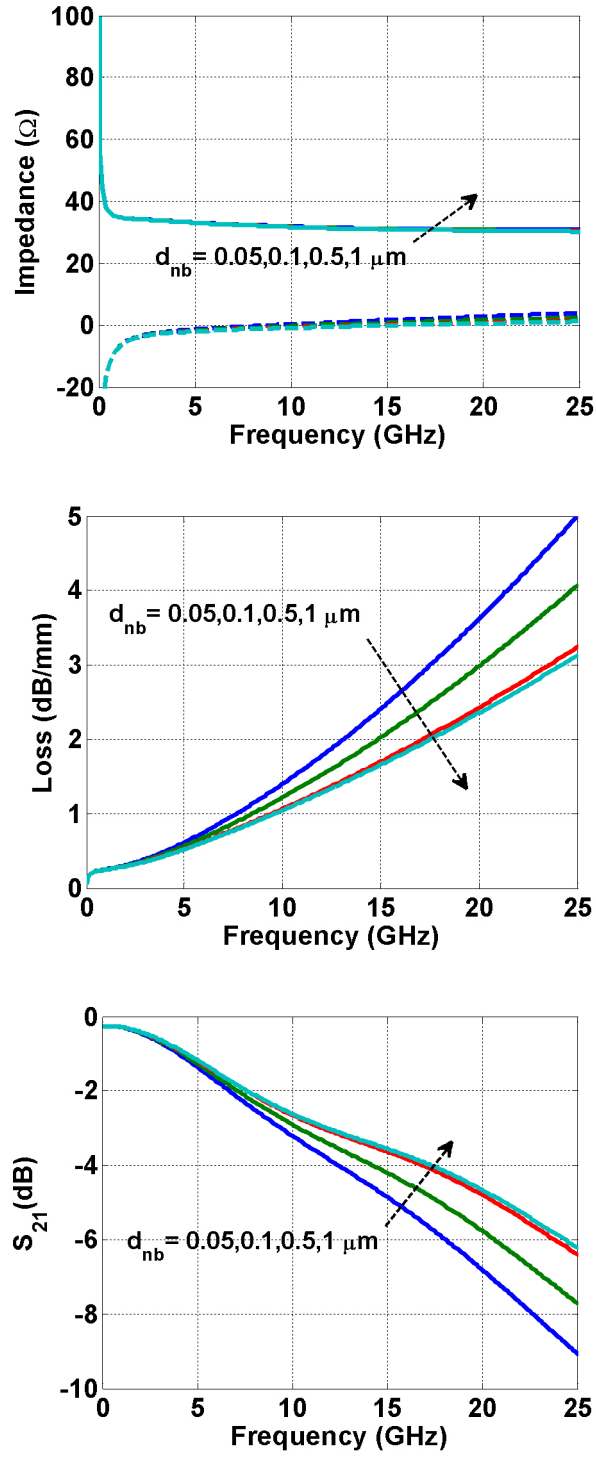


Figure 3.19: Transmission line properties as a function of bottom n-conducting layer thickness(d_{nb}).

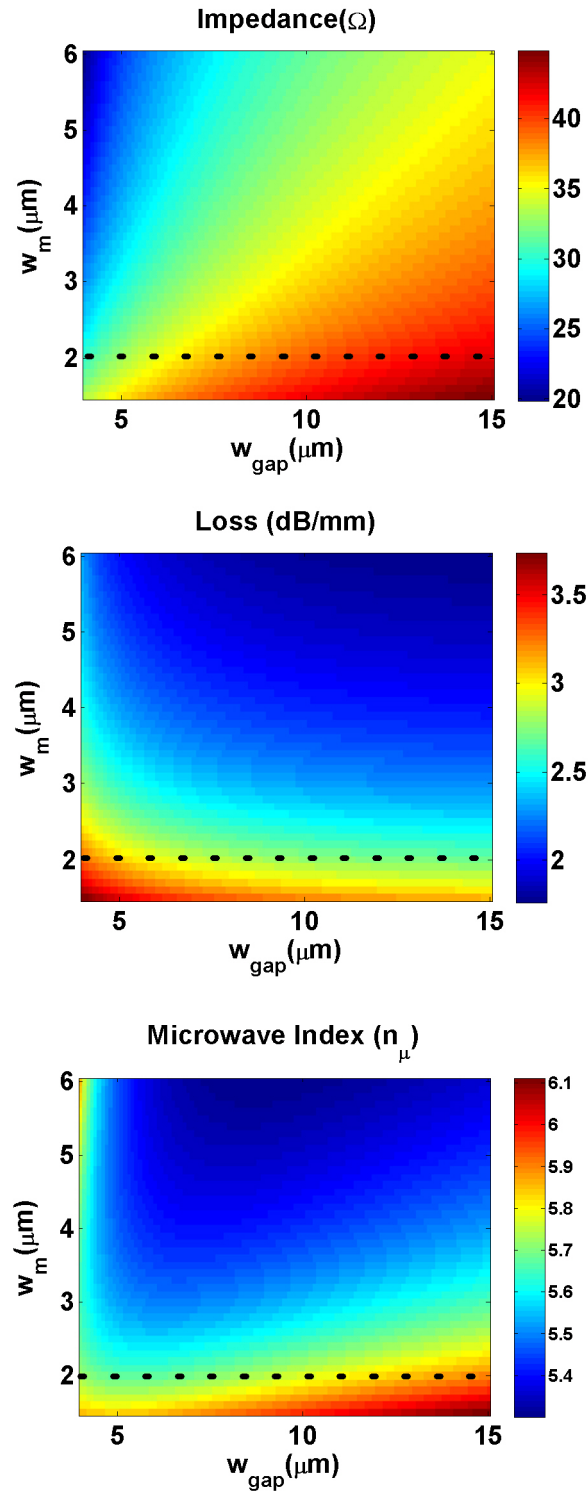


Figure 3.20: Transmission line properties as a function of signal metal width (w_m) and electrode gap (w_{gap}). Dotted line shows the ridge width (w_c)

3.8 Summary

This chapter introduces the electrode design, necessary for the high frequency operation of the MZMs. Merit and demerits of different transmission line structures have been discussed in detail. Based on the traveling wave approach for the electrode design, different bandwidth limiting factors have been highlighted through case studies, using the analytical model to evaluate the frequency response of the modulator. It is shown that the velocity mismatch between electrical and optical co-propagating signals is not the most critical design parameter, specially for the frequencies below 20 GHz. The bandwidth performance of a traveling wave modulator is mainly affected by the electrical/optical losses and impedance mismatch between the modulator structure and driving electronics. After identifying the key design parameters, the transmission line properties of a CPW transmission line on multilayer epitaxial p-i-n structure are determined using an equivalent circuit model. This circuit model is then used to optimize the CPW traveling wave electrode geometry with the goal to minimize the microwave losses and to achieve high characteristic impedance. These optimized electrode dimensions are used to fabricate the InP based MZMs operating the wavelengths of 1550 nm and 2000 nm. The measured high frequency performance of these fabricated devices is evaluated in Chapter 4 and 5 respectively.

References

- [1] W. Getsinger, “An introduction to microwave transmission lines,” in *Circuits and Systems, 1992., Proceedings of the 35th Midwest Symposium on*, Aug 1992, pp. 1016–1019 vol.2.
- [2] D. Pozar, *Microwave Engineering, 4th Edition*. Wiley, 2011.
- [3] R. Griffin, S. Jones, N. Whitbread, S. Heck, and L. Langley, “InP Mach-Zehnder Modulator Platform for 10/40/100/200-Gb/s Operation,” *Selected Topics in Quantum Electronics, IEEE Journal of*, vol. 19, no. 6, pp. 158–166, Nov 2013.
- [4] W. Yao, G. Gilardi, N. Calabretta, M. Smit, and M. Wale, “Experimental and Numerical Study of Electrical Crosstalk in Photonic-Integrated Circuits,” *Journal of Lightwave Technology*, vol. 33, no. 4, pp. 934–942, Feb 2015.
- [5] S. Akiyama, H. Itoh, S. Sekiguchi, S. Hirose, T. Takeuchi, A. Kuramata, and T. Yamamoto, “InP-Based Mach-Zehnder Modulator With Capacitively Loaded Traveling-Wave Electrodes,” *Journal of Lightwave Technology*, vol. 26, no. 5, pp. 608–615, March 2008.
- [6] K. Tsuzuki, T. Ishibashi, T. Ito, S. Oku, Y. Shibata, T. Ito, R. Iga, Y. Kondo, and Y. Tohmori, “A 40-gb/s InGaAlAs-InAlAs MQW n-i-n Mach-Zehnder Modulator with a drive voltage of 2.3 V,” *Photonics Technology Letters, IEEE*, vol. 17, no. 1, pp. 46–48, Jan 2005.
- [7] R. Kaiser, K. Velthaus, T. Brast, B. Maul, M. Gruner, H. Klein, M. Hamacher, D. Hoffmann, and M. Schell, “Monolithic flip-chip compatible twin-IQ Mach-Zehnder modulators for hybrid assembly onto high capacity optical transmitter boards,” in *Compound Semiconductor Week (CSW/IPRM), 2011 and 23rd International Conference on Indium Phosphide and Related Materials*, May 2011, pp. 1–4.

- [8] C. Wen, "Coplanar Waveguide, a Surface Strip Transmission Line Suitable for Nonreciprocal Gyromagnetic Device Applications," in *Microwave Symposium, 1969 G-MTT International*, May 1969, pp. 110–115.
- [9] S. Corzine and P. Evans, "Large-Scale Monolithic Integration of PM-QPSK Modulation Architecture in 500 Gb/s Transmitters," in *Advanced Photonics*. Optical Society of America, 2011, p. ITuC1.
- [10] N. Andriolli, F. Fresi, F. Bontempi, A. Malacarne, G. Meloni, J. Klamkin, L. Poti, and G. Contestabile, "Inp monolithically integrated coherent transmitter," *Opt. Express*, vol. 23, no. 8, pp. 10 741–10 746, Apr 2015.
- [11] S. Kim, S. Jeong, Y. Lee, D. Kim, J.-S. Lim, K.-S. Seo, and S. Nam, "Ultra-wideband (from dc to 110 ghz) cpw to cps transition," *Electronics Letters*, vol. 38, no. 13, pp. 622–623, Jun 2002.
- [12] G. Li, T. Mason, and P. Yu, "Analysis of segmented traveling-wave optical modulators," *Journal of Lightwave Technology*, vol. 22, no. 7, pp. 1789–1796, July 2004.
- [13] I. Betty, M. Boudreau, R. Griffin, and A. Feckes, "An empirical model for high yield manufacturing of 10gb/s negative chirp InP Mach-Zehnder modulators," in *Optical Fiber Communication Conference, 2005. Technical Digest. OFC/NFOEC*, vol. 3, March 2005, pp. 3 pp. Vol. 3–.
- [14] E. Wooten, K. Kissa, A. Yi-Yan, E. Murphy, D. Lafaw, P. Hallemeier, D. Maack, D. Attanasio, D. Fritz, G. McBrien, and D. Bossi, "A review of lithium niobate modulators for fiber-optic communications systems," *Selected Topics in Quantum Electronics, IEEE Journal of*, vol. 6, no. 1, pp. 69–82, Jan 2000.
- [15] A. L. L. Liao, D. Rubin, H. Nguyen, B. Ciftcioglu, Y. Chetrit, N. Izhaky, and M. Paniccia, "High-speed optical modulation based on carrier depletion in a silicon waveguide," *Opt. Express*, vol. 15, no. 2, pp. 660–668, Jan 2007.
- [16] R. Walker, N. Cameron, Y. Zhou, and S. Clements, "Optimized Gallium Arsenide Modulators for Advanced Modulation Formats," *Selected Topics in Quantum Electronics, IEEE Journal of*, vol. 19, no. 6, pp. 138–149, Nov 2013.
- [17] R. Palmer, L. Alloatti, D. Korn, P. Schindler, M. Baier, J. Bolten, T. Wahlbrink, M. Waldow, R. Dinu, W. Freude, C. Koos, and J. Leuthold,

- “Low Power Mach-Zehnder Modulator in Silicon-Organic Hybrid Technology,” *Photonics Technology Letters, IEEE*, vol. 25, no. 13, pp. 1226–1229, July 2013.
- [18] Y. R. Kwon, “Quasi-TEM Analysis of "Slow-Wave" Mode Propagation on Coplanar Microstructure MIS Transmission Lines,” *Microwave Theory and Techniques, IEEE Transactions on*, vol. 35, no. 6, pp. 545–551, Jun 1987.
- [19] R. Walker, “High-speed III-V semiconductor intensity modulators,” *Quantum Electronics, IEEE Journal of*, vol. 27, no. 3, pp. 654–667, Mar 1991.
- [20] R. Spickermann, S. Sakamoto, and N. Dagli, “In traveling wave modulators which velocity to match?” in *Lasers and Electro-Optics Society Annual Meeting, 1996. LEOS 96., IEEE*, vol. 2, Nov 1996, pp. 97–98 vol.2.
- [21] A. Chen and E. Murphy, *Broadband Optical Modulators Science, Technology, and Applications*. CRC Press, 2011.
- [22] S. H. Lin and S.-Y. Wang, “High-throughput GaAs PIN electrooptic modulator with a 3-dB bandwidth of 9.6 GHz at 1.3 μm ,” *Appl. Opt.*, vol. 26, no. 9, pp. 1696–1700, May 1987.
- [23] S. Wang and S. Lin, “High speed III-V electrooptic waveguide modulators at $\lambda=1.3 \mu\text{m}$,” *Journal of Lightwave Technology*, vol. 6, no. 6, pp. 758–771, Jun 1988.
- [24] R. N. Simons, *Coplanar Waveguide Circuits Components & Systems*, 1st ed. Wiley-IEEE Press, Mar. 2001.
- [25] R. Lewen, S. Irmscher, and U. Eriksson, “Microwave CAD circuit modeling of a traveling-wave electroabsorption modulator,” *Microwave Theory and Techniques, IEEE Transactions on*, vol. 51, no. 4, pp. 1117–1128, Apr 2003.
- [26] K. Giboney, M. J. Rodwell, and J. Bowers, “Traveling-wave photodetector design and measurements,” *Selected Topics in Quantum Electronics, IEEE Journal of*, vol. 2, no. 3, pp. 622–629, Sep 1996.
- [27] S. Zhang, “Traveling-wave Electroabsorption Modulators,” Ph.D. dissertation, University of California, Santa Barbara, 1999.
- [28] H.-W. Chen, “High-Speed Hybrid Silicon Mach-Zehnder Modulator and Tunable Microwave Filter,” Ph.D. dissertation, University of California, Santa Barbara, 2011.

- [29] H. T. Chen, "Development of an 80 Gbit/s InP-based mach-zehnder modulator," Ph.D. dissertation, Technical University of Berlin, Berlin, 2007.

Chapter 4

InP based TWE Mach-Zehnder modulators at 1.55 μm

This chapter explains the modulator specific III-V material design, its validation procedure and testing of the fabricated InP based TWE Mach-Zehnder modulators (MZM). In Section 4.1, the design of MQW based materials suitable for InP based MZM and its characterization is discussed. The suitability of the material is tested through room temperature photoluminescence measurement and by measuring the electric field induced phase shift in specially fabricated test waveguide structures. Section 4.2 focuses on the importance of multimode interference (MMI) coupler design. Based on the high frequency design considerations discussed in Chapter 3, MZMs are fabricated and their performance was analyzed through general experimental techniques and explained in Section 4.3. These experimental techniques include DC and RF characterization. Firstly, the basic functionality of fabricated MZM devices is confirmed on bar level through static optical transfer function measurements. The working devices are then tested for small signal electrical and electro-optic response. The tested modulator devices exhibit an EO bandwidth of 7.5 GHz. It was found that small-signal bandwidth is mainly limited by the impedance mismatch which can be further improved by using n-i-p-n epitaxial layer structure explained in Chapter 6 of this thesis. The high frequency experimental results are validated by the simulation results. In the end, large signal modulation response of diced MZM is measured in optical C-band and clearly open eye diagrams were measured up to 28 Gb/s.

4.1 Material design and characterization

The realization of high speed InP MZM starts with the selection of most appropriate material layer structure to exploit electro-optic effects to achieve phase change through refractive index modulation under applied electric field. A high degree of design freedom is available in InP based semiconductor materials, which allows to achieve desirable modulator device performance through band gap engineering. As discussed in Chapter 2, the intrinsic core of the optical waveguide of an InP MZM is based on MQW epitaxy, where thin layers of narrow bandgap material are stacked between the high bandgap material in order to form periodic confinement regions i.e. potential wells for electrons and holes. Layers composition of MQW layers and thicknesses determine the overall absorption response of the modulator material. As opposed to an EAM, direct absorption is undesired in InP MZMs and the absorption band edge is designed to be 120-150 nm below the region of operation. The most desired wavelength range for the modulator operation is the optical C-band (1530-1570 nm), due to the lowest value of fiber attenuation in this window and availability of signal re-amplification through Erbium doped fiber amplifiers (EDFAs). It means that the absorption band edge for an InP MZM material should be engineered to be around 1370-1430 nm.

4.1.1 Modulator material design and structure

Table 4.1 shows the epitaxial layer structure grown to fabricate InP based MZMs for operation around 1550 nm. The epitaxial layer structure was grown using metalorganic vapour phase epitaxy (MOVPE) both on 2" semi-insulating (SI) (100) InP and an n-InP substrate. The optical waveguide structure is simply a separate confinement heterostructure (SCH), with MQW layers, InP cladding layers sandwiched between p and n-doped layers. The MQW and cladding layers were kept undoped to ensure low optical propagation loss through the waveguide. For MQW region, 20 periods of quantum wells of Aluminium (Al) based Quaternary material InAlGaAs were used. Traditionally, Phosphide (P) based Quaternary materials have also been widely used to develop high-speed InP modulators [1,2]. Both the materials show considerable flexibility in terms of bandgap and refractive indices and can be achieved in low defect density InP substrates. However, due to inherent large conduction band-offset in InAlGaAs $\Delta E_c = 0.72 \Delta E_g$ as compared to $\Delta E_c = 0.42 \Delta E_g$ in InGaAsP [3], former is used in this work. Higher conduction band offset leads to a better electron confine-

Table 4.1: Epitaxial layer structure grown (Sample: A-1593).

Material	Thickness (nm)	Doping (cm^{-3})	Conductivity (S/m)
P-InGaAs	20	1e19	69183
P-InGaAs	80	2e18	13864
P-InP	600	1e18	2403
P-InP	100	2e17	480
P-InGaAsP (ESL ¹) ($\lambda=1.1 \mu\text{m}$)	6	1e17	387
P-InP	130	1e17	240.3
i-InP	270	NUD ²	0
InAlGaAs (barrier) ($\lambda=0.97 \mu\text{m}$)	7	NUD	0
20 \times InAlGaAs (well, 0.43%compressive) ($\lambda=1.38 \mu\text{m}$)	9	NUD	0
20 \times InAlGaAs (barrier, 0.32%tensile)	7	NUD	0
i-InP	50	NUD	0
n-InP	1000	1e18	41152
SI/n-InP substrate	-	-	-

1-ESL Etch stop layer
2-Nominally undoped

ment in wells, resulting in sharper excitonic peak with low absorption under no bias around wavelength of operation [4].

Another important factor, which must be considered in the modulator material design is the biaxial strain. Since it is well known that biaxial strain in the wells changes the separation and coupling between the heavy-hole (HH) and light-hole (LH) excitonic transitions. HH absorption dominates the absorption edge if the quantum wells are compressively strained and LH absorption dominates in case of tensile strain. The transverse electric (TE) polarized light couples to HH and transverse magnetic (TM) couples to the LH and biaxial strain also affects the electro-optic properties of the MQW [5]. In order to produce a clear excitonic peak due to TE polarized light, compressive strain of 0.43 % was introduced in the wells. Also, to maintain the pseudo morphic growth, the compression strain in the well layer was balanced by a tensile strain of -0.325 % in the barrier layer to form a strain-balanced structure [6]. The thickness of barrier/well layer was chosen as 7/9 nm respectively. The calculated confinement of the optical mode within the MQW region is 54 % and it is designed

to to have a HH band edge at 1380 nm. Undoped cladding layers were used to keep the optical mode away from doped region. A thicker cladding layer of 270 nm was inserted towards P-side as compared to 50 nm InP layer towards n-contact layer as P-doped layers have 7-8 times higher contribution to optical loss as compared to same level doped n-layer [4]. The total intrinsic region thickness including cladding layers is 647 nm. The thickness of the intrinsic region is optimized for low optical loss, low V_π and characteristic impedance $> 30 \Omega$. To further minimize the optical loss due to overlap with any of the P-doped InP layer, P-doping was graded gradually from 10^{17} cm^{-3} to 10^{19} cm^{-3} towards the P-contact layer. Another reason to introduce graded doping is to reduce the diffusion of P-dopant Zinc (Zn) into the MQW region. To achieve low specific contact resistance, a highly doped 10^{19} cm^{-3} thin layer of $\text{In}_{0.53}\text{Ga}_{0.47}\text{As}$ is used to form an ohmic P-contact. The optical absorption of $\text{In}_{0.53}\text{Ga}_{0.47}\text{As}$ due to its smaller bandgap as compared MQW structure is not a concern as it is too far from the intrinsic region, which confines most of the optical mode.

4.1.2 Photoluminescence characterization

The layer compositions and uniformity of grown wafers was confirmed by room temperature photoluminescence (PL). PL is a very simple, versatile and nondestructive measurement technique. Fig 4.1 shows the measured PL map acquired for the epitaxial layer structure (shown in Table 4.1) grown on SI-InP substrate. The excitation source was continuous wave (CW) YLF laser emitting at 1047 nm and PL spectrum is measured using an InGaAs detector. The measurement was performed at the spatial resolution of 1 mm and spectral resolution of 1 nm. The average peak wavelength of the sample is around 1375 nm, which is well within the range of intended bandgap. The deviation of PL wavelength at the edge of wafer is due to nonuniform temperature distribution at the InP wafer edges during growth. The average full-width half maximum (FWHM) of the PL spectrum map is around 67 nm, which shows the good quality of wafer.

4.1.3 Modulation efficiency

To further determine the modulation efficiency due to electro-optic (EO) effect in the grown material, test structures were fabricated on epitaxy based on n-InP substrate. The quarter wafer was processed into ridge waveguides of different widths varying from 2 to 4 μm using lithography and $\text{Cl}_2/\text{CH}_4/\text{H}_2$ based inductively coupled plasma (ICP) etching. The ridges were then passivated,

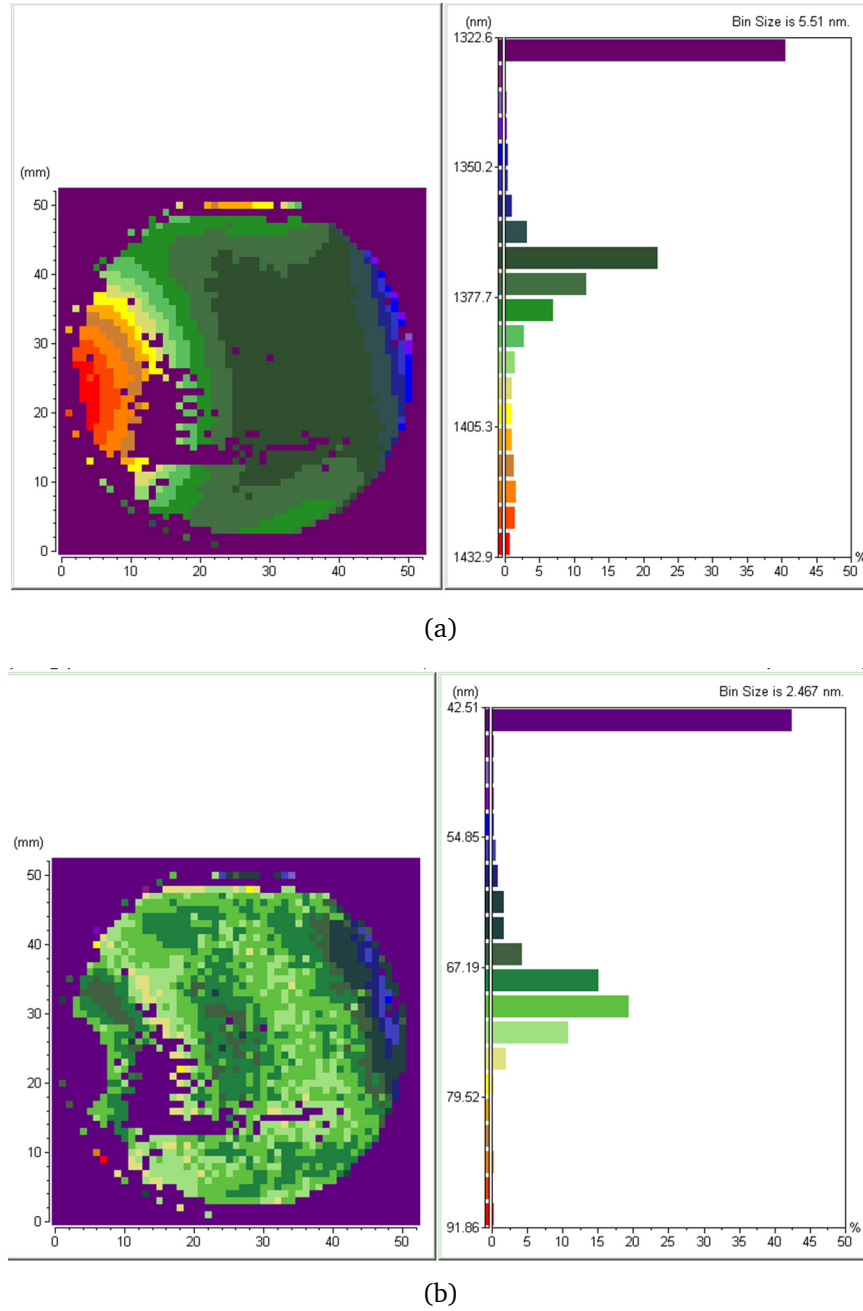


Figure 4.1: (a) PL wavelength map of the Sample A1593C. The wafer is orientated with major flat on the top.(b) FWHM map for different emission wavelengths across A1593C wafer.

metalized and cleaved into 1.5 mm long bars. The fabricated test ridges are shown in Fig 4.2. As discussed in Chapter 2, to maximize the refractive index change with the applied voltage, the test ridges are aligned along the $[01\bar{1}]$ axis. The measured leakage current in the fabricated ridges is less than 10 μA in the dark for all applied biases as shown in Fig 4.3, which is low enough not to induce any significant thermal EO effects. The material has a breakdown voltage

greater than than 16 V.

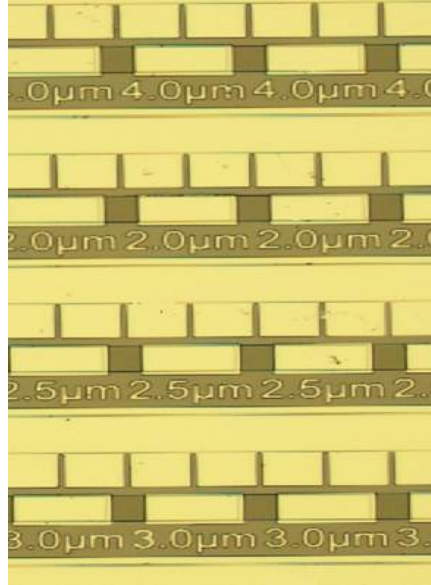


Figure 4.2: Image of fabricated test ridges with ridge widths varying from 2 μm to 4 μm . Both the P and n metal contacts are on the top.

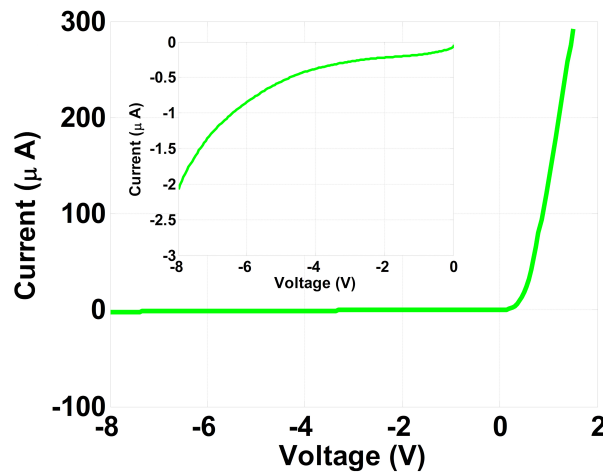


Figure 4.3: Current-voltage (IV) measurement for metalized 2.0 μm wide ridge waveguide. Inset shows the measured leakage current at the reverse bias of 8 V is 2 μA .

The optical transmission measurements were performed on the fabricated test structures by coupling light from a tunable laser source (81600B from Agilent) in to the waveguides using the polarization maintaining lens ended fibers. A polarization controller (PC) is added after laser in order to set the polarization state of interest i.e TE and TM at the facet of the input waveguide. The Fabry-Perot fringes are formed by the reflections from cleaved ends of waveguides and can be used to analyze the fringe contrast (K), phase change ($\Delta\phi$)

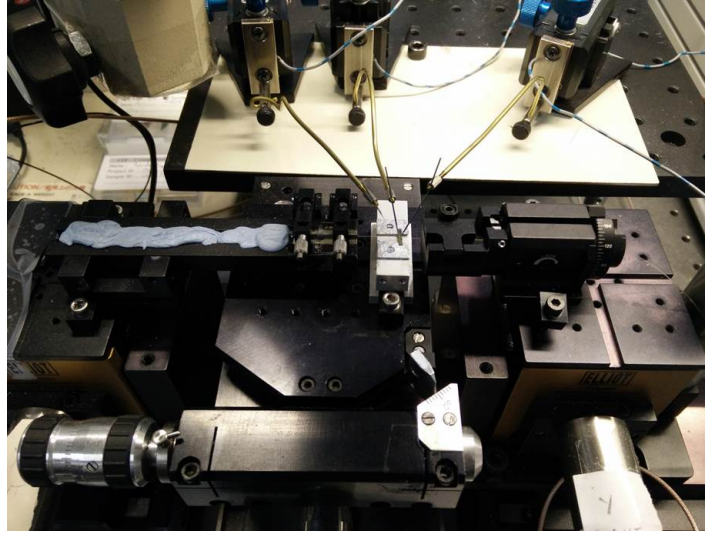


Figure 4.4: Experimental setup showing an optical waveguide device under test.

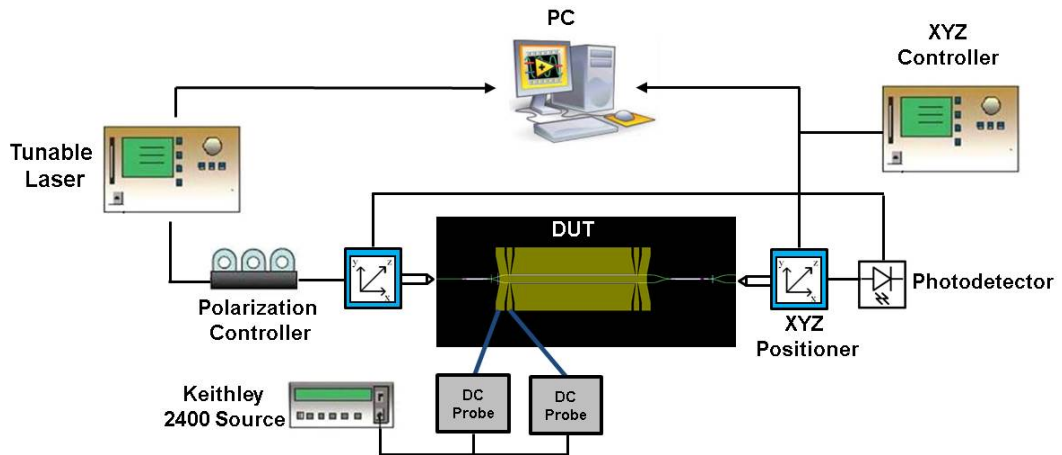


Figure 4.5: Schematic of the experimental setup. DC probes were used to apply voltage to the device. Lensed fibres were aligned precisely to the input and output waveguides of the device using XYZ controllers.

with applied reverse bias and optical group index (n_{opt}) for a given polarization state. Using the experimental setup shown in Fig 4.4, a Fabry-Perot spectrum for 1.5 mm long and 2.5 μm wide optical waveguide was measured over the wavelength span of 1440-1550 nm for both TE and TM polarizations with no applied bias. The recorded spectrum shown in Fig 4.6 is normalized to the input laser power to remove the effect of tunable laser power profile, which is not constant over the measured wavelength range. The main purpose of this measurement is to confirm the HH and LH splitting to the conduction band. The measurement shows that at shorter wavelengths closer to the band edge, TE transmission spectrum is majorly domination by band edge absorption due

to HH transition to the conduction band and TM spectrum has better fringe contrast as compared to TE polarized light due to low absorption. Away from band edge i.e. at wavelengths longer than 1500 nm, the spectrum for both polarizations will be dominated only by the intrinsic loss of the waveguide. Fig 4.7 shows the Fabry-Perot spectrum for TE polarized input light measured over a shorter wavelength span for the same dimensions of the optical waveguide, indicating a high fringe contrast.

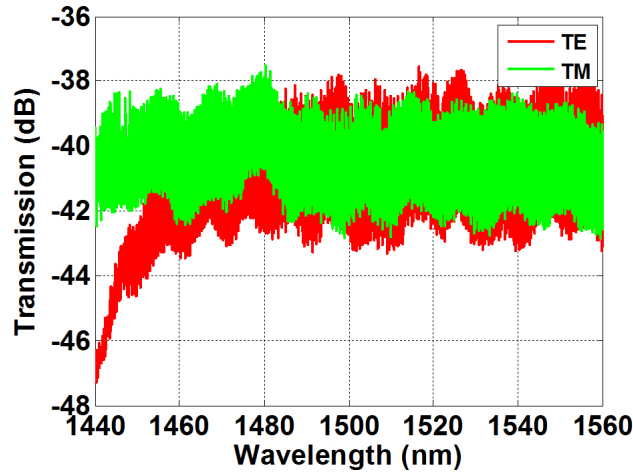


Figure 4.6: Measured TE and TM Fabry-Perot spectrum for ridge of 2.5 μm wide and 1.5 mm long ridge waveguide.

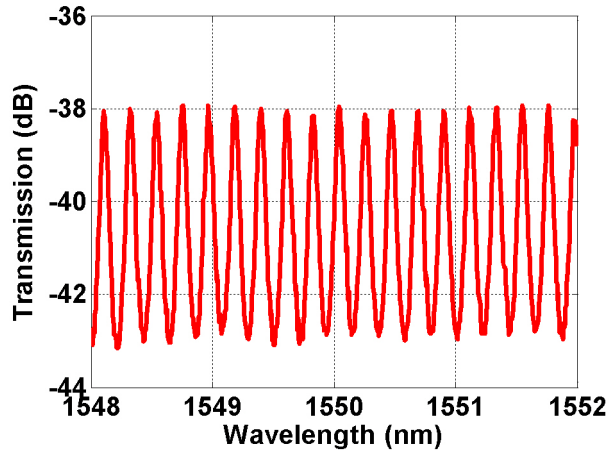


Figure 4.7: Measured TE polarized Fabry-Perot spectrum for ridge of 2.5 μm wide and 1.5 mm long ridge waveguide over a short wavelength span.

The fringe contrast of Fabry-Perot spectrum shown in Fig 4.7 can estimate the waveguide propagation loss using Eq 4.1 given in [7].

$$\ln(1 - \sqrt{1 - K^2}) = \ln(R) - \alpha L \quad (4.1)$$

where K is defined in Eq 4.2,

$$K = \frac{T_{max} - T_{min}}{T_{max} + T_{min}} \quad (4.2)$$

In Eq 4.1, R is the cleaved facet reflectivity, α is waveguide propagation loss coefficient, L is the length of waveguide. In Eq 4.2, T_{max} and T_{min} are the maximum and minimum transmitted optical power. Assuming facet reflectivity of R=0.32, gives the propagation loss 0.33 dB/mm for TE polarized light.

The optical group index (n_{opt}), is related to free spectral range (FSR) using Eq 4.3. FSR is basically the spacing in optical frequency (Δf) or wavelength ($\Delta\lambda$) between two adjacent Fabry-Perot fringes of an optical waveguide etalon.

$$\Delta f = \frac{c}{2n_{opt}L} \quad (4.3)$$

$$f = \frac{c}{\lambda} \quad (4.4)$$

By differentiating, Eq 4.4 with respect to λ ,

$$\Delta\lambda = \frac{\lambda^2}{2n_{opt}L} \quad (4.5)$$

Inserting Eq 4.5 in Eq 4.3, n_{gr} can be determined using Eq 4.6

$$n_{opt} = \frac{\lambda^2}{2\Delta\lambda L} \quad (4.6)$$

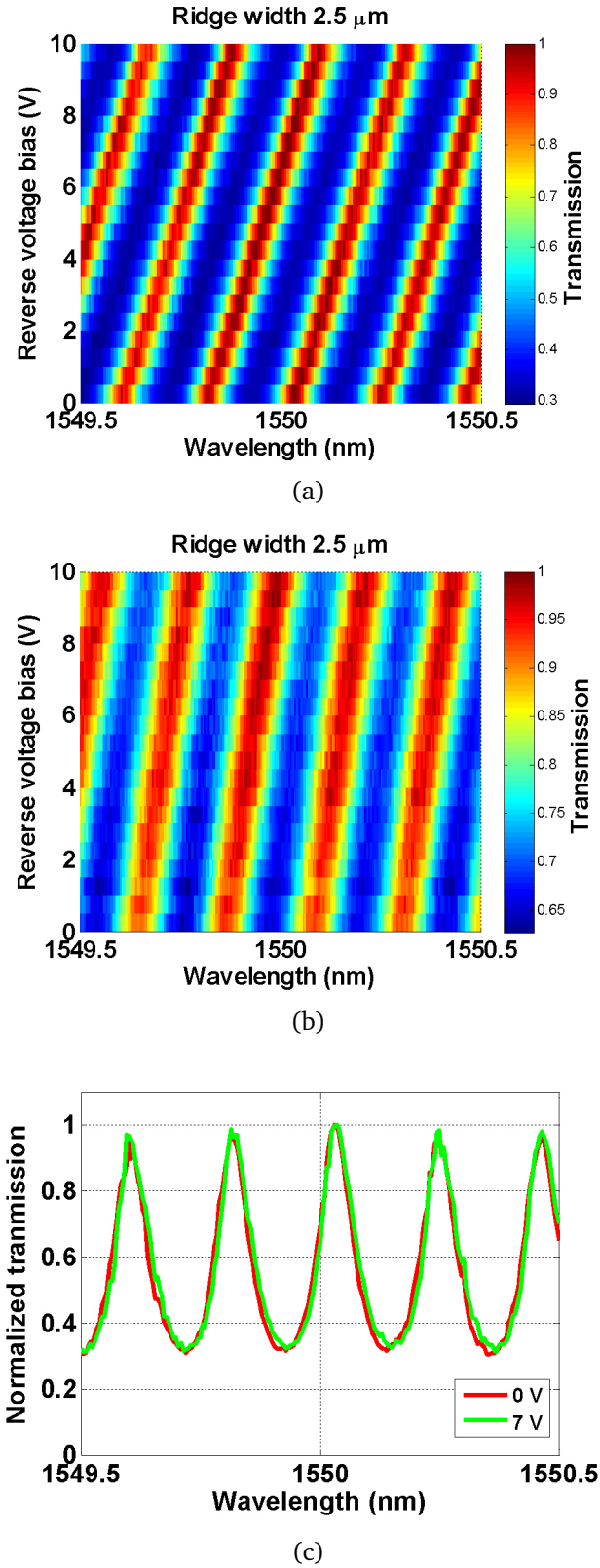


Figure 4.8: Measured fringe shift as a function of reverse bias for a 1.5 mm long waveguide and 2.5 μm wide ridge: (a) TE Polarization (b) TM Polarization (c) The TE Fabry-Perot fringes for reverse biases of 0 V and 7 V.

Using the Eq 4.6, n_{opt} can be extracted from the spectrum shown in Fig 4.7. The average $\Delta\lambda$ between two adjacent peaks is calculated to be 0.2205 nm. The calculated optical group index is 3.8 for TE polarized light. The phase shift ($\Delta\phi$) due to electro-optic effect in optical waveguide is given Eq 4.7.

$$\Delta\phi = \frac{2\pi\Delta nL}{\lambda} \quad (4.7)$$

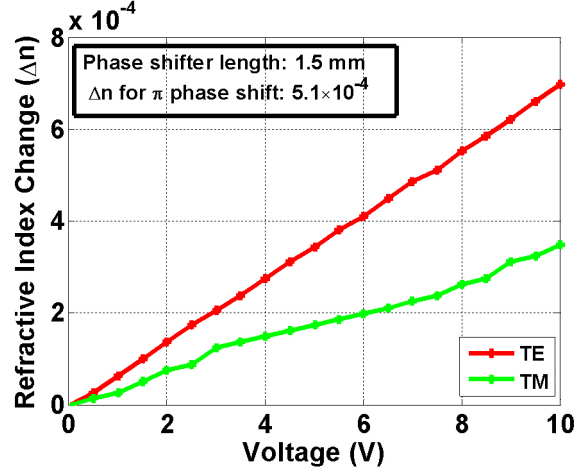
where Δn is the change in refractive index with applied voltage, λ is the wavelength of operation and L is length of waveguide. In Zinc blende semiconductors, the change in refractive index (Δn) is comprised of contributions from both linear (LEO) and quadratic electro-optic effect (QEO) for TE polarization and for TM optical mode QEO is the only contribution [8, 9]. The electro-optic shift is measured by analyzing the Fabry-Perot fringe shift with the applied voltage. The voltage at which the fringes get in phase with the reference spectrum at 0 V is the switching voltage V_π , which is the voltage required to get a π phase shift in one arm of MZM. The $\Delta\phi$ measured in this way can be compared to a push-pull phase shift in a MZM with two arm lengths equal to the length of phase electrode measured here [9]. It means that the measured $\Delta\phi$ for a given wavelength is twice the phase shift of Eq 4.7. The Fabry-Perot fringe shift with applied voltage for TE and TM polarized input light is shown in Fig 4.8a and 4.8b respectively. The measurements are performed at the voltage step of 0.5 V and wavelength step of 0.005 nm. From the experimental results, it can be seen that for 1.5 mm phase electrode, around 7 V is required to get the fringes back in phase to the reference fringe pattern at 0 V for TE orientation. For TM polarization V_π required is even higher than 10 V as compared to TE as expected due to compressive strain enhanced splitting of LH, HH transitions and also due to absence of LEO for TM. However, as the main aim of this work is to maximize the modulator performance for TE polarization as eventually they will be integrated with TE emitting InP-based lasers. The in phase fringe patterns at 0 and 7 V for TE polarized light are shown in Fig 4.8c. By rearranging Eq 4.7 and putting $\Delta\phi = \pi$, Δn required to achieve a π phase shift between two interferometric arms of MZM can be determined analytically.

$$\Delta n = \Delta\phi \frac{\lambda}{2\pi L} = \frac{\lambda}{2L} \quad (4.8)$$

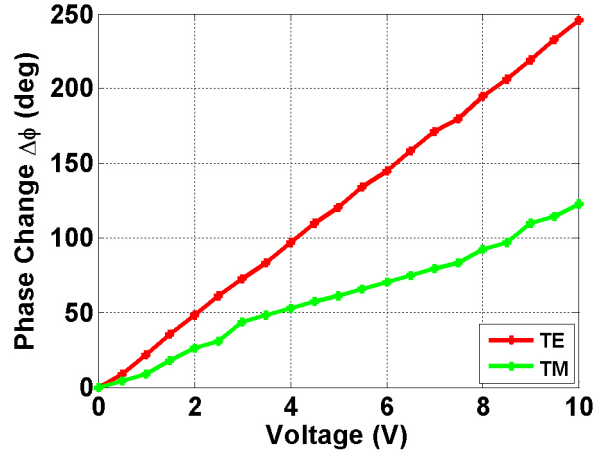
From Eq 4.8, Δn required to achieve a π phase shift for 1.5 mm phase shifting electrode is 5.1×10^{-4} . By measuring the shift of resonance peak versus the applied voltage, with respect to reference peak, the Δn can be extracted

from the measured Fabry-perot fringe pattern shown in Fig 4.8 using Eq 4.9,

$$\Delta n = \frac{\Delta \lambda_{shift}}{\lambda_{ref}} n \quad (4.9)$$



(a)



(b)

Figure 4.9: (a) Measured refractive index change with applied bias for TE and TM polarizations. (b) Measured phase change with applied bias based on refractive index change.

where $\Delta \lambda_{shift}$ is wavelength difference between the λ_{ref} and shifted wavelength, n is the refractive index. The extracted Δn and $\Delta \phi$ at 1550 nm from Fabry-Perot fringe shift with applied bias are shown in Fig 4.9a and 4.9b. It is evident that Δn (green curve) for TM polarization is much lower as compared to TE. It is due to the fact that LEO is not present for TM and refractive index change is only due to QEO. On the other hand, Δn due to TE polarization which

has contributions from both QEO and LEO is higher as compared to TM. Also, phase change of 180° is achieved when Δn is 5.1×10^{-4} as calculated before for phase shifter length of 1.5 mm. The phase change efficiency for TE and TM polarization is $27^\circ/\text{V}/\text{mm}$ and $12.2^\circ/\text{V}/\text{mm}$ respectively.

4.2 MMI coupler design and optimization

In the previous section, the suitability of the grown epitaxial material (Table 4.1) to realize an InP based MZM is discussed and verified through PL and applied field induced Fabry-perot fringe shift measurements. The next step in MZ modulator design is to arrange two phase shifting arms to form an interferometer for light switching operation through phase modulation by adding splitter/combiner at the input/output respectively.

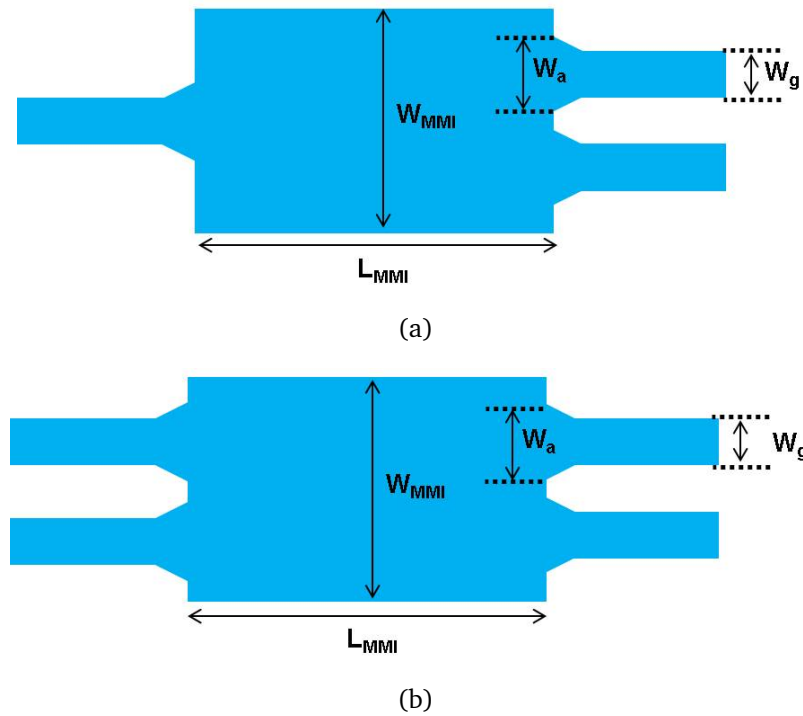


Figure 4.10: Schematic representation of (a) 1×2 MMI. (b) 2×2 MMI.

The design of an optical splitter and combiner is very critical to the key performance parameters of MZM such as optical insertion loss and the extinction ratio. Large extinction ratios for MZMs are only possible using MZ interferometer if the optical power in each arm is balanced. For the optimal function of light splitting/combining, multimode interference (MMI) couplers are considered as the most appropriate structures as they can split/combine op-

tical signals more compactly and efficiently as compared to y-branch and star couplers. MMIs are the integral part of the photonic integrated circuits (PICs) with major advantages of small footprint, better fabrication tolerances and wide wavelength operation [10].

In this work, 1×2 MMI is used at the input and serves as the power splitter for MZM. At the output, 2×2 combiner is used as the power combiner. The use of 2×2 MMI at the output allows further integration of photonic components such as semiconductor optical amplifiers (SOAs) [11,12] or photodetectors (PDs) allowing on chip performance monitoring of InP MZMs. Fig 4.10 shows the schematic representation of both splitter and combiner, where W_{MMI} is the width of MMI section, L_{MMI} is the length of MMI section, W_a is the width of MMI access waveguide and W_g is the width of input waveguide.

A separate lithographic mask was designed to select the optimum MMI dimensions best suited to the grown epitaxial structure. In MMI mask, the ratio of W_a/W_{MMI} was kept as 0.25 (for 1×2 MMI) and as 0.27 (for 2×2 MMI) for both the input/output in order to minimize the excess losses and imbalance between the output arms [13,14]. W_{MMI} was chosen as 13 μm and 14 μm for 1×2 and 2×2 MMI couplers respectively. Keeping the W_{MMI} constant, the length of the MMI section was varied on mask. The initial values of the L_{MMI} and W_{MMI} were chosen by performing basic simulations in FIMMWAVE simulation software by Photon Design Inc. The inbuilt material database was used to define the refractive indices for the material layer stack shown in Table 4.1. In actual material growth, there are always slight variations in the material compositions and designated thicknesses which can lead to deviation of devices from intended performance. Because of this reason, simulations were only used to get the basic MMI parameters and based on them a mask was designed having both 1×2 and 2×2 MMIs with different length of MMI sections. The devices were fabricated on the epitaxial material (A1593- Table 4.1) using the standard lithography and $\text{Cl}_2/\text{CH}_4/\text{H}_2$ ICP etching. Both the MMI section and input/output waveguides were deeply etched through the MQW layer in order to maximize the lateral confinement. It also eliminates uncertainties in index contrast and effective waveguide widths due to etch-depth tolerances [13,15].

The microscopic image of the fabricated MMI devices is shown in Fig 4.11. The s-bends were introduced to increase the separation between MMI output waveguides to 100 μm to make the devices compatible for standard lensed fiber testing. In addition, these s-bands also give an offset to the MMI outputs with respect to the input waveguide. This offset was to ensure that light collected at

the output is only through the MMI waveguides. The fabricated devices were cleaved and then tested using the same fiber coupled setup shown in Fig 4.4 at the wavelength of 1550 nm for TE polarized input light. The experimentally measured MMI dimensions with maximum coupling efficiency are summarized in Table 4.2. Also, in Fig 4.12, the trend of the coupling loss with deviation from optimum L_{MMI} of both 1×2 and 2×2 MMIs is shown. From the measurement results, it is clear that the coupling losses increase for any positive/negative deviations from the optimum length of the MMI sections. It also shows that 2×2 MMIs are more tolerant to fabrication errors as compared to 1×2 MMIs. The coupling loss for a 2×2 MMI is -1.8 dB for +40 μm deviation from the optimum length. Whereas, for 1×2 MMI the coupling loss reaches -3 dB even for half of this variation i.e. $\pm 20 \mu\text{m}$.

Table 4.2: Optimized MMI dimensions (Sample: A-1593 see Table 4.1).

MMI Type	W_{MMI} (μm)	L_{MMI} (μm)	W_a (μm)
1×2	13	188	3.5
2×2	14	288	3.5

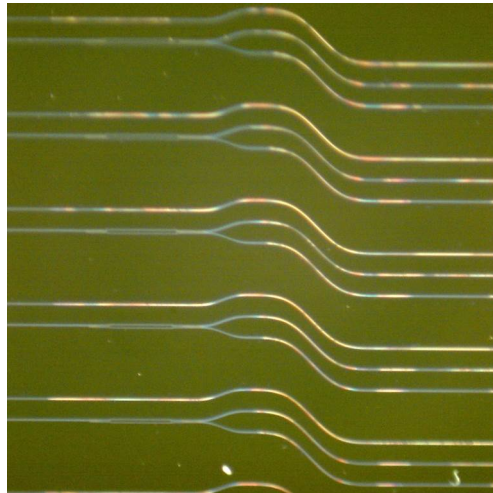


Figure 4.11: Microscopic image fabricated 2×2 MMI devices with variations in length of an MMI sections.

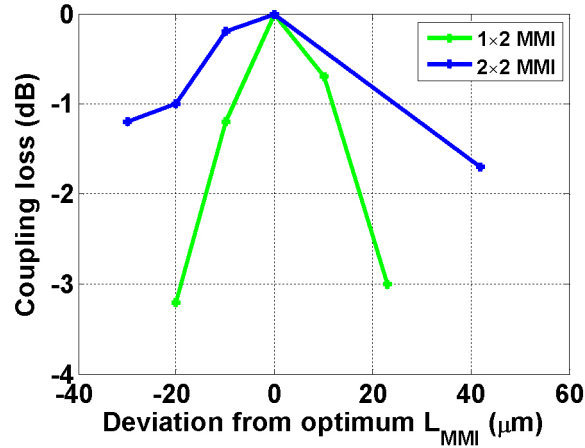
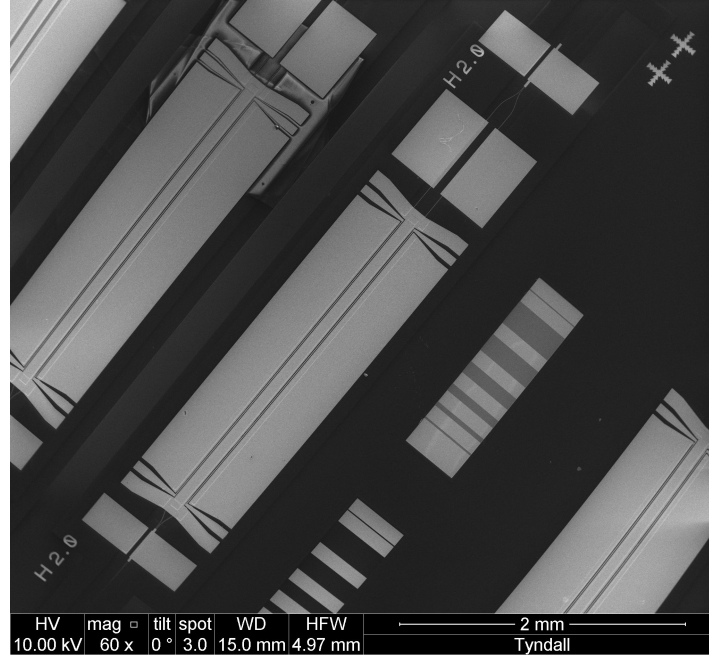


Figure 4.12: Trend of coupling loss with deviation from the measured optimum MMI length.

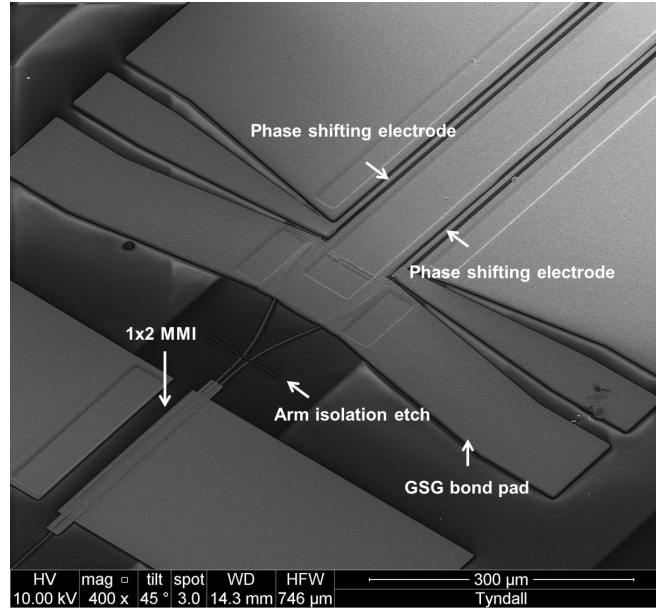
4.3 Modulator characterization

After selecting the most suitable MMI dimensions for combing and splitting operations, full MZM structures were fabricated on the SI-InP based A1593 material. The SEM image of array of fabricated InP based MZM devices is shown in Fig 4.13a. The important features of a single MZM device are highlighted in the scaled up image shown in Fig 4.13b. The chip is comprised of 1×2 MMI coupler at input and 2×2 MMI at the output connected by equal length phase shifters. The CPW GSG bond pads were fabricated on planarized BCB to access the devices through standard microwave/DC probes. BCB planarization helps to reduce the parasitic capacitance of the feed-in paths of the phase shifting electrodes and also provides additional passivation to the optical waveguide. Similar GSG bondpads and traveling wave electrodes (TWEs) were fabricated on both the arms of the MZ interferometer to enable testing of devices in push-pull mode. Dimensions of GSG bond pads were optimized using High Frequency Structural Simulator (HFSS) by ANSYS. The phase shifting electrode dimensions were selected based on the electrode design optimization procedure discussed in detail in the previous chapter. The fabricated devices have phase shifting electrodes of lengths 1.5 mm and 2.5 mm. The electrodes were electroplated to 2 μm of gold (Au) to avoid skin-depth losses. To maximize both the RF and optical performance of the modulator devices, the width of the optical waveguides for the phase shifting sections were selected as 2 μm and 2.5 μm . The effect of ridge width on electrical and optical performance is already discussed in Chapter 3 (See Fig 3.18). The width of the signal electrode

on the top of ridge was kept slightly wider than the final ridge widths and was selected as 2.5 μm and 3 μm respectively for the ease of fabrication. The total size of a single MZM device is 1.5 mm \times 7 mm.



(a)



(b)

Figure 4.13: (a) SEM image of fabricated array of InP based MZM devices. (b) Scaled up image of fabricated MZM device.

4.3.1 DC characterization

The fabricated modulators were tested in three stages which are: first the DC characterization was performed, then RF small-signal characterization and lastly electro-optic (EO) bandwidth and large signal optical response was measured.

Before performing optical transmission experiment, the IV characteristics of all the fabricated MZM devices were measured. The leakage current measured at the reverse bias of -10 V was less than 1 μA for most of the devices. An example of measured IV curves for two arms of fabricated modulator device is given in Fig 4.14. Low leakage current is an indication of a good side wall passivation during fabrication process. It also ensures that the applied electric field is across the MQW region of the optical waveguide and there are no extra resistive paths along the optical waveguide. Low leakage current also enhances the break down voltage of devices under reverse bias, thus increasing the modulator device long term reliability [12].

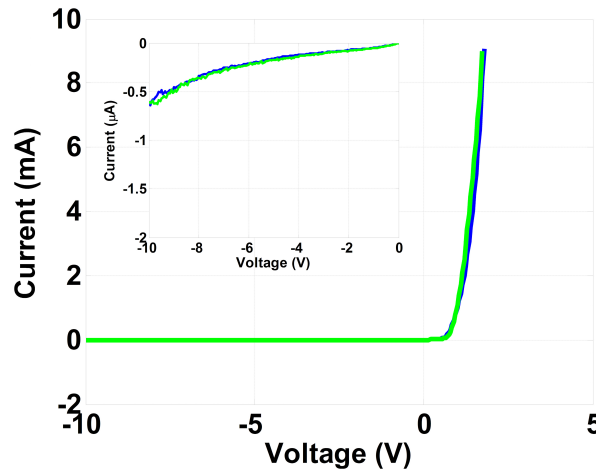


Figure 4.14: IV characteristics of fabricated MZM devices. Inset shows the measured leakage current at the reverse bias of 10 V is less than 1 μA .

The DC extinction characteristics of the fabricated MZM devices were measured using the same setup shown in Fig 4.5. An optical signal of 5 dBm from a tunable laser source was coupled in to the MZM using a lensed fiber and collected using the same type of lensed fiber. The optical coupling to the modulator device was optimized using the XYZ piezoelectric stages at both the input and output of the devices. The polarization was precisely set to TE using polarization controller. Fig 4.15 shows the measured DC transmission response of the MZM devices with the electrode length of 1.5 mm (Fig 4.15a) and 2.5 mm (Fig

4.15b) at the wavelength of 1550 nm for both the outputs of 2×2 MMI coupler. For these measurements, only a single arm of MZM was biased, while the other arm was kept at 0 V, this arrangement is called single electrode operation. The device with 1.5 mm phase shifting electrode shows an extinction ratio (ER) of 20 dB and V_π of 7 V, which is same as measured using Fabry-Perot fringe shift. Also, there is a slight imbalance between two arms of the measured device. For device with electrode length of 2.5 mm, V_π decreases to 4.5 V as expected but ER drops down to 15 dB. The measured devices exhibit fiber-to-fiber insertion loss of 12-14 dB measuring from the maximum of MZM transfer function which can be further reduced by atleast ~ 2 dB per facet using anti-reflective (AR) coating at the input and output facets.

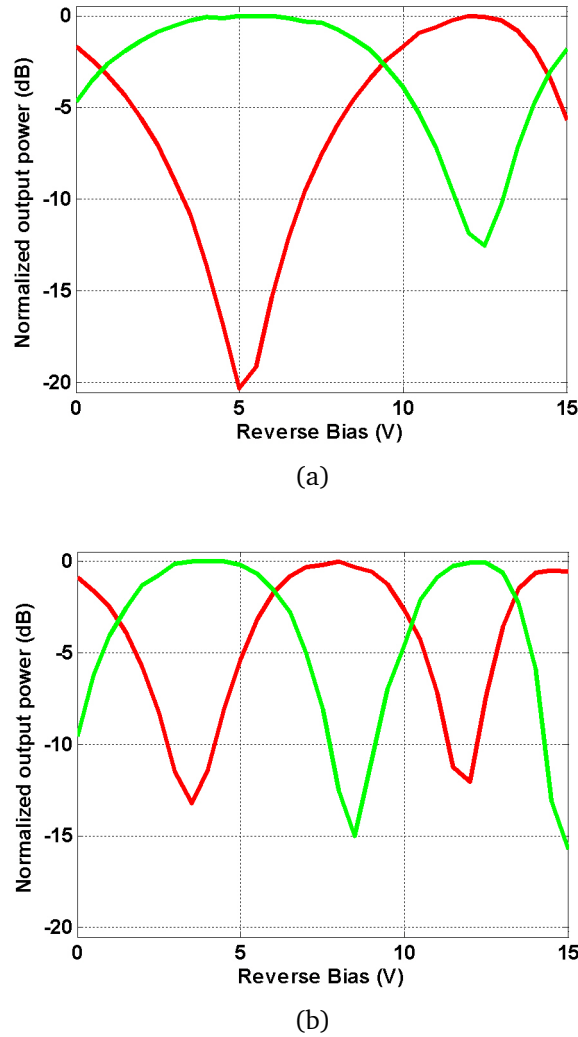


Figure 4.15: Normalized optical transmission characteristics for TE polarized input light for: (a) MZM with 1.5 mm electrode length at 1550 nm. (b) MZM with 2.5 mm electrode length at 1550 nm.

Fig 4.16 shows the dependence of ER and V_π on input wavelengths for TE polarization. Decreasing input wavelength from 1550 nm to 1520 nm improves V_π slightly from 7 to 5.3 V. Also, the transfer function becomes marginally asymmetric at the lower wavelengths. The ER remains between 17 dB to 20 dB over the wavelength range. The slight improvement in V_π is mainly due to decrease in bandgap detuning. It also validates the fact that closer the operating wavelength is to the band edge higher is the refractive index change resulting in lower V_π but at the expense of voltage induced induced absorption. However, in this case, the wavelength dependence of V_π and ER is rather low, which means that the signal wavelength is still far from enough from the waveguide absorption band edge and optical transmission is not degraded drastically by absorption.

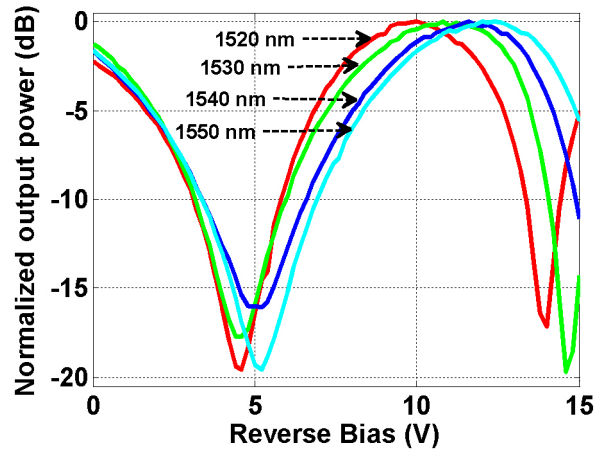


Figure 4.16: Normalized optical transfer function for MZM with 1.5 mm electrode for different input wavelengths for TE polarization.

4.3.2 Electrical small-signal characterization

The high frequency characterization of the fabricated MZM devices starts by first investigating the electrical small-signal response. The small-signal measurement setup is shown schematically in Fig 4.17. On-wafer small signal measurements were performed using two ACP-GSG-40 probes from Cascade Microtech and an Anritsu 37397D Vector Network Analyzer (VNA). To move the reference measurement plane to the probe tips, standard Short-Open-Load-Thru (SOLT) on-wafer calibration has been performed using an on-wafer calibration substrate by Cascade Microtech.

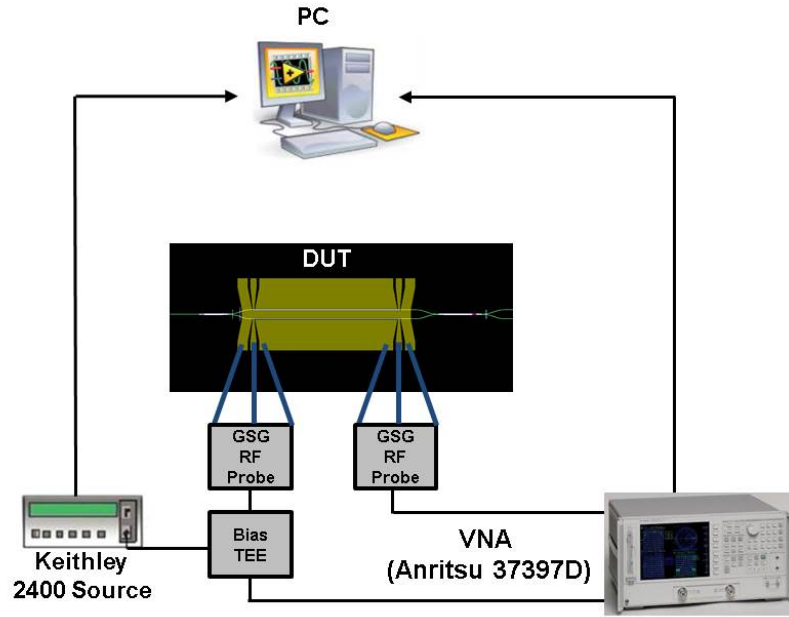


Figure 4.17: Schematic of high frequency measurement setup.

Electrical small signal measurements and their comparison with the simulation results are shown in Fig 4.18. It can be clearly seen that the experimental results agree very well with the simulation model. The measurements were performed for fabricated MZM devices both with 1.5 mm and 2.5 mm TWE. For MZM with 1.5 mm TWE, a 3-dB electrical bandwidth of almost 19 GHz was measured. As expected, for MZM with longer TWE of 2.5 mm, the measured 3-dB electrical bandwidth is 10 GHz. The lower bandwidth for device with longer electrode is due to higher interaction with the doped semiconductors and metal electrode resulting in higher microwave loss. Measured electrical S_{11} less than -9 dB shows that device will perform well if properly terminated in 50 Ω environment. Both the structures were also simulated in HFSS by importing the TWE metal patterns from the fabrication mask design file to simulate as close as possible to the actual fabricated devices. The optical ridge structure was defined manually. The properties of the semiconductor layers in HFSS are defined in terms of bulk conductivity (σ), relative permittivity (ϵ_r) and relative permeability (μ_r). The value of μ_r for all the materials is set as 1 in all simulations except for air ($\mu_r=1.0000004$) and gold ($\mu_r=0.99996$), these values are predefined in material database by HFSS. The TWE losses in the MZ modulator design are strongly dependent on the value of bulk material conductivity and must be very carefully included in the simulation model. The effect of different parameters of material layer structure on TWE RF performance has already been discussed thoroughly in Chapter 3. The calculated σ for each semiconduc-

tor layer are also given in Table 4.1. The formulas for conductivity calculation are given in Appendix A. As the TWE dimensions on both the interferometric arms of MZM are same, so only a single TWE structure is simulated in HFSS. The effect of the contact resistance (R_{pc}) must be included in the simulation model to achieve much more realistic results (See Section 3.7). In all the simulations performed, specific contact resistance ($\rho_{spec,p}$) value of $3 \times 10^{-5} \Omega.cm^2$ is used for the p-contact. The HFSS simulation model is shown in Fig 4.19. Fig 4.19c, shows the model of GSG bond pads connected back to back. The simulated microwave loss due to bondpads is less than 0.35 dB at 30 GHz.

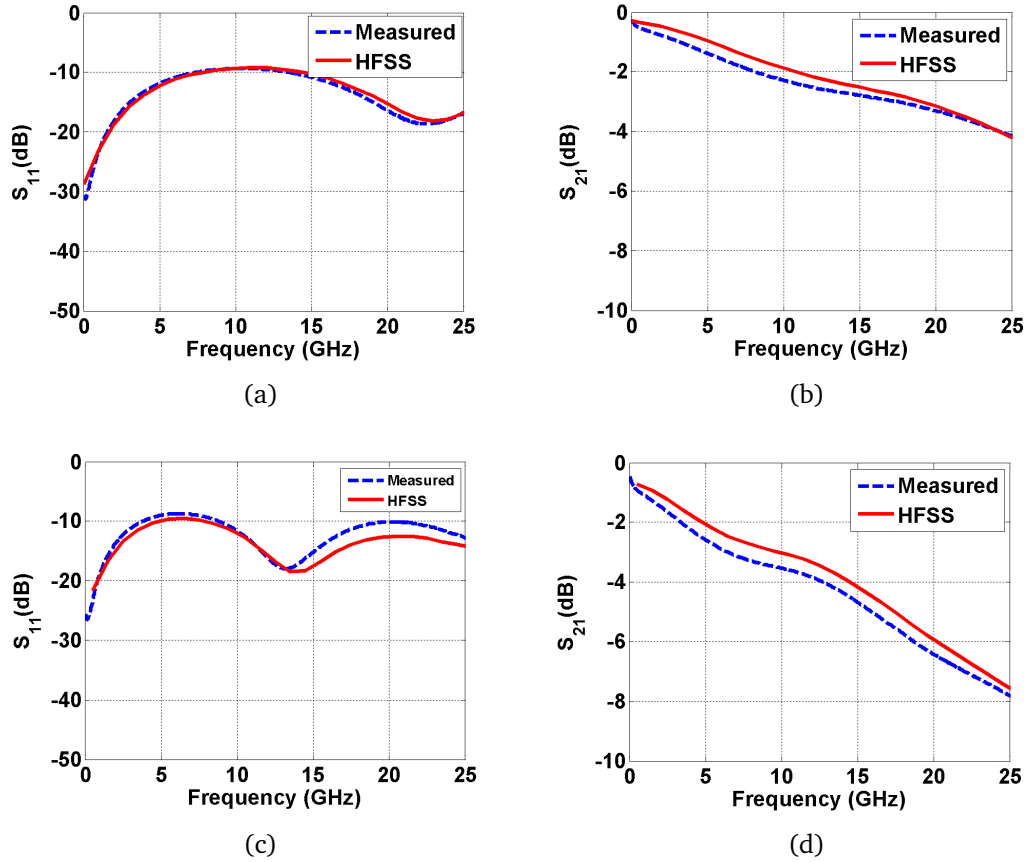


Figure 4.18: Small-signal measurement results for MZM with different TWE lengths. Solids line represent HFSS simulation results: (a) Electrical S_{11} (1.5 mm). (b) Electrical S_{21} (1.5 mm). (c) Electrical S_{11} (2.5 mm). (d) Electrical S_{21} (2.5 mm).

The measured S-parameters can be further used to extract electrical properties of the lossy CPW transmission only excluding the effect the feed-in GSG bond pads. To remove the effect of GSG bondpads, measured S-Parameters of two MZM structures with different lengths of TWEs are used [16]. This procedure is valid only if measured S-parameters of devices are symmetric i.e

$S_{11}=S_{22}$ and $S_{21}=S_{12}$. If this is true then it works well in the desired frequency range. The measured S-parameters can be converted into T-matrix using formulas given in Eq 3.31 (Chapter 3). The pad de-embedding procedure is given in Eq 4.10.

$$T_{long-short} = T_{long}T_{short}^{-1} \quad (4.10)$$

where T_{long} is the T-matrix for device with 2.5 mm TWE and where T_{short} is the T-matrix for device with 1.5 mm TWE. $T_{long-short}$ is the extracted T-matrix of 1 mm transmission line only. The ABCD transmission matrix can then be used to determine different transmission line parameters such as device impedance (Z), microwave loss (α) and microwave index (n_μ) using Eq 4.11-4.13. The conversion from S-parameters to ABCD transmission matrix is given in Appendix B.

$$Z_{mod} = \sqrt{\frac{B}{C}} \quad (4.11)$$

$$\gamma = \alpha + i\beta = \ln \left[\frac{\frac{A+D}{2} + BC}{L} \right] \quad (4.12)$$

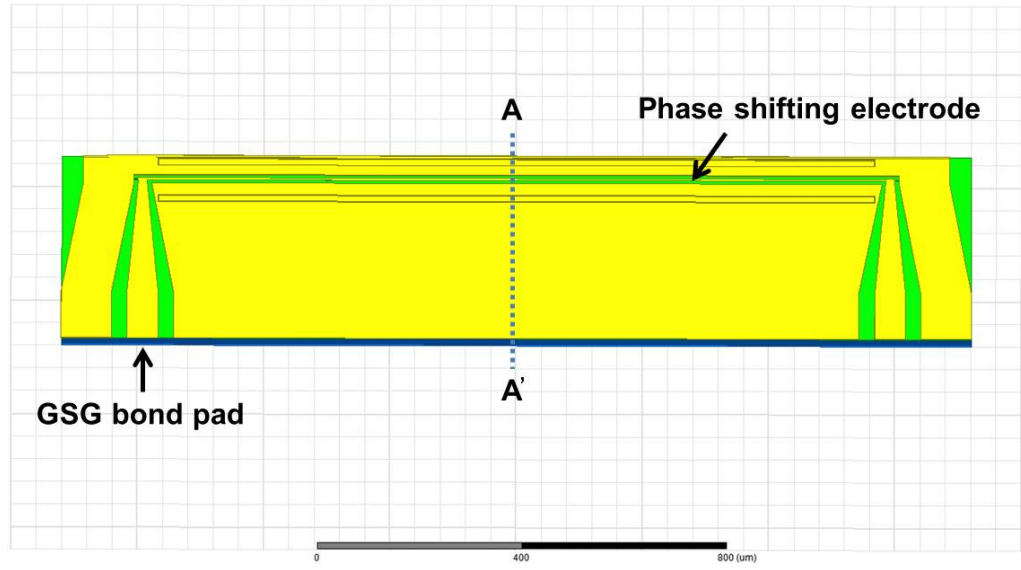
where L is the length of transmission line. The microwave index can be calculated as a function of frequency using Eq 4.13,

$$n_\mu = \frac{\phi(f) \cdot c}{2\pi f L} \quad (4.13)$$

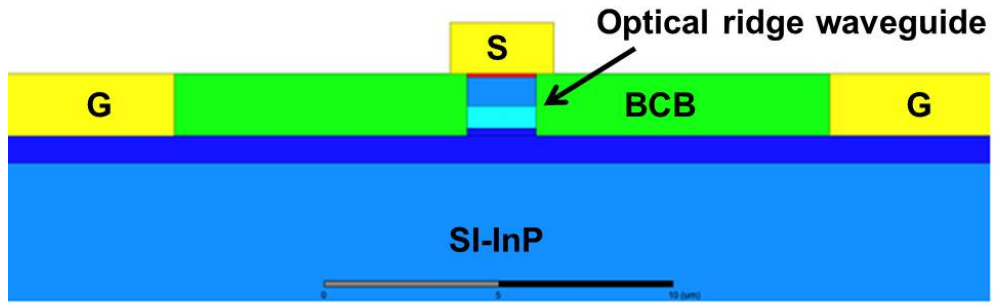
where $\phi(f)$ is accumulated phase delay of S_{21} in radians.

The extracted properties are given in Fig 4.20 and are compared with the properties extracted using HFSS simulations. The extracted device impedance is around 35 Ω and agrees closely with the simulation results. The measured microwave loss is 3.25 dB/mm at 25 GHz, whereas simulation results give 3.02 dB/mm loss value which is in close agreement with the measurement and the difference is negligible. Another important factor is the microwave index (n_μ), which should ideally be as close as possible to the optical group index, in order to achieve velocity matching between propagating optical and electrical waves. The measured value of n_μ at 20 GHz is 3.825 which is very close to the measured optical group index (n_{opt}) of 3.8, the simulation results show higher index value of 4.2 at 20 GHz. Minor deviation of extracted parameters from simulation results may be due to the roughness of the TWE metal due to patterning of BCB during curing process and also the designed doping levels can change

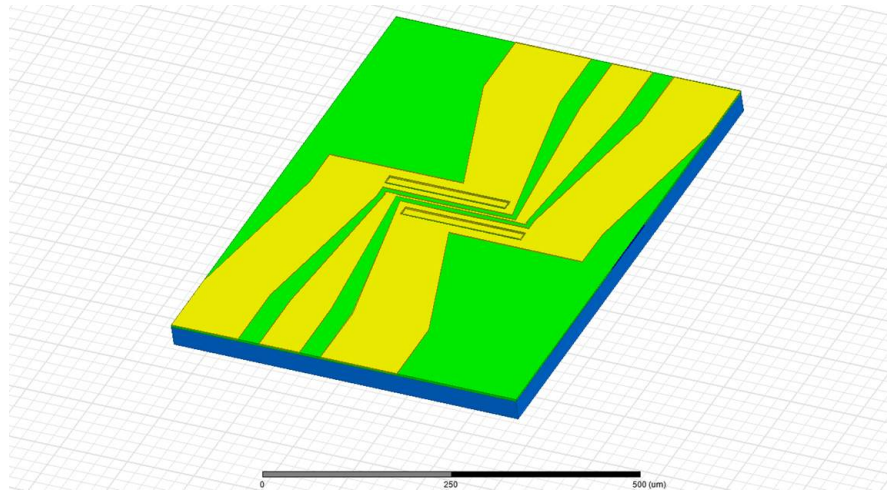
during growth which may lead to a change in depletion width. Another cause can be lack of reliable material parameters at RF frequencies. In addition, the ridge profile and etch depth variation can be another cause of slight deviation of results. However, generally, the measurement results are within 10% of the simulation results obtained using HFSS and equivalent circuit model presented in Chapter 3 over the frequency range of interest.



(a)



(b)



(c)

Figure 4.19: (a) Top view of the simulated CPW TWE structure in HFSS. (b) Cross section of the simulated CPW TWE structure (along A-A'). (c) HFSS model of G-S-G bondpads connected back to back.

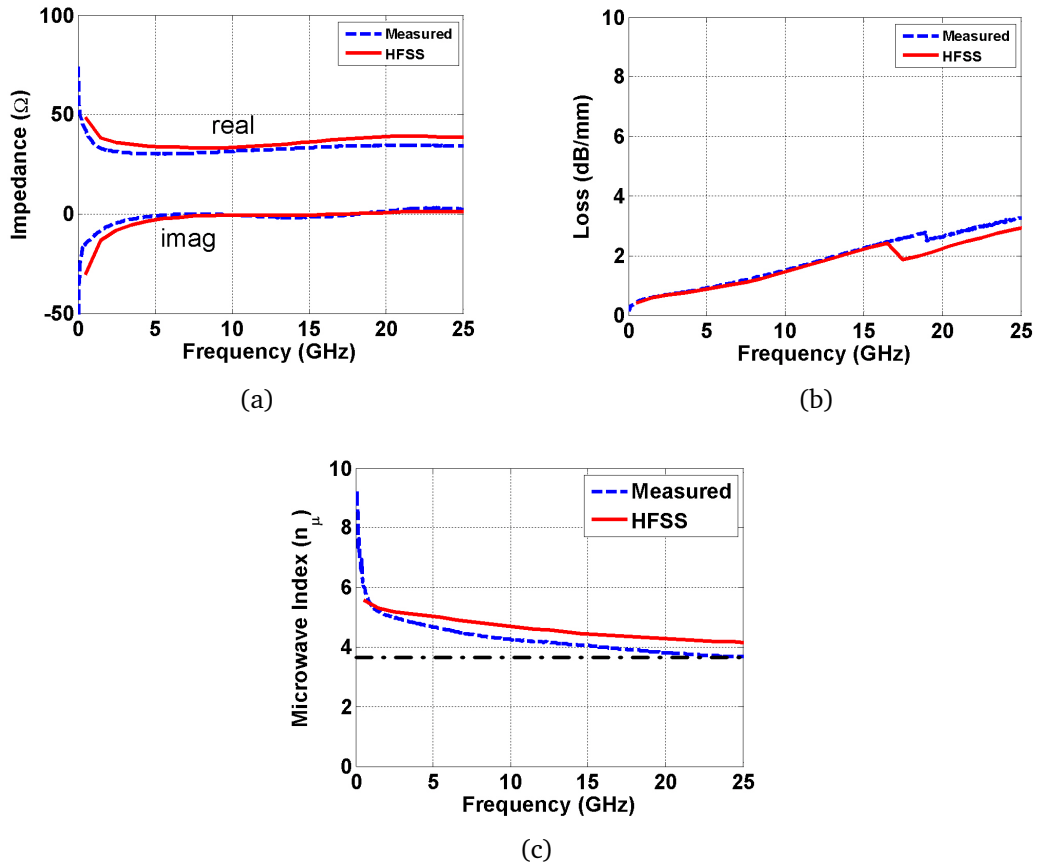


Figure 4.20: Extracted transmission line parameters: (a) Characteristic impedance. (b) Microwave loss. (c) Microwave index. Black dotted line represents the optical group index ($n_{opt}=3.8$).

4.3.3 Electro-optic response

The experimental setup to measure the electro-optic (EO) response of fabricated MZM devices is shown in Fig 4.22. The measurements were performed from 40 MHz up to a frequency of 15 GHz using two ACP-GSG-40 probes from Cascade Microtech and an Anritsu 37397D VNA. The electrical signal was fed into the modulator using GSG probe at the input GSG pad with the output GSG pad terminated through 50 Ω . The EO response was measured at electrical signal power of -7 dBm from VNA. The input optical power to the modulator was 0 dBm from a tunable laser source at 1550 nm and input polarization was set to TE using a PC. The optical signal was delivered using polarization maintaining lens ended fiber and output was collected using the same type of fiber. To compensate for the insertion loss of the modulator device, the output modulated signal was amplified optically using an EDFA followed by a 1.5 nm wide tunable optical filter to remove amplified spontaneous emission (ASE) noise from

the EDFA. The modulated optical was measured by a DC-coupled photodetector (U²T XPDV2320R, 3-dB bandwidth 50 GHz). Such mixed probe/connectors measurements required a two-tier RF calibration, which was performed using Wincal XE software by Cascade Microtech [17]. Before the final measurement of modulator EO-response, the modulator bias was adjusted to the quadrature working point of the modulator transfer function. In addition, the input polarization was also adjusted to achieve the maximum modulation response at 1 GHz. The quadrature operating point in modulator transfer function has the maximum slope and gives the highest response under small-signal modulation. The measured EO-response for the MZM device with a 1.5 mm TWE is shown in Fig 4.21 at -2.27 V reverse bias. Experimentally, measured 3-dB EO S21 bandwidth is 7.5 GHz with a linear roll-off, which is sufficient for at least 10 Gb/s data modulation. The measured EO response follows the the simulated response very closely, which predicts a 3-dB bandwidth of 8.5 GHz. The small offset between the measured and simulated modulation response may be due the reflections from cleaved facets, which can result in counter propagating optical waves lowering the modulation efficiency. The simulated EO response is calculated using Eq 3.5 in Chapter 3 and takes into account only the co-propagation of electrical and optical waves in a TWE.

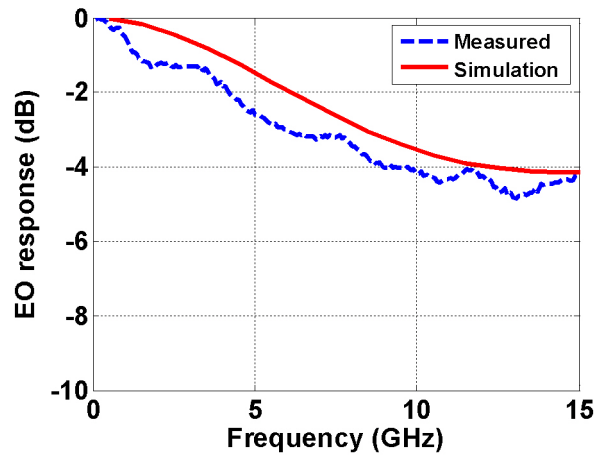


Figure 4.21: Measured EO response of InP MZM with 1.5 mm TWE.

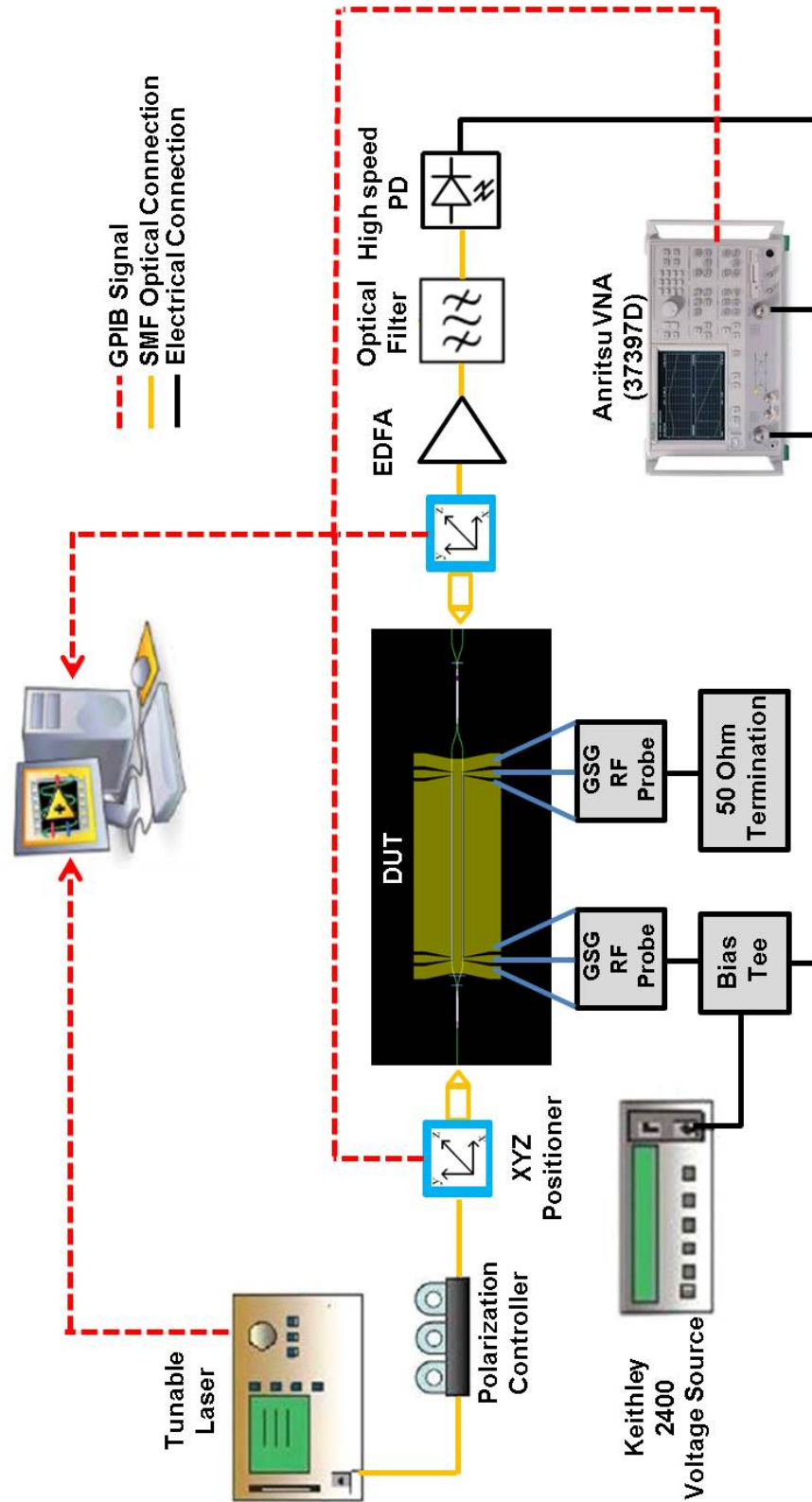


Figure 4.22: EO response measurement setup.

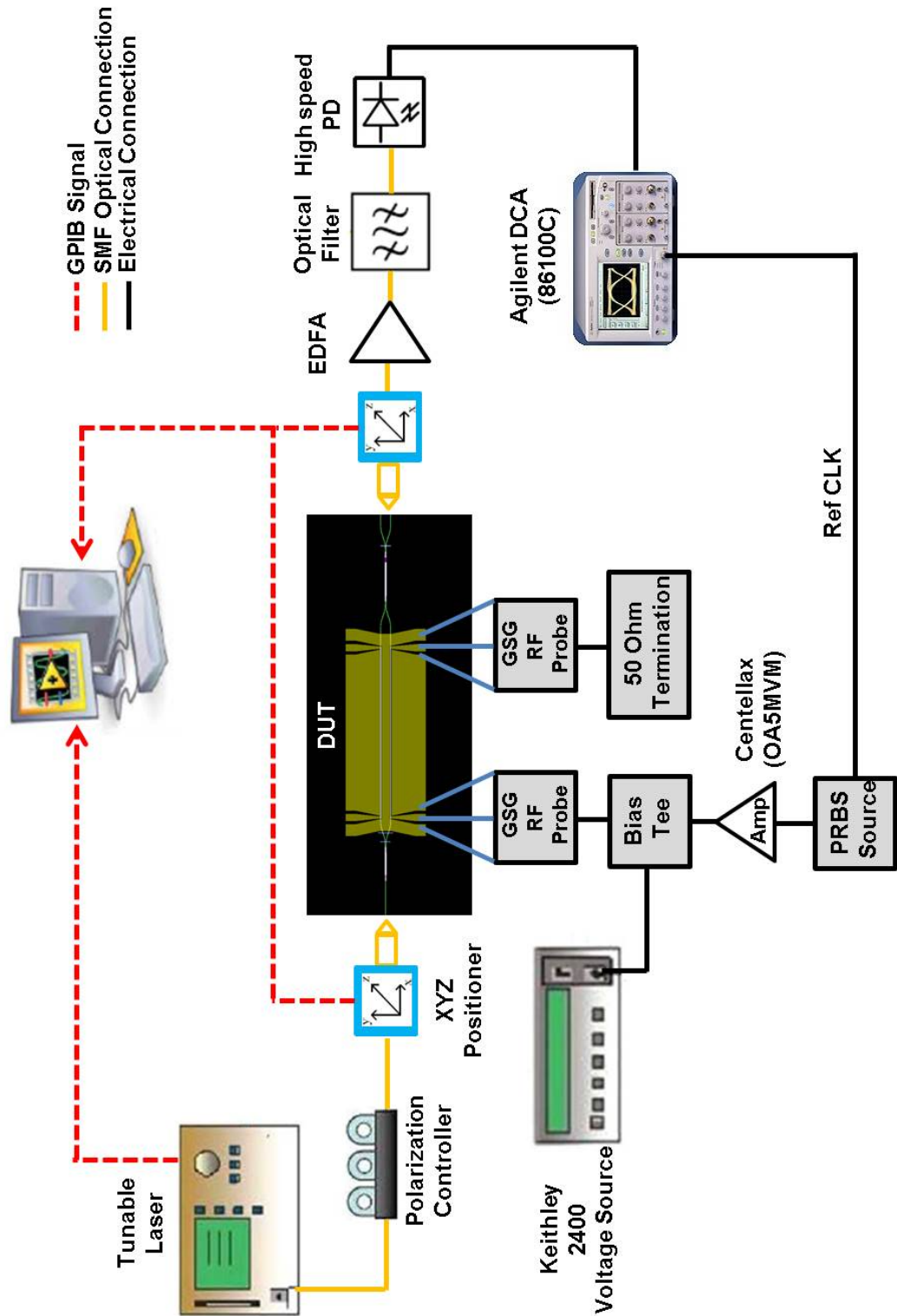
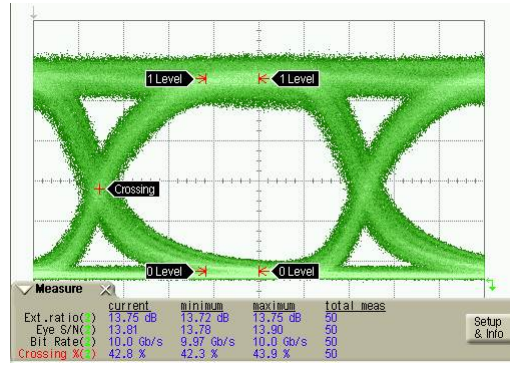
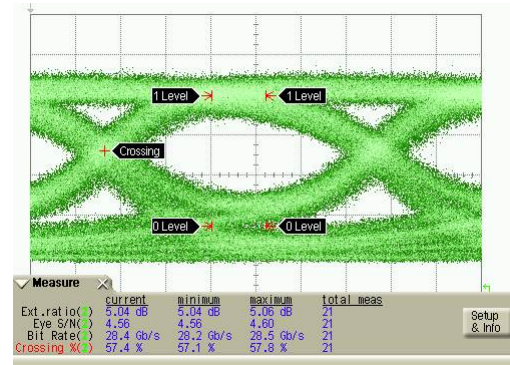


Figure 4.23: Large signal response measurement setup.



(a)



(b)

Figure 4.24: Large signal modulation response at 1550 nm: (a) 10 Gb/s. (b) 28 Gb/s.

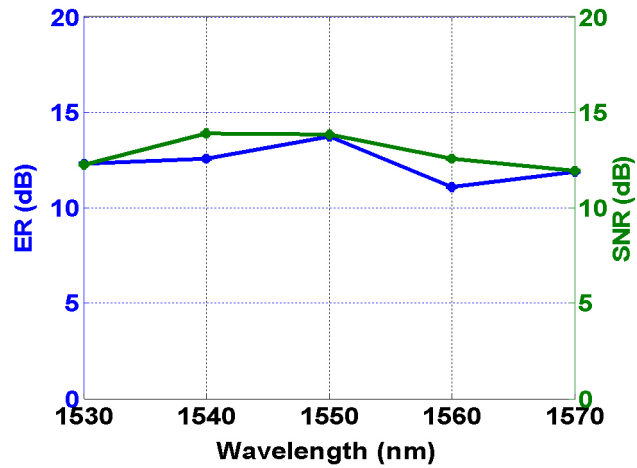


Figure 4.25: Measured ER and SNR for 10 Gb/s NRZ eye.

After measuring the small-signal EO response, the modulator devices were tested for large signal modulation response. The experimental setup is shown in Fig 4.23. A 10 Gb/s non-return to zero (NRZ) pseudo-random binary sequence (PRBS) of length 2^7-1 drive signal was provided by the pseudo-random

bit sequence (PRBS) generator by Centellax TG2P1A PRBS source. The source provides only 250 mV peak to peak signal which was then amplified to $\sim 6.6 V_{p-p}$ using a Centellax (OA5MVM) 40 Gb/s driver amplifier. The electrical signal was fed into MZM using the same probing arrangement explained before. The modulated optical signal was amplified and filtered before photodetector. The resulting eye diagram after photodetector was measured using an Agilent 86100C digital communication analyzer (DCA). Fig 4.24a shows the measured eye diagram at the input signal wavelength of 1550 nm for 10 Gb/s NRZ signal. The same MZM device used for the measurement of EO response was tested for large signal modulation. The measured dynamic extinction ratio for 10 Gb/s signal at 1550 nm was 13.75 dB with signal-to-noise ratio of 13.81 dB. To test the performance of the fabricated devices in optical C-band, eye diagrams were measured at different wavelengths. The plot of the dynamic extinction ratios and SNR over C-band is given in Fig 4.25. Both the ER and SNR are higher than 11 dB for 10 Gb/s eye diagram. In addition, Fig 4.24b shows the resulting eye diagram for 28 Gb/s NRZ signal. It can be seen that the eye is still open at the center with ER and SNR of 5.06 dB and 4.58 dB. Large signal modulation results shows that the fabricated devices have high potential to be deployed in high-speed optical communication systems up to the data rate of 28 Gb/s.

4.4 Summary

This Chapter highlights the design process flow to realize high-speed InP based MZMs. The importance of each step from the choice of right epitaxy material, its growth and device fabrication to the measurement techniques involved in testing of InP based modulator have been discussed in depth. The InP based MZM modulators with different length of TWEs were fabricated and tested. The modulators with 3-dB EO bandwidth of 7.5 GHz and V_{π} as low as 4.5 V have been demonstrated. The V_{π} can be further improved by operating the modulator devices in dual arm drive arrangement i.e. by biasing both the arms of the MZM and by increasing the length of the phase shifting arms. The lowest value of V_{π} reported by Teraxion for InP MZM modulator operated in dual arm is 1.5 V (See Table 1.1). Further, the number of MQWs in the intrinsic region of phase shifter can be increased to enhance the EO efficiency and reduce V_{π} . This effect is demonstrated in Chapter 5, where the number of wells are increased from 15 to 25 and considerable reduction in V_{π} is achieved. The operation of the modulator and dependence of V_{π} on operating wavelength in

optical C-band is also discussed briefly. The operation of modulator up to 28 Gb/s is demonstrated by measuring the large signal response. In addition, CPW transmission line parameters extracted from the measurements show that as microwave index is reasonably close the optical group index so velocity mismatch is not the main bandwidth limiting factor. The major factor affecting the affecting the EO bandwidth is the low impedance of the TWE (35Ω). The modulation bandwidth response can be enhanced by terminating the devices with with low impedance values at the expense of reduced SNR of the large signal due to peaking effect in modulation response. The details to further enhance the EO bandwidth and reducing the switching voltage will be discussed in next chapters.

References

- [1] S.-K. Han, R. Ramaswamy, W.-Q. Li, and P. Bhattacharya, “Efficient electrooptic modulator in InGaAlAs/InP optical waveguides,” *Photonics Technology Letters, IEEE*, vol. 5, no. 1, pp. 46–49, Jan 1993.
- [2] I. Betty, M. Boudreau, R. Longone, R. Griffin, L. Langley, A. Maestri, A. Pujol, and B. Pugh, “Zero chirp 10 Gb/s MQW InP Mach-Zehnder transmitter with full-band tunability,” in *Optical Fiber Communication and the National Fiber Optic Engineers Conference, 2007. OFC/NFOEC 2007. Conference on*, March 2007, pp. 1–3.
- [3] S. Selmic, T.-M. Chou, J. Sih, J. Kirk, A. Mantle, J. Butler, D. Bour, and G. Evans, “Design and characterization of 1.3 μm AlGaInAs-InP multiple-quantum-well lasers,” *IEEE Journal of Selected Topics in Quantum Electronics*, vol. 7, no. 2, pp. 340–349, Mar 2001.
- [4] R. Griffin, S. Jones, N. Whitbread, S. Heck, and L. Langley, “InP mach-zehnder modulator platform for 10/40/100/200-Gb/s operation,” *IEEE Journal of Selected Topics in Quantum Electronics*, vol. 19, no. 6, pp. 158–166, Nov 2013.
- [5] J. Pamulapati, J. P. Loehr, J. Singh, P. K. Bhattacharya, and M. J. Ludowski, “Refractive index and electro-optic effect in compressive and tensile strained quantum wells,” *Journal of Applied Physics*, vol. 69, no. 7, pp. 4071–4074, 1991.
- [6] N. J. Ekins-Daukes, K. Kawaguchi, , and J. Zhang, “Strain-balanced criteria for multiple quantum well structures and its signature in x-ray rocking curves,” *Crystal Growth & Design*, vol. 2, no. 4, pp. 287–292, 2002.
- [7] R. Deri and E. Kapon, “Low-loss III-V semiconductor optical waveguides,” *IEEE Journal of Quantum Electronics*, vol. 27, no. 3, pp. 626–640, Mar 1991.

- [8] X. Zhao, B. Xiong, C. Sun, and Y. Luo, "Low drive voltage optical phase modulator with novel InGaAlAs/InAlAs multiple-quantum-barrier based n-i-n heterostructure," *Opt. Express*, vol. 21, no. 21, pp. 24 894–24 903, Oct 2013.
- [9] T. H. Stievater, D. Park, W. S. Rabinovich, M. W. Pruessner, S. Kanakaraju, C. J. K. Richardson, and J. B. Khurgin, "Enhanced electro-optic phase shifts in suspended waveguides," *Opt. Express*, vol. 18, no. 2, pp. 885–892, Jan 2010.
- [10] P. Besse, M. Bachmann, H. Melchior, L. Soldano, and M. Smit, "Optical bandwidth and fabrication tolerances of multimode interference couplers," *Journal of Lightwave Technology*, vol. 12, no. 6, pp. 1004–1009, Jun 1994.
- [11] N. Kikuchi, Y. Shibata, K. Tsuzuki, T. Yasui, M. Ishikawa, H. Ishii, M. Arai, T. Sato, Y. Kawaguchi, and F. Kano, "Full C-band 40-gbit/s DPSK modulation using lossless InP n-p-i-n Mach-Zehnder modulator monolithically integrated with soa," in *Optical Fiber Communication - includes post deadline papers, 2009. OFC 2009. Conference on*, March 2009, pp. 1–3.
- [12] M. Nielsen, K. Tsuruoka, T. Kato, T. Morimoto, S. Sudo, T. Okamoto, K. Mizutani, H. Sakuma, K. Sato, and K. Kudo, "SOA-Booster Integrated Mach-Zehnder Modulator: Investigation of SOA Position," *Journal of Lightwave Technology*, vol. 28, no. 5, pp. 837–846, March 2010.
- [13] M. Hill, X. Leijtens, G. Khoe, and M. Smit, "Optimizing imbalance and loss in 2×2 3-db multimode interference couplers via access waveguide width," *Journal of Lightwave Technology*, vol. 21, no. 10, pp. 2305–2313, Oct 2003.
- [14] D. Thomson, Y. Hu, G. Reed, and J.-M. Fedeli, "Low Loss MMI Couplers for High Performance MZI Modulators," *Photonics Technology Letters, IEEE*, vol. 22, no. 20, pp. 1485–1487, Oct 2010.
- [15] L. Spiekman, Y. Oei, E. Metaal, F. Green, I. Moerman, and M. Smit, "Extremely small multimode interference couplers and ultrashort bends on InP by deep etching," *Photonics Technology Letters, IEEE*, vol. 6, no. 8, pp. 1008–1010, Aug 1994.

- [16] R. Lewen, "High speed electroabsorption modulators and p-i-n photodiodes for fiber-optic communications," Ph.D. dissertation, Royal Institute of Technology, 2003.
- [17] "Application of a Two-Tier Vector Network Analyzer RF Calibration," <http://www.cascademicrotech.com/blog/2012/application-of-a-two-tier-vector-network-analyzer-rf-calibration/>, accessed: 2016-02-10.

Chapter 5

InP based Mach-Zehnder modulators at 2 μm

In the previous two chapters, simulation and experimental results for InP based MZMs operating in the optical C-band were discussed. High frequency bandwidth limitations and design constraints of a TWE were elaborated in detail. The main purpose of developing the high speed InP MZMs at 1550 nm was to develop know-how of the complexities involved in design, fabrication process and testing of the InP MZMs. This chapter is focused on the design and fabrication of InP MZM for a new optical transmission wavelength of 2000 nm using the knowledge base developed in previous chapter. Section 5.1 briefly discusses the importance of photonic components working around 2000 nm wavelength. Two different generations of InP MZM suitable for operation around 2000 nm were fabricated and experimentally evaluated. Material design and testing of both the generations of fabricated devices have been discussed in detail in Sections 5.2 and 5.3 respectively. It is demonstrated that V_π of InP based MZMs can be reduced to 2.7 V or even less for longer TWEs by increasing the electro-optical overlap in the optical waveguide without changing the electro-optic bandwidth. In addition, Section 5.4 describes the RF packaging of the modulators and highlights important aspects involved in the design of a RF package. As the ultimate evaluation of the performance of any photonic device developed for telecommunications is by deployment in real fiber-optic transmission systems. For this purpose, an externally modulated 4x10 Gb/s NRZ-OOK WDM signal was transmitted over 1.15 km of low-loss HC-PBGF employing a packaged InP based MZM in the transmitter for the first time and an OSNR requirement of 25 dB on 100 GHz spaced channels is determined using a direct detection scheme in Section 5.5.

5.1 The need of InP based MZMs for 2000 nm

There are an increasing number of applications that would benefit if high performance, low-cost photonic components, developed and commercialized at wavelengths between 1300 nm and 1600 nm for telecommunication applications, were to be extended to wavelengths beyond 1600 nm. For example, a large range of important environmental gas species can be readily sensed using tunable laser spectroscopy around 2000 nm. LIDAR systems can be used at 2050 nm for the 3-dimensional mapping of CO₂ in the environment [1–3]. In this thesis, we focus on a particular opportunity in telecommunications enabled by the potential ultra-low loss that could be achieved with hollow-core photonic bandgap fibers (HC-PBGF) [4]. Such fibers offer low latency and low non-linearity due to light propagation through the air core and, in combination with the ultra-broad bandwidth of Thulium doped fiber amplifiers (TDFA) [5], will permit the extension of the transmission band from the conventional C and L-bands to 2000 nm. As discussed in the introduction of this thesis, the current single mode fiber (SMF) infrastructure will ultimately be limited by the total capacity per fiber due to exponential growth in high bandwidth data traffic per year. In future, the network operators will be challenged with a decision as how to best upgrade the current fiber links with new type of optical fibers with potential to fulfill the ever increasing capacity requirements. One solution is to use the new fiber types such as HC-PBGF at entirely new wavelength band i.e. at 2000 nm. The first communication system experiments using HC-PBGF at 2000 nm have already been performed and have shown promising results [5–7]. The shift to the new transmission window will require a development of full range of photonic components capable of operating at a telecommunications grade [8], which includes modulators operating around 2000 nm for data encoding. For an error free and spectrally efficient data communication such modulators must have a high bandwidth and operate with low modulation voltages. Lithium Niobate (LiNbO₃) modulators can be configured to operate in this wavelength range, but generally at the expense of high drive voltages with a large footprint.

The semiconductor materials operating in the wavelength range around 2000 nm can be grown either on gallium antimonide (GaSb) or indium phosphide (InP) substrates. The Sb based materials are generally grown by molecular beam epitaxy (MBE) technique and it is very difficult to control the growth quality specially on industrial scale. As compared to Sb based materials, InP based materials are a better choice for large scale industrial applications due to mature growth and device fabrication processes [9]. In addition, InP based

materials have the advantage that high quality quantum well structures can be achieved, monolithic integration with other devices is possible, and these materials have been validated by widespread deployment at the 1550 nm waveband [10–12]. For 2000 nm wavelength range, we have already successfully demonstrated both the active and passive InP based photonic components including laser, photodetector and arrayed waveguide grating coupler (AWG) [13]. In this work we focus on the realization of the InP based MZM operating at 2000 nm.

5.2 Mach-Zehnder modulator - First generation

As discussed earlier, InP MZMs operate by applying a differential phase modulation between the two arms of an interferometer using materials with a large electro-optic effect. A variety of electro-optic (EO) effects can be used with semiconductor materials to achieve the desired refractive index modulation. Carrier depletion, for example, is limited in the achievable index change and has an associated change in material absorption [14]. The linear Pockels effect, which is relatively wavelength independent, is limited in the index change achievable. A preferable effect, widely used at 1550 nm wavelengths, is the QCSE in quantum wells due to the large dependence of the refractive index change on the applied field. The InP based modulators based on QCSE operating around 1550 nm wavelength of operation are demonstrated in Chapter 4. The strength of the QCSE is dependent on the wavelength offset from the band-edge and thus, to access wavelengths longer than 1650 nm on an InP substrate, multiple strained quantum wells are required. Furthermore these wells can only be compressively strained [13]. For the design of material suitable for modulator operation around 2000 nm, the bandgap of the quantum wells is selected to be ~ 150 nm (43 meV) below the operating wavelength in order to provide a good balance between minimizing residual absorption while achieving useful index changes through electro-refraction. The bandgap of the material can be further shifted closer to 2000 nm to exploit electro-absorption effect of the QCSE in the modulation. Higher optical modulation bandwidths are achievable using electro-absorption modulators (EAMs) but they have high inherent optical loss, chirp and more complex implementation of the phase modulation formats as compared to the MZM [15]. For this reason, in this work we implement MZM which can be used to generate advanced multi-level optical phase modulation formats such as differential phase shift keying (DQPSK) and quadrature

amplitude modulation (QAM).

5.2.1 Modulator material design and structure

For InP based MQW structures, an effective way to achieve material bandgap at wavelengths longer than 1800 nm is to use InGaAs layer with high Indium (In) content. The $\text{In}_{0.53}\text{Ga}_{0.47}\text{As}$ when lattice matched to InP has a bandgap of 0.75 eV (~ 1650 nm). By increasing the Indium (In) content x from 0.53 in $\text{In}_x\text{Ga}_{1-x}\text{As}$ layer, the bandgap increases [16]. Fig 5.1, shows the trend of bandgap variation with the increase of In content both in a 10 nm quantum well and bulk layer. The quantum wells with high In content exhibit compressive strain due to larger lattice constant as compared to InP substrate (5.8687 \AA) and must be carefully strain balanced. In order to have a band-edge around 1850 nm we used a 10 nm thick quantum well with 0.66 % compressive strain ($\text{In}_{0.63}\text{Ga}_{0.37}\text{As}$). To accommodate the strain in the multi-quantum well (MQW) structure a 10 nm thick barrier layer with -0.84 % tensile strain ($\text{Al}_{0.145}\text{Ga}_{0.445}\text{In}_{0.41}\text{As}$) and bandgap of 1.05 eV was used. This composition provides a large confinement barrier [17]. To avoid generation of dislocations despite strain balancing in grown epitaxial layer structure, only 15 QW structures were initially used in the material grown for the first generation devices. However, the number of quantum wells using the same composition were increased from 15 to 25 for the second generation devices discussed in the Section 5.3. Increasing the number of MQWs beyond 25 may need additional MOVPE growth optimizations which is out of scope of this work.

As mentioned above, for the first generation MZM devices, the grown epitaxial structure had 15 quantum wells which were cladded by undoped InP spacer layers providing an 810 nm thick intrinsic region. The intrinsic region was bound by p- and n-type contacting regions. The calculated overlap of the transverse mode with the quantum wells was 22% and the mode had a transverse $1/e^2$ width of just over 1 μ m. The grown epitaxial layer structure grown for modulator operation around 2000 nm is shown in Table 5.1. The structure was grown by Metal Organic Vapor Phase Epitaxy (MOVPE) on both n-type and semi-insulating (SI) InP substrates.

Table 5.1: Epitaxial layer structure grown (Sample: A-1545).

Material	Thickness (nm)	Doping (cm^{-3})	Conductivity (S/m)
P-InGaAs	20	5e19	69183
P-InGaAs	80	1e19	13864
P-InP	800	1e18	2403
P-InP	200	5e17	1201
i-InP	400	NUD	0
InAlGaAs (barrier)	10	NUD	0
15 \times InGaAs (well, 0.66% compressive) ($\lambda=1.85 \mu\text{m}$)	10	NUD	0
15 \times InAlGaAs (barrier, 0.84% tensile) ($\lambda=1.18 \mu\text{m}$)	10	NUD	0
i-InP	100	NUD	0
n-InP	100	5e17	27000
n-InP	100	1e18	41152
SI/n-InP	-	-	-

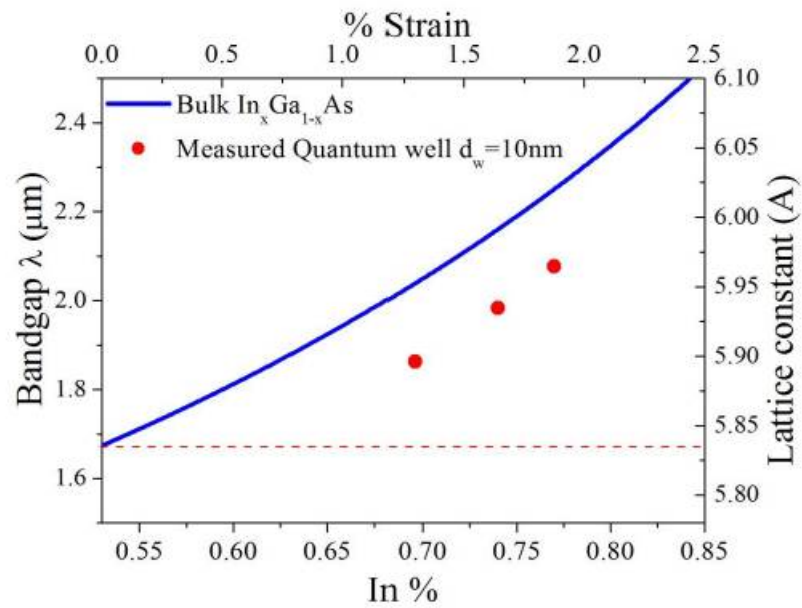
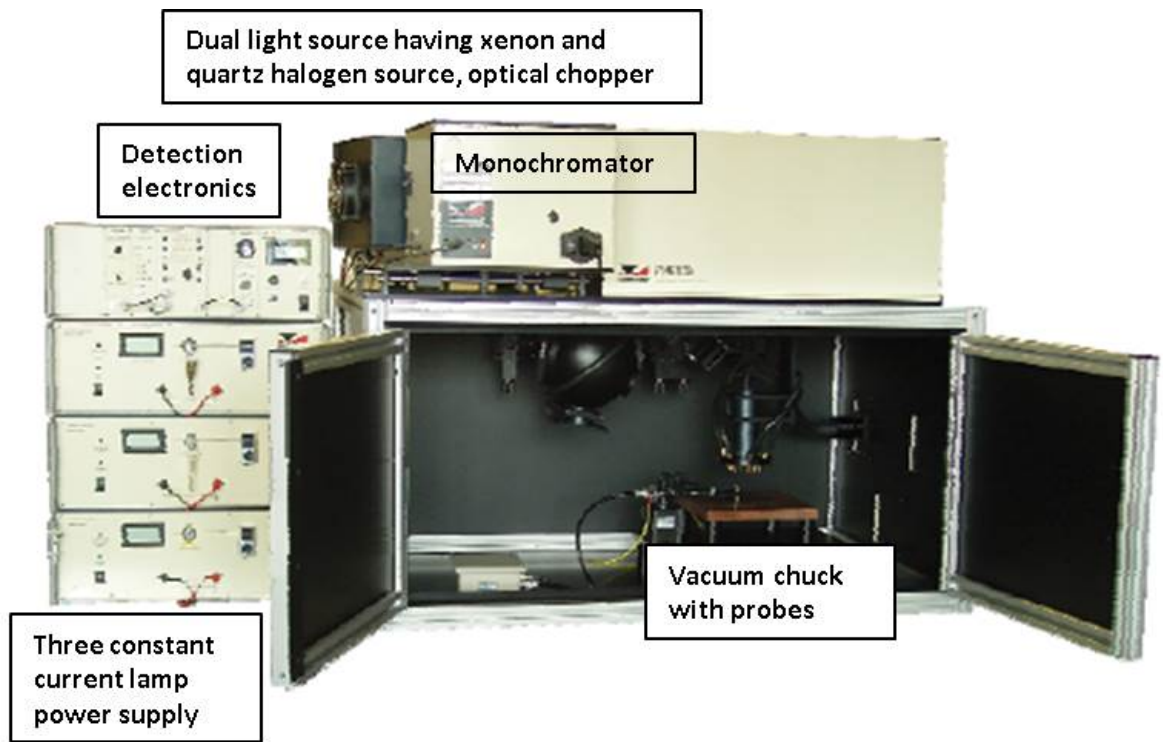


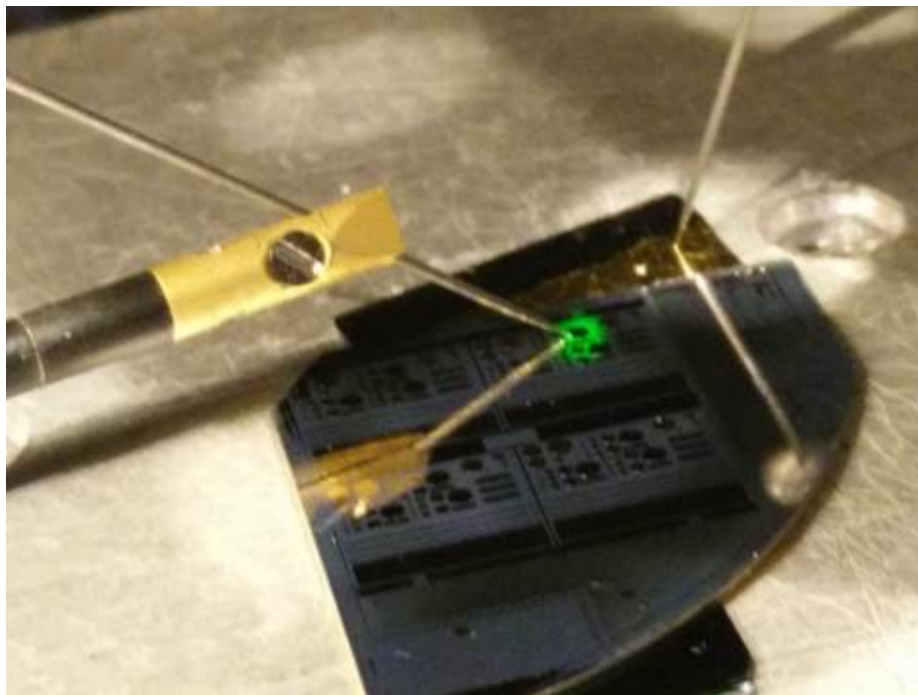
Figure 5.1: Variation of bandgap by increasing In composition from 0.53 to 0.85 in bulk $\text{In}_x\text{Ga}_{1-x}\text{As}$. Red dots show the measured bandgap variation in 10 nm thick quantum well. Dotted line represents the lattice constant of InP [8].

5.2.2 Photoabsorption response

The EO properties of the quantum well structure were investigated by fabricating photodiodes with surface normal access. This configuration allows the measurement of absorption associated with in-plane TE polarization only which is appropriate for the compressively strained wells used. The absorption spectra were recorded by the photocurrent measurement with applied reverse bias voltages using the commercial photoresponse measurement kit by Bentham Instruments Ltd. The measurement setup is shown in Fig 5.2. The probe light source employed is a dual Xenon/Quartz halogen source followed by a monochromator with 0.74 mm (FWHM bandwidth ~ 4 nm) exit slit width and 600 lines/mm grating. The light is chopped with an optical chopper operating at a frequency of 470 Hz and illuminated normally onto the fabricated photodiodes. The photocurrent is measured using a lock-in amplifier. The photocurrent generated as a function of incident wavelength and reverse bias is shown in Fig 5.3a. It demonstrates an excitonic absorption resonance at 1850 nm which marginally broadens and shifts to longer wavelength with applied reverse voltage in line with the QCSE. It can be observed that even at a high reverse bias i.e. at 9 V, the absorption peak associated with the exciton is still present but it is slightly broadened which means that the exciton confinement is reduced. The ideal QCSE behavior required for MZM operation should cause a large red shift of the absorption bandedge with applied reverse bias and should maintain exciton confinement with the minimal broadening of the associated peak [18]. The broadening of the exciton peak at high reverse bias i.e. after 7 V will result in a higher absorption tail at 2000 nm which will in turn affect the device performance in terms of IL and ER. The exciton absorption peak wavelength shift with reverse bias is shown in Fig 5.3b and exhibits a weak quadratic dependence. The capacitance of the material was measured using capacitance-voltage (CV) measurement and it is ~ 140 pF/mm² when fully depleted at bias greater than -3 V (measurement shown in Section 5.3).

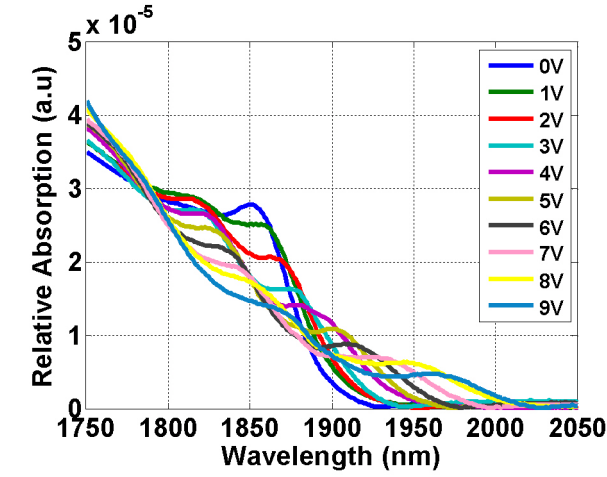


(a)

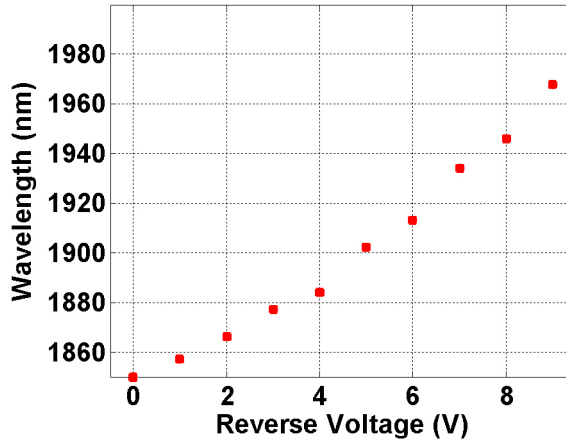


(b)

Figure 5.2: (a) Photoabsorption measurement setup. (b) Sample under test with DC probes to apply the reverse bias. Visible green light is used to show the surface normal illumination.



(a)



(b)

Figure 5.3: (a) Bias dependent spectral response of 15 quantum well strain-balanced structure under surface normal illumination. (b) Exciton absorption peak wavelength with the applied reverse voltage.

5.2.3 Modulator design and layout

The mask layout of a single InP based MZM designed is shown in Fig 5.4. The basic device architecture is same as MZM operating at 1550 nm. At the input of the MZM passive multi-mode interference (MMI) couplers were used for low loss 1×2 and 2×2 splitting and combining of the light paths to realize the MZM structure. A CPW TWE was again selected for delivering the RF signal to the MZM. As explained in previous chapters, the main reason of using TWE is to allow the synchronous co-propagation of RF and optical signal in the phase shifting section of the MZM with low loss. The signal electrode resides on the top of the optical ridge waveguide while the ground electrodes connected to the

n-doped layer are placed on both sides of ridge. Such Ground-Signal-Ground (GSG) coplanar arrangement allows the applied electric field to be confined in the intrinsic region of the optical waveguide i.e. MQW and the InP spacer layers.

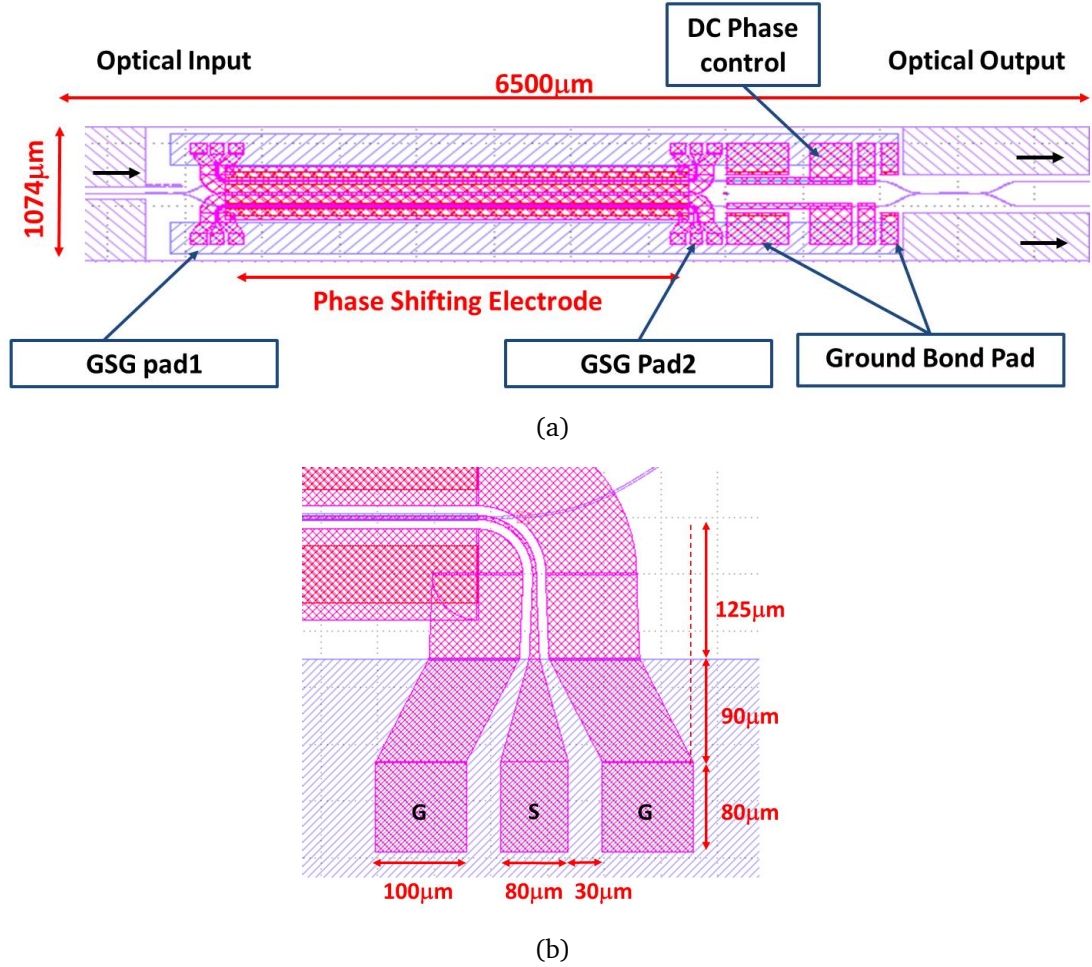


Figure 5.4: (a) Mask layout of a single MZM showing RF GSG pads, DC phase control electrodes, input and output MMIs. (b) Dimensions of the input/output RF GSG pad.

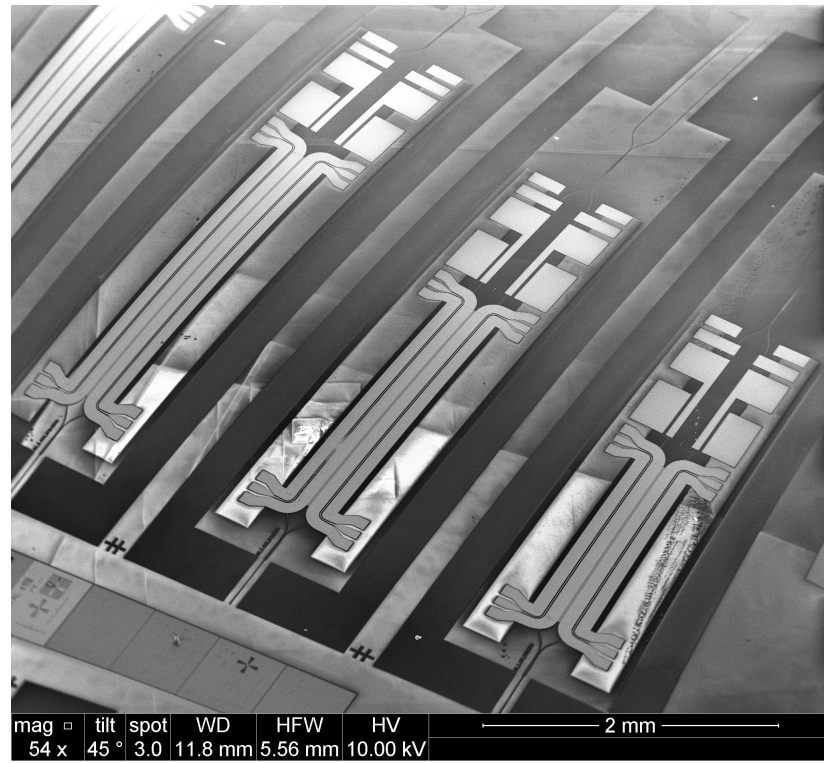
Both the electrical and optical signals should travel at the same velocity with low optical and electrical losses. The overall device impedance should also be close to 50 Ω to reduce the electrical reflections along the phase shifter and maximize the electro-optic (EO) response. Keeping in mind the design requirements, rigorous design optimizations were carried out to determine the optimum performance point of the CPW-TWE (See Chapter 3) [19]. Optical waveguides based on a deep etched ridge of widths 2 μm and 2.5 μm were selected for the phase shifting sections. Optical waveguides are deeply etched to provide strong lateral confinement of the optical mode within the intrinsic

region. It also allows the compact waveguide routing and input/output couplers to be miniaturized. The width of the Au signal electrode on the top of ridge was kept slightly wider than the final ridge widths and was selected as 2.5 μm and 3 μm respectively. The gap between the signal and ground electrodes around optical ridge was optimized to be 8.5 μm . In order to minimize the RF signal loss due to the metal, the electrode thickness on the top of the ridge was electroplated to 2 μm . The RF signals were delivered to the phase shifters via GSG feed in lines which were designed to accommodate the dimensions of the coplanar GSG probes as in Fig 5.4b). The signal pad is 80 μm wide and the ground pads are kept at the spacing of 30 μm from the central conductor. The GSG pads were then linearly tapered and bent at a certain radius to match the dimension of the ridge waveguide as shown in Fig 5.4b. Both the GSG pads and ridge waveguide were designed to be close to 50 Ω .

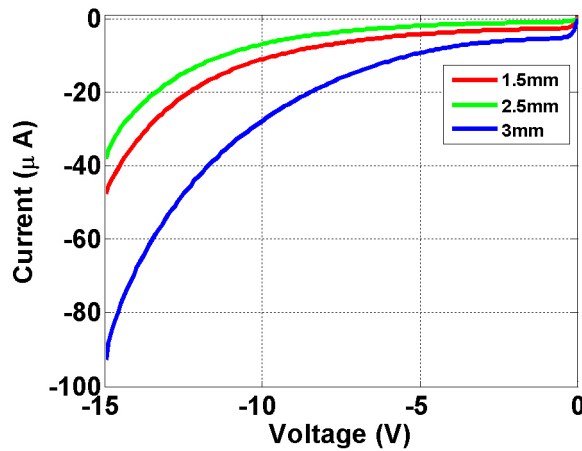
MZMs with lengths for the TWE ranging from $L = 1.5 \text{ mm}$ to 3 mm were fabricated. The structures included contacts for phase and amplitude control to allow balancing of the two arms of the MZM. Waveguide sections were used to produce an overall chip length of 6.5 mm. Ridge waveguides with widths of 2 μm and 2.5 μm were etched through the quantum well region using $\text{Cl}_2/\text{CH}_4/\text{H}_2$ inductively coupled plasma (ICP) etching. Ridges were fabricated along the $[01\bar{1}]$ axis. The deeply etched ridges were buried in planarised benzo-cyclobutene (BCB). The BCB planarisation allows the signal and ground electrode to be on the same height which helps to reduce the parasitic capacitance formed in the GSG pad feed-in region. The electrical isolation between different sections was achieved using a shallow etched slot with length of 10 μm . The measured value of isolation between two MZM arms is 0.72 $\text{M}\Omega$.

5.2.4 DC characterization

The array of fabricated devices with varying length of phase shifting arms is shown in Fig 5.5a. Total cleaved length of the chip remains the same i.e. 6.5 mm. The measured leakage current of the devices with different lengths is indicated in Fig 5.5b. It can be seen that DC leakage current in devices is well below 50 μA at a 10 V reverse bias, which shows that the side wall passivation of the optical waveguide is fully intact.



(a)



(b)

Figure 5.5: (a) SEM image of the fabricated devices with different lengths of phase shifting arm. (b) Measurement showing the leakage current with varying length of the phase shifting arm.

To measure the DC transmission characteristics of the modulator, a single frequency laser emitting at 1996 nm (Eblana Photonics) was coupled into the input waveguide using a lens ended fiber and collected with a similar lens ended fiber. The reverse voltage was applied to the single arm of the MZM with the other arm left unbiased. The input polarization was set to be to be transverse

electric (TE) using polarization controller (PC) as there is an enhanced electro-optic response for TE as compared to transverse magnetic (TM) polarization due to the compressive strain and the ridge orientation. The optical transmission response of the modulator with 3 mm TWE for the TE polarized light is shown in Fig 5.7a. The voltage required for a π phase shift (V_π) is 3.2 V which leads to a voltage length product ($V_\pi L$) of 9.6 V.mm. The measured DC extinction ratio (ER) and fiber to fiber insertion loss (IL) of the device is 9 dB and 16 dB respectively. Since the induced phase shift due to QCSE is a nonlinear function of the applied reverse voltage, it can be seen that the period between successive maxima and minima of the transmission curve is not constant. It also suggests that at a high reverse bias, the voltage induced absorption will be dominant and will affect the device throughput, ON-OFF switching voltage V_π and DC ER as measured in Fig. 5.3a and 5.7a.

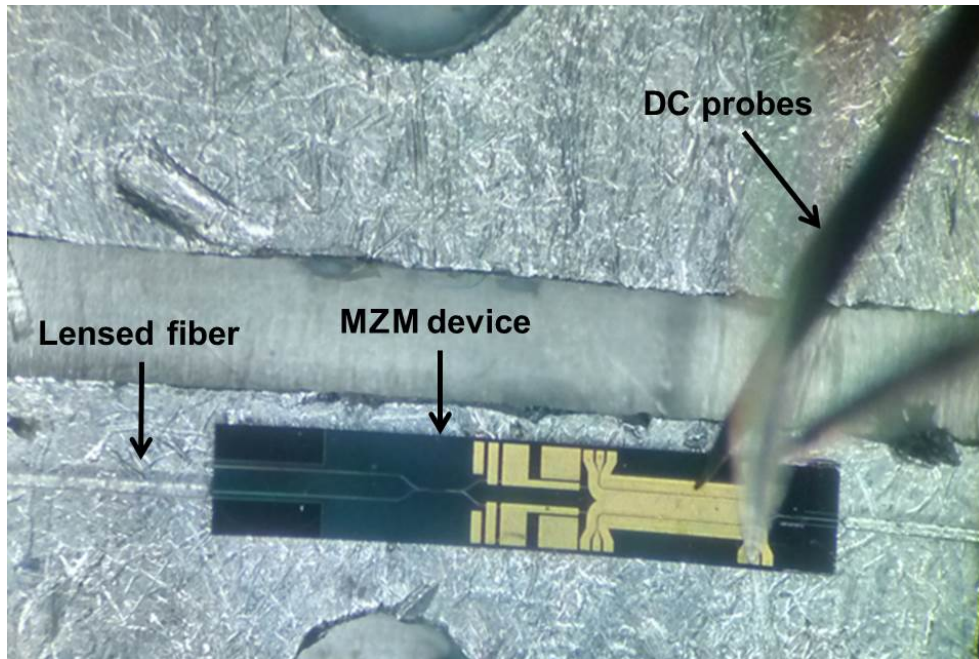
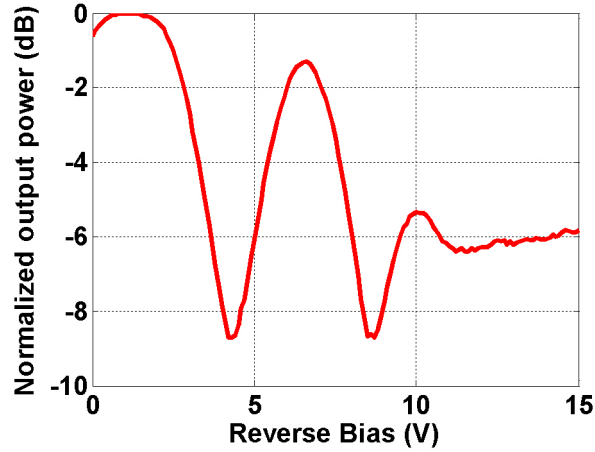
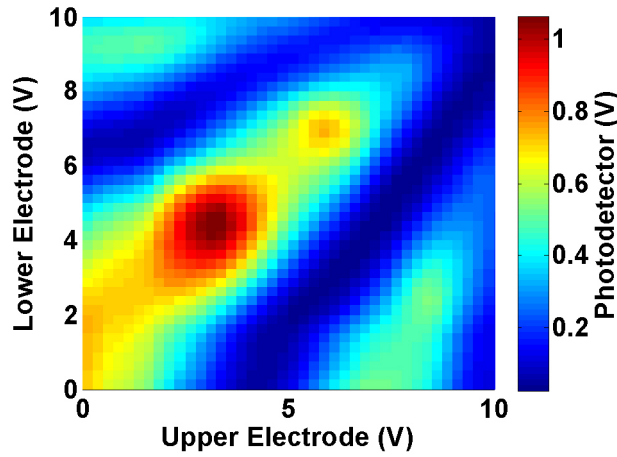


Figure 5.6: DC testing of a single modulator device. Reverse bias is applied to single arm of the modulator through DC probes.



(a)



(b)

Figure 5.7: (a) Optical transmission characteristics of modulator as a function of DC voltage supplied to one arm of the interferometer. (b) Dual-electrode (push-pull) operation of modulator.

In addition to the single electrode characterization, the optical transmission is also measured for the dual electrode (push-pull) operation of the modulator. However, for the high frequency characterization, the modulator was only tested in a single electrode configuration. Fig 5.7b shows the two dimensional DC transmission matrix plot for a 1.5 mm long device. In push-pull operation, voltages on both the phase shifting arms i.e. lower electrode and upper electrode of the modulator were swept simultaneously. By careful biasing of both arms, push-pull operation will allow for the chirp free operation of the modulator at a reduced switching voltage [20]. Measurement shows that the transmission is not entirely symmetric around 0 V in transmission matrix. The asymmetry arises due to a slight variation in the fabricated dimensions of 2×2

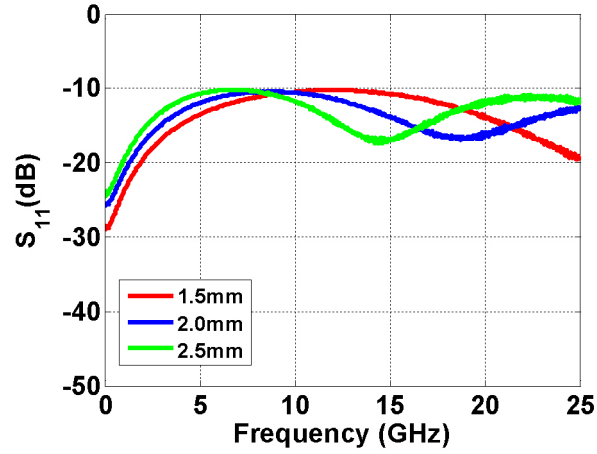
output MMI coupler during the fabrication process. This asymmetry can be compensated by the careful tuning of the DC phase control electrode shown in the device layout in Fig 5.4a. Also, the DC transmission matrix shows a change in transmission when the electrodes are swept simultaneously. This behavior is believed to originate from the constructive and destructive interference of the reflections of the optical field from the cleaved end facets with the modulated light. This effect can be eliminated by applying anti-reflecting (AR) coatings on the end facets of the fabricated device.

5.2.5 Electrical small-signal characterization

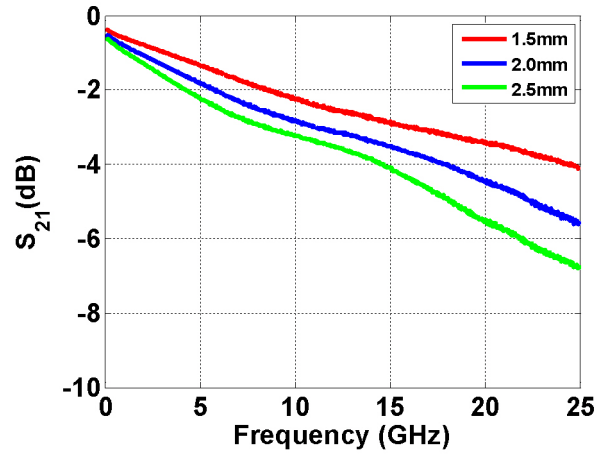
The electrical S-parameters of the TWE MZM were measured using the same setup shown in Chapter 4 (See Fig 4.17). On wafer SOLT calibration was performed before measuring the electrical S-parameters of the devices. The measured electrical S11 and S21 are presented in Fig 5.8a and 5.8b respectively. Devices with phase shifting regions of different lengths were also characterized. It can be seen from Fig 5.8b that with increasing length of the phase shifter, the 3-dB electrical bandwidth reduces, which is primarily due to the increase in overall RF loss due to the increased length. The measured 3-dB electrical roll-off frequencies are 19.8 GHz, 15 GHz and 12.5 GHz for the devices with 1.5 mm, 2.0 mm and 2.5 mm long phase sections respectively. The electrical S-parameter measurements match the full wave simulations performed in High Frequency Structural Simulator (HFSS) software. The measured RF S21 for 1.5 mm phase electrode at 40 MHz starts at around -0.351 dB instead of 0 dB, this is due to the metal track series resistance and RF probe contact resistance. This value decreases further to -0.57 dB as the metal series resistance increases with the increase in electrode length.

5.2.6 Electro-optic response

The high speed optical performance of the fabricated modulators was demonstrated by measuring the 3-dB electro-optical (EO) bandwidth. For EO-response measurement, the setup is shown in Fig 5.9. The basic arrangement of setup is almost similar as one discussed in Chapter 4. A single wavelength laser in a butterfly package from Eblana Photonics emitting at 2002 nm was used as input optical signal source instead of a tunable laser source. An EOtech ET-5000F photodetector which has a 3-dB bandwidth of 12.5 GHz was used to measure the modulator EO bandwidth. The high speed RF signal of -1 dBm and DC bias



(a)



(b)

Figure 5.8: Measured Electrical S-parameters for devices with different electrode length: (a) S_{11} . (b) S_{21} .

was applied to the modulator input arm through a bias-tee and a high speed GSG probe. The output RF pad of modulator arm was terminated using a $50\ \Omega$ terminated GSG probe for the EO measurement. The TE polarized light centered at 2002 nm was coupled into the sample using the lensed fiber. The PC ensured that the coupled light was TE-polarized. The input optical power was 2 dBm. To compensate for the optical insertion loss of the modulator, the output light was again collected using another lensed fiber and then amplified to 1 dBm using a TDFA. In order to reduce the amplified spontaneous emission (ASE) of the amplified optical signal, a tuneable optical filter with a 3-dB passband of 1.6 nm was used at the output. Fig 5.11 shows the measured EO response of the 2 mm long phase shifter modulator at a bias voltage of -6.74 V. A 3-dB EO band-

width of 9 GHz was achieved (no signal processing was used). Ideally, if there is a complete velocity and impedance match between electrical and optical waves, then the frequency at which the electrical loss of the modulators has decreased to -6.4 dB can be taken as 3-dB EO bandwidth. However, measurements show that the 3-dB EO bandwidth of 9 GHz is less than the 6.4 dB electrical response of the 2 mm long electrode device. This difference is mainly due to the velocity and impedance mismatch, which can be improved by reducing the capacitance i.e. making the intrinsic region slightly thicker. The thicker intrinsic region will increase V_π due to low electric field (kV/cm) across the MQWs which will lead to a reduced EO effect. To enhance EO effect and reduce V_π , the number of the quantum wells can be increased within the thicker intrinsic region. The improvement in V_π by increasing the number of wells keeping the total thickness of intrinsic region same is described in the next section.

We further demonstrate the large signal response of the device at -6.74 V shown in Fig 5.12. A 10 Gb/s non-return to zero (NRZ) pseudo-random binary sequence (PRBS) of length 2^7-1 was generated using a Centellax TG2P1A PRBS source. The output electrical signal from PRBS source had a 250 mV_{p-p}, which was amplified to ~ 6 V_{p-p} using a JDSU H301 10 Gb/s driver amplifier. The device probing and termination arrangement was the same as described for the EO response measurement. The optical signal output was amplified and then filtered before the EOtech photodetector. An external electrical amplifier (SHF A824H) with maximum available gain of 26 dB was used to amplify the photodetected signal. The resulting eye diagram was measured using an Agilent 86100C digital communication analyzer (DCA). The measured eye diagram is clearly opened at the center. The large noise observed may have roots from different sources: broadband ASE falling into the detector, larger noise figure of the optical amplifiers, and even impedance mismatches between RF probes and devices.

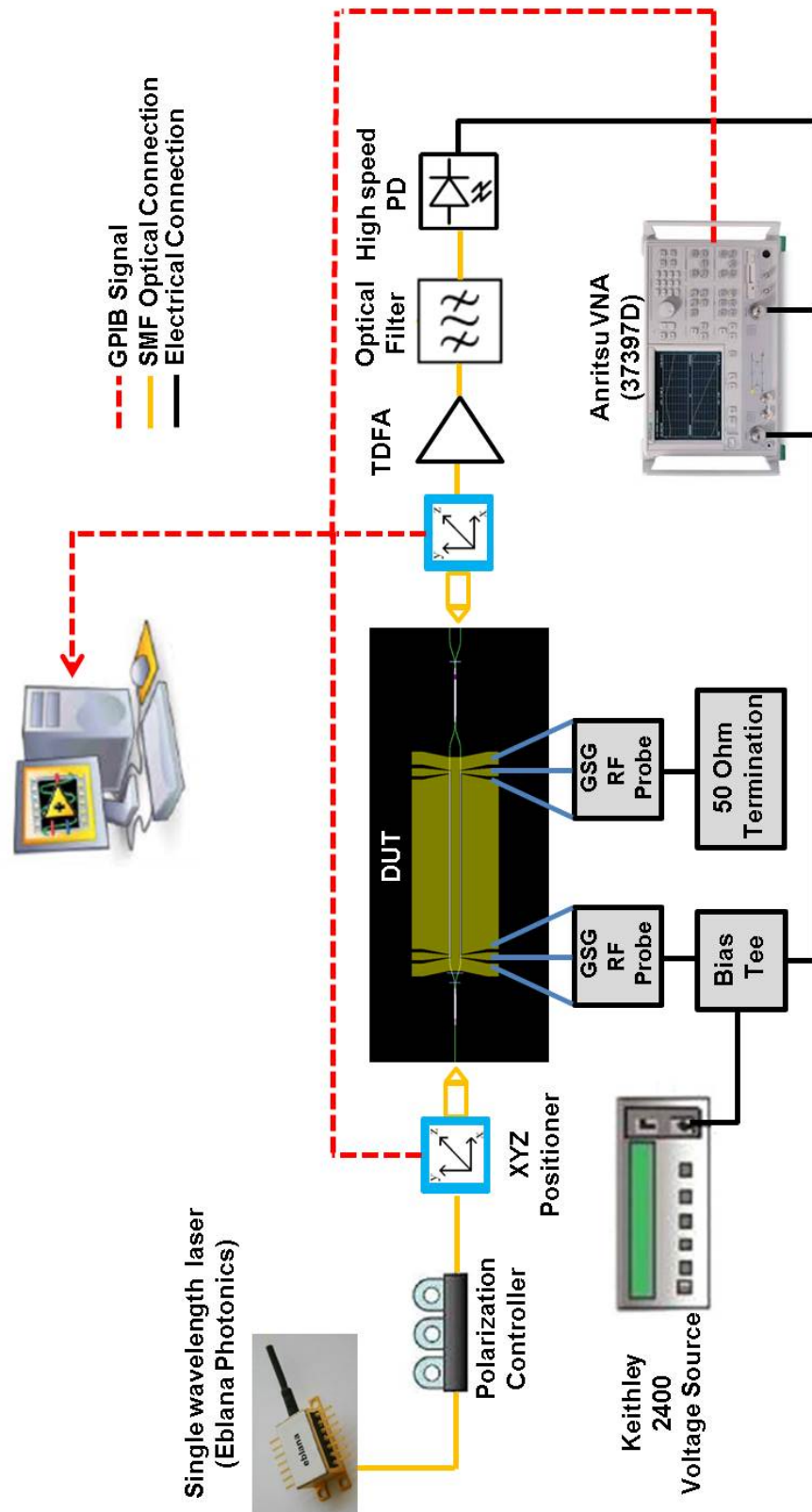


Figure 5.9: EO response measurement setup at 2000 nm.

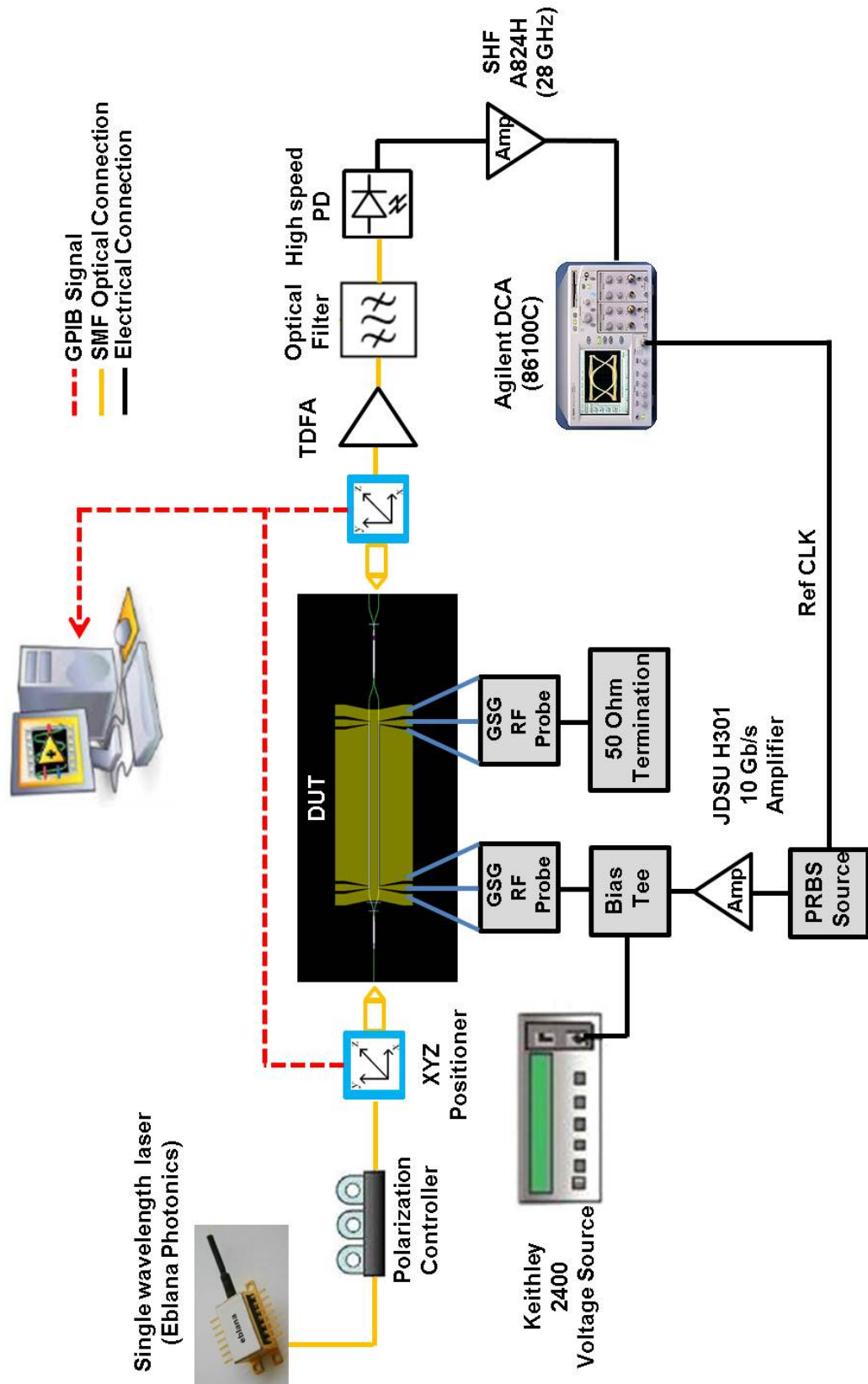


Figure 5.10: Large signal response measurement setup.

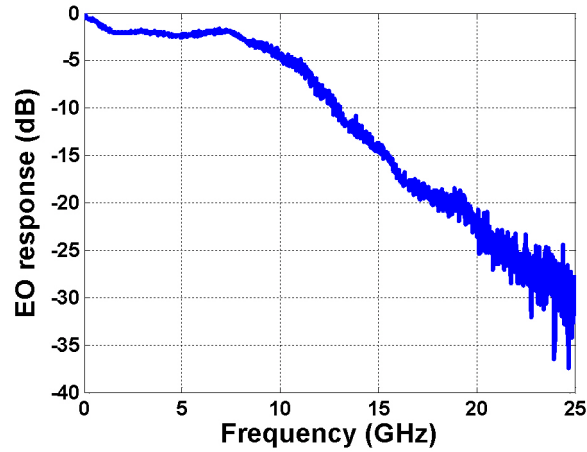


Figure 5.11: Measured EO response of the 2 mm TWE MZM at a bias voltage of 6.74 V.

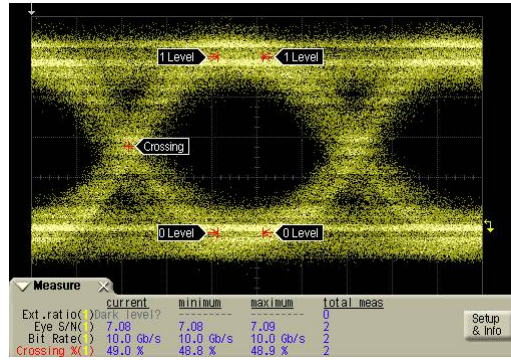


Figure 5.12: Measured optical eye diagram at 10 Gb/s for 2^7-1 PRBS signal.

5.3 Mach-Zehnder modulator - Second generation

The performance of an InP MZM is usually evaluated by four figure-of-merits (FOM) which are V_π , insertion loss (IL), Electro-Optic (EO) bandwidth and the length of the device. The MZM design is a compromise between these. The V_π can be reduced by increasing the DC bias across the MQW layers but at the expense of voltage induced absorption which will in turn degrade the DC extinction ratio (ER) and IL. Another way to decrease V_π without a considerable effect on the other FOM is to increase the electro-optical overlap i.e. increase the slope of change in refractive index with applied voltage for a fixed capacitance per unit length of the phase electrode [21]. The capacitance is determined by the total thickness of the intrinsic region and the width of the optical waveguide.

5.3.1 Modulator material design and structure

To establish the effect of an increase in the overlap on the overall device performance, an epitaxial layer structure with an increased number of MQWs was grown on n-doped (100)-oriented InP substrates using MOVPE. The NUD region thickness was kept comparable to first generation of the modulator i.e. 710 nm. The epitaxial layer structure with increased number of wells is shown in Table 5.2. The number of wells was increased by 66% from 15 to 25 while the thickness and composition of the well and barrier is kept the same as previously. The optical confinement within the wells is improved by 25% (72 % confinement in MQW region), which leads to an enhanced electro-optic overlap. The calculated mode field profile in 2 μm wide deep etched ridge in structures with different number of wells is shown in Fig 5.13.

Table 5.2: Epitaxial layer structure grown (Sample: A-1914).

Material	Thickness (nm)	Doping (cm^{-3})	Conductivity (S/m)
P-InGaAs	20	5e19	69183
P-InGaAs	80	1e19	13864
P-InP	800	1e18	2403
P-InP	200	5e17	2403
i-InP	100	NUD	0
InAlGaAs (barrier)	10	NUD	0
25 \times InGaAs (well, 0.66% compressive) ($\lambda=1.85 \mu\text{m}$)	10	NUD	0
25 \times InAlGaAs (barrier, 0.84% tensile) ($\lambda=1.18 \mu\text{m}$)	10	NUD	0
i-InP	100	NUD	0
n-InP	100	5e17	27000
n-InP	200	1e18	41152
n-InP	-	-	-

The capacitance of the i-region of p-i-n diode is be related to the thickness of intrinsic region by simple relation i.e. ($C_i = \frac{\epsilon_o \epsilon_r A}{d}$), where d is the thickness of i-region, A is the area of the, ϵ_r is the perimittivity of i-region. The capacitance of the grown epitaxial layer structures i.e. with 15 MQW and 25 MQW was measured using C-V measurements. A series of circular diodes with a diameter of 1 mm were fabricated on both the structures and then CV measurements were performed at room temperature using Agilent B1500A Semiconductor Device

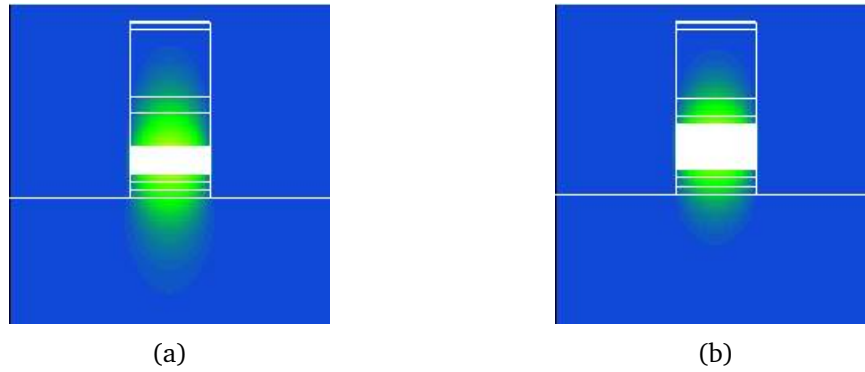


Figure 5.13: Simulated mode profile in 2 μm deep etched ridge structure using Fimmwave by PhotonD: (a) 15 MQW (47 % confinement). (b) 25 MQW (72 % confinement).

Analyzer. To remove the influence of probes and cables short open calibrations were performed. The comparison of measured capacitance normalized to area for both the grown structures is shown in Fig 5.14. It can be seen that capacitance of the structure with 25 MQW (Sample A1914) is slightly lower when fully depleted as compared to the other structure (Sample A1545). The behavior of the C-V measurement shows slight deviation from the expected results. As the intrinsic region of Sample A-1914 was kept 100 nm thinner than than A1545, it was expected that the sample with higher number of wells will show slightly higher capacitance. However, the measurements shows that the grown intrinsic region of the Sample A1914 is slightly thicker than A1545. The slight deviation is due to difference in growth conditions of MOVPE as both the samples were not grown sequentially. Despite the thicker intrinsic region than intended, it is important to determine the EO behavior of the grown structure, which is discussed in the next sections.

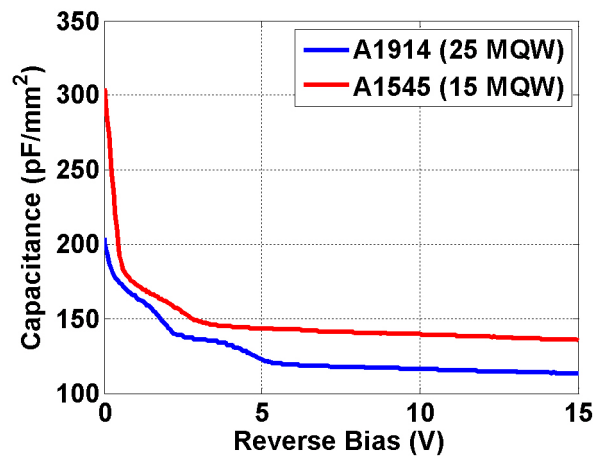


Figure 5.14: Measured capacitance-voltage properties of the circular diodes.

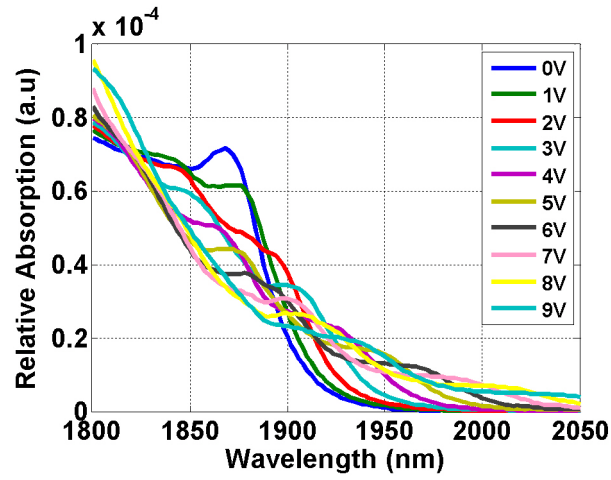
5.3.2 Photoabsorption response

The behavior of the pin structure with the increased number of wells was characterized by photo-absorption measurements using surface normal photo-diodes. This configuration results in absorption associated with in-plane TE polarization. The photo-absorption spectra using photocurrent measurements with the applied reverse voltage are shown in Fig 5.15. The measurements show an excitonic absorption at 1868 nm as compared to 1850 nm for the structure containing 15 MQWs. The absorption peak broadening with applied reverse bias is higher than the structure with 15 wells. Fig 5.15b shows the comparison of excitonic peak shift with the applied voltage for both the structures. At 6 V reverse bias, the structure with 25 MQW has a peak at 1964 nm with an absorption tail around the wavelength of operation. Increasing the reverse bias further shifts and broadens the excitonic peak due to decrease in electron-hole overlap but at the same time increases the absorption around 2000 nm. The effect of the higher absorption will be clear in the DC transfer function of the fabricated MZM devices.

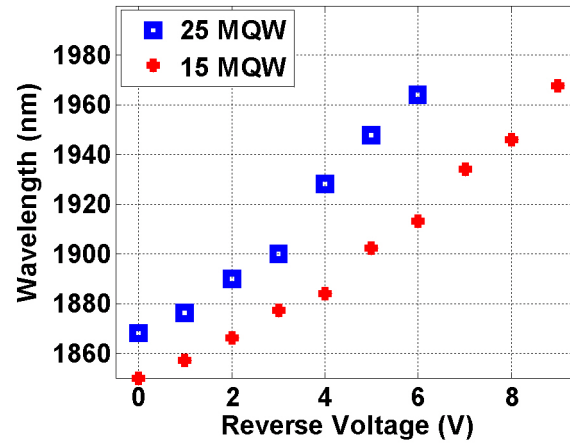
5.3.3 DC characterization

The grown wafer was then further processed to form MZMs with phase shifting regions with different lengths of TWE varying from 1.5 mm to 3.0 mm. The device layout remained the same as shown in Fig 5.4. The total size of a cleaved single modulator chip was the same as i.e. 1.1 mm x 6.6 mm. The measured leakage current for devices is less than 25 μA at -10 V. Fig 5.16 reports the measured DC transmission response of the modulator with the TWE length of 2 mm for both the outputs of the 2×2 MMI. The transfer function was measured at the wavelength of 1994.260 nm for TE polarized input light with the reverse bias voltage applied only to a single arm of the modulator. The modulator achieved a V_π of 2.7 V with DC extinction ratio of around 16 dB. There is a significant improvement of around 1.3 V in V_π with the increase in the number of wells. However, it was also observed that the fiber-to-fiber device IL is increased to ~ 19.8 dB as compared to 16 dB in the first generation MZMs containing 15 MQWs. The 3.8 dB increase in the loss can be attributed to the increased absorption around 2000 nm due to slight shift ~ 18 nm in excitonic absorption peak with the increase in QW number. This shift can also be due to slight variations in the growth conditions of the respective wafers resulting in a slight increase in quantum well/barrier thickness. In addition to the intrinsic

losses of the optical waveguide, the major source of the high IL of the devices is the fiber to modulator chip coupling losses. The coupling efficiency can be greatly improved by integrating spot-size converters (SSC) both at the input and output of the modulators. Integrated SSCs will produce a more circularly symmetric spot for efficient optical coupling to the input fiber with much higher misalignment tolerance and hence the IL can be reduced to < 10 dB, making the 2 μm MZM device performance more comparable to the currently available InP MZMs operating at 1.55 μm [21]. Also, the absorption spectrum shift with applied electric field is much stronger due to enhanced electro-optical overlap as shown in Fig 5.15a and Fig 5.15b. The modulator transmission response shows that the period between the successive maxima and minima is not constant which depicts that the induced phase shift with applied reverse bias is not the linear function of applied voltage. This nonlinear phase shift is caused by the voltage induced residual absorption which severely affects the ER and IL of the device as evident from the reduced transmission and degraded DC ER in Fig 5.16 at high reverse bias.



(a)



(b)

Figure 5.15: (a) Bias dependent spectral response of 25 quantum well strain-balanced structure under surface normal illumination. (b) Excitonic peak shift with the applied reverse bias measured for the PIN diode structures with 15 and 25 multiple quantum wells.

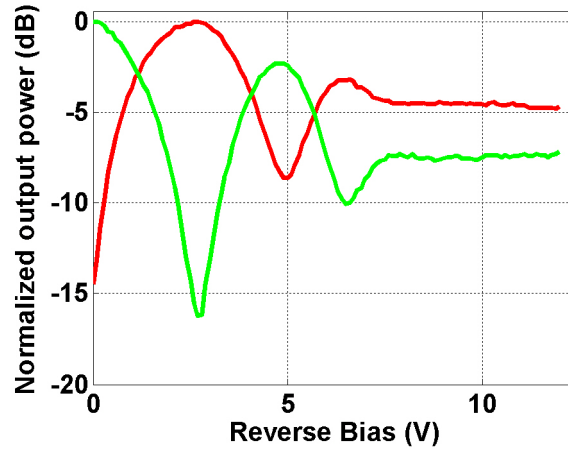


Figure 5.16: MZM transmission response with reverse bias applied to a single arm of modulator with 25 quantum wells. The length of phase shifting arm is 2.0 mm.

5.3.4 Modulator electro-optic response

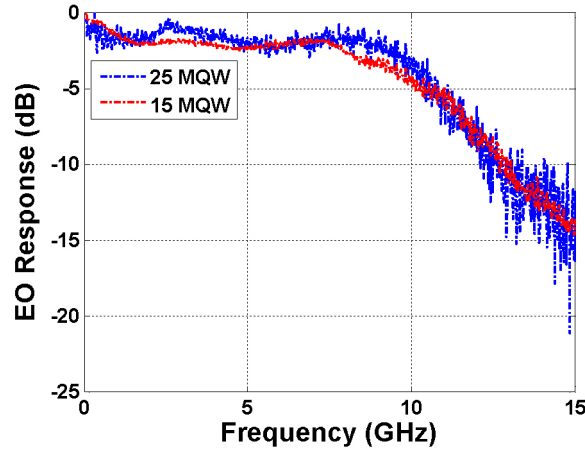
In the previous sections, the comparison of the absorption response and DC transmission function for the grown epitaxial layer structures with different number of quantum wells has been discussed. In this section, the high frequency response of the fabricated second generation TWE MZMs is shown. Following the procedure adapted previously, the electrical small signal response of the modulators were measured at first. Table 5.3 shows the comparison of 3-dB electrical bandwidths of both the generations of MZMs measured for different lengths of TWE.

Table 5.3: Comparison of 3-dB electrical small-signal bandwidth of MZM devices fabricated on two epitaxial layer structures.

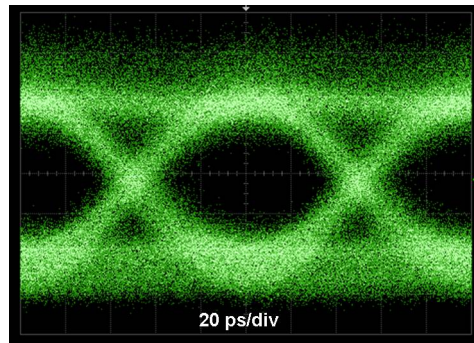
TWE Length (mm)	A1545 (15 MQW/SI-InP) (GHz)	A1914 (25 MQW/n-InP) (GHz)
1.5	19.5	12.82
2.0	15	11.5
2.5	12	10

It can be seen that that the 3-dB electrical bandwidth for MZM with TWE length of 1.5 mm is reduced from 19.5 GHz to 12.82 GHz. Similar trend was observed for devices with longer TWE lengths. The difference in bandwidth is believed to be due to the fact that first generation devices were fabricated on SI-InP substrate, whereas second generation devices were fabricated on n-doped InP substrate. Higher microwave losses were incurred in the feed in GSG

pads of the devices fabricated on n-InP substrate, which increased the over all microwave propagation loss and reduced the 3-dB electrical bandwidth. It can be also observed that with the increase in length of the TWE, the difference in 3-dB electrical bandwidth of devices on SI-InP and n-InP substrate decreases. It means that with the increasing length of the TWE, the microwave loss in TWE starts dominating as compared to the loss in feed in probe paths.



(a)



(b)

Figure 5.17: (a) Normalized EO response for modulators based on 15 and 25 MQWs. (b) Measured NRZ eye diagram of the 25 MQW modulator at 10 Gb/s.

Despite the lower electrical bandwidth of the second generation devices, the electro-optic response of the devices was measured using the same setup shown in Fig 5.9. The normalized small signal response of the modulators with 15 and 25 MQW respectively measured using on chip probe arrangement is shown in Fig 5.17a. Both the measured devices have a TWE length of 2 mm. It can be seen that increasing the number of wells does not affect the small-signal S21 EO response and both the devices exhibit a 3-dB EO bandwidth of 9 GHz. Fig 5.17b shows the large signal response of the second generation modulator at

10 Gb/s. The clearly open eye diagram shows the suitability of the fabricated devices for 10 Gb/s operation. The large signal response measurement setup is shown in Fig 5.10. The only difference in measurement was the gain setting of the input amplifier placed soon after PRBS source. Due to lower V_π of the second generation devices, the input PRBS sequence with 250 mV_{p-p} was only amplified to $\sim 3.5 V_{p-p}$ as compared to $\sim 6 V_{p-p}$ for the first generation devices with the same length of TWE i.e. 2.0 mm.

5.4 Modulator packaging

In order to evaluate the performance of the fabricated InP modulators in a transmissible system environment, the developed devices must be packaged. Before packaging, all the fabricated modulators devices were tested on DC and RF probe stations, which are mechanically very stable. However, probe stations are bulky and pose extra difficulties for testing the device in a transmission setup, which has many other photonic components in addition to the modulator device itself. For this purpose, a special low cost RF package was designed in HFSS and fabricated. The main idea of this package design was to reduce the testing complexity of the modulator by eliminating the need of RF probes. This was done by designing special RF interposer to deliver the RF modulating signal to the fabricated modulator devices. The main design goal was to keep the electrical insertion loss of the RF interposer assembly as low as possible upto 20 GHz in order to minimize its effect on the overall 3-dB electrical electrical bandwidth of the modulator.

5.4.1 RF interposer design

The first step in the design of RF interposer is the selection a suitable low cost RF coaxial connector with low insertion loss and high return loss in the desired range of frequency of operation. There is a variety of RF connectors available which have very small size and low insertion losses for frequencies upto 65 GHz such as V and K-connectors RF connectors. However, from the measurement of the electrical small-signal bandwidth of the modulator devices, it is clear that the fabricated modulators have 3-dB bandwidth of ~ 20 GHz for the shortest TWE. Keeping the device performance in view, high-speed mini-SMP connector PE 44490 from Pastenack were selected. The connector is low cost and can be soldered directly to the RF interposer board. It has a return loss of better than

15 dB in the 0-18 GHz frequency range. The insertion loss of the connector is 0.42 dB from 6-18 GHz [22]. The connector layout is shown in Fig 5.18. The central conductor pin of the coaxial connector is 0.5 mm with the ground pins spaced at 1 mm.

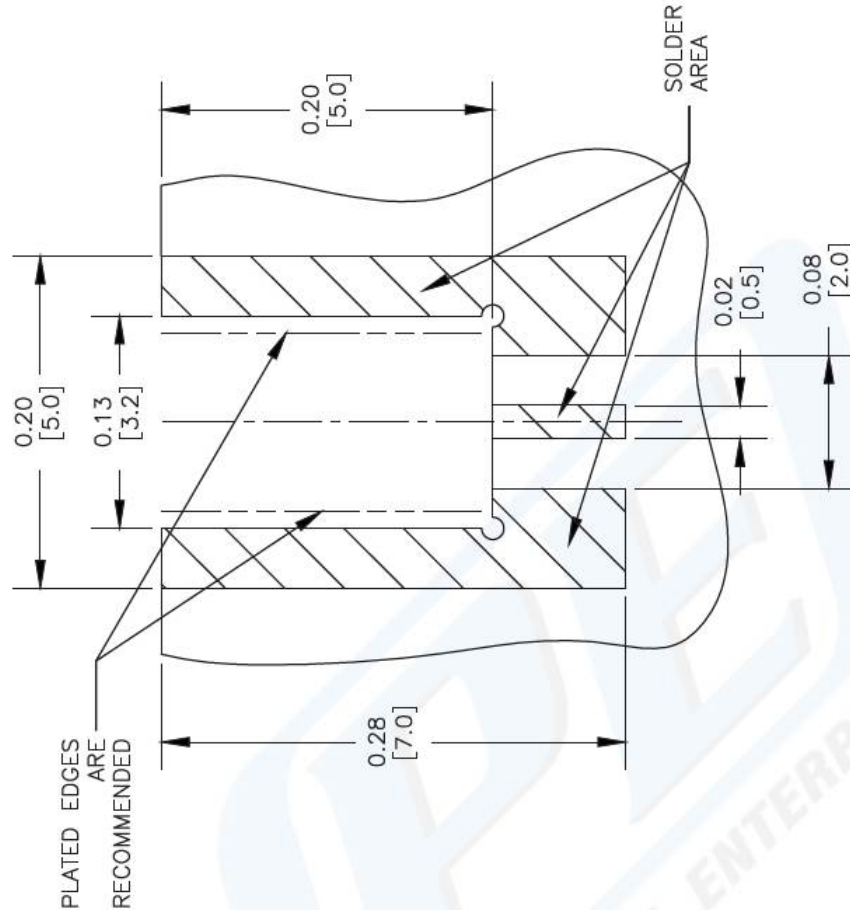


Figure 5.18: Layout of the mini-SMP connector from Pasternack (PE 44490). The dimensions in square brackets are in mm.

The RF connector cannot be soldered directly to the modulator device due to its small dimension and fragile nature. The wideband transition of RF signal from coaxial connector to the modulator devices is usually supported by conductor backed coplanar waveguide transmission (CBCPW) structures. The CBCPW structure acts as a bridge between coaxial RF connector and the device to be packaged. The presence of back metallization in the CBCPW structure makes it mechanically more robust and provides better heat sinking [23]. The signal from coaxial connector is launched into CBCPW intermediate block (RF interposer), which can be then connected to the modulator device through standard wire bonding. However, the transition from coaxial connector to CBCPW is very crucial and it is well known to excite the higher order modes. Due

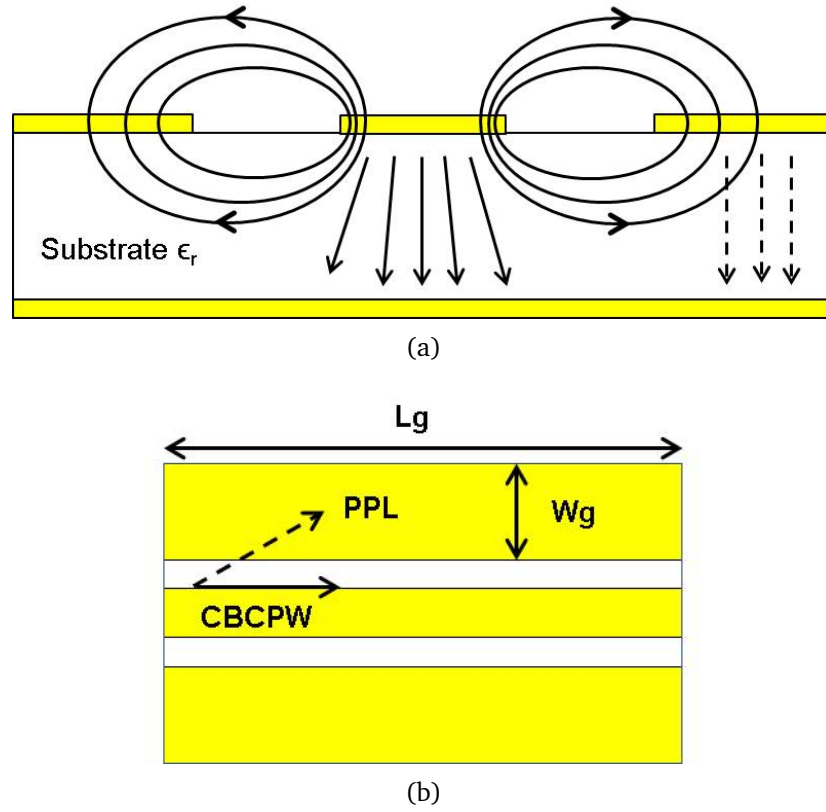


Figure 5.19: (a) Cross section CBCPW with finite width side ground planes. Solid lines show the CBCPW mode and dashed line show the parallel plate (PPL) mode. (b) Plan view of CBCPW. L_g is the length and W_g is width of ground plane.

to conductor backing, CBCPW becomes a multi modal structure resulting in the leakage of the dominant CPW mode into parasitic modes such as surface, parallel plate (PPL) and microstrip-like modes. The metal base represents an additional ground in addition to the side ground planes of CPW, which can alter the wave propagation properties of the structure [23, 24]. Fig 5.19 shows the cross section of a typical CBCPW transmission line. The dominant mode is CBCPW which can couple into side ground planes of CBCPW resulting in excitation of parallel plate (PPL) mode. These spurious modes will propagate along the waveguide and can generate patch antenna mode resonances specially in mm-wave frequency range depending on the width and length of ground plane of CBCPW [24]. To achieve only single mode propagation in CBCPW structure and suppress the excitation of parallel plate modes, several methods have been proposed over years such as inclusion of vias and use of air bridges [23–26]. In this work, vias were used to keep the bottom and top ground planes at the same potential and to avoid the leakage of RF energy into the substrate at any

discontinuity resulting in spurious mode propagation. For the interposer design high frequency laminate 4350B from Rogers was selected. The laminate has dielectric constant of 3.66 (up to 40 GHz) with substrate thickness of 0.508 mm. The substrate dielectric loss tangent ($\tan\delta$) is 0.004 and metal finish on the top of laminate is copper (Cu), electroplated to 32 μm .

Based on the material parameters full wave simulations were performed in HFSS and optimum dimensions of RF interposer were determined for the lowest insertion loss in desired frequency range. The final layout of the RF interposer is given in Fig 5.20. Table 5.4 shows the values assigned to different variables. The width of signal track (S1) on connector side is selected as 1 mm to accommodate the 0.5 mm wide central pin of the RF connector. The gap between signal and ground electrode is G1 and it has a value of 0.5 mm. Again the distance of central pin of conductor to ground pin was taken into account. The RF connectors layout with dimensions is shown in Fig 5.18. The signal track width and gap to ground planes i.e 1 and 0.5 mm gives the characteristic impedance of 50 Ω for the selected R4350B laminate. It is important to keep the characteristic impedance as close as possible to 50 Ω to avoid any impedance mismatch to the coaxial connector and also to ensure smooth transition of RF signal from coaxial connector to RF interposer. The value of L1 was selected as 2.3 mm to accommodate the 2 mm long central conductor pin of the RF connector. The width of the side ground plane (W1) towards the connector side was kept as 1.75 mm. It was kept as short as possible to move the resonant mode frequencies out of frequency band of interest (0-20 GHz) [24]. The GSG signal track was then tapered to dimensions as close as possible to dimension of the modulator input GSG pad. However, the low value of substrate permittivity ϵ_r restricts the minimum achievable dimensions. The length of the linear taper (Lt) was kept as 1 mm. The final dimension of the signal track (S2) was selected to be 0.4 mm and the gap between signal and ground electrode was 0.08 mm. This was the minimum achievable clearance given by the manufacturer. Based on the minimum clearance value, the width of signal track towards connector side was chosen to achieve 50 Ω impedance. The width of ground plane (W2) towards the device side was kept as 0.92 mm. This value was selected to allow the CPW termination resistance chip to be placed as close as possible to the output GSG pad of the modulator. In order to avoid the leakage of CPW mode into PPL mode, a number of vias were placed on both sides of the central signal track. These vias act as a fence to leakage of RF energy into spurious modes and must be strategically placed. The via radius and distance between vias were

optimized in order to achieve resonance free response and low insertion losses. The via radius was 0.150 mm with center to center spacing of 0.5 mm. The effect of number of vias and their effect on the RF insertion loss will be explained later. A 2.1 mm diameter (for M2 screw) clearance hole was introduced at the right side of interposer, so that the whole assembly including the terminated modulator device can be mounted on a test bench.

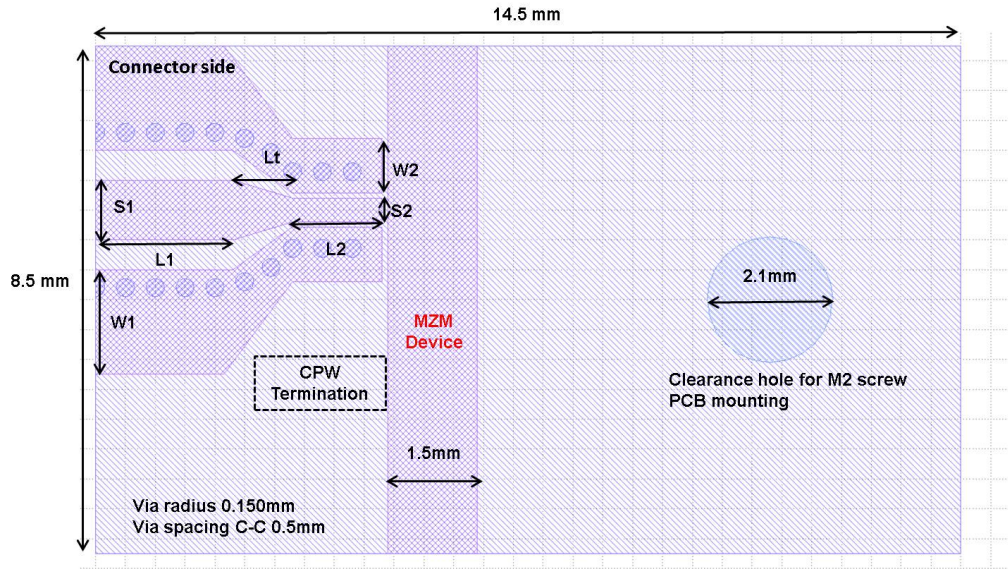


Figure 5.20: Layout of the RF interposer.

Table 5.4: Table listing dimensions of the RF interposer.

Parameter	Value (mm)
S1	1
G1	0.5
W1	1.75
L1	2.3
Lt	1
S2	0.4
G2	0.08
W2	1.75
L2	1.5

5.4.2 EM simulation setup and results

The RF interposer was simulated in HFSS to optimize its performance. The simulated structure and port setup is shown in Fig 5.21. Ideally the whole

structure including the RF connector should be simulated. However, modeling a connector is not a straight-forward task because very accurate information regarding structural dimensions and material used in connector assembly is required which is not provided by the vendor usually. As the insertion loss of the connector is very low, so is ignored in these simulations connector. In HFSS, a 3D structure can be excited either using wave port (external) or a lumped port (internal). A wave port is not suitable to emulate CBCPW structures because the port edge shorts the coplanar waveguide side ground planes and bottom ground plane, which introduces an artificial edge via holes at the start of the structure [27]. In addition, the correct size and placement of the wave port is mandatory to obtain the correct modal propagation characteristics. To avoid this situation, we have used lumped port for the excitation of CBCPW structure in these simulations. To set up the lumped port, the two side ground planes of the structure were shorted by perfect electrical conductor (PEC) bridge and lumped port was defined from center of the bridge to the central signal track. The only drawback of the lumped port is that there are parasitics associated with the bridge structure used to excite the RF interposer. In this case, the size of the bridge structure was optimized by reducing its span and height as much as possible to minimize parasitics. In mm-wave frequency range (30-300 GHz) effect of such parasitics must be de-embedded using the techniques given in [27].

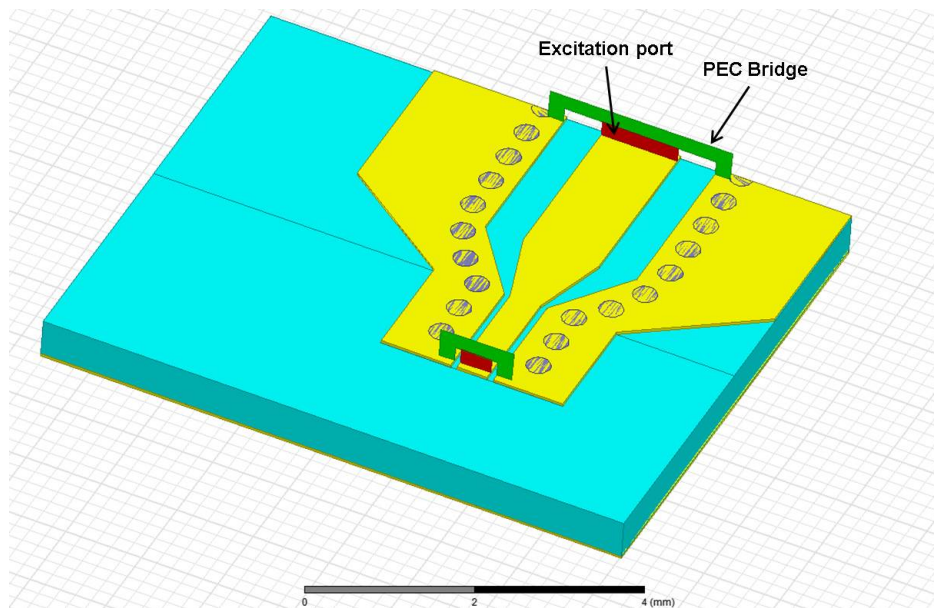
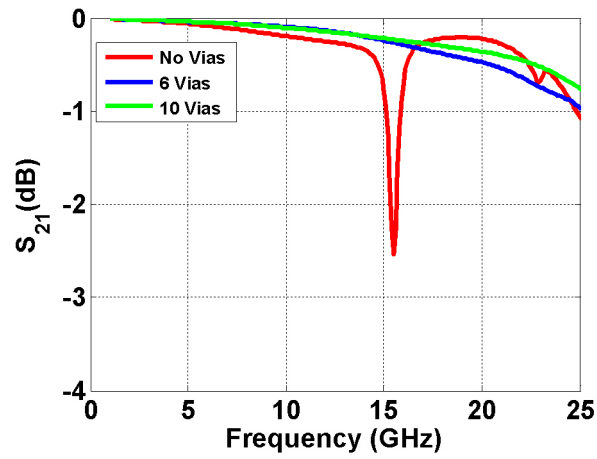


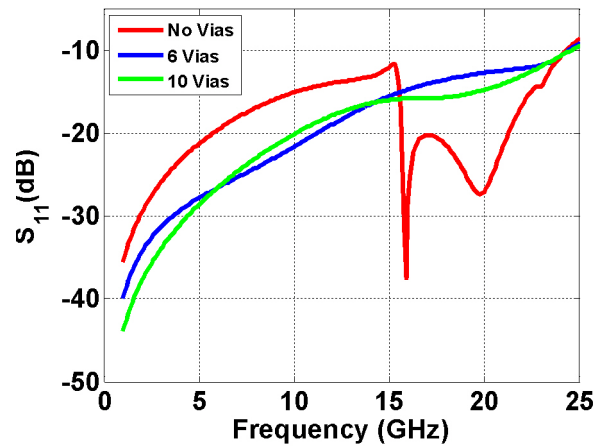
Figure 5.21: 3-D simulation model in HFSS.

The simulation results of the RF interposer layout described in the previous

section are shown in Fig 5.22. It shows the effect of presence of vias on the electrical S_{21} and S_{11} of the interposer. It can be observed that if there are no vias in the structure, there is a large resonance peak in S_{21} (red trace) at 15.5 GHz which degrades the transmission drastically. By adding vias, the resonance free response can be obtained up to 25 GHz with an insertion loss less than 1 dB. For 10 vias in the structure, an insertion loss of 0.35 dB was obtained through simulations as compared to 0.4726 dB for the case of 6 vias at 20 GHz. The simulated value of S_{11} is just below -14.5 dB at 20 GHz for the interposer with 10 vias. Because of low insertion loss, the RF interposer design with 10 vias was selected for the final fabrication.



(a)



(b)

Figure 5.22: HFSS simulation results of the interposer structure with different number of vias (a) S_{21} . (b) S_{11} .

After optimizing the RF interposer structure, the next step was to determine

the performance of the interposer when connected to the modulator device through Au bonding wires (BW) through HFSS simulations. The Au wires used in the simulations have a diameter of 18 μm . The length of BWs were kept as short as possible to keep the inductance low. Fig 5.23 shows different structures simulated in HFSS. The only difference between the two structures is the ground of the wire bonded MZM device. In Fig 5.23a, the ground between the input and output GSG bond pad of the MZM is not continuous, which is similar to the fabricated MZMs. On the other hand, MZM device shown in Fig 5.23b has a continuous ground which allows more BWs to be connected. The dimensions of RF interposer were kept same as described in the previous section. The MZM device used in simulations is based on an SI-InP substrate with TWE length of 2 μm and the device layout is the same as the actual fabricated device. The simulation results of the modulator device closely follow the measured results for MZM with 2 mm TWE shown in Fig 5.8 previously. The simulated S_{21} and S_{11} of RF interposer wire bonded to MZM are shown Fig 5.24. It can be seen that when the MZM with discontinuous ground was wire bonded to RF interposer, a resonance was observed in simulated S_{21} at the frequency of 13.06 GHz (blue trace). However, this resonance goes away, when the grounds were connected and extra BWs were added. The addition of more BWs gives more smoother S_{21} (red trace). The simulation results also show that the insertion loss of the RF interposer has negligible effect on overall electrical small-signal performance of MZM, which was one the main design goal of the interposer design. Also, as mentioned above, the actual fabricated MZM devices are with discontinuous ground planes, which means only 3 BWs can be used to connect the RF interposer due to space limitation.

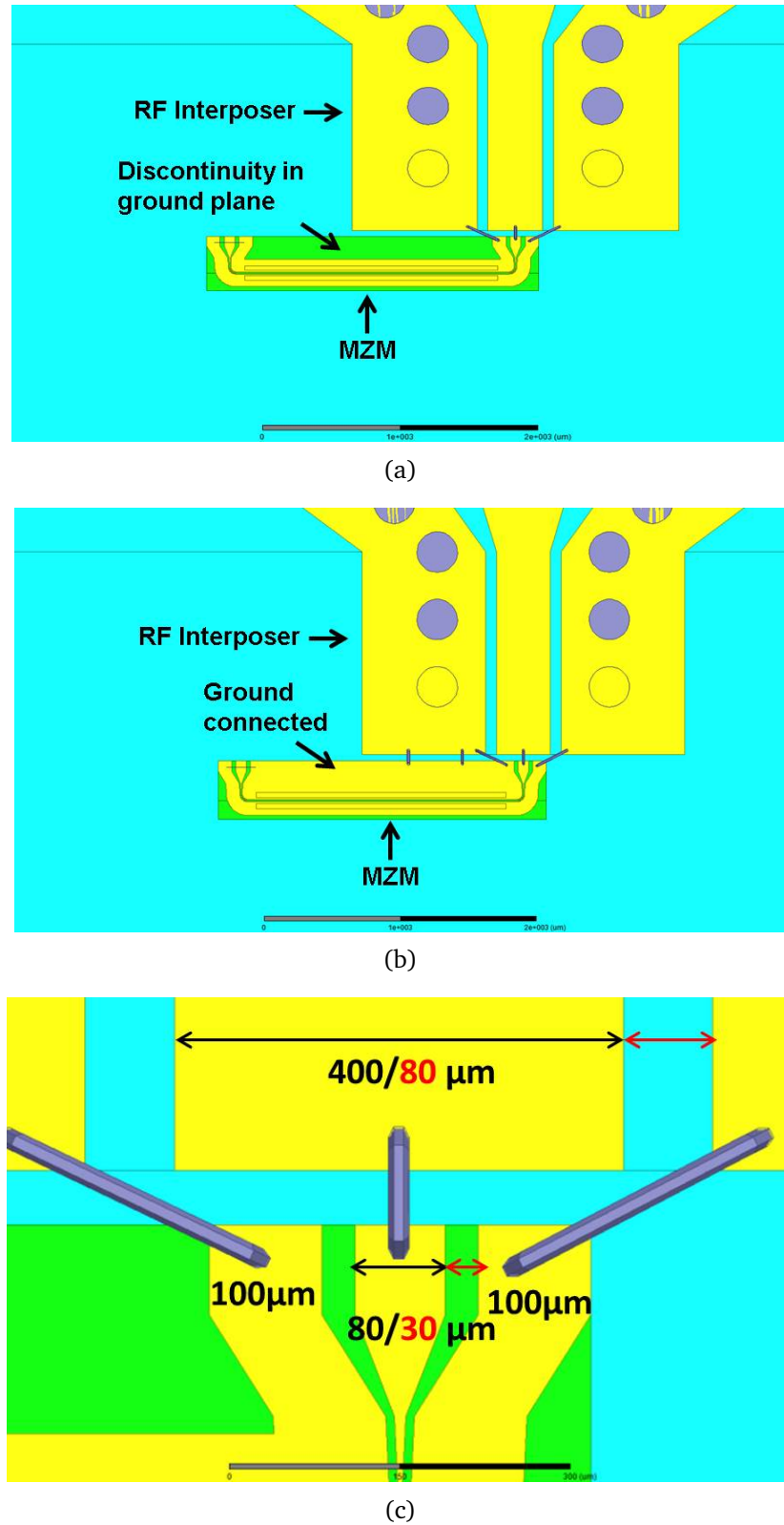


Figure 5.23: Plan view of the different structures simulated in HFSS: (a) RF interposer wire bonded to MZM with discontinuous ground. (b) RF interposer wire bonded to MZM with continuous ground and additional BWs. (c) Scaled up image of wire bond transition of RF interposer to MZM with dimensions.

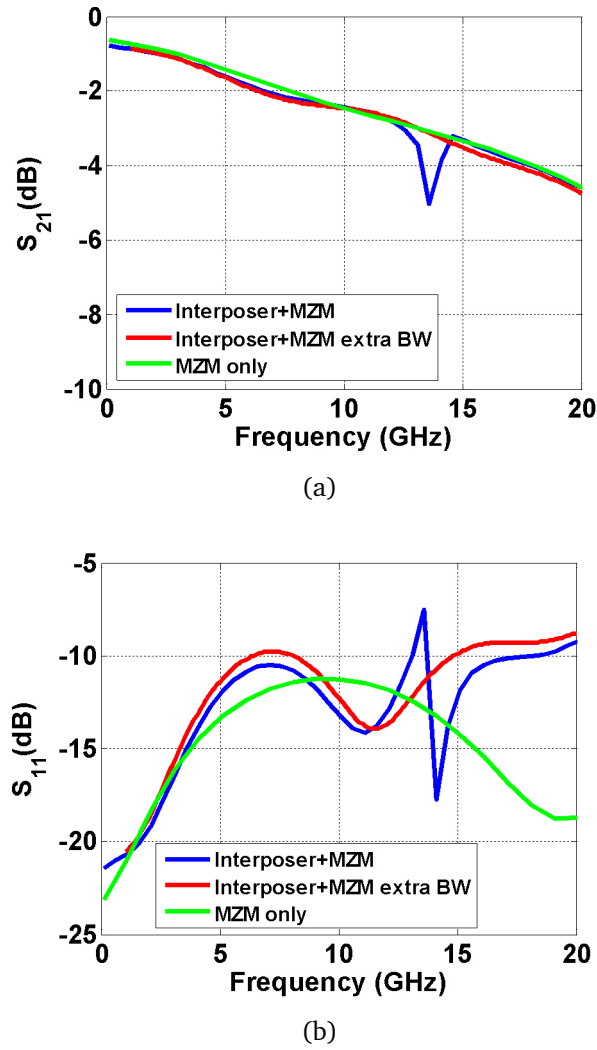


Figure 5.24: Simulation results of RF interposer wire bonded to a MZM device. Blue trace represents the MZM with discontinuous ground + RF interposer, red trace shows the the MZM with continuous ground + RF interposer and green trace represents the MZM device only. (a) S_{21} . (b) S_{11} .

5.4.3 Experimental verification of packaged modulator

An array of fabricated RF interposer chips is shown in Fig 5.25. Due to the large size of a single RF interposer board, it cannot be fixed in a standard butterfly package. Because of this reason the RF interposer was only helpful to eliminate the need of GSG RF probe for input RF+DC signal and termination of the modulator. However, input optical signal into the modulator device was still manually coupled using a pair of lensed fibers arranged on XYZ manual alignment stages to align the fibers to the input and output waveguide facets of MZM. For the ease of testing of the modulator, a special mounting assembly was

designed according to the dimensions of interposer board and fiber alignment tolerance. The CAD model of the optical test setup is shown in Fig 5.26.

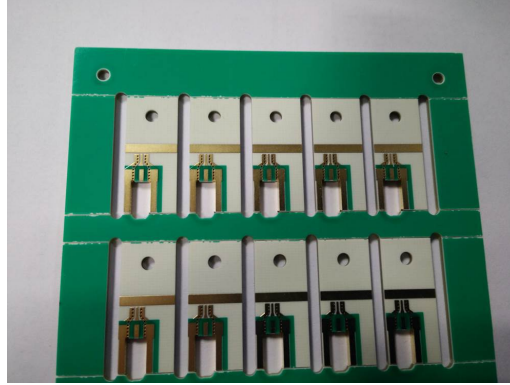


Figure 5.25: Array of fabricated RF interposer boards before soldering of the connectors.

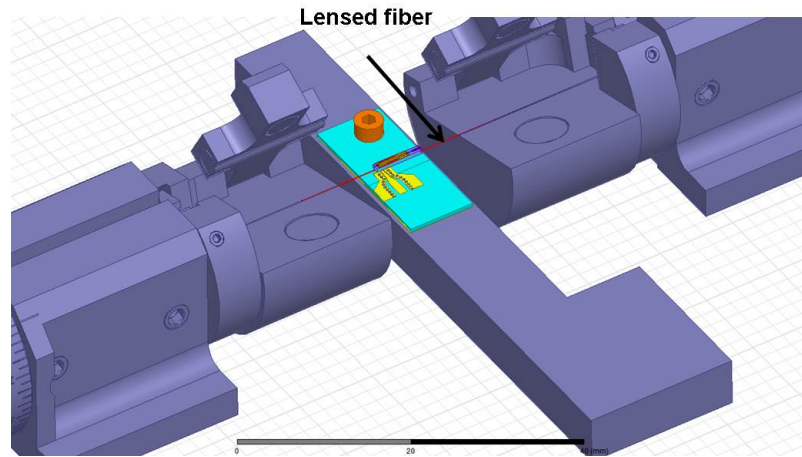
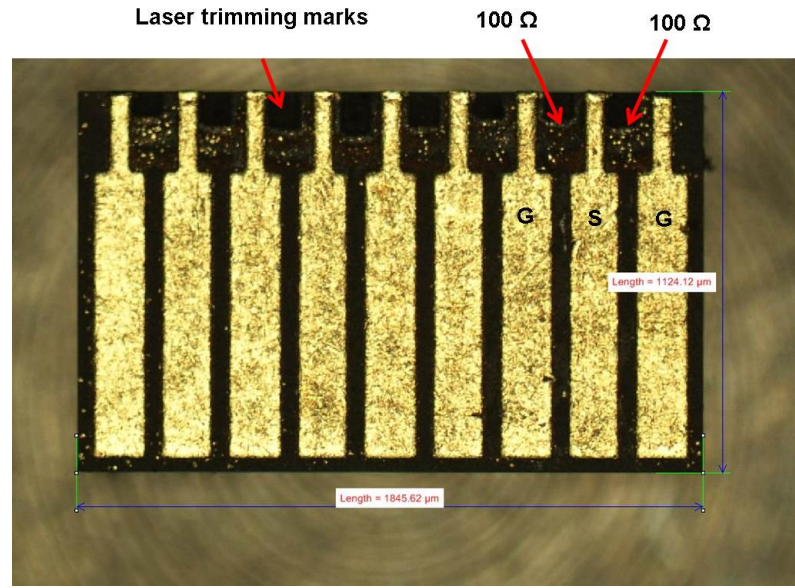
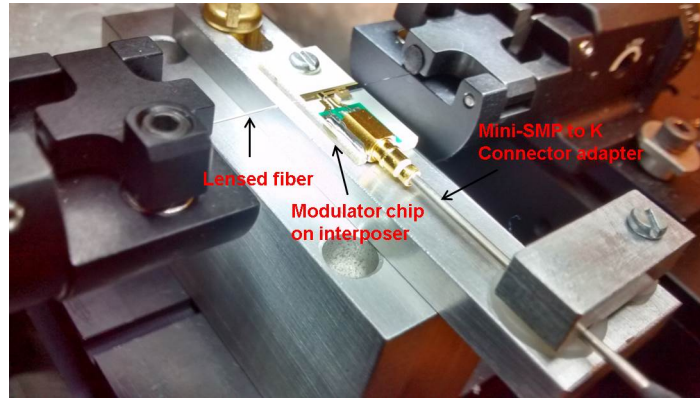


Figure 5.26: CAD model of the mounting assembly designed for testing of the packaged modulator.

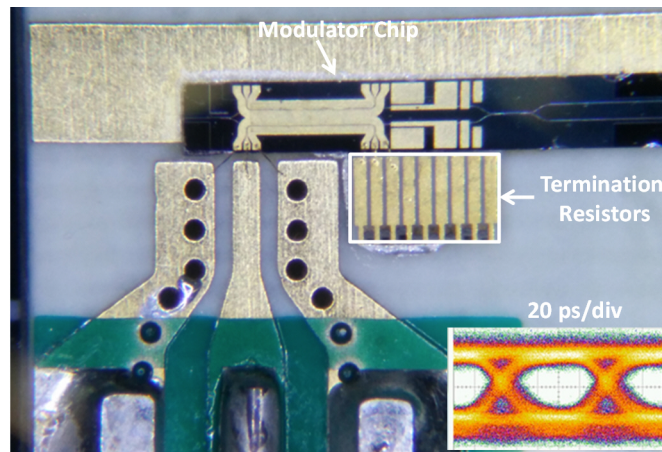
The modulator chips were then cleaved and wire bonded to a low-cost PCB RF interposer and $50\ \Omega$ off-chip termination. The off-chip termination resistor is basically an array of CPW transmission lines terminated with $100\ \Omega$ resistors which act as $50\ \Omega$ when connected in parallel to GSG pads of the MZM. The chips were fabricated on Aluminium Oxide substrate (Al_2O_3) and termination resistors were trimmed to adjust the value of resistors. The design and fabrication of termination resistors was performed by IMST (Germany). Fabricated array of termination resistors is shown in Fig 5.27a.



(a)



(b)



(c)

Figure 5.27: (a) Image of the fabricated off-chip termination resistor. (b) Image of test bench with packaged modulator device. (c) Optical image of the packaged InP MZM chip. Inset shows the measured diagram at 10Gb/s after packaging.

To test the performance of the RF interposer board wire bonded to MZM and off-chip termination resistor, it was mounted on the test bench as shown in Fig 5.27b. A clear optical image of the MZM and termination resistor wire bonded to the RF interposer is shown in Fig 5.27c. The DC and RF modulating signal was delivered to the modulator through a bias-tee. A 10 Gb/s modulating signal was provided by the PRBS source and was amplified before bias-tee. DC bias was adjusted carefully at the quadrature point of MZM transfer function. A mini-SMP to K-connector adapter from SHF Technologies (CA292M119SMPM) was used to connect the output of bias-tee to high-speed mini-SMP connector which was soldered on to the PCB board. Optical signal from a packaged laser emitting 2 dBm peak power at 2002 nm was launched in to MZM using lensed fibers. The high-speed performance of the packaged modulator was confirmed by measuring a clearly open eye diagram at 10 Gb/s. The inset of Fig 5.27c shows the large signal response of the modulator chip after the packaging.

An important observation made during the wire bonding process of the second generation modulator devices was the delamination of the bond pads. The bondpad delamination is shown in Fig5.28. This can occur due to poor adhesion of the Au contacts to the planarised BCB. To improve the adhesion silicon dioxide layer must be deposited on the top of planarized BCB. This adhesive layer was not included during fabrication process of the second generation devices resulting in failure of wire bonding. Because of this reason only the first generation devices were packaged and further tested for optical transmission performance.

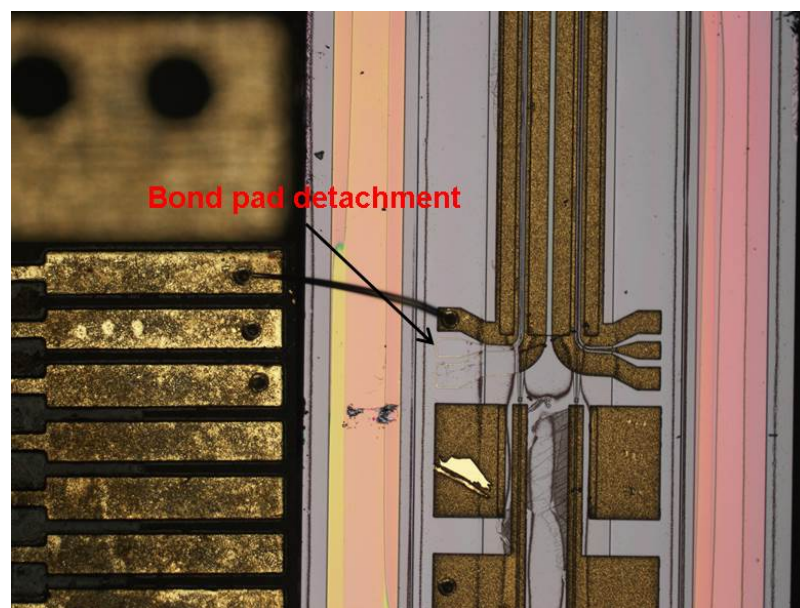


Figure 5.28: Delamination of bondpad during wire bonding process.

5.5 40 Gb/s WDM transmitter

The packaged modulator was then used to perform the WDM transmission experiment. To analyze the transmission performance, a 40 Gb/s WDM signal is transmitted over 1.15 km HC-PBGF. The total capacity is achieved by externally modulating four lasers with NRZ-OOK at 10 Gb/s each, spanning a total bandwidth of 300 GHz. The transmission performance of the modulator is discussed in details in this section.

5.5.1 Experimental setup for WDM transmission

The complete experimental setup is shown in Fig 5.29. The transmitter consisted of four externally modulated channels with the spacing of 100 GHz at 1991.32, 1992.67, 1994.00, 1995.29 nm respectively. The lasers used in the transmitter have maximum output power of 2 dBm and are based on highly strained $\text{In}_{0.75}\text{Ga}_{0.25}\text{As}$ MQW structure grown on InP substrate optimized for single mode operation at these wavelengths with SMSR > 40 dB [8]. The lasers were packaged in 14-pin butterfly modules with a TEC, thermistor, and dual-stage optical isolators. The four channels were passively multiplexed and then externally modulated using the InP MZM driven by a $2^{31}-1$ PRBS from a pulse pattern generator PPG. The fiber-based passive multiplexer had an insertion loss of 10 dB.

Keeping in view the polarization sensitive nature of the QCSE effect in strained quantum wells, PCs were added after each laser channel to set the input light to TE polarization. Prior to the transmission, the signal was amplified using a TDFA to compensate for the losses incurred at the transmitter. WDM signal was launched in to HC-PBGF of 1.15 km, typically consisting of 19 cells, with a loss of 2.8 dB/km. Single mode operation was ensured by splicing to SMF at both ends via a short large mode area (LMA) buffer fiber with mode, resulting in an end-to-end total loss of ~ 9.8 dB at 2000 nm. The attenuation spectrum of HC-PBGF used in the experiment is shown in Fig 5.30. The fiber has a reported 3-dB spectral bandwidth of 85 nm [6, 28]. To date, the longest available HC-PBGF for operation around 2 μm wavelengths is 3.85 km which has been very recently reported in [29]. The measured full WDM spectrum before and after transmission over 1.15 km HC-PBGF is shown in Fig 5.31.

The pre-amplified receiver comprised of a variable optical attenuator followed by a 2nd TDFA which was used to amplify the received WDM signal after transmission over HC-PBGF. The optical attenuator was used to vary the op-

tical signal-to-noise ratio (OSNR) measured within a 0.1 nm bandwidth. The OSNR was varied by controlling the input power to the 2nd TDFA. The output of the TDFA was fed into a fully packaged in-house developed arrayed waveguide grating (AWGr) which was designed to act as 100 GHz filter. The AWGr chip size was 13 mm \times 7 mm and it was packaged in a housing containing a Peltier device for temperature control with single input channel and 10-channel output array. The measured adjacent crosstalk was better than 18 dB. The thermal dependence of the AWGr chip was measured to be 0.108 nm/ $^{\circ}\text{C}$ while the average insertion loss per channel was up to 18 dB. Further details on the AWGr design and performance can be found in [13, 30].

To compensate for the losses of the packaged AWGr, a 3rd TDFA was required to ensure constant optical power to the receiver PD. The amplified optical signal after the 3rd TDFA was filtered using a commercially available optical tunable filter with a 3-dB bandwidth of 1.6 nm to minimize the effect of out-of-band ASE. Another variable attenuator was incorporated before PD, and it was adjusted to guarantee a constant optical power of -3 dBm at the PD for all the wavelengths. A 7 GHz bandwidth, 2 μm PD was used in combination with an RF amplifier for the direct detection. The resulting amplified electrical signal was then analyzed using an Agilent 86100C DCA for eye diagram and error detector for bit error rate (BER) measurement.

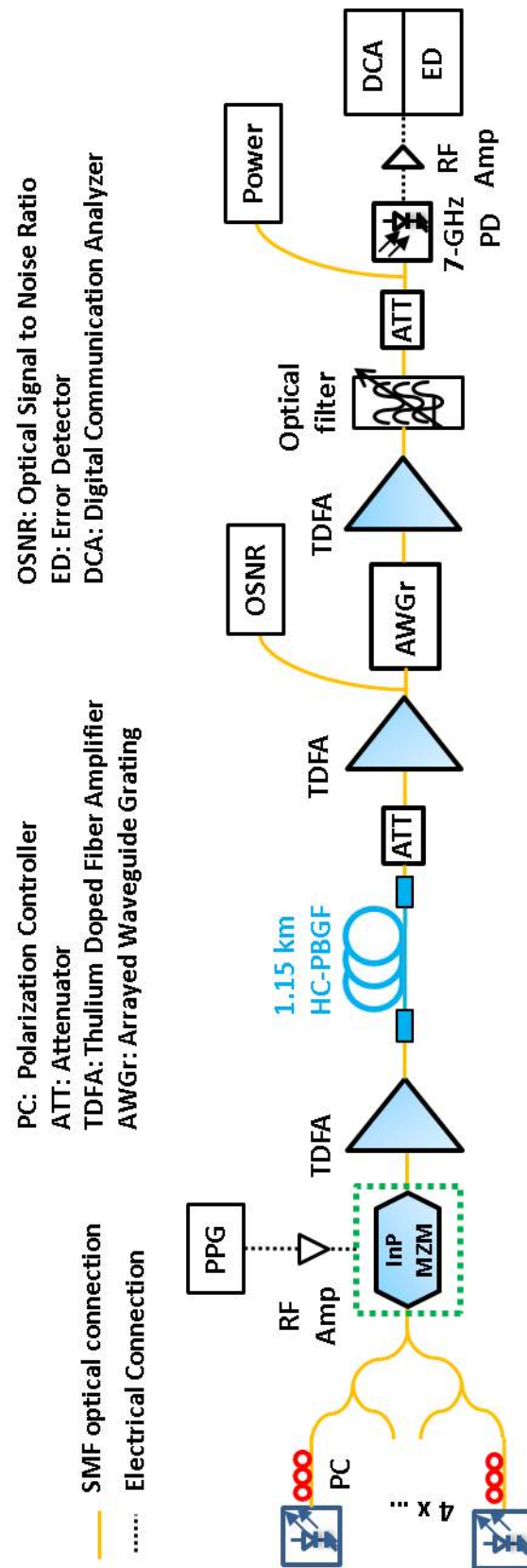


Figure 5.29: WDM transmission experimental setup.

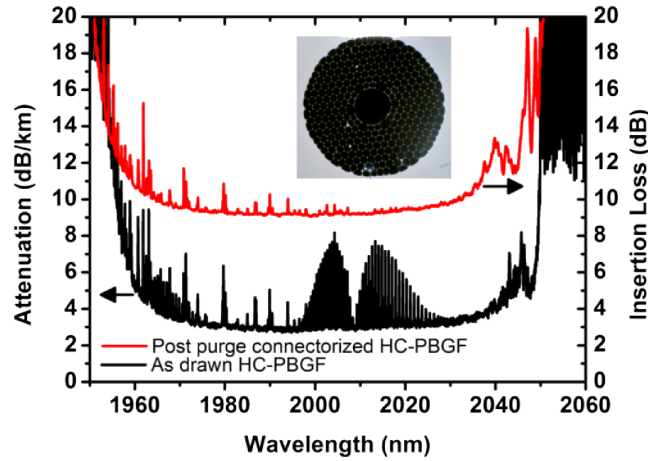


Figure 5.30: Transmission spectra of the HC-PBGF sample used in the experiment; black trace: attenuation of the as-drawn fiber; red trace: insertion loss of the pigtailed sample. The inset shows an optical microscope image of the HC-PBGF [7].

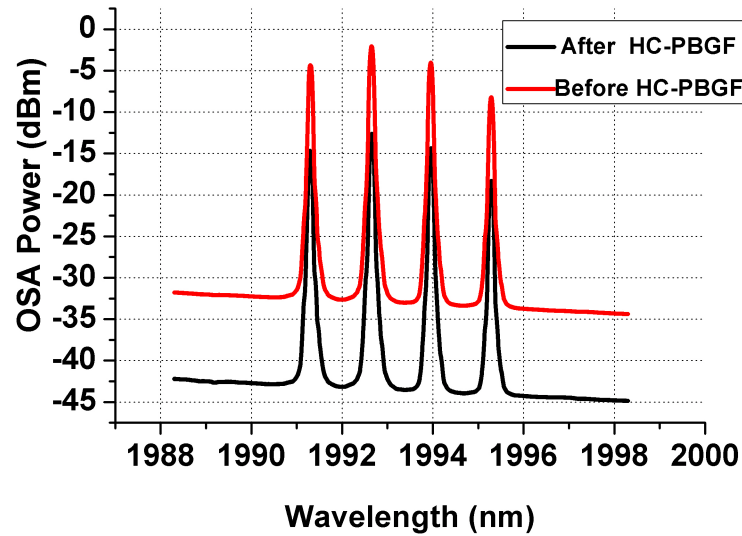


Figure 5.31: WDM spectrum before (after 1st TDFA) and HC-PBGF transmission.

5.5.2 Transmission performance of InP MZM

Fig 5.32 shows the transmission performance of the WDM system at 2 μm . The performance is evaluated in terms of BER vs. OSNR for each channel externally modulated at the data rate 10 Gb/s using a PRBS sequence length of $2^{31}-1$ after transmission over 1.15 km HC-PBGF. The average OSNR required to achieve a BER of 10^{-9} is 25.76 dB and OSNR spread between the channels is around 2 dB. The spreading is believed to be due to the limited extinction ratio of the AWGr.

Another probable cause can be the unequal amplifier gain for different channels as shown in the WDM spectrum of Fig 5.31. Also, it should be noted that due to the short length of HC-PBGF used in the experiment the OSNR penalty due to the transmission for the externally modulated channels is negligible, <0.5 dB as reported earlier [6]. This is also evident from the received eye diagram of externally modulated channels at 1994.00 nm and 1995.29 nm respectively after transmission as shown in Fig 5.33. It can be seen clearly that the eye is fully-open even after the transmission over 1.15 km HC-PBGF showing no significant effect of fiber induced impairment.

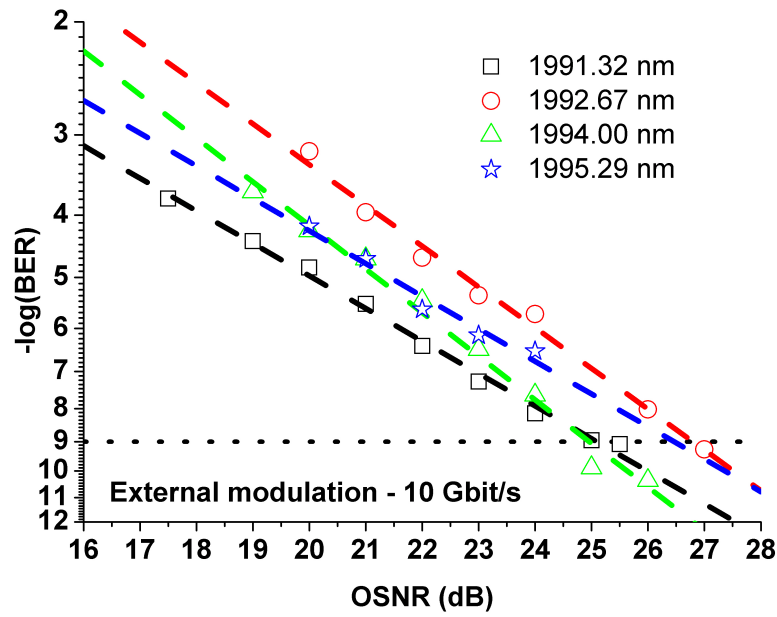


Figure 5.32: BER vs. OSNR performance of individual externally modulated WDM channels on 100 GHz grid after transmission over 1.15 km HC-PBGF.

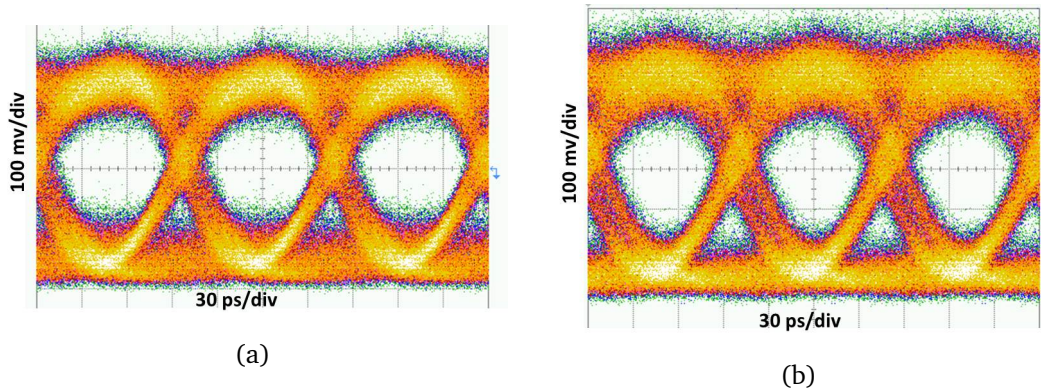


Figure 5.33: Eye diagram of NRZ-OOK externally modulated channel after transmission at: (a) 1994.00 nm. (b) 1995.29 nm.

5.6 Summary

In this chapter, InP based modulators working around 2000 nm with EO bandwidth of 9 GHz suitable for 10 Gb/s NRZ modulation rate were demonstrated for the first time. Two generations of the devices were fabricated on two different epitaxial material and fully tested. The number of MQWs in material (A1545) used for the fabrication of the first generation devices were 15 with total i-region thickness of 810 nm. On the other hand, second generation of devices were fabricated on material (A1914) with higher number of MQWs (66% higher-25 MQWs) with total i-region thickness of 710 nm. The C-V measurements on specially fabricated circular diodes structures for both the epitaxial materials reveal that the second generation devices have lower capacitance as compared to the first generation devices. Despite the thicker growth of i-region than intended, second generation devices have lower V_π as compared to first generation devices for the same length and dimensions of TWE. The photabsorption response measurements on surface entry diodes also shows the higher shift of excitonic peak. Lower V_π and higher excitonic peak shift means that even with the thicker i-region, second generation devices have higher electro-optic overlap due to higher number of MQWs. The thicker i-region may be due to the increase in thickness of wells/barriers during MOVPE growth in A1914 material as both the materials were not grown sequentially. This may lead to slight deviation in growth conditions.

The fabricated MZMs were also packaged using a specially designed RF interposer with electrical insertion loss less than 0.5 dB at 20 GHz. The packaged devices were then deployed in a high-capacity WDM transmitter for communications in the 2 μm spectral region. A WDM capacity of 40 Gb/s was achieved by using four 10 Gb/s NRZ-OOK externally modulated channels employing the InP MZM. An OSNR requirement of 25-27 dB was measured to achieve a BER of 10^{-9} . The OSNR requirement can be relaxed through reduction in the insertion loss of the modulator and AWGr by improving the design which will in turn reduce the need for TDFAs, thus reducing the noise in the system. Due to low V_π , the presented modulators can also be used to develop the integrated IQ modulator to implement higher order phase modulation formats at 2000 nm.

References

- [1] G. J. Koch, B. W. Barnes, M. Petros, J. Y. Beyon, F. Amzajerdian, J. Yu, R. E. Davis, S. Ismail, S. Vay, M. J. Kavaya, and U. N. Singh, "Coherent differential absorption lidar measurements of CO₂," *Appl. Opt.*, vol. 43, no. 26, pp. 5092–5099, Sep 2004.
- [2] T. Refaat, S. Ismail, G. Koch, M. Rubio, T. Mack, A. Notari, J. Collins, J. Lewis, R. De Young, Y. Choi, M. Abedin, and U. Singh, "Backscatter 2- μ m lidar validation for atmospheric CO₂ differential absorption lidar applications," *Geoscience and Remote Sensing, IEEE Transactions on*, vol. 49, no. 1, pp. 572–580, Jan 2011.
- [3] S. Moro, A. Danicic, N. Alic, N. G. Usechak, and S. Radic, "Widely-tunable parametric short-wave infrared transmitter for CO₂ trace detection," *Opt. Express*, vol. 19, no. 9, pp. 8173–8178, Apr 2011.
- [4] P. J. Roberts, F. Couny, H. Sabert, B. J. Mangan, D. P. Williams, L. Farr, M. W. Mason, A. Tomlinson, T. A. Birks, J. C. Knight, and P. S. Russell, "Ultimate low loss of hollow-core photonic crystal fibres," *Opt. Express*, vol. 13, no. 1, pp. 236–244, Jan 2005.
- [5] Z. Li, A. M. Heidt, J. M. O. Daniel, Y. Jung, S. U. Alam, and D. J. Richardson, "Thulium-doped fiber amplifier for optical communications at 2 μ m," *Opt. Express*, vol. 21, no. 8, pp. 9289–9297, Apr 2013.
- [6] H. Zhang, Z. Li, N. Kavanagh, J. Zhao, N. Ye, Y. Chen, N. Wheeler, J. Wooler, J. Hayes, S. Sandoghchi, F. Poletti, M. Petrovich, S. Alam, R. Phelan, J. O'Carroll, B. Kelly, D. Richardson, B. Corbett, and F. Garcia Gunning, "81 Gb/s WDM transmission at 2 μ m over 1.15 km of low-loss hollow core photonic bandgap fiber," in *Optical Communication (ECOC), 2014 European Conference on*, Sept 2014, pp. 1–3.

- [7] M. N. Petrovich, F. Poletti, J. P. Wooler, A. Heidt, N. Baddela, Z. Li, D. Gray, R. Slavík, F. Parmigiani, N. Wheeler, J. Hayes, E. Numkam, L. Grúner-Nielsen, B. Pálsdóttir, R. Phelan, B. Kelly, J. O'Carroll, M. Becker, N. Mac-Suibhne, J. Zhao, F. G. Gunning, A. Ellis, P. Petropoulos, S. Alam, and D. Richardson, "Demonstration of amplified data transmission at 2 μm in a low-loss wide bandwidth hollow core photonic bandgap fiber," *Opt. Express*, vol. 21, no. 23, pp. 28 559–28 569, Nov 2013.
- [8] R. Phelan, J. O'Carroll, D. Byrne, C. Herbert, J. Somers, and B. Kelly, "In_{0.75}Ga_{0.25}As/InP multiple quantum-well discrete-mode laser diode emitting at 2 μm ," *Photonics Technology Letters, IEEE*, vol. 24, no. 8, pp. 652–654, April 2012.
- [9] S. Luo, H. M. Ji, F. Gao, F. Xu, X. G. Yang, P. Liang, and T. Yang, "High performance 2150 nm-emitting InAs/InGaAs/InP quantum well lasers grown by metalorganic vapor phase epitaxy," *Opt. Express*, vol. 23, no. 7, pp. 8383–8388, Apr 2015.
- [10] E. Rouvalis, C. Metzger, A. Charpentier, T. Ayling, S. Schmid, M. Gruner, D. Hoffmann, M. Hamacher, G. Fiol, and M. Schell, "A low insertion loss and low v_π InP IQ modulator for advanced modulation formats," in *Optical Communication (ECOC), 2014 European Conference on*, Sept 2014, pp. 1–3.
- [11] N. Kikuchi, E. Yamada, Y. Shibata, and H. Ishii, "High-Speed InP-based Mach-Zehnder Modulator for Advanced Modulation formats," in *Compound Semiconductor Integrated Circuit Symposium (CSICS), 2012 IEEE*, Oct 2012, pp. 1–4.
- [12] S. Heck, S. Jones, R. Griffin, N. Whitbread, P. Bromley, G. Harris, D. Smith, L. Langley, and T. Goodall, "Miniaturized InP dual I & Q Mach Zehnder modulator with full monitoring functionality for cfp2," in *Optical Communication (ECOC), 2014 European Conference on*, Sept 2014, pp. 1–3.
- [13] N. Ye, M. Gleeson, M. Sadiq, B. Roycroft, C. Robert, H. Yang, H. Zhang, P. Morrissey, N. Mac Suibhne, K. Thomas, A. Gocalinska, E. Pelucchi, R. Phelan, B. Kelly, J. O'Carroll, F. Peters, F. Gunning, and B. Corbett, "Inp-based active and passive components for communication systems at 2 μm ," *Journal of Lightwave Technology*, vol. 33, no. 5, pp. 971–975, March 2015.

- [14] A. Liu, L. Liao, D. Rubin, H. Nguyen, B. Ciftcioglu, Y. Chetrit, N. Izhaky, and M. Paniccia, "High-speed optical modulation based on carrier depletion in a silicon waveguide," *Opt. Express*, vol. 15, no. 2, pp. 660–668, Jan 2007.
- [15] C. Doerr, L. Zhang, P. Winzer, J. Sinsky, A. Adamiecki, N. Sauer, and G. Raybon, "Compact High-Speed InP DQPSK Modulator," *Photonics Technology Letters, IEEE*, vol. 19, no. 15, pp. 1184–1186, Aug 2007.
- [16] S. Tomonari, M. Mitsuhashi, and Y. Kondo, "InAs Quantum-well Distributed Feedback Lasers Emitting at 2.3 μm for gas sensing applications," *NTT Technical Review*, vol. 7, no. 1, Aug 2009.
- [17] J. Nkanta, "Characterization and Simulations of Long Wavelength InAlGaAs/InP Lasers," Ph.D. dissertation, University of Ottawa, Ottawa, 2008.
- [18] E. Chen and A. Murphy, *Broadband Optical Modulators Science, Technology, and Applications*. CRC Press, 2011.
- [19] M. Sadiq, B. Roycroft, J. O'Callaghan, P. Morrissey, W. Han, F. Peters, and B. Corbett, "Efficient modelling approach for an InP based Mach-Zehnder modulator," in *Irish Signals Systems Conference 2014 and 2014 China-Ireland International Conference on Information and Communications Technologies (ISSC 2014/CIICT 2014)*. 25th IET, June 2014, pp. 123–128.
- [20] D. Penninckx and P. Delansay, "Comparison of the propagation performance over standard dispersive fiber between InP-based π -phase-shifted and symmetrical mach-zehnder modulators," *Photonics Technology Letters, IEEE*, vol. 9, no. 9, pp. 1250–1252, Sept 1997.
- [21] G. Letal, K. Prosyk, R. Millett, D. Macquistan, S. Paquet, O. Thibault-Maheu, J.-F. Gagne, P.-L. Fortin, R. Dowlathshahi, B. Rioux, T. SpringThorpe, M. Hisko, R. Ma, and I. Woods, "Low loss InP C-band IQ modulator with 40GHz bandwidth and 1.5v v_{π} ," in *Optical Fiber Communications Conference and Exhibition (OFC)*, 2015, March 2015, pp. 1–3.
- [22] Pasternack, "Mini SMP Male connector Solder Attachment End Launch PCB," 2013.
- [23] J. Chen, S. Chen, and P. Hsu, "Leakage-reduced conductor-backed coplanar waveguide with periodic structures and its antenna application," *An-*

- tennas and Propagation, IEEE Transactions on*, vol. 59, no. 6, pp. 2078–2086, June 2011.
- [24] W. Haydl, “On the use of vias in conductor-backed coplanar circuits,” *Microwave Theory and Techniques, IEEE Transactions on*, vol. 50, no. 6, pp. 1571–1577, Jun 2002.
 - [25] M. Yu, R. Vahldieck, and J. Huang, “Comparing coax launcher and wafer probe excitation for 10 mil conductor backed cpw with via holes and airbridges,” in *Microwave Symposium Digest, 1993., IEEE MTT-S International*, June 1993, pp. 705–708 vol.2.
 - [26] W. Haydl, “Resonance phenomena and power loss in conductor-backed coplanar structures,” *Microwave and Guided Wave Letters, IEEE*, vol. 10, no. 12, pp. 514–516, Dec 2000.
 - [27] C. Jiang, “Microwave and millimeter-wave integrated circuit systems in packaging,” Ph.D. dissertation, Technical University of Denmark, 2010.
 - [28] H. Zhang, N. Kavanagh, Z. Li, J. Zhao, N. Ye, Y. Chen, N. V. Wheeler, J. P. Wooller, J. R. Hayes, S. R. Sandoghchi, F. Poletti, M. N. Petrovich, S. U. Alam, R. Phelan, J. O’Carroll, B. Kelly, L. Grüner-Nielsen, D. J. Richardson, B. Corbett, and F. C. G. Gunning, “100 Gbit/s WDM transmission at 2 μ m: transmission studies in both low-loss hollow core photonic bandgap fiber and solid core fiber,” *Opt. Express*, vol. 23, no. 4, pp. 4946–4951, Feb 2015.
 - [29] Y. Chen, Z. Liu, S. Sandoghchi, G. Jasion, T. Bradley, E. Numkam Fokoua, J. Hayes, N. Wheeler, D. Gray, B. Mangan, R. Slavik, F. Poletti, M. Petrovich, and D. Richardson, “Multi-kilometer long, longitudinally uniform Hollow Core Photonic Bandgap Fibers for broadband low latency data transmission,” *Journal of Lightwave Technology*, vol. PP, no. 99, pp. 1–1, 2015.
 - [30] H. Zhang, M. Gleeson, N. Ye, N. Pavarelli, X. Ouyang, J. Zhao, N. Kavanagh, C. Robert, H. Yang, P. E. Morrissey, K. Thomas, A. Gocalinska, Y. Chen, T. Bradley, J. P. Wooller, J. R. Hayes, E. N. Fokoua, Z. Li, S. U. Alam, F. Poletti, M. N. Petrovich, D. J. Richardson, B. Kelly, J. O’Carroll, R. Phelan, E. Pelucchi, P. O’Brien, F. Peters, B. Corbett, and F. Gunning, “Dense WDM transmission at 2 μ m enabled by an arrayed waveguide grating,” *Opt. Lett.*, vol. 40, no. 14, pp. 3308–3311, Jul 2015.

Chapter 6

Summary and future work

In this chapter, a summary of the research work presented in thesis is discussed and major conclusions drawn from it are highlighted. In addition, an alternative epitaxial layer structure design to further improve the performance of an InP based MZM is discussed for future extension of this research work.

6.1 Summary

External optical modulators are the main building block of an optical fiber transmission system, which are deployed at the start of an optical link to encode the electrical data on to an optical carrier before transmitting it down the optical fiber. The primary goal of this dissertation was to design and develop the traveling wave electrode (TWE) InP based Mach-Zehnder modulators (MZMs) for the current and future optical communication systems. A complete overview of the important steps involved in an InP MZM design, from epitaxial material and traveling wave electrode design to the demonstration of a packaged modulator device in an optical communication system is given in thesis.

Epitaxial materials based on InP are naturally well suited for use in the optical transmitters and receivers operating in 1.3 μm to 1.6 μm and beyond. Also, the use of InP based materials enable integration of a number of devices on a single chip using various photonic integration techniques. The potential to integrate a number of otherwise discrete photonic devices on a single chip will lead to a compact, power efficient and cost effective solution to the next generation optical networks to fulfill ever increasing demand of the bandwidth. A brief discussion on the current state-of-the-art InP MZMs and their use to achieve spectrally efficient advanced modulation formats to increase the data rate per wavelength channel has been included in the **Chapter 1** of this thesis.

It is also shown that the possibility to achieve the driving voltages as low as 1.4 V with compact foot-print MZM devices on InP platform has made them front-runner for deployment in coherent pluggable transceiver modules.

Chapter 2 discussed different electro-optic (EO) effects present in III-V semiconductor compounds. The phase shifting regions in an interferometric arrangement in InP based MZMs make use of these EO effects i.e. quantum confined Stark effect (QCSE) in addition to linear electro-optic effect (LEO) in the multiple quantum wells (MQWs) sandwiched between p and n doped layers to achieve refractive index change (Δn) through externally applied electric field. The efficiency of the phase change ($\Delta\phi$) in the phase shifting arms of an InP based MZ interferometer is mainly dependent on the design of MQWs. The operational wavelength of an InP MZM is detuned from the excitonic absorption edge to achieve the modulation only due to change in real part of the refractive index with minimum residual absorption. Generally, the phase shifter sections in an InP MZM, make use of rectangular MQW structures to achieve the refractive index modulation at a detuned wavelength. In this work, we experimentally compared the QCSE induced Δn in asymmetrically ramped In-GaAlAs MQW structures grown sequentially on two n-doped InP wafers. Both the wafers with oppositely ramped MQWs were first characterized using photoabsorption measurement using surface-entry p-i-n diodes. The Δn and $\Delta\phi$ were extracted for TE polarized light using the Fabry-Perot fringe shift method in 1 mm long deep etched metallized ridge waveguides. It was observed that at 1550 nm wafer with ramp up MQWs achieves a V_π of 6 V as compared to 7 V in the other wafer with ramp down MQWs at the expense of higher absorption due to loss of excitonic peak confinement.

In **Chapter 3**, high frequency design of a traveling wave electrode (TWE) is presented. The main advantage of using the traveling wave approach for electrode design in an InP based MZM is that the bandwidth of the modulator is not limited by the RC constant as in the case of a lumped electrode. The three most important design considerations of a TWE design i.e. velocity mismatch (between co-propagating optical and electrical signals), microwave losses and impedance mismatch (between the TWE structure and termination impedance) were identified and the effect of each parameter on the analytically derived frequency response of the TWE was studied individually. These design parameters are directly related to the structural and material properties of the optical waveguide used in the phase shifter of an InP MZM. An equivalent circuit model approach was used to study the dependence of these variables on the

modulator waveguide layer stack. Based on this model, rigorous simulations were performed to identify the key design trade-offs in the modulator performance and the effects of structure parameters on the modulators characteristic impedance (Z_m), microwave attenuation constant (α) was established.

In **Chapter 4**, the optimized TWE design obtained using the equivalent circuit model was used to fabricate InP based MZMs. The fabricated modulator devices used 20 InGaAlAs/InGaAlAs MQWs in the p-i-n optical waveguide structure with a total intrinsic region thickness of 647 nm. MQWs were designed to operate in the optical C-band with the measured average PL peak at 1375 nm. The measured small-signal electrical response for the MZMs with the TWE lengths of 1.5 mm and 2.5 mm respectively were found to agree well with the simulated TWE structures with the GSG bond pads in HFSS. Also, the fabricated modulator devices exhibited a 3-dB EO bandwidth of 7.5 GHz with a V_π of 5.3 to 7 V in C-band. Large signal measurements showed that the modulators give a clearly open eye diagram up to 28 Gb/s NRZ-OOK despite the limited EO-bandwidth due to linear roll-off of the frequency response. Further investigations showed that the main limiting factor of the EO-bandwidth was the impedance mismatch between the TWE structure (measured value 35 Ω) and 50 Ω termination. The EO-bandwidth can be improved by terminating modulators with a lower value of impedance.

The highlight of this research work was presented in **Chapter 5** of this thesis. To avoid the predicted capacity crunch in the current SSMF based optical transmission systems, the 2000 nm wavelength range has emerged as a low loss and low latency optical transmission window when using hollow-core photonic band gap fiber (HC-PBGF) and high gain Thulium Doped Fiber Amplifiers (TDFA). In this work, we successfully developed and demonstrated the InP based MZMs to be used in optical transmitters operating at these wavelengths for the first time. These modulators employed strained rectangular InGaAs/InGaAlAs well/barrier MQW structures to achieve bandgap ~ 1850 nm and mainly used QCSE to achieve refractive index modulation at 2000 nm. Two generations of InP MZMs were designed and fully characterized for DC and high frequency performance. The TWE design remained the same as used in modulators operating at 1550 nm. First generation of MZM devices used 15 MQWs with total intrinsic region thickness of 810 nm. Fabricated devices demonstrated a V_π of 4 V for TWE length of 2 mm. In terms of high frequency performance, an EO-bandwidth of 9 GHz was achieved with clearly open open eye diagram for NRZ-OOK at 10 Gb/s. In order to further reduce the size and

power consumption of the InP MZM at $2\ \mu\text{m}$, we optimized the MQW core for an enhanced electro-optical overlap by increasing the number of MQWs to 25, resulting in the reduction of the V_π from 4 V to 2.7 V while maintaining the chip dimensions and EO bandwidth of ~ 9 GHz. The demonstrated modulator with a V_π of 2.7 V is the lowest reported so far at $2\ \mu\text{m}$. The modulator devices were packaged in a specially designed low cost RF interposer with an insertion loss of ~ 0.35 dB at 20 GHz to be used in a WDM transmitter. A WDM capacity of 40 Gb/s was achieved by using four 10 Gb/s NRZ-OOK externally modulated channels employing the packaged InP MZM. An OSNR requirement of 25-27 dB was measured to achieve a BER of 10^{-9} using direct detection.

6.2 Future work

In all the InP based MZMs demonstrated in this work operating at the wavelengths of 1550 nm and 2000 nm, used p-i-n epitaxial layer structures in the phase shifting regions of the interferometer arms. As discussed in detail in **Chapter 3** of this thesis, one of the main design goal in the high frequency design of the CPW-TWE in InP MZM is to match the characteristic impedance of the TWE structure to the system impedance of $50\ \Omega$ to avoid any reflections of RF modulating signal due to impedance mismatch which eventually limits the EO-bandwidth. However, in TWE based on p-i-n structure, this impedance matching is generally very difficult without sacrificing the modulation efficiency due large capacitance associated with sub-micron thick intrinsic region. The impedance of a TWE structure can be increased to $50\ \Omega$, by increasing the thickness of intrinsic region. However, this in turn increases the switching voltage (V_π) of the modulator due to low field across the MQW structure. Although, the increase in V_π can be compensated by increasing the length of TWE, which increases the microwave loss due to increase in RF field overlap specially with the lossy p-doped cladding layers. For p-doping between 10^{17} to 10^{18} per cm^3 p-doped InP is ~ 100 times more resistive as compared to n-doped InP layer.

In order to achieve the $50\ \Omega$ impedance in the TWE, many solutions have been proposed in recent years such as using n-i-n [1], n-p-i-n [2] or n-i-p-n [3] layer stack instead of a simple p-i-n structure for the TWE InP based MZMs. Using n-doped InP layers for both the signal and ground contact layers is useful to achieve low contact resistance which minimizes the RF attenuation. In addition, intrinsic region can be made thicker to achieve TWE with $50\ \Omega$ impedance. Low RF loss associated with n-doped InP layers due to high mobility allows to

overcome the reduction in phase efficiency due to thicker intrinsic region by increasing the length of the TWE.

The possible future extension of this work on InP MZMs can be to use n-i-p-n waveguide layer stack for TWE design to further increase the EO-bandwidth of the demonstrated modulators currently limited mainly by impedance mismatch. A schematic representation of conventional p-i-n and proposed n-i-p-n structure is shown in Fig 6.1.

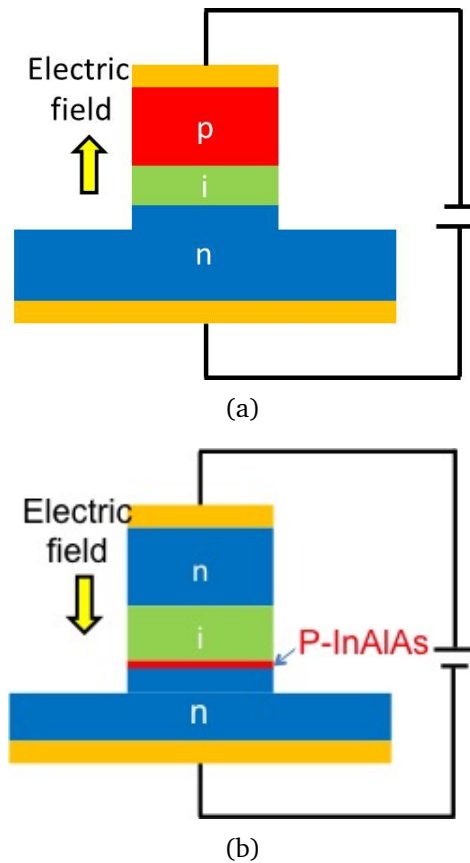
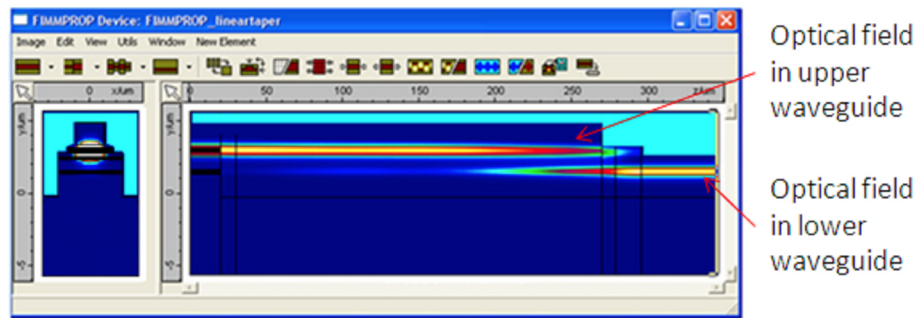


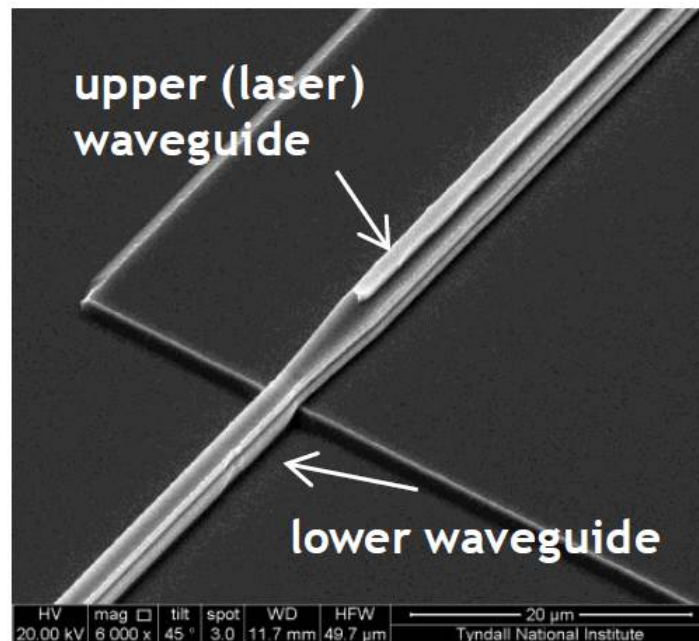
Figure 6.1: Schematic representation of biasing arrangement for: (a) Conventional p-i-n . (b) n-i-p-n.

The advantage of using an n-i-p-n structure is not only limited to increase EO-bandwidth of a MZM. Such an arrangement can also be used to integrate laser on the top of n-i-p-n layer stack using multi-guide vertical integration (MGVI) also called twin waveguide integration (TWI) platform. The main advantage of using MGVI to realize laser integrated MZM is that the laser and MZM waveguide can be grown in one epitaxial growth process which can improve the yield and cost issues associated with photonic integration approaches based on multiple growth methods [4]. Also, both the fabrication and growth process can be decoupled and optimized separately. In 2013, our group has al-

ready demonstrated the slotted tunable laser coupled to lower waveguide using the TWI approach with the coupling efficiency of 90 % [5]. Further developing n-i-p-n modulators will allow to take this TWI approach one step further by integrating laser to a MZM to realize a tunable, compact and power efficient optical transmitter. Fig 6.2 shows the implementation of this approach.



(a)



(b)

Figure 6.2: (a) Simulated optical coupling between upper and lower waveguide. (b) SEM image of laser to lower waveguide coupler using MGVI approach [5].

6.2.1 DC characterization of n-i-p-n

In order to investigate the properties of a n-i-p-n structure, an epitaxial layer structure was grown on SI-InP (100) substrate using MOVPE growth technique and characterized using different experimental techniques already discussed

in this thesis. The grown layer structure consisted of 20 InGaAlAs/InGaAlAs strained MQW structure with the total intrinsic region of 790 nm. A thin layer (120 nm) of p-doped InAlAs layer was used as a current blocking layer. InAlAs forms a type II hetero-junction with InP and acts as an effective current blocking layer. Also, it should be noted that for p-doping InAlAs, carbon (C) can be used as a dopant instead of widely used zinc (Zn) due to its low diffusion coefficient [6, 7].

Due to time limitation, in this thesis only basic work was performed to investigate the DC properties of n-i-p-n structure. The electro-optic (EO) properties of n-p-i-n structure were experimentally investigated by fabricating surface entry photodiodes using wet etching process and measuring the photabsorption reponse under applied bias. Before the photoabsorption measurements, current voltage (IV) characteristics of the fabricated circular diodes were measured. It is important to point out that in n-i-p-n structure, two back to back photodiodes are formed. In order to reverse bias the upper n-i-p diode, positive bias must be applied to the upper n-contact with respect to the lower n-contact as shown in Fig 6.1b. Figure 6.4 shows the IV response of a fabricated circular test structure. It can be seen that in forward bias the upper n-i-p diode is reverse biased and the measured leakage current is less than $50 \mu\text{A}$ even at the bias voltage of 15 V, which shows that InAlAs layer is working properly as a current blocking layer.

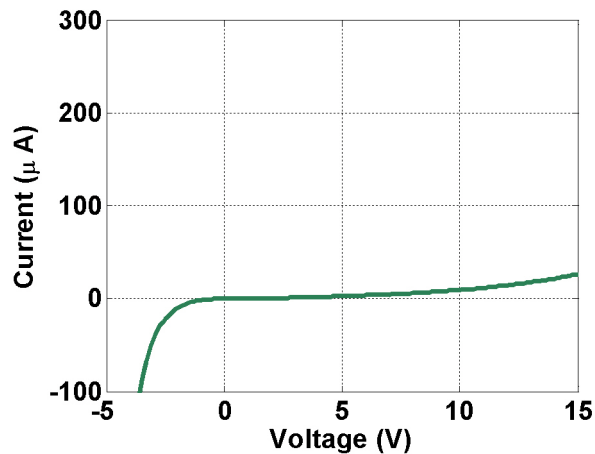
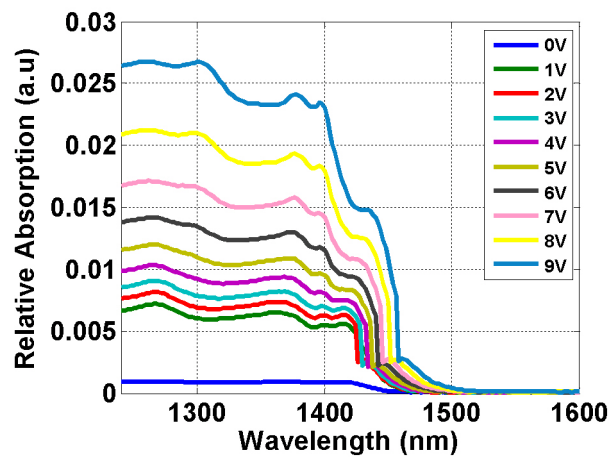


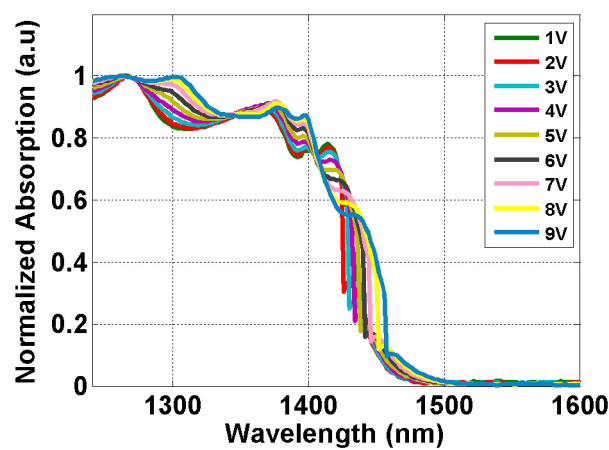
Figure 6.3: Current-voltage characteristics of circular test structure fabricated on n-i-p-n. Measured leakage current is $26 \mu\text{A}$.

Fig 6.4a, presents the measured photoabsorption response of a surface-entry test structure. Measurement results show that with the increasing bias the photocurrent increases as compared to the photoabsorption spectra measured for

the normal p-i-n epitaxial layer structures. This shows n-i-p-n semiconductor layer structure behaves as a phototransistor. For any finite absorption of light, the accumulation of generated holes occur at the p-blocking layer. The hole accumulation results in the decrease in barrier height and the current starts flowing across the barrier. It can be observed that this phototransistor behavior is much more dominant near and below bandgap where the light absorption is stronger. To visualize the QCSE in n-i-p-n structure in a better way, the measured spectra are normalized to maximum absorption as shown in Fig 6.4b. An excitonic absorption peak can be clearly seen at ~ 1410 nm, which red shifts with the applied voltage. However, the shift of excitonic peak is just 20 nm at applied bias of 9 V.



(a)



(b)

Figure 6.4: (a) Photoabsorption spectra for the n-i-p-n epitaxial layer structure under applied bias showing the phototransistor behavior. (b) Normalized photoabsorption spectra for the n-i-p-n .

The n-i-p-n wafer was further processed to form the metallized ridges using standard lithography and $\text{Cl}_2/\text{CH}_4/\text{H}_2$ inductively coupled plasma etching (ICP) to determine Δn and $\Delta\phi$ using Fabry-Perot fringe shift method. Initial IV measurements showed that all the fabricated ridges were short circuit. After further investigations, it was figured out that short circuit was due to the hydrogen passivation of C-doped InAlAs layer during the dry etch process based on hydrogen chemistry [8]. This problem was solved by using the hydrogen free dry etching chemistry during fabrication process. The fabricated devices were then used to measure Δn and $\Delta\phi$ for TE polarized input light at 1550 nm. Again an important observation was made that Δn is higher for the ridges fabricated along [011] direction i.e. perpendicular to major flat as compared to ridges fabricated along $[0\bar{1}1]$ direction i.e. parallel to major flat. This trend is opposite as compared to a normal p-i-n structure where phase shifters in MZMs should be fabricated along the $[0\bar{1}1]$ to maximize the Δn due to both LEO and QCSE. The higher Δn for ridge along [011] direction is due to the fact that LEO depends on the both the waveguide orientation and direction of applied electric field. As for n-i-p-n, the direction of applied electric field is reversed (shown in Fig 6.1) which results in positive Δn in direction perpendicular to major flat. Another important observation is that measured Δn is mainly due to LEO only in the grown n-i-p-n wafer and QCSE plays almost no role in refractive index variation as Δn becomes almost negligible along $[0\bar{1}1]$. The measured V_π to achieve $\Delta\phi$ in a 1mm long ridge waveguide was 14 V, which can be further minimized by optimizing the intrinsic region.

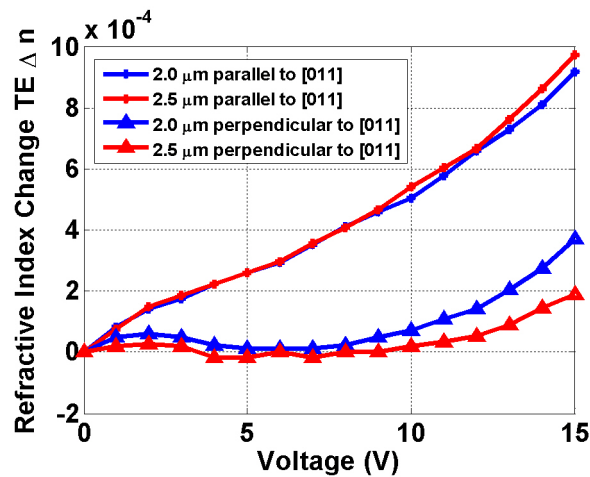


Figure 6.5: Measured Δn for TE polarized light at 1550 nm in 1 mm long ridge waveguides. The ridges were fabricated both along [011] direction (perpendicular to major flat) and $[0\bar{1}1]$ (parallel to major flat) for ridge widths of 2.0 and 2.5 μm .

DC characterization results show that n-i-p-n waveguide structure is a suitable candidate to replace the p-i-n structure and can be used to achieve InP based MZMs with EO-bandwidth 20 GHz.

References

- [1] K. Tsuzuki, T. Ishibashi, T. Ito, S. Oku, Y. Shibata, T. Ito, R. Iga, Y. Kondo, and Y. Tohmori, "A 40-gb/s InGaAlAs-InAlAs MQW n-i-n Mach-Zehnder Modulator with a drive voltage of 2.3 V," *IEEE Photonics Technology Letters*, vol. 17, no. 1, pp. 46–48, Jan 2005.
- [2] N. Kikuchi, H. Sanjoh, Y. Shibata, K. Tsuzuki, T. Sato, E. Yamada, T. Ishibashi, and H. Yasaka, "80-Gbit/s InP DQPSK modulator with an n-p-i-n structure," in *Optical Communication (ECOC), 2007 33rd European Conference and Exhibition of*, Sept 2007, pp. 1–2.
- [3] Y. Ogiso, Y. Ohiso, Y. Shibata, and M. Kohtoku, "[011] waveguide stripe direction n-i-p-n heterostructure InP optical modulator," *Electronics Letters*, vol. 50, no. 9, pp. 688–690, April 2014.
- [4] V. Tolstikhin, "Multi-Guide Vertical Integration in InP: PIC Technology for Cost-Sensitive Applications," in *2013 Conference on Lasers and Electro-Optics Pacific Rim*. Optical Society of America, 2013, p. TuN13.
- [5] J. R. O'Callaghan, B. Roycroft, W.-H. Guo, Q.-Y. Lu, C. L. Daunt, K. Thomas, E. Pelucchi, J. Donegan, F. H. Peters, and B. Corbett, "Slotted tunable laser with monolithic integrated mode coupler," in *Indium Phosphide and Related Materials (IPRM), 2012 International Conference on*, Aug 2012, pp. 273–276.
- [6] K. Kurihara, N. Arai, and K. Shimoyama, "Characteristics of 1.3 μm Laser Diode with Carbon-Doped InAlAs layer," *Japanese Journal of Applied Physics*, vol. 44, no. 3L, p. L451, 2005.
- [7] M. L. P. Ribeiro, B. Yavich, C. V. B. Tribuzy, and P. L. Souza, "Carbon doping of InAlAs layers grown by metalorganic vapor phase epitaxy," *Brazilian Journal of Physics*, vol. 32, pp. 362 – 365, 06 2002.

- [8] R. F. Kopf, R. A. Hamm, R. J. Malik, R. W. Ryan, M. Geva, J. Burm, and A. Tate, "ECR plasma etch fabrication of c-doped base InGaAs/InP DHBT structures: A comparison of CH₄/H₂/Ar vs BCl₃/N₂ plasma etch chemistries," *Journal of Electronic Materials*, vol. 27, no. 2, pp. 69–72.

Appendix A

Material Properties

The relation of the material conductivity (σ) to the applied electric field (E) and current density (J) is given in Eq A.1,

$$J = \sigma E \quad (\text{A.1})$$

Where σ can be defined as the the product of the mobile charge carriers and their mobilities as shown in Eq A.2

$$\sigma = q\mu_e n + q\mu_h p \quad (\text{A.2})$$

where q is the charge of the carrier ($q=1.6021766208 \times 10^{-19}$ C), μ_e and μ_h are the electron and hole mobilities in the semiconductor. The values of electrical properties of InP semiconductor material used in this thesis are summarized in Table A.1¹.

Table A.1: Electrical peroperties of InP.

Properties	Units	InP
Relative permittivity (ϵ_r)		12.56
Electron mobility (μ_e)	cm ² /V.s	4600
Hole mobility (μ_h)	cm ² /V.s	150

If the doping concentration (n,p) and electron,hole mobilities (μ_e, μ_h) of a doped semiconductor material are known, its electrical conductivity can be readily calculated using the above formulas.

¹S. Chuang, Physics of Optoelectronic Devices. Wiley, 707-708 (1995)

Appendix B

ABCD transmission matrix

The ABCD transmission matrix for the two port network is defined in terms of total voltages and currents as Eq B.1.

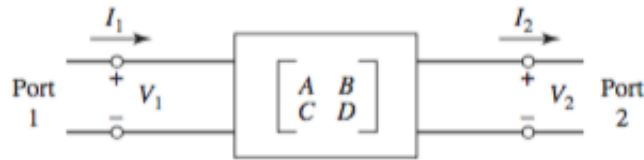


Figure B.1: A two port network.

$$\begin{bmatrix} V_1 \\ I_1 \end{bmatrix} = \begin{bmatrix} A & B \\ C & D \end{bmatrix} \cdot \begin{bmatrix} V_2 \\ I_2 \end{bmatrix} \quad (\text{B.1})$$

Using the ABCD matrix, propagation constant (γ) and impedance (Z) of the transmission line of length L can be determined as shown in Eq 4.11 and 4.12. The following relations are used to convert the measured S-parameters to ABCD transmission matrix².

$$\begin{aligned} A &= \frac{(1 + S_{11})(1 - S_{22}) + S_{12}S_{21}}{2S_{21}} \\ B &= Z_0 \frac{(1 + S_{11})(1 + S_{22}) - S_{12}S_{21}}{2S_{21}} \\ C &= \frac{1}{Z_0} \frac{(1 - S_{11})(1 - S_{22}) - S_{12}S_{21}}{2S_{21}} \\ D &= \frac{(1 - S_{11})(1 + S_{22}) + S_{12}S_{21}}{2S_{21}} \end{aligned} \quad (\text{B.2})$$

²David M Pozar, Microwave Engineering. 4th Ed. Wiley, 188-192 (2011).

B. ABCD TRANSMISSION MATRIX

Where Z_0 is the measurement system impedance, which is usually $50\ \Omega$.